COMPOSITE STRUCTURE OF TROPICAL CYCLONES IN THE SW INDIAN OCEAN

Bhawoodien A. Parker

Oceanography Department, University of Cape Town

A thesis submitted in fulfilment of the requirements

for the degree of Master of Science

September 1994

The copyright of this thesis vests in the author. No quotation from it or information derived from it is to be published without full acknowledgement of the source. The thesis is to be used for private study or non-commercial research purposes only.

Published by the University of Cape Town (UCT) in terms of the non-exclusive license granted to UCT by the author.

University of Cape Town

22 MAR 1995

ABSTRACT

This work examines SW Indian Ocean tropical cyclone (TC) structure as a function of movement using ECMWF gridded data. Analyses of the mean summer climate for the period 1987-1992 shown that conditions conducive to the development of TCs are present between the latitudes 5° and 15°S. Six westward moving TCs are selected to form the westward moving composite TC and four are used in the recurving TC composite from 3-days before the maximum surface intensity to 1-day after. The westward moving composite was found to have a steady TC signature. Comparisons were made with TC Firinga which passed near Mauritius on 29 January 1989. The recurving TC composite was found to exhibit rapid growth with sharp parameters tendencies. Interaction with a sub-tropical trough is seen in both TC composites. Upper level westerly winds create effective uplift which strengthens the recurving TC on the poleward side.

Spectral analysis of a rainfall index compiled from Mauritius data demonstrates spectral peaks at the seasonal and intra-seasonal scale. Three peaks were identified, one within the 40-60 day Madden-Julian Oscillation, one at 23 days and one with a 16 day oscillation. The 23 day oscillation was found to have a highest spectral power. The results of TC and rainfall analyses offer useful insights to the climate and weather of the SW Indian Ocean.

CONTENTS

PREFACE

Tropical cyclones (TCs) of the SW Indian Ocean constitute approximately 14% of the world annual total. SW Indian Ocean TCs are initiated in latitudes 5° to 15°S, 50° to 90°E and move generally southwest. These tropical storms are the cause of considerable destruction and loss of life due to strong winds, tidal surges and flooding. TCs which follow a consistent southwesterly track enable forecasters to predict the time of arrival, relative intensity of destructive winds and the region of heaviest rainfall allowing for adequate time for the issuing of warnings to the public. When TCs recurve towards the southeast their destructive potential appears to increase, particularly if landfall is in the SE quadrant. When track changes occur re-assessment of public warnings needs to be done within a short period of time, often increasing the forecast errors. The ability to distinguish between westward tracking TCs and those that recurve is of importance for increasing the forecasting accuracy and consequently reducing the destructive impact of these events.

ECMWF mean and anomaly composites of westward moving and recurving TCs are analysed to increase understanding of the kinematics and thermodynamics of these systems. Contour map and vertical section composites are used to:

1. identify features in the upper and lower level circulation which distinguish westward and recurving varieties, and
2. establish how the meteorological parameters evolve as the TC intensifies.

This thesis is divided into six chapters. In **Chapter 1**, the climatology of the region is reviewed with particular emphasis placed on TC activity. The initiation parameters required for TC formation and growth and the stages of TCs maturation are addressed. The motivation and goals of this thesis are outlined at the end of the chapter. In **Chapter 2**, the data and parameters used as well as the methodology followed are discussed. Intra-seasonal oscillations found in Mauritius rainfall are highlighted. In **Chapter 3**, the mean summer climatology of the region is analysed. Factors influencing the development and decay of TCs are emphasised. In **Chapter 4**, the evolution of westward moving and recurving TC composites is examined and discussed, and compared to TC Firinga. In **Chapter 5**, comparisons between the westward moving and recurving TCs are performed with the aid of anomaly composites. In **Chapter 6** an interpretation and discussion of the results is offered. The conclusions in this chapter address the needs of short-term forecasting.

Chapter 1

INTRODUCTION

The meteorology of the SW Indian Ocean region has only recently been studied on a scale comparable to that undertaken over other ocean basins a few decades ago The main cause of this lack of scientific effort has been attributed to greater interest in the Indian summer monsoon (MONEX) and the low economic status of the island countries of the region (Jury, 1993). SW Indian Ocean tropical cyclone (TC) climatology has been limited to keeping records of tracks, estimates of intensity, and overall TC frequency due to the sparsity of data. The commercial shipping lanes and air routes across the SW Indian Ocean are relatively busy, however compared to the Atlantic and Pacific basins, atmospheric data collection by these methods is less frequent (Merrill, 1988). The use of aircraft for retrieving information on the internal structure and dynamics of TC's still needs to be implemented in the SW Indian Ocean region (Middlebrooke, 1988; Weatherford and Gray, 1988a; Weatherford and Gray, 1988b). This thesis is aimed at filling part of this void by studying the area from 25°E to 100°E and 0° to 35°S (**Figure 1-1**).

Pathack (1993) suggested that the vertical tropospheric circulation systems, namely the African and Indian Ocean Walker circulation cells modulate the climate of southern Africa. It was also concluded that with relatively high sea surface temperatures (SST's) in the Central Equatorial Indian Ocean (CEI: 0-10°S and 60-80°E), the increased TC activity results in a 'poleward energy transport'. In cases with lowered

SSTs in the CEI ocean region and less TC's moving to the south, the 'transport of energy is zonal'.

1.1 Atmospheric circulation of the Southwest Indian Ocean region

Past studies of climate and weather variability over the tropical SW Indian Ocean has been hampered by a lack of knowledge of the region's atmospheric circulation and synoptic scale variability. This has been the result of inadequate observations and documentation of meteorological data due to the limited number of land based observation stations and scattered ship reports (Hastenrath, 1985). Indeed, only two radiosonde stations have operated regularly in the study period 1987 - 1992, namely Antananarivo, Madagascar and Diego Garcia, south of India. This is still the situation today despite the recognised importance this region has in modulating the climate and weather of the adjacent south-east African subcontinent and the island mass of Madagascar and its smaller island neighbours. For example, adjustments in the austral summer monsoon circulation have been shown to drive rainfall variations over Mauritius (Dennet, 1978; Padya, 1989), Madagascar (Williams, 1990), and southern Africa (Lindesay, 1988; Walker, 1989; Jury, 1992).

The presence of a climatic dipole between southern Africa and the SW Indian Ocean, for rainfall and outgoing longwave radiation (OLR) has been recorded in recent papers (Jury and Pathack, 1991). The climatic dipole was concluded to be a regional response to global oscillations, and found to govern the interannual variability of summer convection (Jury, 1992).

Although satellite based data are recorded, irregularity and poor resolution have deterred many scientists from studying this region intensively. International studies have, in the past, also been carried out in the region, such as the International Indian Ocean Expedition (IIOE) in the early 1960's. However a sustained, intensive study of the region has not been made.

In a study conducted by Martin et al. (1993) on the monthly rainfall over the Indian Ocean, Scanning Multichannel Microwave Radiometer (SMMR) data were used to identify stationary and mobile rainbands. The lack of island arcs and clusters such as in the Pacific and heavy ship traffic as in the Atlantic necessitated the use of satellite observations for their study. Of the five stationary bands found only one, an E-W band along and south of the equator, maintained a strong presence through all the seasons. This band extended from Sumatra's Selat Mentawi (Mentawi Strait) to the Mozambique Channel, with only its eastern extremity approaching the equator. It was speculated by these authors that this 'south equatorial' rainband was associated with the persistent south Indian Ocean equatorial trough and its concomitant ITCZ. From this study it was also shown that an annual cycle with a maximum monthly rain rate of over 200 mm in January dominated this rainband.

The mean surface wind (**Figure 1-2**) over the Indian Ocean exhibits a broad region of horizontal convergence in the lower latitudes north of Mauritius as well as some centres of convergence both to the west near Madagascar and to the east. Regions of mean surface divergence occur in the trades south of Mauritius during most months (Padya, 1989). The overlapping of weak upper easterly shear and warm SST's

conducive to easterly wave, monsoon vortex and TC genesis occurs in a narrow band from 10°-15°S latitude within the SW Indian Ocean (Riehl, 1979; Anyamba et al., 1982; Arkin et al., 1986). The intrusion of subtropical westerly flow above the 500 hPa level over TC's reduces the potential for development and maintenance of these systems (Padya, 1989) and consequently affect their frequency, intensity and regional impact (Jury and Pathack, 1991). This is often the case during global El Niños and during the winter season.

1.1.1 Anticyclones

The subtropical SW Indian Ocean is crossed by a succession of anticyclones, the centres of which are most frequently in the latitudes 32°S to 36°S but often migrate several degrees to the south or north of this belt, depending on the position of circumpolar standing waves (Preston-Whyte and Tyson, 1988; Padya, 1989). These anticyclones usually start as elongated ridges which bud off from the South Atlantic anticyclone south of or across the South African Plateau, intensifying on the SW Indian Ocean side of South Africa. The newly-budded anticyclone then grows and intensifies, and moves eastward first with a pronounced northerly component, then almost due east (Padya, 1989).

Mean wind charts reveal a distinct area of convergence in the 200 hPa wind field off the southeast coast of South Africa (Preston-Whyte and Tyson, 1988; Padya, 1989). This region, together with an area of strong convergence at the 200 hPa level near

100°E, are the main locations where anticyclones occur. These are more frequent in winter.

Although the above mentioned budding off process is the origin of the majority of anticyclones affecting this region, many cases have been documented where anticyclone cells with centres several degrees south of South Africa, i.e. 40°S latitude, cross into the SW Indian Ocean and continue moving east or north-eastward (Padya, 1989).

1.1.2 Air Masses and Fronts

Although under the influence of maritime tropical air north of 35°S, the SW Indian Ocean region also feels the effects of colder air, having its origins in the mid-latitudes. This cold air is gradually modified as it moves over the warm waters in the subtropics and tropics, becoming similar to the warm air-mass having its origin in the tropics (Hastenrath, 1985).

The boundary between the tropical and subtropical maritime air-masses is in constant movement, whether equatorward or poleward but seldom advancing further north than 15°S, coinciding with the mean southern limit of the 28°C SST isotherm (**Figure 1-1**). The advancing of a warm front, a southward moving zone of convergence, is seldom seen in this region of the southern subtropics.

Although cold fronts are seen to reach, and cross the latitude of Mauritius, especially in winter, the process is diminished in the austral summer when the ITCZ (thermal equator) is located further poleward at approximately 15°S near Madagascar, but 10°S north of Mauritius (Jury and Pathack, 1991; Jury et al., 1994), limiting the penetration of northward moving fronts.

In spite of the persistent subtropical trade winds, mid-latitude systems are able to induce variations of weather equatorward of 25°S, primarily in the winter in the lower atmosphere and in the upper troposphere in summer (Hastenrath, 1985).

1.1.3 Lower Tropospheric Waves

The presence of a wave in the easterlies is often a precursor to the formation of tropical cyclones in the Northern Hemisphere, but has been shown to be of less importance in the SW Indian Ocean (Padya, 1989; Jury, 1993; Jury et al., 1994). Even when these perturbations do not give rise to TC's they can produce copious rainfall, and can occur in any season irrespective of the depth of the surface easterlies at the time. Transient barotropic waves of the SW Indian Ocean have in recent years received some attention (Jury, et al., 1991). The presence of weak easterly winds through the troposphere is a requirement for the formation of tropical tropospheric waves (Holton, 1971; Riehl, 1979; Hastenrath, 1985), a condition often met there.

Through Hovmoller analysis of daily satellite imagery, OLR anomalies and ECMWF precipitable water departures Jury et al. (1991) was able to establish that SW Indian

Ocean transient convective waves travel westward with phase speeds of 2 to 4 m s^{-1}, have a 10 to 20 day period, a convective width of 800 km and wavelengths of approximately 3000 km. These waves were shown to exhibit a wide variety of structure and are slower and less coherent than in other tropical cyclogenesis regions (Jury et al, 1991).

With the aid of case studies Jury et al. (1991) demonstrated that summer rainfall events over southern Africa could be traced to westward moving tropical weather systems originating in the SW Indian Ocean. Upper easterly winds strengthening on the lee of a wave, a mid-tropospheric ridge guiding the system westward, while convergence within the system lifted the moist unstable layer by 5 km, were observed to coincide with major rainfall events over the escarpment of the sub-continent, as well as pulsing the supply of latent heat energy and cyclonic momentum regionally. This situation is especially common during wet years over SE Africa, but not during dry years when SW Indian Ocean convective waves are observed to be quasi-stationary (Jury et al.. 1991). The disruption of tropical inflow over the Mozambique Channel by southerly (westerly) wind components in the lower (upper) tropospheric levels (Matarira and Jury, 1992) allow for preferential development of TC's east of Madagascar when surges in the NW monsoon occur.

1.2 Tropical Cyclones

All cyclones, whether in the tropics or the extratropical regions, develop from depressions that intensify. The intensification often occurs over a few days depending on whether the surrounding atmospheric structure is conducive to further development. Cyclones that have their origins in the tropics (within 20° latitude of the equator) exhibit a very different character from those cyclones that originate in the midlatitude zones.

Tropical cyclones are renowned for their notoriously destructive powers owing to the extremely strong surface winds they produce and because of the huge waves and abnormal storm surges they can generate. TC's typically have life-spans of several days during which copious rainfall is released at rates of up to 100 mm hr^{-1}. Born out of the warm tropical oceans, bringing highly destructive winds to the areas they traverse, tropical cyclones have for many years held captive the imagination of people they affect in both awe and fear.

Wherever tropical cyclones are known to occur, loss of life and damage to property has always been a constant threat. One of the most economically important islands in the SW Indian Ocean region, Mauritius, is said to have spent most of its history recovering from successive tropical cyclones. This threat remains even with modern weather forecasting resources available to meteorologists who specialise in tracking and predicting the occurrence of these atmospheric phenomena.

This was clearly illustrated on August 24, 1992, when Atlantic tropical cyclone Andrew caused destruction and economic loss to Miami, Florida USA as had never been experienced from a natural disaster. It has been estimated that property to the value of US$ 30 billion was destroyed (Gore, 1993). The loss of less than 65 lives (Gore, 1993) can be attributed to residents taking heed of the evacuation and emergency calls broadcast by the National Hurricane Centre (NHC). The NHC, itself in the path of the storm, estimated sustained winds of 233 km hr^{-1} with gusts of up to 280 km hr^{-1}, after its wind measuring instruments were damaged by the storm.

Such disasters are however not confined to the tropics. In January 1984 a SW Indian Ocean tropical cyclone named Domoina made landfall in the north of the Natal province of South Africa (Preston-Whyte and Tyson, 1988). Inundation of low-lying regions occurred with a large number of lives lost. Road, rail and air transport was also disrupted for a lengthy period. Huge amounts of fertile topsoil were washed into the Indian Ocean during this event, resulting in a tremendous disruption to agriculture.

Since timely warning can make all the difference between loss of life or mitigation, tropical storms were a focal point of interest and study for many Europeans setting out for distant tropical lands in the age of discovery. Missionaries had built up a tradition of experience in many tropical cyclone areas based on local observations of wind, high cloud drift, sky colour and ocean state.

The study of TC's has received widespread attention from the scientific community all over the world resulting in the publication of numerous books on tropical meteorology

in which extensive knowledge is imparted to the reader about these destructive weather phenomena. Examples of such literature are Climate and Weather in the Tropics by Riehl (1979), Hurricanes: Their formation, structure and likely role in the tropical circulation by Gray (1979), The Hurricane and Its Impact by Simpson and Riehl (1981), Tropical cyclones, their evolution, structure and effects by Anthes (1982), Climate and Circulation of the Tropics by Hastenrath (1985) and Tropical Meteorology by Asnani (1993).

1.2.1 TC Life-Cycle

The life-span of tropical cyclones, although variable, averages out globally to about six days from the time of formation near the ITCZ, until they dissipate over land or are consumed by midlatitude weather regimes (Riehl, 1979). Study of the formation of tropical cyclones has highlighted that certain parameters are simultaneously pre-requisite for genesis to occur. The parameters which investigators have identified as climatologically essential (Gray, 1968, 1979) include:

1. *Sea surface temperatures* > 27 ℃,
2. *high degree of convective instability, as represented by* $\partial\theta_e/\partial p$,
3. *increased middle tropospheric relative humidity* > 50 %,
4. *low-level relative vorticity of order* $10^{-4}\ s^{-1}$, *and*
5. *Minimal vertical shear of the horizontal wind of* $< 10^{-4}\ s^{-1}$.

While these parameters are essential for the formation of tropical cyclones, their presence however does not guarantee that development will occur. These parameters are not all independent; for example, the vertical profile of θ_e is dependent on the sea surface temperature and middle level tropospheric relative humidity amongst other factors.

1. Sea surface temperature

The presence of a sea-surface temperature (SST) threshold below which TC's do not form was first recognised by Palmén (1948). The critical temperature of 27 °C found by Palmén has remained unchanged in spite of many individual and climatological studies since then. Using the SST criteria the SW Indian Ocean is seen to be favourable for TC genesis (SST > 27 °C up to 20 - 25°S in the months December to April), while the cooler SST's of the South Atlantic explain the lack of TC formation there. The exponential relationship between saturation vapour pressure and temperature, resulting in a rapid increase in specific humidity and equivalent potential temperature with temperature at a constant relative humidity explains, for example, why ocean temperatures of 29°C should produce more TC's than with 28°C, but not why genesis below 27°C is uncommon. Although a positive correlation between SST and TC genesis is found, the reason for there being a threshold temperature likely involves non-linear positive feedback between moisture convergence and diabatic heating. It should be noted that although TC genesis requires SST's > 27°C, TC's, once established can attain maximum intensities where SST's are > 25 °C (Evans, 1991).

2. *Convective instability*

The presence of deep cumulus convection in mature TC's, indicates that strong convective instability (large $\partial\theta_e/\partial p$) is associated with TC genesis. The tropical atmosphere is conditionally unstable (Xu and Emanuel, 1989; Montgomery and Farrell, 1993) more so in summer. Daily variations in $\partial\theta_e/\partial p$ are small and apparently unrelated to individual tropical cyclogenesis events. This may explain the relationship between cumulus convection and the environment. It is thought that as long as conditional instability exists, the intensity and properties of cumulus convection are correlated with parameters other than $\partial\theta_e/\partial p$ (Anthes, 1982). Sustained cumulus convection also works to saturate the environment and reduce the vertical gradient of θ_e; thus high values of θ_e in the mid-troposphere often accompany tropical convective systems.

3. *Middle tropospheric relative humidity*

To understand the need for high tropospheric relative humidity in TC formation, it is easier to ask why regions with low relative humidities are unfavourable for tropical cyclogenesis. Two reasons are apparent, the first is that convective clouds originating in the boundary layer are eroded by entrainment of dry air as they rise through the middle troposphere. Second, since the bulk of mass convergence in a TC occurs above the boundary layer, dry middle-level air would result in less total moisture convergence and reduced diabatic heating. High relative humidities throughout the troposphere thus contribute significantly to the total latent heat released via convergence above the boundary layer (McBride, 1979; Anthes, 1982).

4. Low-level relative vorticity

Unlike the previous parameters low-level vorticity has been found to have a strong correlation with intensification of TC's on the synoptic as well as climatological level. Intense convection is known to produce a low-level convergent wind field, as air flows towards the convection region. If the region contains zero absolute vorticity, such as along the equator in the Indian Ocean region, this convergence will produce ageostrophic convective systems rather than rotation systems. Cyclonic vorticity produces upward motion, while anticyclonic vorticity results in sinking motion owing to divergence terms in the vorticity equation (Holton, 1973). Since TC genesis requires strong convection and upward motion it is apparent that only in regions of cyclonic vorticity will strong convection be able to sustain TC's. The tropical monsoon regions of relative cyclonic vorticity have been recognised as quasi-steady features (Asnani, 1993).

5. Minimal vertical shear

The vertical shear of the horizontal wind in regions favourable for TC genesis has been found to be very weak. Asnani (1993) quoted that vertical shear not exceeding 10 m s^{-1} between the 950 and 200 hPa is generally found in these regions. The requirement of weak vertical shear can be traced to the need of TC's to maintain an upper-level ridge over the area of low surface pressure where cumulus convection will be enhanced by the large-scale lifting and the low-level convergence. Increased vertical shear of the horizontal wind will result in a tilting of the system inhibiting cumulus convection, convergent surface inflow and divergent upper-level outflow resulting in weak or non-developing tropical systems (Padya, 1989; Asnani, 1993).

The life cycle of a tropical cyclone is commonly divided into three stages by investigators. This is done primarily to aid in describing the processes occurring during its life-cycle, as well as a means of classifying and grouping certain types of storms. The three stages of the tropical cyclone are:

1. *the formative stage,*
2. *the mature stage, and*
3. *the decaying stage.*

Experience has shown that although TC's can be classified and described using the above notations it is almost impossible to ascribe time periods to each of the stages as each TC follows a unique genesis process. Some TC's spend most of their life in the formative stage, and others in the decaying stage, but very seldom do TC's persist in the mature stage for any length of time greater than the formative or decaying stages. A description of each of the stages of development follows:

1. Formative Stage

This stage of the life-cycle of TC's is not as well understood as the mature stage. In the absence of reliable forecast capability of TC formation, priority has been given to providing sufficient warning to inhabited coastal areas by predicting the track of the mature TC (Elsberry 1987; Elsberry and Abbey, 1991; Montgomery and Farrell, 1993). The formative stage may take from hours to days to complete depending on the strength and interaction rates of the five aforementioned initiation parameters.

This stage is associated with a relatively disorganised array of clouds and squalls. 80 - 85 % of mature TC's form from cloud clusters (CC's) originating in or just poleward of the ITCZ or monsoon trough, while the remainder form in the trade wind systems at a considerable distance from the ITCZ but often associated with special upper tropospheric flow patterns such as the tropical upper-tropospheric trough (TUTT) (Gray, 1968; Sadler, 1978). Strengthening of the surface equatorial monsoon surge, low-level cyclonic vorticity, high-level anticyclonic outflow and increased vertical velocities occur at this stage. Cross-equatorial interactions of the type described by Love (1985a; 1985b), where the winter hemisphere monsoonal outflow is enhanced and is subsequently followed by TC development in the summer hemisphere, appears to often modulate TC development in the SW Indian Ocean (Jury, 1993).

Maximum wind speeds occur at a radius of about 50 km from the centre, and surface pressure continues to fall (Simpson and Riehl, 1981). The presence of very weak vertical shear enhances growth by increasing the duration of upper-level support for an efficient energy 'evacuation' mechanism, which has been hypothesised to be essential for growth of the CC into a mature TC (Riehl, 1979; Montgomery and Farrell, 1993).

Additional intensification mechanisms, such as conditional instability of the second kind (CISK) and air-sea interaction theory, proposed as mechanisms for realising development of the mature TC structure, are however unsatisfactory when applied to the formation stage of a TC. A theoretical approach which focuses on the tropical CC environment effected by eddy angular momentum fluxes and associated upper-level

wave asymmetries (Pfeffer and Challa, 1981; Challa and Pfeffer, 1990) is an improvement on the CISK and air-sea interaction theories as it does not assume that transformation from a tropical disturbance to a rotary system has already taken place (Montgomery and Farrell, 1993). The momentum flux approach views TC's as forming efficiently in conjunction with cumulus convection and external forcing by the upper-level wave asymmetries rather than by solely internal co-operative processes between cumulus convection and frictional boundary layer convergence.

Research done by Lee (1989a; 1989b) on tropical cyclogenesis in the Western North Pacific has helped to define the important characteristics of TC formation by comparing composites of non-developing and pre-cyclone CC's. It was found that pre-cyclone CC's usually have stronger mid- to low-level inflow and cyclonic circulation (i.e. mean vorticity) over a larger radial extent than the non-developing CC's (Lee, 1989a). Within a radius of 6° - 8°, pre-cyclone CC's have lower surface pressure as well as a warmer middle- to upper-tropospheric warm core than the non-genesis CC. Similar mean vertical motions found for both the genesis and the non-genesis CC make this parameter an unreliable determinant of continued growth. It was however found that mean vertical motion reaches maximum strength during the transition phase from CC to TC, and was frequently manifested by a convective burst. The large inward eddy vorticity flux was found to be important as it allowed the tropical disturbance to increase its mean vorticity without increasing its transverse circulation (Lee, 1989b), maintaining an export of energy to the higher levels (McBride, 1981). When transition from the formative to the mature stage occurs eddy vorticity transport was found to be less important, as the mean TC circulation

(internal dynamics) produced sufficient inward vorticity flux to maintain the circulation (Ooyama, 1982; Lee, 1989a).

2. *Mature Stage*

Mature TC's from all the major TC regions show similarity in structure and organisation, resulting from the strong physical forcing associated with the release of latent heat and the relatively uniform characteristics of the lower boundary layer, i.e. the sea surface (Anthes, 1982). A strong rotational circulation with a large axisymmetric component and well organised deep convective clouds are present at this stage, often extending up to 12 km. The duration of this stage is even more variable than the previous; ranging from days to weeks, but most often lasting for a few days. During this stage the circulation extends to cover several hundred kilometres. The radius of storm inflow, upward motion and cumulus convection is 400 km. Central pressure can vary from just below the atmospheric mean (1013 hPa) to below 950 hPa in the case of extreme TC's, such as the SW Indian Ocean TC Monica in March 1968, where a pressure of 933 hPa was recorded at Rodrigues (Padya, 1989).

If no cirrus capping is present an eye is often discernible on satellite images. It is at this stage that the TC is at its most stable and destructive when rain as well as surface winds are at their strongest. The largest amount of energy for TC maintenance is obtained from convective heating in deep convection.

As mentioned in the formative stage section CISK and air-sea interaction theory has proven to be adequate in explaining the growth of the TC once a rotating vortex has been set up. CISK was initially described by Charney and Eliassen (1964) and Ooyama (1964) as the growth of tropical depressions by the utilisation of convective available potential energy (CAPE) through a co-operative feedback between cumulus clouds and large-scale flow.

Recent work suggests the importance of external forcing in regulating TC intensity and structural change (Shapiro and Willoughby, 1982; Holland and Merrill, 1984; Molinari and Vollaro, 1989, 1990). This has raised the hypothesis that the transformation from a tropical storm to a mature TC may require continual upper-level support, which may consist of one slowly moving upper-trough favourably located to promote the deep saturated convective ascent, or multiple encounters with upper-level troughs near the TC's trajectory (Montgomery and Farrell, 1993). These external forcing mechanisms have only been examined for individual cases as high density upper-level data is scarce, and is therefore inadequate to infer how common these processes are and to form any generalisations. Case studies such as that done by Molinari and Vollaro (1990), have however reinforced the idea of external forcing by fluxes of heat and eddy angular momentum from the upper-troposphere. They however caution that until a larger body of knowledge is acquired on this subject, the fluxes must be interpreted as arising from TC interaction with the environment and not a simple forcing in one direction or the other, since without the presence of the TC the eddy fluxes would not have occurred.

3. Decaying Stage

In the decaying stage the circulation weakens, expands further in size and becomes asymmetric or tilted about the centre. This weakening can very often be traced to the reduction or elimination of one or more of the parameters needed to initialise and maintain the system as described earlier. The eye wall becomes disorganised and is shielded by clouds. If the system maintains its strength until it reaches land, weakening will rapidly occur due to the friction caused at the lower levels where it is in contact with the land surface. The retardation of the TC in the surface layer results in a progressive tilting, and weakening of the system. When decay occurs over the ocean, the terminal stages may last for many days during which copious rain may still occur, but with lower wind velocities.

A numerical study undertaken by Tuleya (1994) on TC sensitivity to surface boundary conditions showed that when evaporation, the prime source of energy of TC's, is retarded the decay of the system quickly ensued. This would be analogous to the TC moving into a region of lowered SST and subsequently decreased surface relative humidity. The introduction of a surface boundary with heat capacity and conductivity similar to that of land, showed a decrease in the ground temperature beneath the storm. This has the impact of reversing the known positive feedback between low-level winds and evaporation (mature stage) to sustain TC's. A reduction in the equivalent potential temperature in the low-levels near the centre of the TC arises, and opposes that observed in TC's over the ocean.

1.2.2 SW Indian Ocean TC Prediction

Tropical cyclone prediction in the SW Indian Ocean is still in its infancy compared to the amount of attention it has received in other regions of the world where tropical cyclones are formed. Vermuelen and Jury (1992) assessed the accuracy and precision of tropical cyclone model forecasts by comparing the United Kingdom Meteorological Office (UKMO) track predictions with actual recorded track records, for the years 1989 - 1991. They found that track prediction up to day 3 was useful, with errors of over 500 km only occurring after day 3 from an initial TC placement error of 172 km. It was also noted that day 0 (zero) initialisation errors (163 - 182 km), often due to the lack of a distinguishable eye, compounded the errors in subsequent forecasts. Problems were encountered when TC's moved across the mountainous island mass of Madagascar, and model errors were found to decrease with increased westerlies in the 15°S latitude zone.

The inconsistency of forecast errors was suggested to have arisen due to parameterization problems. Predictability in the SW Indian Ocean region was found to be complicated by low-frequency surges of the north-west monsoon (Wang and Rui, 1990), the absence of background easterly flow in the 500 - 300 hPa layer, the irregular nature of high frequency barotropic waves, and a lack of upper-level observations near the ITCZ over the central ocean basin. A positive attribute found was the ability of the UKMO model to predict TC genesis in response to upper level dynamical forcing.

In a study conducted by Jury (1993) on climatological associations and TC characteristics of the SW Indian Ocean, it was found that the quasi-biennial oscillation (QBO) modulated the seasonal occurrence of TC's in the region, while a weaker correlation was found between the southern oscillation index (SOI) and TC frequency.

TC frequency was found to be highlighted by spectral peaks at 2.2 - 2.85, 4 and 10 years. The 2.2 and 4 year periods were suggested to be correlated to QBO and SOI type signals. The TC season prior to a global El Niño (-SOI) event was observed to have increased TC activity. A conflicting response to the El Niño, in which increased SST's in the CEI (Halpert and Ropelewski, 1992) favouring TC formation, and an increase in the upper subtropical westerlies unfavourable for TC formation was observed for the El Niño event.

Significant correlations of -0.37 (0 lag) and +0.38 (+1 lag) were found between TC frequency and QBO above the 90 % confidence limit in the period 1960-1992, suggesting increased TC's during an east phase QBO. This QBO forecast indicator for TC frequency found by Jury (1993) for the SW Indian Ocean region is opposite to that found for Atlantic TC prediction by Gray (1984), Gray and Landsea (1992) and Gray et al. (1992, 1993). In the Atlantic more TC's occur in west phase summers owing to the presence of a tropical easterly jet. In the SW Indian Ocean upper easterlies are weak and ' look for assistance' from the QBO.

1.3 Goals

In this thesis, composites are made of South West Indian Ocean tropical cyclone kinematic and thermodynamic properties, so that by comparing westward moving and recurving TC's, answers can be found to the following questions:

- What features in the lower and upper level circulation, pressure and thermodynamic fields distinguish westward and recurving TC's, before and during the period of maximum intensity?
- How do the meteorological fields evolve as the TC intensifies?
- What do the answers to the above questions tell us about the physical processes of TC development in the SWIO?

A secondary purpose of this study is to establish whether a substantial difference in the structure and mechanism of the two TC types is evident, and can improve the prediction of cyclone tracks as an aid in the early warning systems of countries in this region.

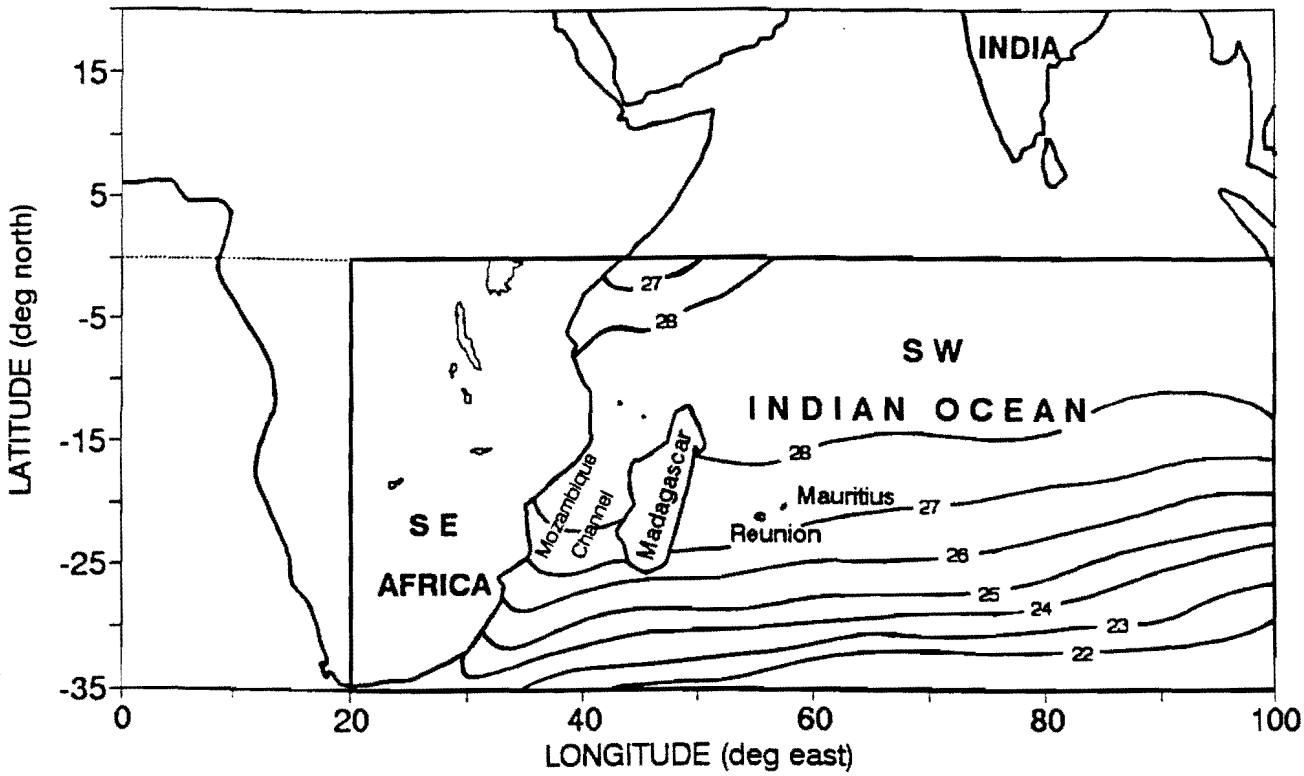

Figure 1-1: Location of the study region, 0°S - 35°S and 20°E - 100°E, with respect to the African continent and south-east Asia. February SST's are shown after Jury and Pathack (1991).

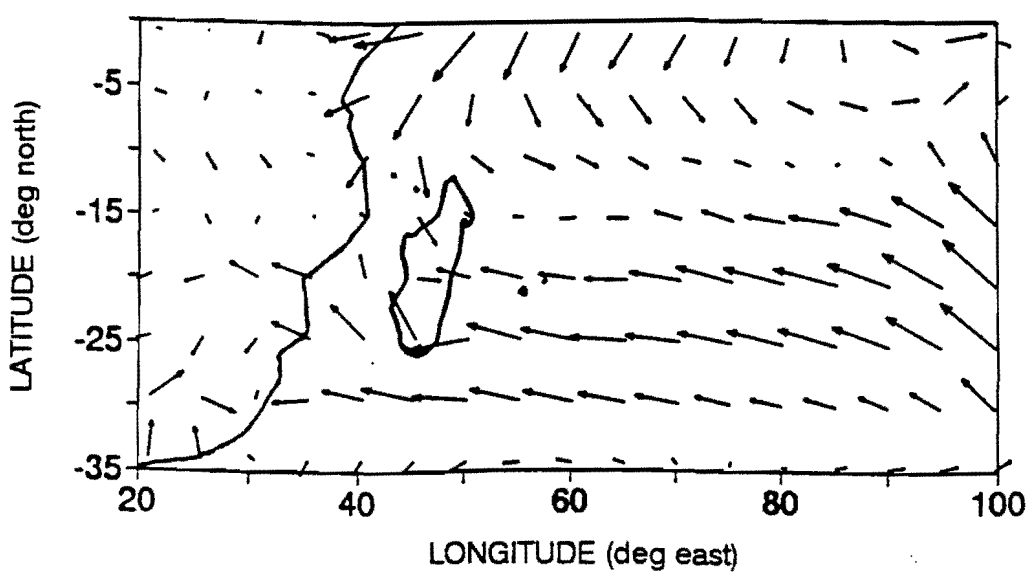

Figure 1-2 : Mean surface wind vectors for the period December to March, including years 1987 to 1992.

Scale ⟶ = 10 m s^{-1}, → = 5 m s^{-1}.

Chapter 2

DATA AND METHODOLOGY

In this chapter the procedures used to assimilate meteorological data by the European Centre for Medium Range Weather Forecasts (ECMWF) are outlined. Following this, the process of producing derived parameters will be presented and discussed. Finally the procedures used to form the mean composites and anomalies will be presented.

Studies concerning regional climatology and weather frequently make use of model enhanced global data sets of the atmospheric circulation. These data sets are especially useful for studying the physical processes of the atmosphere in regions where conventional data acquisition is limited. These model based data sets have, in studies by Bengston and Shukla (1988), been shown to be adequate for use in global climatic change studies. Early data assimilation techniques were imprecise. Riehl (1979), for example cautioned against the unscrupulous use of satellite derived upper wind data, owing to inherent bias towards cloudy areas. It is with this knowledge that caution is required when interpreting the fine detailed results of this thesis as almost all the data, except the Mauritius rainfall data used in this study, originates from the ECMWF.

2.1 Rainfall Data

Rainfall data from Pamplemousses, Mauritius are used to statistically define the period in which the SW Indian Ocean region receives maximum convective inputs. The island of Mauritius is located centrally in the region of study and rainfall records from this island have been found to be of a higher quality than records from other islands. Another factor considered was that it is the centre of the rapidly growing SW Indian Ocean tourist industry, geographically as well as financially. The annual monthly mean rainfall for the period 1960 to 1990 is 126 mm at Pamplemousses a low-lying station on Mauritius. The lack of a spatially extensive area over which daily rainfall data could be collected in the SW Indian Ocean region to create an areally averaged rainfall data set, necessitated the use of one station to identify months with greatest rainfall. Because of the spatially confined nature of TC's cases selected for analysis do not make use of rainfall data.

The months of December to April receive 160, 235, 232, 190 and 170 mm of rainfall respectively. The collective total for these months was 66 % of the annual total (1502 mm). Martin et al. (1993) used three years of Nimbus-7 SMMR data to map rainfall values for the Indian Ocean (1979 to 1981), yielding an estimated annual rainfall value of 1339 mm. The rain rate as presented by Martin et al. (1993) shows that in the region of Mauritius the monthly average is estimated to be between 100 mm and 150 mm. The monthly average of 126 mm calculated from the Pamplemousses rainfall data for the period 1960 to 1992 falls within this range. The annual cycle established by Martin

et al. (1993) using satellite radiometer data is highlighted by the spectral analysis (**Figure 2-2**) of nine-day filtered rainfall data (**Figure 2-1**).

The daily rainfall data for Pamplemousses was subjected to a nine-day running mean filter to reduce event scale noise and preserve intra-seasonal variations in rainfall. From **Figure 2-1** it is observed that the rainy season, i.e. November to May, is punctuated by periods of high rainfall from December to February, while a relatively steady decline in rainfall is experienced to mid April. At the end of April another rainfall peak is observed. From June steady light rainfall is received until the beginning of the next rainy season in November. Rainfall 'pulses' occur in early and late December, in mid January and early February, with an approximate mean interval of 20-30 days. This suggests that intra-seasonal oscillations (ISO) may interact in a regular manner with the seasonal cycle and monsoon.

Spectral analysis (**Figure 2-2**) of the filtered data reveals a dominant peak with a spectral power of 1328 and a period of approximately 370 days. This value is expected and consistent with the annual cycle seen in the mean monthly rainfall. On closer examination of **Figure 2-2** three more spectral peaks were observed, although the largest of these was only 1/40th the power of the annual peak. The smaller spectral peaks show cycles operating at 44 days, 23.5 days and 16 days, with the 23.5 day peak having a spectral power of 35, the 44 day peak a spectral power of 24 and the 16 day peak a spectral power of 10. A study by Singh et al. (1992) highlighted the 30-60 day ISO's found over the Indian monsoon region referred to as the Madden-Julian oscillations associated with a globally eastward-moving wavenumber 1 and 2 in the

tropics. The ISO with a period of 23.5 days and a spectral power of 35, occurs in the 20-30 day region for which Levey (1993) found 70% of the total rainfall (precipitation - evaporation) ISO of the southern Africa summer, and is in agreement with Anyamba (1993) who found poleward propagating outgoing longwave radiation (OLR) departures in the SW Indian Ocean.

Figure 2-3, representing the November-May 9 point smoothed daily rainfall for various 5 year epochs, shows the presence of high rainfall events interspersed with periods of relatively dry conditions. The ISO's observed in the October-September 1960 to 1990 average rainfall and described in **Figure 2-2**, is present for each of the 5-year periods represented in **Figure 2-3**. The highest rainfall average occurs in 1976-1980, where a value of > 20 mm is observed in mid January. The epoch with the lowest intra-seasonal variability is that of 1966-1970, when the average rainfall never exceeded 15 mm. For the epoch years of 1961-1965 and 1976-1980 the highest average rainfall occurred in January. The month of February received the highest average rainfall during the pentad years of 1971-1975, 1981-1985 and 1986-1990. The highest average rainfall thus always occurs in January or February except for the 1966-1970 epoch when March experiences higher rainfall.

Extreme rainfall events are not always associated with TC's. A case in point was the high rainfall of January 1980 and 1987 resulting from an exaggerated southward movement of the ITCZ to 20°S east of Madagascar, caused by a surge in the northwest monsoon (Padya, 1989).

2.2 ECMWF Data

The ECMWF forecast model came into operation at the end of 1978, coinciding with the FGGE to provide data for 'calibration' purposes from special research projects carried out in specific areas. The ECMWF maintains a high resolution global dataset from the FGGE year to enable assessment of parameterization changes that are constantly being introduced to improve the products. Re-analyses of the data carried out in 1985-1986 by Uppala (1987) found that the quality of the FGGE analyses was comparable to that of later years.

The ECMWF data assimilation system has been significantly improved in the last decade. A diagnostic study of global atmospheric circulation based on ECMWF data for the period 1979 to 1989 highlighted the revisions and changes performed on the data set (Hoskins, et al. 1989). The revisions undertaken since the beginning of 1985, to enhance forecasting and data reliability, are listed below:

February 1985 : Analyses scheme affecting large scale wind modified, TOVS high resolution satellite soundings introduced.

May 1985 : Model with reduced horizontal diffusion, shallow convection, modified Kuo-scheme and new representation of cloudiness introduced.

March 1986 : Inclusion of satellite precipitable water content data improves humidity analyses.

May 1986 : Three new levels in stratosphere introduced.

September 1986 : Introduction of new analyses, including analyses at model levels and further refined structure functions.

April 1987 : New parameterization of land surface processes and vegetation.

December 1987 : Tighter quality control of cloud drift winds.

January 1988 : Divergent wind analyses improved.

July 1988 : Modification to the analyses to increase effective resolution of analyses to 1°.

September 1988 : NOAA/NESDIS satellite data retrieval revised.

The tropical circulation analysis was improved, when in September 1982 diabatic initialisation was introduced, creating more realistic and intense Hadley and Walker circulations (Levey, 1993). The introduction of the T106 model in May 1985 (Hoskins, et al., 1989) resulted in higher temperatures in the tropical troposphere, increasing by 1.5°K at the 700 mb level. Temperatures at the 850 mb level correspondingly cooled by 1 °K, consistent with real data.

The data which are obtained by the ECMWF centre from the many independent sources require careful screening by constant correspondence with the data collectors. The quality and quantity of the data extracted from the variety of recording sources are often an indication of the source reliability. These data sets are obtained from observations made from rawinsondes, satellite sensors, pilot balloons, surface observations from ships, oceanic buoys, land stations and aircraft reports.

The atmospheric satellite data consist of temperature and moisture soundings as well as cloud tracked winds. Although satellite retrieved data has enhanced studies of the global circulation in sparsely populated land areas and expansive oceanic regions, extrapolation of data is still required to produce a regularly spaced grid of data for input into model forecasts. Comparison of the ECMWF output data with satellite

retrieved data, e.g. sea-surface temperatures, has been satisfactory in the model runs (Eymard, 1989).

With the discussion presented above on the evolution of the ECMWF model analyses, especially the important changes made with respect to the moisture parameters, it was considered that only data generated after 1985 would be used. Here six years of data, from 1986 to 1992 were analysed with the data window encompassing the area between 25°E and 100°E and 0°S and 35°S. Although data having a resolution of as high as 1° x 1° are available, the processed model data used for this study had a resolution of 2.5° x 2.5°. This was considered appropriate as the data resolution originating from actual measured values does not outweigh those having come from interpolated model analyses. The finer resolution data would thus not have significantly improved the quality of the analyses in the specified domain required for this thesis.

The six basic parameters obtained from the ECMWF centre were geopotential height, temperature, zonal wind component (u), meridional wind component (v), vertical movement (ω) and relative humidity. These parameters were obtained for the 1000, 850, 700, 500, 300, 200 and 100 hecto-pascal (hPa) atmospheric levels. It should be noted at this stage that the zonal and the meridional wind components were combined to enable the plotting of horizontal wind vectors. The vertical movement is analysed at the level of non-divergence where the maximum vertical movement would occur. The 500 hPa surface is used as the highest level for relative humidity as it is characterised by a mid-tropospheric minima between 20°S and 30°S (Hastenrath, 1985).

The size of the processed data files and time constraints resulted in the analyses of not more than three atmospheric levels. Parameters considered to be significant at only one pressure surface were only analysed at that surface. **Table 2-1** displays the primary parameters, the atmospheric levels at which they are calculated and the units used.

Table 2-1

List of primary ECMWF parameters used in this thesis.

PARAMETER	PRESSURE SURFACE (hPa)			UNITS
Geopotential height	850	---	200	gpm
Temperature	850	---	200	°C
Zonal wind	850	500	200	$m\ s^{-1}$
Meridional wind	850	500	200	$m\ s^{-1}$
Vertical movement	---	500	---	$Pa\ s^{-1}$
Relative humidity	850	500	---	%

2.3 Derived Meteorological Parameters

The reason for producing secondary parameters is that such values, when used in combination with primary parameters yield results which elucidate meteorological kinetic and thermodynamic structure. The derived parameters as well as the levels at which they are represented are listed in **Table 2-2**.

Table 2-2

Table of derived parameters calculated and used in this thesis.

DERIVED PARAMETER	PRESSURE LEVEL (hPa)			UNITS
divergence	---	---	200	s^{-1}
vorticity	850	500	200	s^{-1}
kinetic energy	850	---	200	$J\ kg^{-1}$
precipitable water	integrated	surface	to 300	mm
water vapour flux	integrated	surface	to 500	$g\ kg^{-1}\ ms^{-1}$
equivalent potential temperature	850	500	200	°K

2.3.1 Divergence and Vorticity

Divergence (δ) is the stretching experienced by the air in the local horizontal, while vorticity (ζ) is the rate of change of spin experienced by the air in the local horizontal. These two parameters are calculated using the following relationships:

$$\delta = \partial u / \partial x + \partial v / \partial y \qquad \textbf{Eq. 2.1}$$

$$\zeta = \partial v / \partial x - \partial u / \partial y \qquad \textbf{Eq. 2.2}$$

where: u = zonal wind component

v = meridional wind component

x = longitudinal distance

y = latitudinal distance

Comparing **Eq. 2.1** and **Eq. 2.2** a relationship between the divergence and the vorticity is evident and can be expressed as follows:

$$f\delta = -\partial\zeta / \partial t \qquad \textbf{Eq. 2.3}$$

where: t = time and f = coriolis parameter

From **Eq. 2.3** we see that the tendency of anticyclonic (cyclonic) vorticity is associated with positive (negative) divergence. As expressed in this thesis, negative divergence represents convergence and negative vorticity is cyclonic in the southern hemisphere.

2.3.2 Horizontal Kinetic Energy

Kinetic energy (KE) is the energy of motion and can be calculated readily from the horizontal wind components using the following formula (Hastenrath, 1985) :

$$KE = \tfrac{1}{2} V_h^2 \qquad \text{per unit mass} \qquad \textbf{Eq. 2.4}$$

where: V_h = horizontal wind speed

The wind speed, V_h, is easily defined in terms of the longitudinal and latitudinal components of the horizontal wind as follows:

$$V_h = (u^2 + v^2)^{\frac{1}{2}} \qquad \textbf{Eq. 2.5}$$

where: u = longitudinal wind component

v = latitudinal wind component

Since the production of kinetic energy is a function of the horizontal wind and it in turn is a result of pressure gradients (air moving quasi-geostrophically around high and low pressure), kinetic energy is thus considered to be exported by the high pressure cells as work is being done, through pressure, on its boundary. Padya (1989) has explained that the high kinetic energy found in TC's should thus be looked upon as resulting, in part, from the work done by pressure forces on the convergent winds at the boundaries of the low, and of transport into the low by these converging winds.

2.3.3 Precipitable Water

Precipitable water (PW) is a useful parameter which depicts the moisture content of the atmosphere calculated between two points situated vertically above each other. PW of a column of air is theoretically defined as the thichness of water in millimetre that would be obtained if all the water of the column were condensed onto a horizontal plane of unit area. It is defined mathematically using the following formula:

$$PW = (\rho g)^{-1} \int_{p_1}^{p_2} x \, \delta p \qquad \textbf{Eq. 2.6}$$

where: x = the mean humidity mixing ratio,

p_1, p_2 = the pressure levels between which the PW is being determined, and

g = 9.8 m s^{-2}, gravitational constant.

ρ = density of water

For this study precipitable water values were integrated between the surface and the 300 hPa level, acknowledging that surface moisture over the oceans is essential to TC genesis. The presence of land masses having altitudes in excess of 1000 metres (i.e. Africa) necessitated that PW integration over such areas were made from the 850 hPa level to the 300 hPa level. An explanation of the mean humidity mixing ratio and its calculation is supplied in **Appendix A**.

2.3.4 Water Vapour Flux

Water vapour flux (Q) is defined as the advection of precipitable water by the horizontal wind. The total horizontal mean flux of water vapour (g cm^{-1} s^{-1}) obtained through vertical integration as represented below:

$$Q = g^{-1} \int_{p_1}^{p_2} q \, V \, \delta p \qquad \textbf{Eq. 2.7}$$

where: q = specific humidity (g kg^{-1}),

g = 9.8 m s^{-2}, gravitational constant,

V = horizontal wind vector in the layer (δp)

p_1, p_2 = the pressure levels between which Q is being determined.

The individual qu and qv components of the total two-dimensional horizontal wind are combined to give a water vapour flux vector, QV, which has both magnitude and direction. The magnitude is represented by:

$$\sqrt{(qu)^2 + (qv)^2} \qquad \textbf{Eq. 2.8}$$

and the direction by:

$$\arctan\left(\frac{qu}{qv}\right) \qquad \textbf{Eq. 2.9}$$

Since the concentration of atmospheric moisture is highest in the lowest levels of the troposphere and Walker and Hadley overturning results in upper flows often opposing lower levels, it was felt that incorporating the horizontal wind above 500 hPa may distort the results. Integration was thus carried out from the surface up to the 500 hPa level.

2.3.5 Equivalent Potential Temperature

Equivalent potential temperature, θ_e, is a useful parameter for studying cumulus convection, as it combines temperature and moisture variables (Preston-Whyte and Tyson, 1988). It is defined as the final temperature which a parcel of air attains when it is lifted dry adiabatically to its lifting condensation level, then pseudo-wet adiabatically to a great height (releasing all its water), then finally brought down dry adiabatically to 1000 mb (Holton, 1972; Bolton, 1980). With this definition it is

apparent that if $\partial\theta_e / \partial z$ is negative the atmosphere is potentially unstable. Malkus and Riehl (1960) showed that the warmest possible column consisting of air which ascended from the surface at 1000 mb, under moist adiabatic conditions would have a θ_e value of 350 °K. Anthes (1982) showed that the minimum θ_e value obtained for the mean tropical cyclone is above 335 °K while that of the mean tropical atmosphere attains a minimum of less than 330 °K. θ_e values within the eye of tropical cyclones are often reported to be above 350 °K (Anthes, 1982). Since very few in-depth TC studies incorporating θ_e calculations have been carried out in the SW Indian Ocean region, there is limited information on the θ_e profile for the average TC in this region. Case studies of single TC's do exist such as that for TC Danielle (Jury, 1993) which will be used in the TC composite section to check for reliability. Due to the intensive TC studies carried out in other regions, individual θ_e profiles there can be compared. The equivalent potential temperature algorithm was obtained from Bolton (1980) and is expressed mathematically as follows:

$$\theta_e = T_K \left(\frac{1000}{p}\right)^{A\,(1 - Br)} \times \exp\left[\left(\frac{3.376}{T_L} - C\right) \times r\,(1 + Dr)\right] \qquad \textbf{Eq. 2-10}$$

where: T_K = the absolute temperature (°K),

T_L = the temperature at the lifting condensation level (°K),

p = the pressure (hPa),

r = the mixing ratio at the initial level,

and constants:

$A = 2.854 \times 10^{-1}$

$B = 2.8 \times 10^{-4}$

$C = 2.54 \times 10^{-3}$

$D = 8.1 \times 10^{-1}$

(See Appendix A for a discussion on the computation of θ_e)

2.4 Composite Analyses

In the study of climate and weather, experience has shown that when there is a scarcity of data available for the study of specific atmospheric phenomena, compositing of data representing similar cases can and will, often yield results which would not otherwise have been identified. Although the characteristics of individual cases may become diminished when composites are formed, this may be desirable feature when it eliminates the small-scale variations peculiar to each individual case. The outstanding feature that makes this method of studying atmospheric phenomena exciting is that it enhances and highlights the features which are common to those specific atmospheric phenomena.

The advantage is that many observations over a period of years can be collected and located with respect to the cyclone centre, resulting in a dense network of observations that can then be averaged in the individual grid boxes defined by the appropriate co-ordinate scheme. From this, average fields of various meteorological parameters can be

analysed. If enough data is available, the data set can be stratified according to characteristics such as intensity, movement (as used in this thesis), or structure, and comparisons can be made between the different data subsets.

From the perspective of investigating tropical cyclone activity in the SW Indian Ocean and its related effects on SE Africa it is clear that the lack of land based radiosonde stations was the major reason for using ECMWF model data in this investigation. Although there are stations in the active cyclone region that record data at regular intervals, the possibility that any one station is within 10° latitude of a tropical cyclone centre at any given time is very small. In addition most SW Indian Ocean islands are very mountainous and distort TC structure.

The ECMWF model data are distributed much differently with respect to cyclone centres than are data from radiosonde stations. Whereas radiosonde stations collect data at fixed times from fixed locations, the ECMWF data offers a more even distribution in time and space.

The composite analysis technique is relied upon extensively in this study. Two basic compositing procedures are used to produce, i) a mean January - February climatology for the SW Indian Ocean, and ii) a mean composite structural map for westward moving (WM) and recurving (REC) TC's. A third type of composite is produced by subtracting the mean January - February climatology from the mean composite TC structure for the WM and REC cases to produce anomalies.

A description of the techniques used to produce the three different composite types is given below. It should be noted that vertical sections are plotted with pressure linearly to emphasise boundary layer structure.

2.4.1 Mean Climatology Compositing Procedure

As mentioned earlier the mean SW Indian Ocean summer climatology is calculated using the months of January and February, omitting 29 February in leap years for the purposes of consistent computations. Only these two months are used to form the mean composite as the analyses of the rainfall data (**Figure 2-1**) shows that they are the months during which the SW Indian Ocean receives the largest volume of rain, as well as being the only two months during which greater than 200 mm has been recorded. SW Indian Ocean SST's and TC frequency also peak during February (see **Figure 2-1**). The omission of December, March and April in forming the mean is partially due to time and space constraints.

The mean structure for each of the basic parameters as well as the derived parameters (to be discussed later in this chapter) was calculated by simply adding the values at each specific grid location, at the specified pressure surface for each day. This value is then divided by the number of days added, to produce an average representing the mean climatology. Since the region over which the mean summer climatology (MSC) is calculated remains the same, unlike the mean TC composite which 'move' with the TC centre as explained in the previous section, only horizontal maps are produced for this analyses. Vertical sections for the mean climatology are not presented since the

calculation of vertical section anomalies resulted in unclear, noisy structure suggesting that the removal of the vertical background mean was not suitable here.

2.4.2 Mean TC Compositing Procedure

The procedure for calculating the two TC composites is similar to that used for producing the mean climatology composite, except that the composite area is not fixed in space or time. This is because the centre of the composite grid used to form the TC mean is relative to the TC centre for the particular composite day, and is thus moving with the TC. Since three days of TC activity are analysed, two before the day of maximum intensity and one after, the need arises at this stage to define what is meant by the 'day of maximum intensity' as well as defining the two categories of TC composites produced.

Firstly the day of maximum intensity (D-0) is defined as the day on which maximum surface wind speed is attained after tropical cyclone status (surface winds > 32.5 m s^{-1}) is acquired. Secondly, the two composite categories described in this thesis are the westward moving (WM) and the recurving (REC) tropical cyclone. Movement here referring to the track followed by a TC one day prior to it reaching maximum intensity to one day after. Westward moving (WM) cyclones are thus TC's moving from the northeast to the southwest, while recurving (REC) cyclones are those that move southeastward prior to the day of maximum intensity. The TC dates are listed in **Tables 2-3a** and **b** according to the following designation:

a) three days prior to (D-0), designated (D-3),

b) one day prior to (D-0), designated (D-1), and

c) one day after (D-0), designated (D+1).

The compositing grid used in this study is a square grid that uses cartesian co-ordinates, its dimensions are 20° latitude by 20° longitude. Grid points are situated at every 2.5° latitude and longitude resulting in 9 x 9 point grid, with the centre of the grid coincident with the estimated centre of the TC.

Table 2-3a

SW Indian Ocean TC's used in forming the Westward Moving (WM) TC composite (1987 - 1991).

TC NAME	SEASON	D - 3	D - 1	D + 1
Ezinina	Feb 1988	11	13	15
Barisaona	Nov 1988	14	16	18
Edme	Jan 1989	21	23	25
Firinga	Jan 1989	25	27	29
Hanitra	Feb 1989	20	22	24
Gregoara	Mar 1990	15	17	19

Table 2-3b

SW Indian Ocean TC's used in forming the Recurving (REC) TC composite (1987 - 1991).

TC NAME	SEASON	D - 3	D - 1	D + 1
Gasitao	Mar 1988	17	19	21
Alibera	Dec 1989	18	20	22
Dety	Feb 1990	02	04	06
Bella	Jan 1991	27	29	31

For each of the TC cases, the position of the centre was determined for each individual cyclone day (D-3, D-1, D+1). The position of the centre was obtained from the annual Mauritius tropical cyclone reports, the Reunion tropical cyclone reports and computer data records of SW Indian Ocean tropical cyclone track analysis (Appadu and Ragoonadeen, 1989a, 1989b,1990; Appadu and Goolaup, 1991; Ecomier, 1992). **Figures 2-4a** and **b** show the tracks that the individual TC's followed across the SW Indian Ocean study region in the 1986 - 1992 study period.

Once the individual grid data was extracted for each parameter, calculation of the average for each day was performed in the same way as had been done for the mean SW Indian Ocean climatology. In addition to parameters being represented in the

horizontal, those that exhibited measurable changes with increasing height are analysed in the vertical along the meridional section through the composite TC centre. The mean TC composites calculated for the WM and the REC cases are used to analyse structural evolution while the anomalies (next section) are used to contrast the WM and REC cases. Comparisons are also made with an individual TC case Firinga, to assess how the compositing procedure 'masks' the observed structure and intensity of the SW Indian Ocean TC.

2.4.3 TC Anomaly Calculation

The TC anomalies are calculated by subtracting the MSC from the WM and the REC TC composites to produce anomaly composites. As no vertical sections were produced for the MSC, the anomaly composites are represented by horizontal maps. Calculation of the average position of the WM and REC TC's required that the position of the individual TC be known, as shown in **Tables 2-4a** and **b**. A mean position is obtained by adding the WM and REC TC day centres and obtaining the average composite centre of 72.5°E, 15°S.

As will be explained in the chapter concerning the TC anomalies, the composites are used to compare the structure of the WM and the REC TC for each day analysed in a similar time frame from D-3 to D+1. Recognising kinematic, thermodynamic and moisture differences should enable one to produce a conceptual model in which the progression of the WM and the REC TC is recognised for operational forecast purposes.

Table 2-4a

WM TC's centre positions and calculated mean centre (1987 - 1991).

TC NAME	POSITION of CENTRE (°E, °S) D - 3	D - 1	D + 1
Ezinina	90 10	87.5 12.5	80 12.5
Barisaona	80 10	72.5 12.5	67.5 17.5
Edme	82.5 15	82.5 20	75 25
Firinga	65 12.5	65 15	55 20
Hanitra	85 12.5	82.5 12.5	80 17.5
Gregoara	85 12.5	82.5 15	80 20
WM TC	82.5°E,12.5°S	80°E,15°S	72.5°E,20°S
WM TC D-3, D-1 and D+1 average :			**77.5°E,15°S**

Table 2-4b

REC TC's centre positions and calculated mean centre (1987 - 1991).

TC NAME	POSITION of CENTRE (°E, °S) D - 3	D - 1	D + 1
Gasitao	65 15	62.5 17.5	72.5 22.5
Alibera	60 10	57.5 12.5	55 12.5
Dety	70 10	67.5 15	67.5 17.5
Bella	65 17.5	62.5 17	62.5 20
REC TC	65°E,12.5°S	62.5°E,15°S	75°E,17.5°S
REC TC D-3, D-1 and D+1 average :			**65°E,15°S**

Synthesis

A methodology for the analyses of the ECMWF meteorological data has been presented. The limitations of this work have been recognised and outlined. Where appropriate it has also been emphasised how this work aims to fill a gap concerning the understanding of TC structure and movement in the SW Indian Ocean region to aid short-term forecasting. Definitions of derived parameter calculations were presented, although some are kept for the appendix.

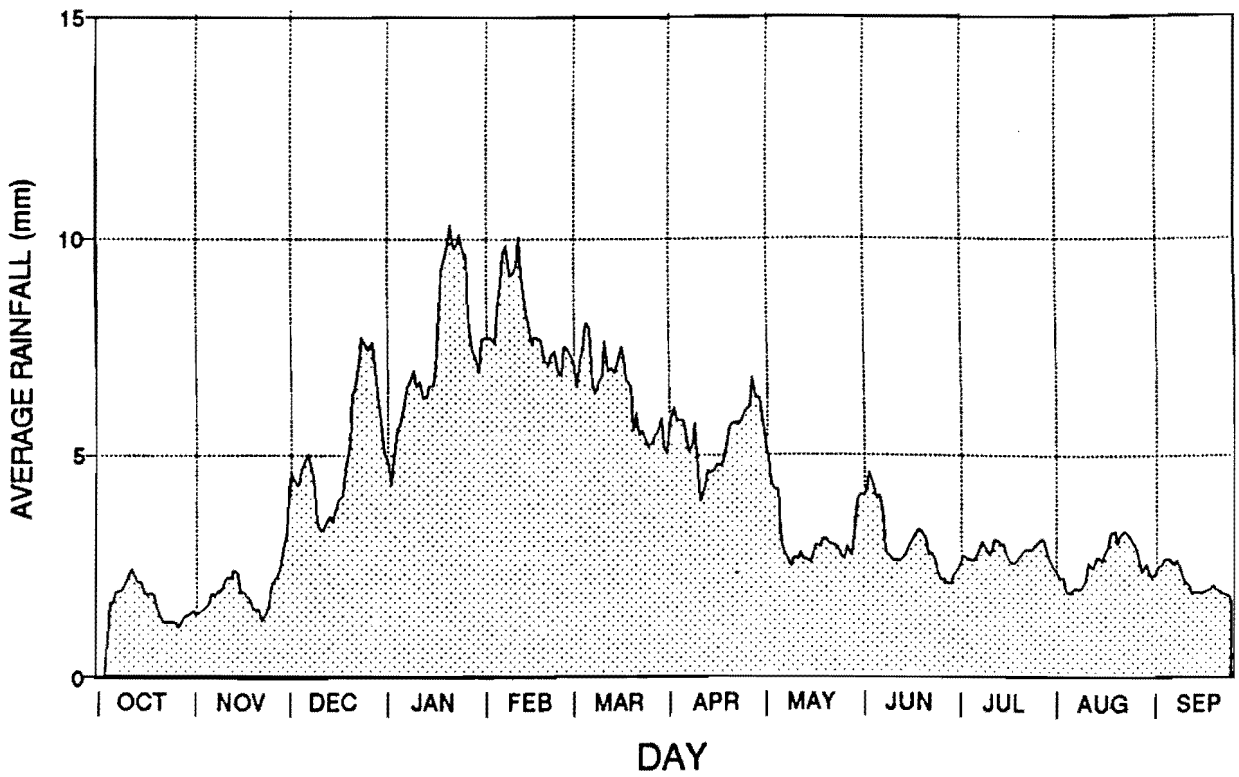

Figure 2-1 : Pamplemousses 9-day filtered average rainfall.
Period 1960 to 1990.

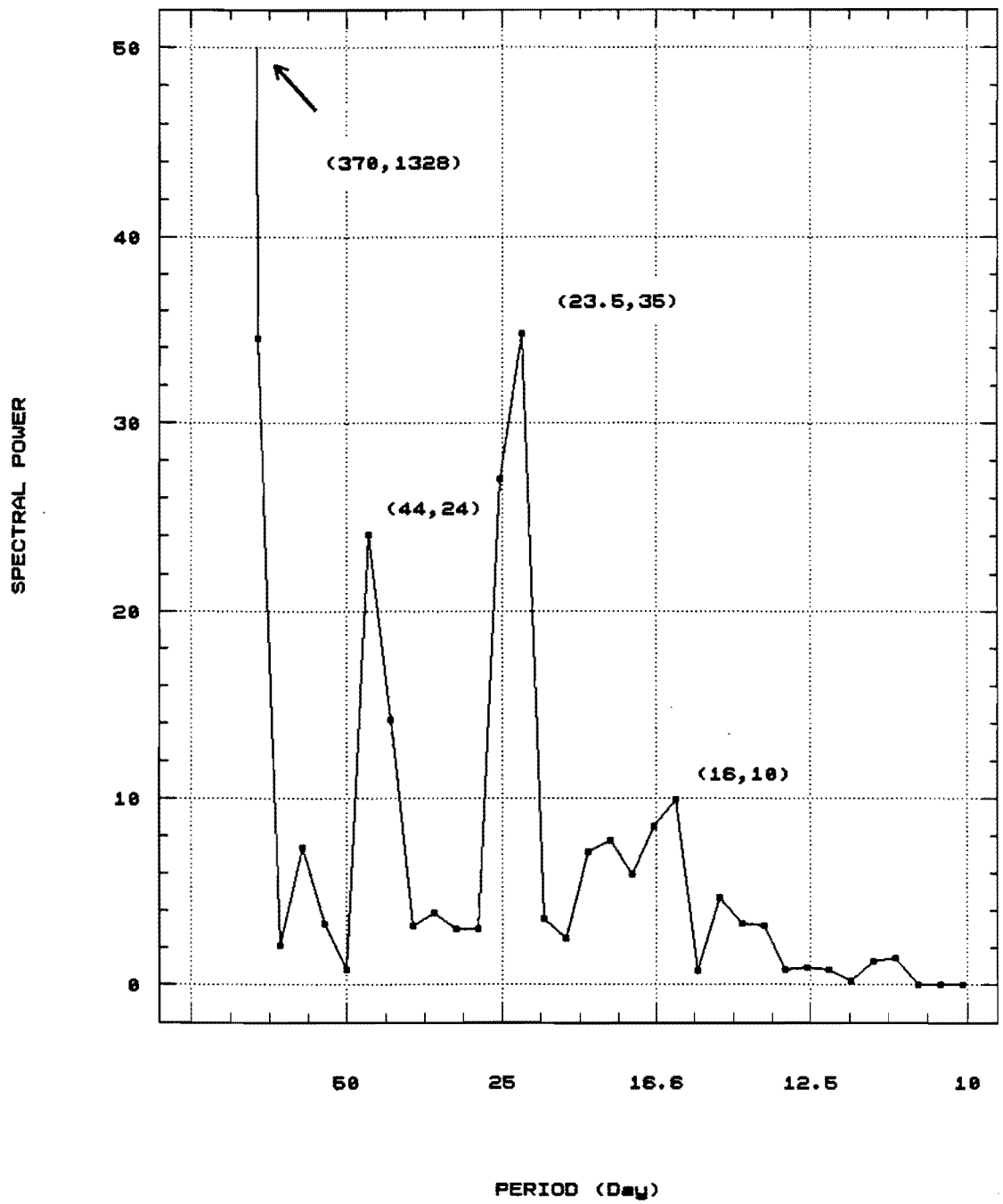

Figure 2-2 : Spectral power plot of 9-day filtered data.
Period 1960 to 1990.

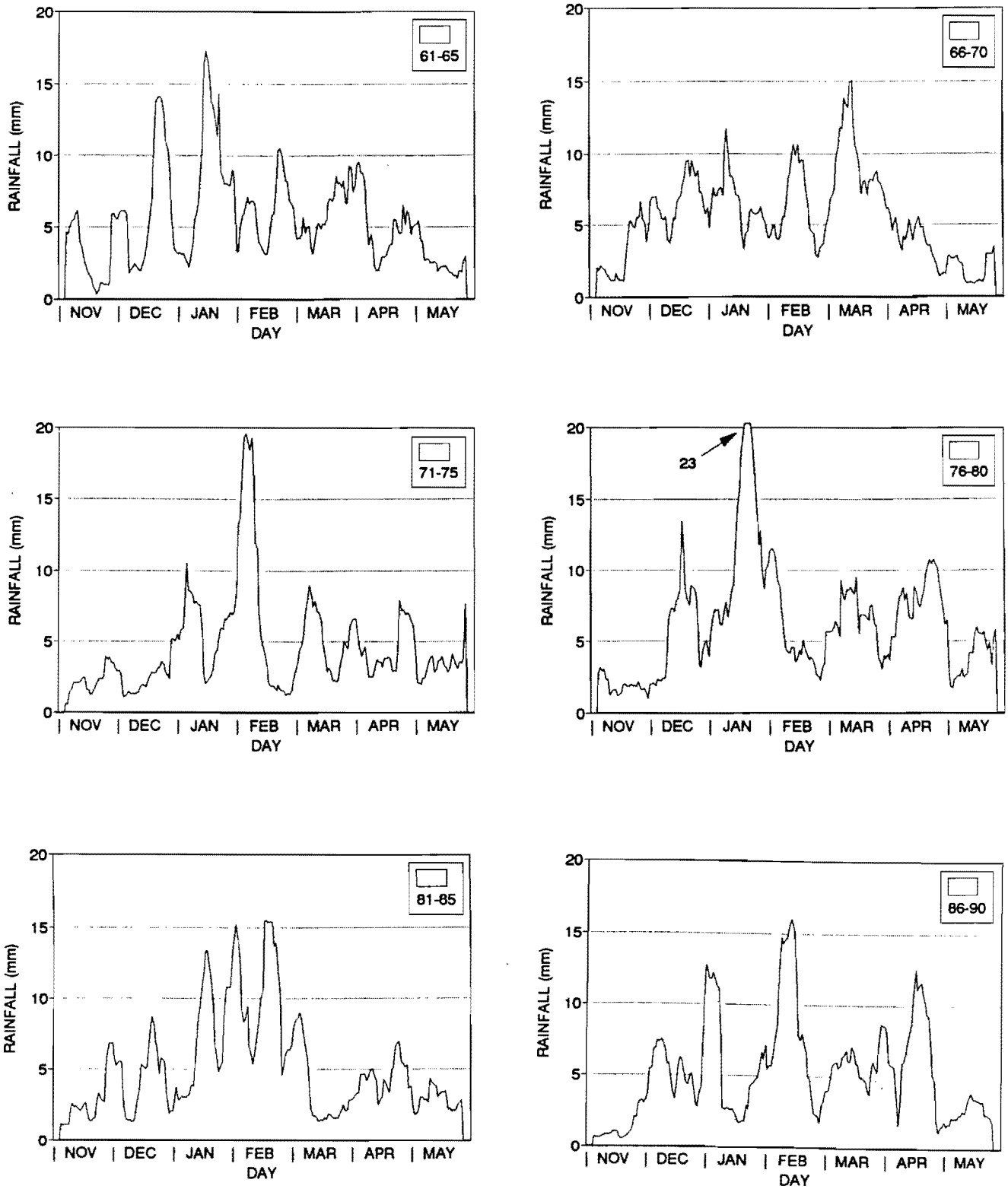

Figure 2-3 : Filtered 9-day seasonal composite rainfall for Pamplemousses.

For 5-year epochs in the period 1960 - 1990.

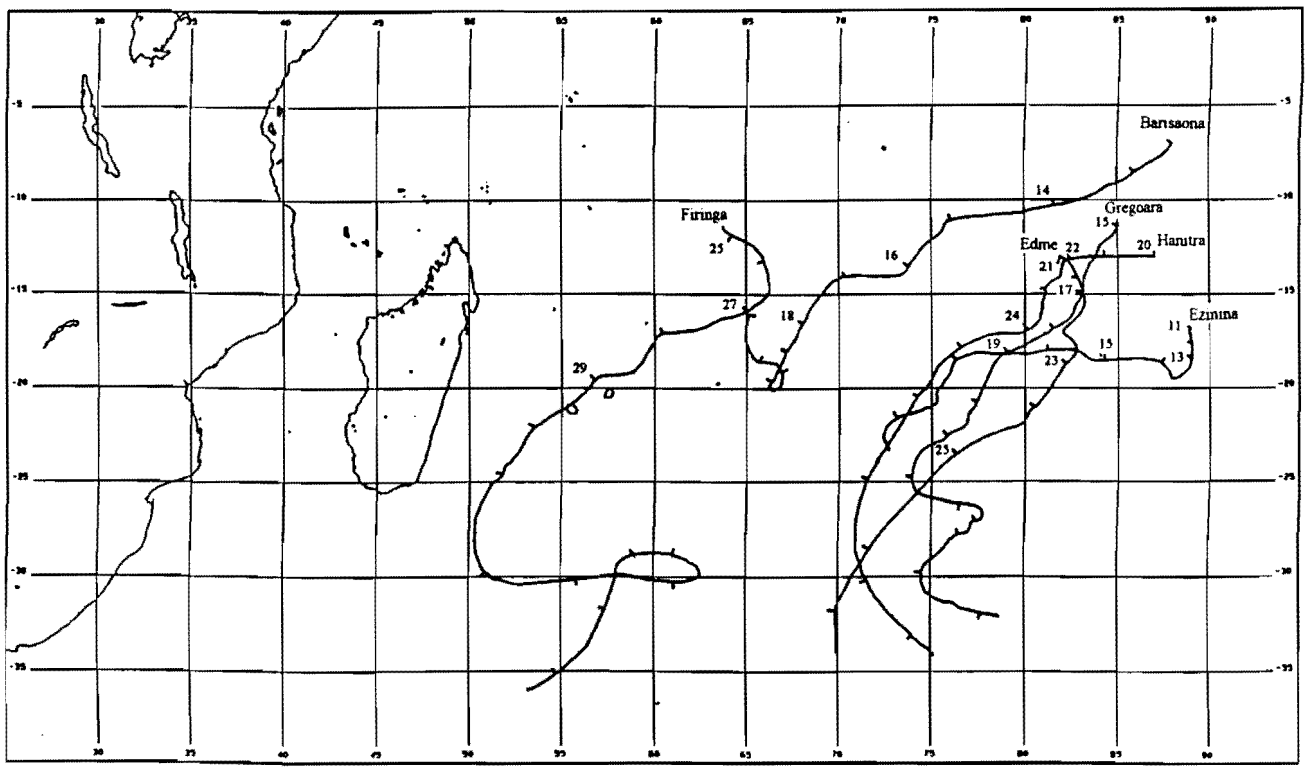

Figure 2-4a : Westmoving TC tracks used to form the WM TC composite.
Numbers refer to dates, tick marks show daily positions.

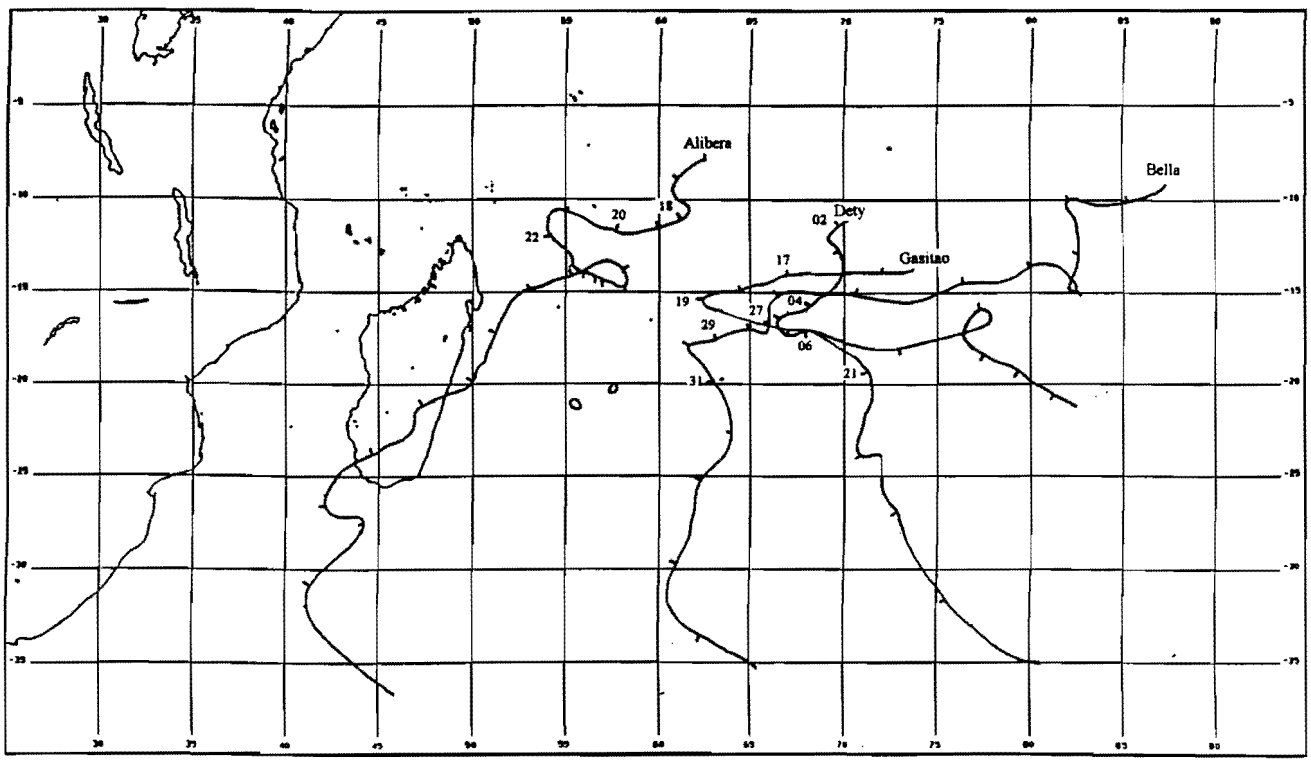

Figure 2-4b : Recurving TC tracks used to form the REC TC composite.
Numbers refer to dates, tick marks show daily positions.

Chapter 3

MEAN SUMMER COMPOSITE ANALYSES

This chapter will analyse the summer climatology of the SW Indian Ocean and adjacent SE Africa. Studies in which the atmospheric conditions of the SW Indian Ocean had been evaluated previously (Hastenrath and Lamb, 1979; Hastenrath, 1985; Padya, 1989; Jury, 1993) will be compared with the present mean summer composite (MSC). Reviewing the calculated MSC in this way will not only enhance the confidence in the results but will assist in determining how stable the characteristics and circulations are over the SW Indian Ocean during the southern hemisphere summer.

The MSC represents the mean circulation and thermodynamic characteristics calculated using the two months of highest Mauritius rainfall, namely January (235 mm) and February (232 mm) as mentioned in **Chapter 2**. The MSC is used as the background for the calculation of anomaly fields for the westward moving and recurving TC composites, with negative degrees north corresponding to positive degrees south. The mean composite domain (20° longitude by 20° latitude), as calculated from the individual TC cases presented in **Chapter 2**, is located by the box, centred at 72.5°E, 15°S, placed on each MSC parameter plot. Vertical sections are not presented for the MSC since they offered ambigious results with respect to the TC composite anomalies.

3.1 Kinematics

3.1.1 Geopotential

850 hPa

Figure 3-1a representing the geopotential field at the 850 hPa surface (P_{850}) shows the dominance of the Subtropical South Indian Anticyclone (SSIA), centred at 87°E and 32°S. A ridge extends from the SSIA (1540 gpm) towards Southern Africa. A steep pressure gradient exists around the SSIA up to 20°S, while over the tropical Indian Ocean north of 20°S the geopotential varies little from 1495 gpm. Across SE Africa the eastern sector of the continental low, produced by increased surface heating, is observed at 15°S.

200 hPa

The geopotential at the 200 hPa surface (P_{200}), **Figure 3-1b**, exhibits a steep gradient to the south of 25°S, while a relatively gradual one exists to the north of it, forming a well demarcated area between the tropical and temperate regions. The influence of the upper continental high pressure system extends to northern Madagascar (12440 gpm) from where a ridge of high pressure (> 12430 gpm) extends eastward along 15°S towards the anticyclone over northwestern Australia (east of 100°E).

The MSC geopotential field represented at the lower and upper tropospheric levels show the typical circulation patterns as seen from previous studies done by Preston-Whyte and Tyson (1988). Warm core weather systems are likely to develop within a pre-existent band of low geopotential as found along 10°S for P_{850}. The eastward displacement of the SSIA in

summer has the effect of slackening the trade winds and associated inversions (Preston-Whyte and Tyson, 1988) resulting in greater tropical convective influences.

3.1.2 Horizontal Wind

850 hPa

The wind vectors at P_{850} (**Figure 3-2a**) show the presence of a strong easterly flow along 25°S from 90°E to the east coast of Madagascar where a cyclonic deviation occurs around the southern tip of Madagascar and onto the Mozambique coast. The southern 'leeside' region of Madagascar was previously found to be an area with a high percentage of cyclone centres in summer (Taljaard, 1967). The presence of high wind velocities (> 5 m s^{-1}) to the northwest of Madagascar is a result of the cross-equatorial flow from the northern hemisphere winter monsoon (Padya, 1989). The axis of this lower tropospheric meridional wind maxima has previously been found near 50°E (Hastenrath, 1985; Padya, 1989), 10° further east than determined here. The narrow band of low wind velocities (< 2 m s^{-1}) between the subtropical easterlies and the tropical westerlies approximates the summer position of the ITCZ across the Indian Ocean (Padya, 1989). A notable feature across SE Africa is the presence of an area of anticyclonic rotation at 25°S fed by strong southeasterly winds from the south Mozambique Channel interacting with the cyclonic flow from the eastern sector of the continental low.

500 hPa

The temperate westerlies are expressed above P_{500} (**Figure 3-2b**) as far north as 30°S with speeds of between 2.5 to 10 m s^{-1}. Northerlies along the east African coast evident at this level, gives an indication of the depth of the northern hemisphere Indian winter monsoon outflow. Anticyclonic flow centred around 85°E, 22°S is a remnant of the easterly flow below this level. The anticyclonic flow at 25°S across SE Africa is sustained by the recurvature of subtropical westerlies across the southern Mozambique Channel.

200 hPa

In **Figure 3-2c** the upper westerlies are observed to extend as far north as 20°S across SE Africa and adjacent oceanic regions. The expression of the tropical easterlies, as well as having higher speeds (> 5 m s^{-1}) across SE Africa, is observed to extend to 12.5°S across the land while only to 10°S across the oceans. A calm zone of wind speeds < 5 m s^{-1}, of approximately 5° latitude is found between the tropical easterlies and the temperate westerlies.

Looking at the area demarcated by the box and the region around it, strong surface (P_{850}) equatorial westerlies (± 4 m s^{-1}) are found in the north, while strong subtropical easterlies (± 5 m s^{-1}) cover the southern half. This background cyclonic flow enhances TC development (Riehl, 1979; Jury, 1992). The circulation at P_{200} shows greater similarities to the 'more TC' that to the 'less TC' scenario found by Jury (1992). Strong easterly winds

at P_{200} in the 0 - 10°S equatorial zone would increase anticyclonic shear available to divergent outflows from TC's, aiding their development (Merrill, 1988; Jury, 1992).

3.1.3 Horizontal Kinetic Energy

850 hPa

The highest kinetic energy values of over 30 J kg^{-1}, at P_{850} are distributed south of 30°S (**Figure 3-3a**), and are coincident with the mid-latitude edge of the SSIA. The area of kinetic energy values > 25 J kg^{-1} centred at 55°E, 28°S occurs at the same location where the horizontal wind at P_{850} was found to deviate around the south of Madagascar. The presence of this high kinetic energy region outside of an anticyclone area can partly be looked upon as resulting from the work done by topographic pressure forces on the convergent winds in this region (Padya, 1989).

200 hPa

At P_{200} the gradient of the kinetic energy increases dramatically towards the temperate latitudes (**Figure 3-3b**). Kinetic energy values of over 100 J kg^{-1} occur south of Mauritius, while the maximum value within the tropics is 90 J kg^{-1} at 45°E, 5°S. Two minima centres are located at 25°E, 17°S (40 J kg^{-1}) and 80°E, 10°S (35 J kg^{-1}). These centres are located along a band of low kinetic energy values having its axis from 18°S, 20°E to 10°S, 100°E which overly the > 28°C SST area (**Figure 1-1**). It is notable that the Indian Ocean sector of the ITCZ is well expressed by the band of low kinetic energy values along 10°S at P_{200}.

The generally higher kinetic energy values at P_{200} relative to P_{850}, especially in the subtropic-temperate zone, arises from the equatorward tilt of westerly thermal winds. The high kinetic energy values at P_{200} infer the possibility of large eastward mass transport, a requirement of the upper tropospheric divergent outflow essential for TC growth via energy and mass overturning.

3.1.4 Vertical Movement

500 hPa

The dominant feature present in the vertical movement field at P_{500} is the large negative values of -14 x 10^{-2} Pa s^{-1} (upward motion) centred over northeast Madagascar (**Figure 3-4**). The high negative values occurring over Madagascar are not exclusively associated with the elevated terrain, but also coincide with the area in which easterlies and northern hemisphere winter monsoonal outflow converge. The presence of the ITCZ, although not clearly defined, can be seen by the strong uplift, < -4 x 10^{-2} Pa s^{-1}, occurring along a line over the SW Indian Ocean to the northeast of Madagascar. The area of downward motion (2 x 10^{-2} Pa s^{-1}) off the coast of E Africa (Tanzania) is a function of the low level wind diffluence within the Indian monsoon outflow (Hastenrath and Lamb, 1979, **Figure 3-2a**). The presence of background uplift in the MSC atmosphere (encompassed by the box), would aid TC development in this region.

3.1.5 Divergence

200 hPa

Comparing the divergence field at P_{200} (**Figure 3-5**) to the vertical movement at P_{500} (**Figure 3-4**), it is immediately evident that the two parameters are superposed. A spatial statistical correlation of over 0.85 was found to exist between the divergence at P_{200} and the vertical movement at P_{500} over the SW Indian Ocean. The presence of the highest P_{200} divergence value of $> 7 \times 10^{-5}$ s^{-1} over the northeastern part of Madagascar confirms that vertical uplift over this region is relatively deep as seen in **Figure 3-4**. The band of strong uplift along the ITCZ as seen for the vertical movement is reflected in the divergence at P_{200}, giving another good indication of its summer location over the SW Indian Ocean region. Since strong upper tropospheric divergence is a requirement for the intensification of tropical storms into TC's, the high divergence values northeast of Madagascar would assist the divergent outflow of energy via mass transport. The region of negative divergence in the southern Mozambique Channel associated with downward motion at P_{500} (**Figure 3-4**) helps to explain why TC's forming there are often short-lived (Nassor, 1994) even though the moisture content is relatively high.

3.1.6 Vorticity

850 hPa

The vorticity at P_{850} (**Figure 3-6a**) shows a very marked zonal distribution, with a negative (cyclonic) region along 15°S dividing the positive tropical area from the positive temperate area south of 30°S. The maximum cyclonic vorticity of -8×10^{-5} s^{-1} in the south of

Madagascar occurs where the easterly wind was observed to deviate around the island. Likewise the areas of maximum anticyclonic vorticity are found in the regions where counter-clockwise curvature in the easterly wind (coastal plain of southern Mozambique) and monsoonal outflow occurs north of Madagascar. The mean summer position of the ITCZ can be distinguished by the area of negative values along 15°S.

500 hPa

At P_{500} (**Figure 3-6b**) a similar zonal distribution of vorticity occurs as was found at P_{850}, although with a substantially reduced cyclonic area. The expression of the ITCZ at this level (cyclonic area) reinforces the idea of the depth of vertical uplift. It is notable that the high cyclonic vorticity area in the south of Madagascar is absent at this level indicating that the uplift in this region has lost its cyclonic rotation owing to reduced topographic influence. The region of maximum cyclonic vorticity ($< -4 \times 10^{-5}\ s^{-1}$) has however shifted to the east.

200 hPa

Figure 3-6c, P_{200}, consists almost entirely of anticyclonic vorticity with a maximum of greater than $20 \times 10^{-5}\ s^{-1}$ occurring over the African subcontinent. The area of cyclonic vorticity north of Madagascar associated with convergence as seen in **Figure 3-5** and that of downward motion in **Figure 3-4**.

The high cyclonic vorticity at P_{850} of $< -6 \times 10^{-5}\ s^{-1}$ in the region demarcated by the box, is a mechanism which would induce and aid horizontal inflow in the surface layer, causing an

increase in uplift, reinforcing vertical ascent favourable for TC development. The decreasing cyclonic vorticity from P_{850} to P_{200} found along 15°S, is similar to the vertical structure present in developing and mature TC's, and is a determining factor for their development.

3.2 Moisture and Thermodynamics

3.2.1 Temperature

850 hPa

The structure of the temperature field at P_{850} reflects the differential heating between the land and the ocean, clearly illustrated by the 20 °C isotherm which closely follows the east coast of Africa (**Figure 3-7a**). Temperatures over the continent are observed to be approximately 5 °C higher than at corresponding latitudes over the ocean mainly owing to the use of 12UT (14-15h00 local) data. A maximum value of over 26 °C occurs at approximately 20°E, 24°S over the southern African plateau, with a steep gradient to the south of this point. The temperatures over tropical Africa, although higher than any value over the ocean at this latitude, are still 5 °C below the continental maximum. Sensible heat fluxes over the island mass of Madagascar cause an increase in the temperature in the leeward Mozambique Channel resulting in an eastward excursion of the 19 °C isotherm towards the island.

200 hPa

At P_{200} (**Figure 3-7b**) a band of higher temperatures exists along 20°S (> -53.3 °C) with a maximum of -52.8 °C occurring at 100°E , 20°S. Poleward of this band a steep temperature gradient exists, equatorward it is more gradual. The equatorward decrease in temperature reflects the position of the tropical tropopause near 100 hPa (Hastenrath, 1985). The band of higher temperatures is situated approximately on the poleward edge of where the ITCZ is located.

Temperatures at both P_{850} and P_{200} correspond well with the tropical values calculated by previous authors (Newell et al., 1972) and still considered relevant (Asnani, 1993). The weak temperature gradient across the SW Indian Ocean north of 25°S offers little potential energy for shear production, a requirement for convective uplift in the TC formative stage.

3.2.2 Relative Humidity

850 hPa

Relative humidity at P_{850} is another parameter which shows the position of the ITCZ (**Figure 3-8a**). Values > 75 % are found along a band near 10°S. A relative humidity minimum of < 40 % is found over the southern part of the African continent, in contrast with the wet conditions experienced there during summer (Preston-Whyte and Tyson, 1988). At this pressure surface Madagascar does not appear to cause any major deviations of the relative humidity contours crossing it, intimating that the depth of moisture around Madagascar is not affected by the island's size, position or elevation.

500 hPa

At P_{500} (**Figure 3-8b**) evidence for the ITCZ in the relative humidity values > 45 %, is still easily recognisable. The maximum values are however found over the continent, > 55 %, whereas at P_{850} a very large area of over 75 % is located over the ocean. The effect of Madagascar at this level is seen through the expansion of the continental maximum over the Mozambique Channel to the northern reaches of the island where moisture is uplifted. At P_{500}, the peaks in northern Madagascar enhance the vertical transport of moisture.

As discussed in **Chapter 1**, in consideration of the parameters essential for TC development and growth, high relative humidity in the lower and middle troposphere are required to support the convective growth of updrafts by entraining moist air from the surrounding atmosphere. It is notable that although relative humidity values are high off the coast of Tanzania at P_{850} it is lower at P_{500} perhaps an indication of the depth of the moisture layer of the Indian monsoon outflow and the P_{850} divergence. The horizontal transport of moisture from the Congo basin to approximately 30°E, 10°S may help explain the higher continental relative humidity values compared to that encountered over the ocean (see **Figure 3-10**).

3.2.3 Precipitable Water

Surface - 300 hPa

A band of precipitable water values over 50 mm stretches from Madagascar to the strait of Mentawi in the eastern equatorial Indian Ocean (**Figure 3-9**), coinciding with the south-equatorial rainband identified by Martin et al (1993) using satellite data. The

precipitable water values over the ocean decrease with a gentle gradient towards the south, reaching a minimum of just under 35 mm south of 30° S. Due to the elevation of the east African plateau, there is a rapid decline in precipitable water values, from 50 mm to 35 mm from 40°E to 30°E. This is an important feature of the tropical atmosphere showing that almost 50 % of precipitable water is contained below the 850 hPa level. The poleward extension of the 40 mm contour along the east coast of southern Africa is a reflection of the high SST's and associated moisture content found over the warm Mozambique-Agulhas current.

3.2.4 Water Vapour Flux

Surface - 500 hPa

The vertically integrated horizontal water vapour flux field (**Figure 3-10**) has a structure similar to the horizontal wind field at P_{850}. Two distinct regions of influx affect the region around Madagascar. To the east, water vapour is transported to this region along the easterly wind belt (80 - 100 g kg^{-1} ms^{-1}), while influx from the monsoon region occurs to the north of Madagascar (> 100 g kg^{-1} ms^{-1}). The spatial correlation between the wind field and the water vapour flux if only high (0.87) at P_{850}, which suggests that the transport of moisture into and through this region is restricted to the layer extending from the surface to P_{700}. From the water vapour flux diagram it is evident that in addition to moisture inputs from the southeast and the northwest into the region enclosed by the box, the convergence and vorticity of this derived field would enhance TC formation and growth.

3.2.6 Equivalent Potential Temperature

850 hPa

In **Figure 3-11a** a marked increase of equivalent potential temperature over tropical Africa is observed at P_{850}, with values > 350 °K occurring at 25°E, 10°S. Over the ocean a maximum value of just over 340 °K is attained along a broad band stretching from the northern tip of Madagascar to approximately 95°E, 5°S near the Strait of Mentawi. On the poleward side of this band the equivalent potential temperature decreases at about double the rate observed on the equatorward side.

500 hPa

At P_{500} (**Figure 3-11b**) a maximum value of 338 °K occurs over the continent, while over the ocean a broad band of equivalent potential temperature values, between 336 °K and 337 °K, occurs in the same area as the maximum at P_{850}. The zonal distribution either side of this band has the same structure as at P_{850} even over the southern part of the continent. These high values are again a good reflection of the summer position of the ITCZ over the SW Indian Ocean.

The upward decrease in equivalent potential temperature (increased instability) in the area north of 25°S enhances the lifting of air parcels from sea level to its level of free convection as required by the CISK model (Charney and Eliassen, 1964; Ooyama, 1964). Within the composite box, equivalent potential temperature decreases from 340 °K at P_{850} to 335 °K at P_{500}, whereas to the south an increase occurs with height.

3.3 Synthesis

The MSC, as represented by the parameters analysed in this chapter, is observed to agree well with previous studies conducted on the atmospheric conditions of the SW Indian Ocean region. The relatively short time period (1987 - 1992 inclusive) used to compute the mean summer atmosphere is shown to be of adequate length, since the spatial correlation between the MSC used in this thesis and the mean atmospheric conditions represented in previous studies (carried out on different data sets of longer periods) are very high.

For the kinematic analyses, the summer position and strength of the SSIA compares favourably with values presented by Preston-Whyte and Tyson (1988) as well as previous researchers. Of the three pressure surfaces used to analyse the horizontal wind vector field, P_{850} shows the most variation in structure with the SSIA, the cyclonic region across southern Madagascar and the northern hemisphere winter monsoon outflow all being represented by prominent circulation regimes, the most prominent in TC development (Asnani, 1993). The representation of the ITCZ by confluent near surface winds was previously observed by Jury (1993) and Jury et al. (1994). The high correlation (>0.85) between the vertical movement field (P_{500}) and the divergence field (P_{200}) lends itself to an assessment of convective strength attained within these areas. The sign and magnitude of the vorticity field suggests that background flows are positively disposed to TC development. The kinetic energy results could only be compared to the work done by Padya (1989) since their is a lack of SW Indian Ocean regional studies incorporating kinetic

energy. A peculiarity of the kinetic energy field is the better representation of the ITCZ at P_{200} than at P_{850}, in contrast to what is experienced for most of the other parameters.

The moisture and thermodynamic parameters show some interesting, yet expected, results over the study region. The temperature distribution over the ocean at P_{850} closely follows the SST distribution. The relative humidity field at both P_{850} and at P_{500} show the location of the ITCZ as does the precipitable water field when the contours with the highest values are considered. The poleward dip of the precipitable water contours in the southwestern sector of the SW Indian Ocean over the warm Mozambique-Agulhas current reflects the depth of the moisture convergence occurring in this area. The water vapour flux, as expected, shows a very similar structure to the horizontal wind vector field at P_{850}. This high correlation is understandable when one considers that the winds closest to the sea surface will receive direct latent heat fluxes and gain a greater overall influence on the transportation of moisture than winds higher up in the atmosphere. It is also notable that the vertical movement is small compared with the horizontal transport and can thus be disregarded when producing mean values. When considering the equivalent potential temperature diagrams a relatively constant zonal structure was observed, but with a diminishing spatial variance with increasing height. The decrease of equivalent potential values in the lower troposphere is an indication of the strength of convective instability present equatorward of 25°S.

The release of diabatic heat in moist ascending air is a driving force of the SW Indian Ocean climate which enables the development of intense TC's. Their interaction with the synoptic environment is the focus of the next chapter.

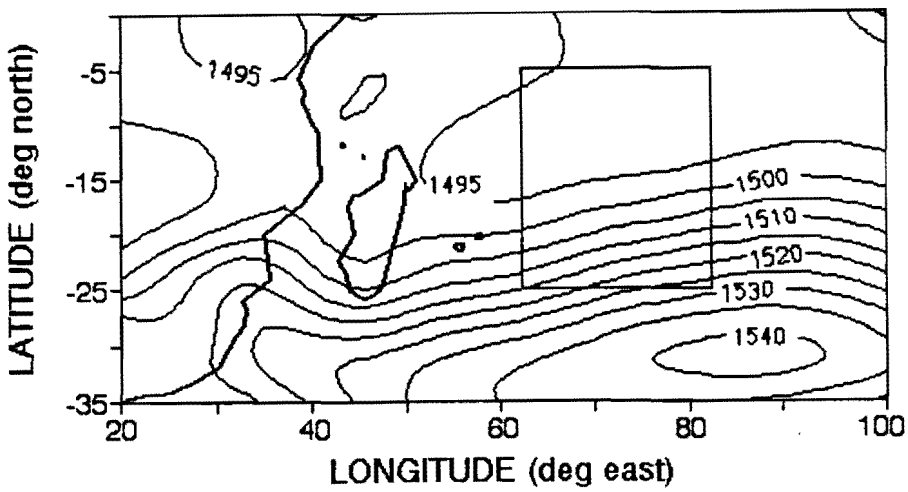

Figure 3-1a : MSC geopotential field @ 850 hPa.

Contour interval is 5 gpm.

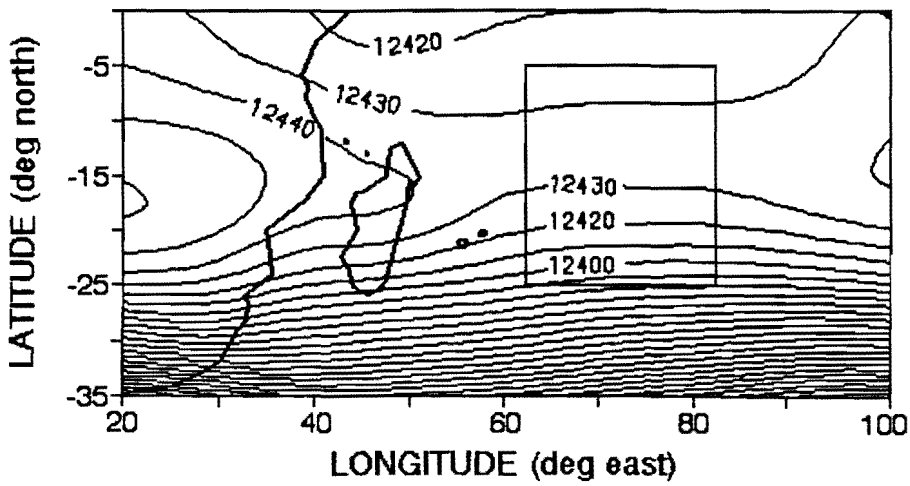

Figure 3-1b: MSC geopotential field @ 200 hPa.

Contour interval is 10 gpm.

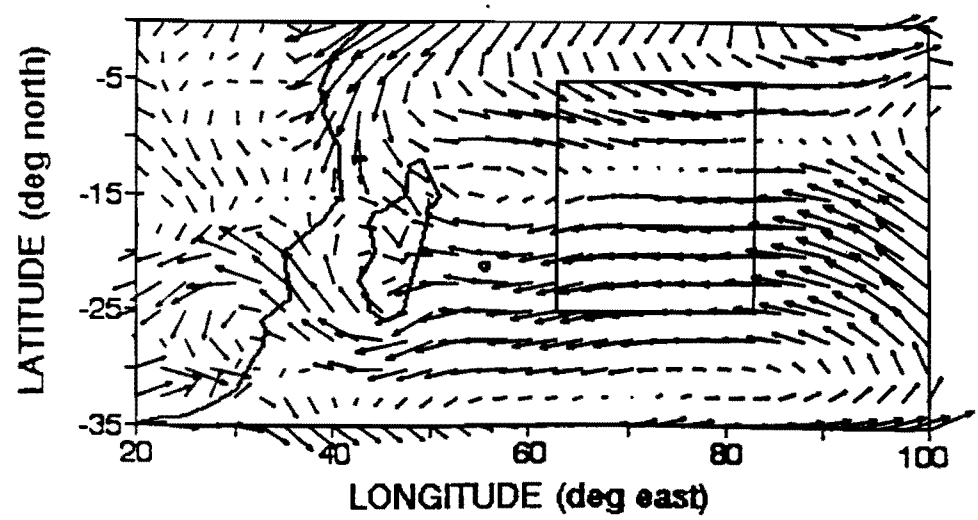

Figure 3-2a : MSC horizontal wind field @ 850 hPa.

Vector scale : ⟶ = 5 m s^{-1}.

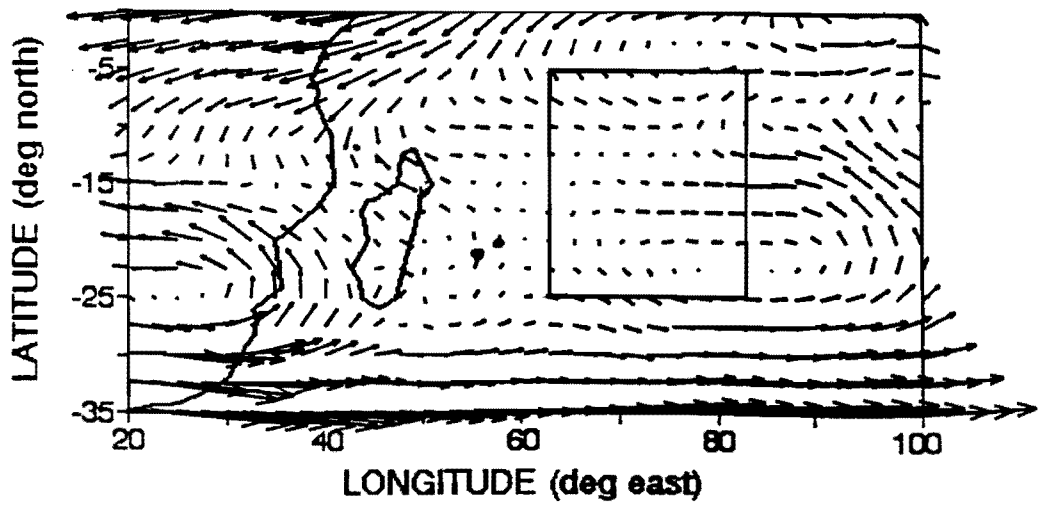

Figure 3-2b : MSC horizontal wind field @ 500 hPa.

Vector scale : ⟶ = 5 m s^{-1}.

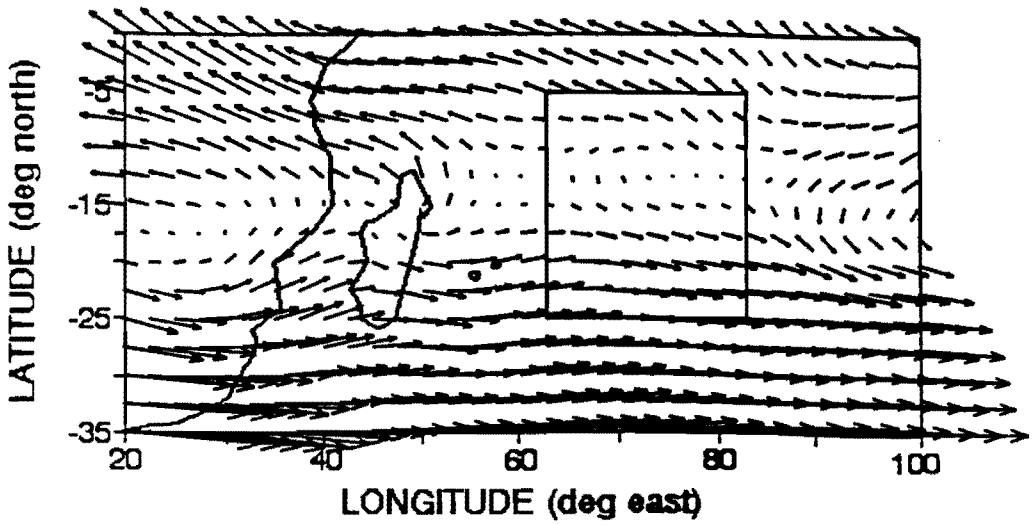

Figure 3-2c : MSC horizontal wind field @ 200 hPa.

Vector scale : ⟶ = 10 m s^{-1}.

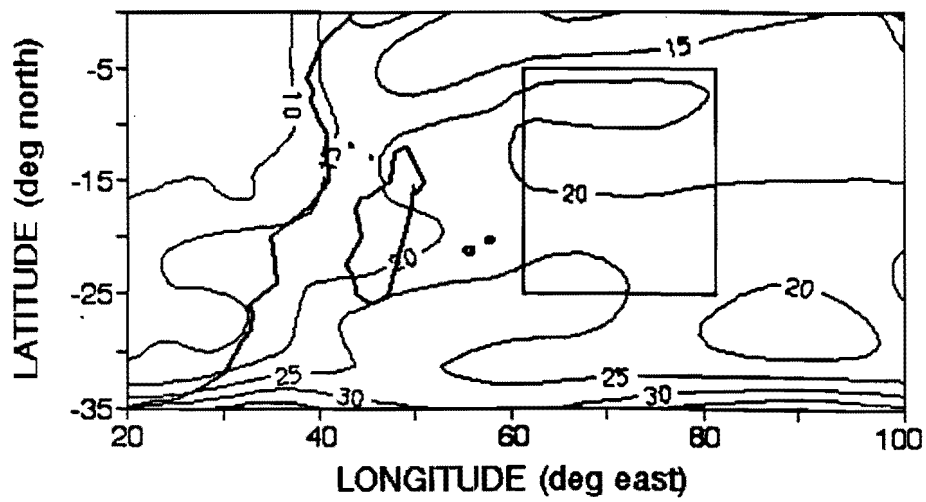

Figure 3-3a : MSC kinetic energy field @ 850 hPa.

Contour interval is 5 J kg^{-1}.

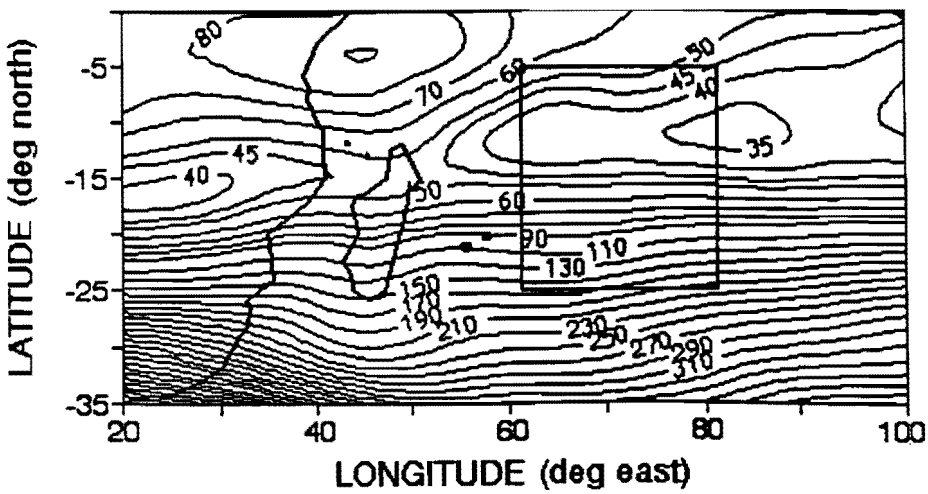

Figure 3-3b : MSC kinetic energy field @ 200 hPa.

Contour interval is variable in J kg^{-1}.

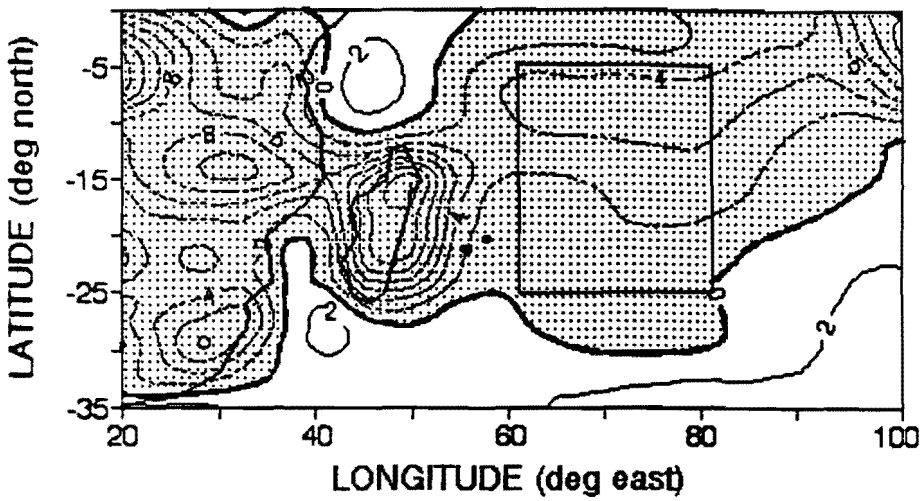

Figure 3-4 : MSC vertical motion field @ 500 hPa.
Contour interval is 2 x 10^{-2} Pa s^{-1}.

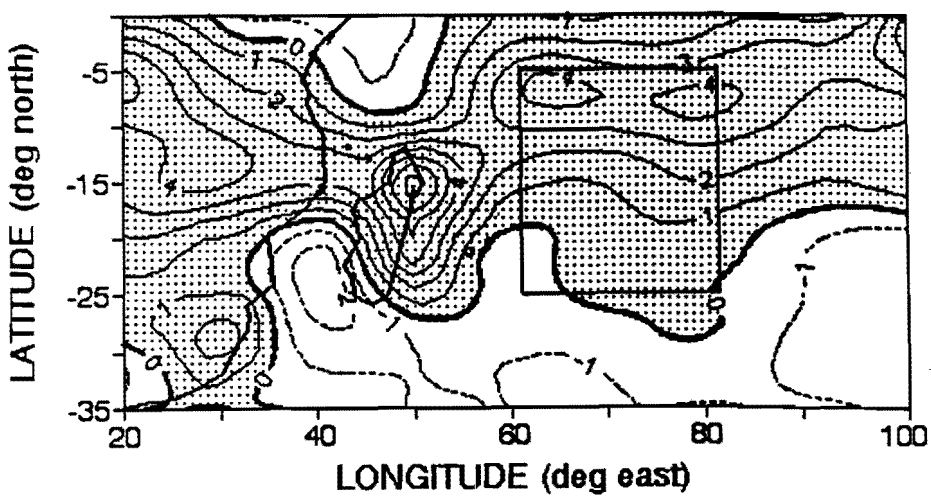

Figure 3-5 : MSC divergence field @ 200 hPa.
Contour interval is 1 x 10^{-5} s^{-1}.

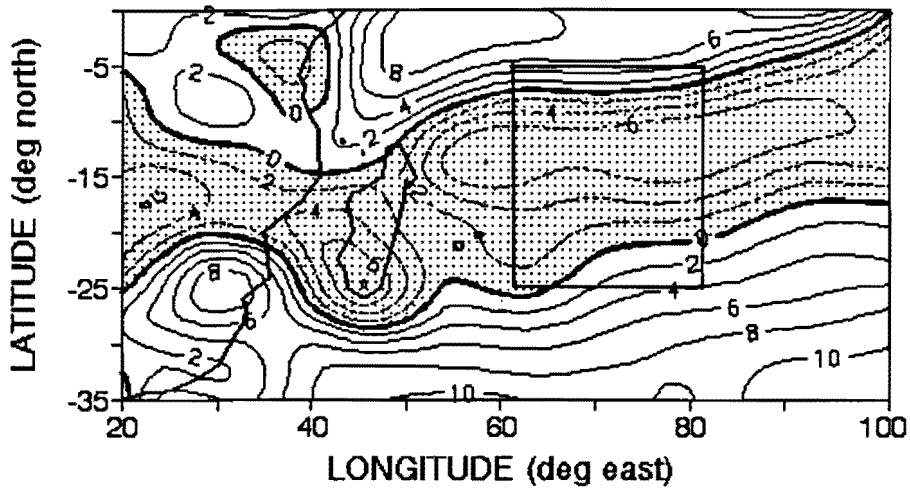

Figure 3-6a : MSC vorticity field @ 850 hPa.

Contour interval is 2 x 10^{-5} s^{-1}.

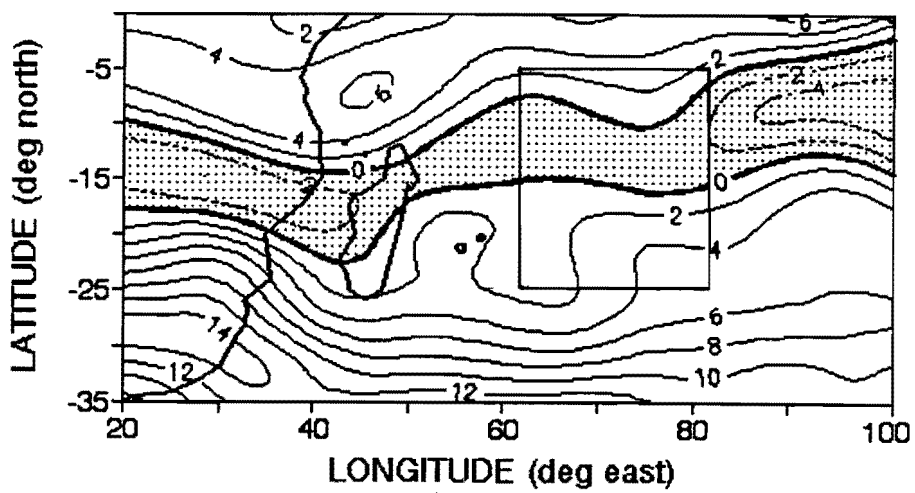

Figure 3-6b : MSC vorticity field @ 500 hPa.

Contour interval is 2 x 10^{-5} s^{-1}.

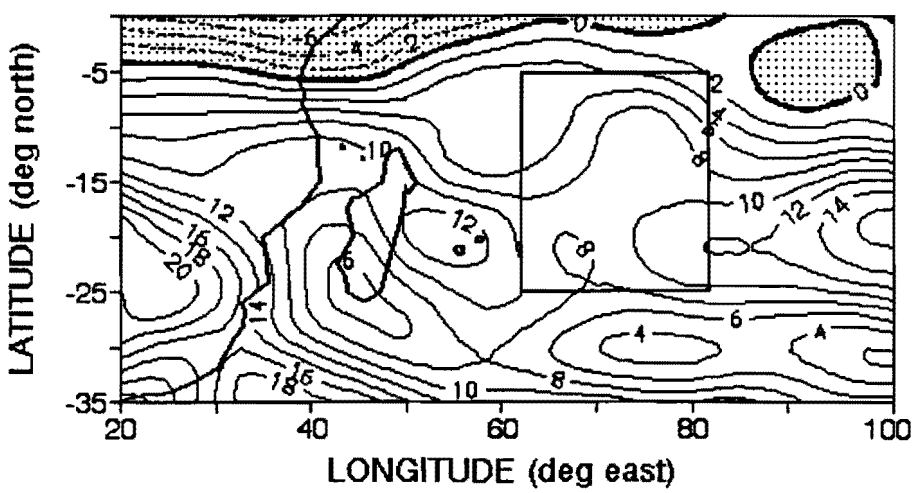

Figure 3-6c : MSC vorticity field @ 200 hPa.

Contour interval is 2 x 10^{-5} s^{-1}.

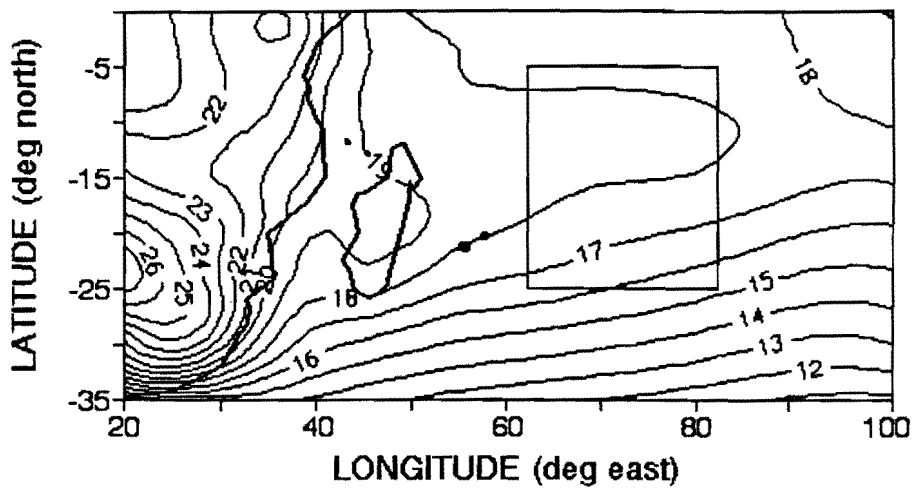

Figure 3-7a : MSC temperature field @ 850 hPa.

Contour interval is 1 °C.

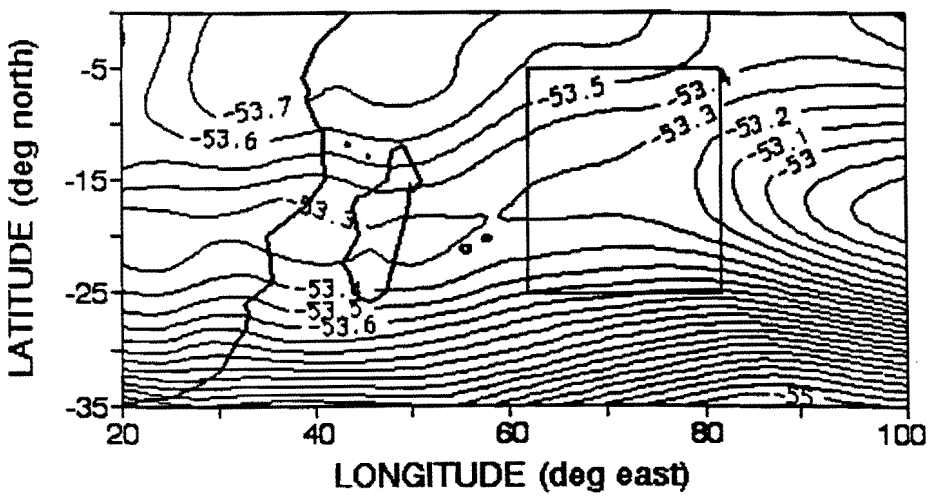

Figure 3-7b : MSC temperature field @ 200 hPa.

Contour interval is 0.1 °C.

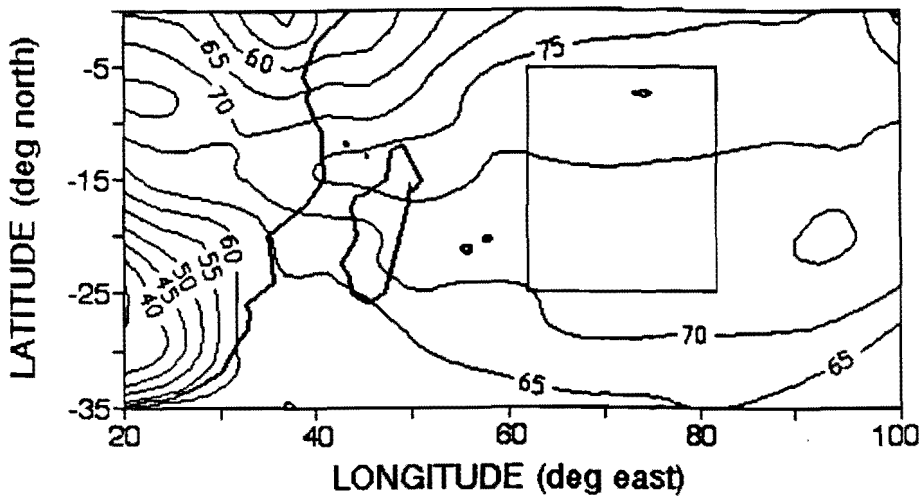

Figure 3-8a : MSC relative humidity field @ 850 hPa.

Contour interval is 5 %.

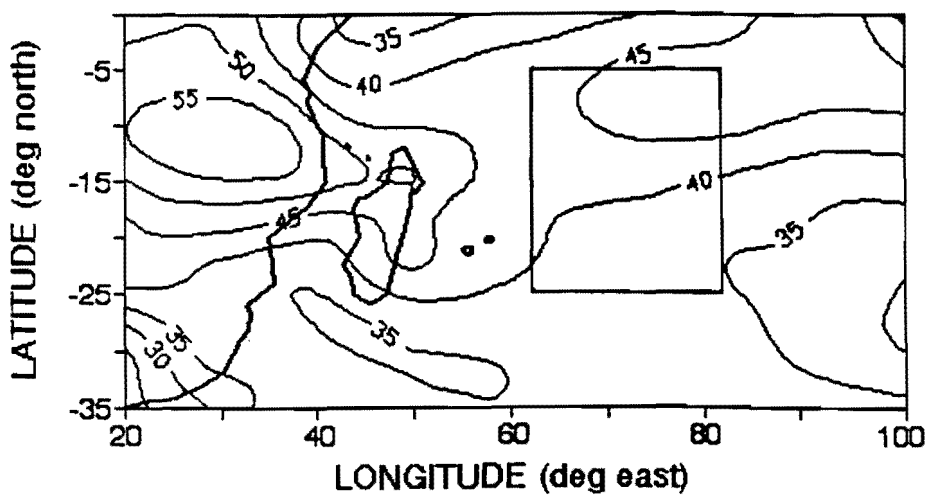

Figure 3-8b : MSC relative humidity field @ 500 hPa.

Contour interval is 5 %.

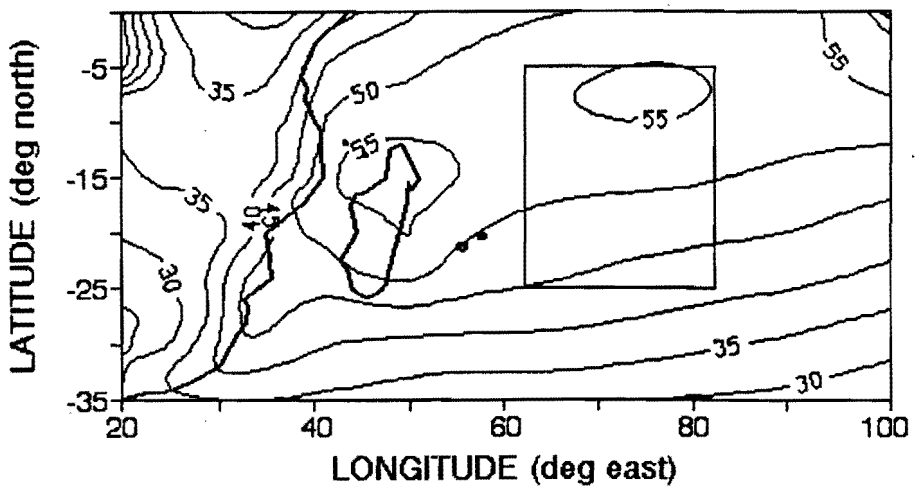

Figure 3-9 : MSC precipitable water field between the surface and 300 hPa.
Contour interval is 5 mm.

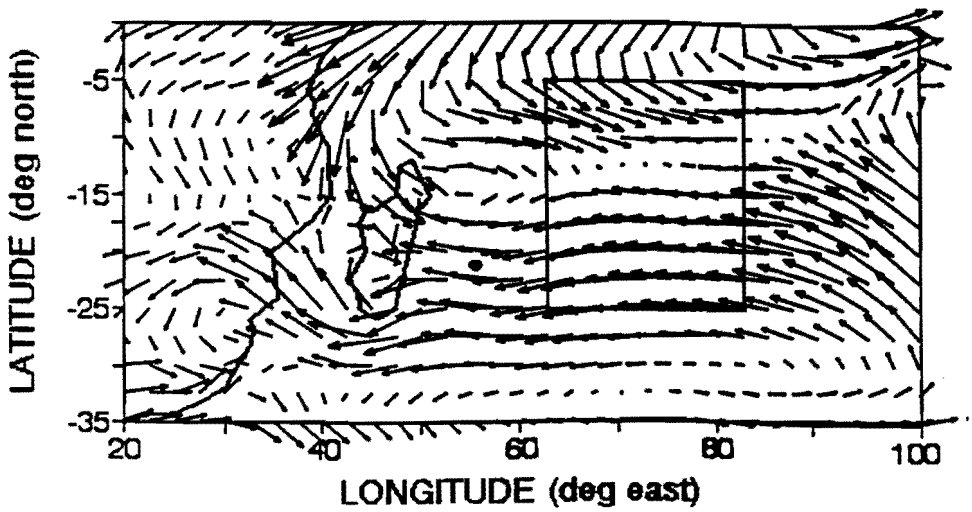

Figure 3-10 : MSC water vapour flux field between the surface and 500 hPa.
Vector scale : ⟶ = 100 g kg^{-1} m s^{-1}.

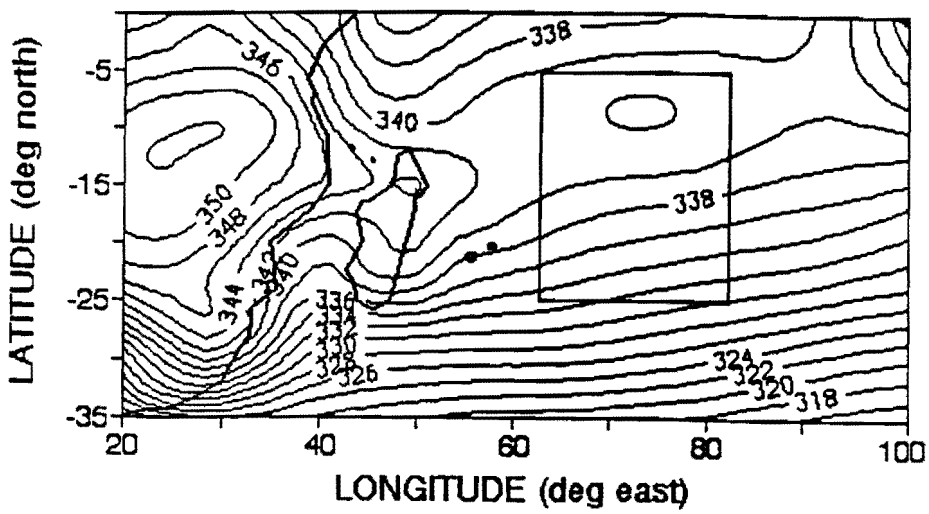

Figure 3-11a : MSC equivalent potential temperature field @ 850 hPa.

Contour interval is 2 °K.

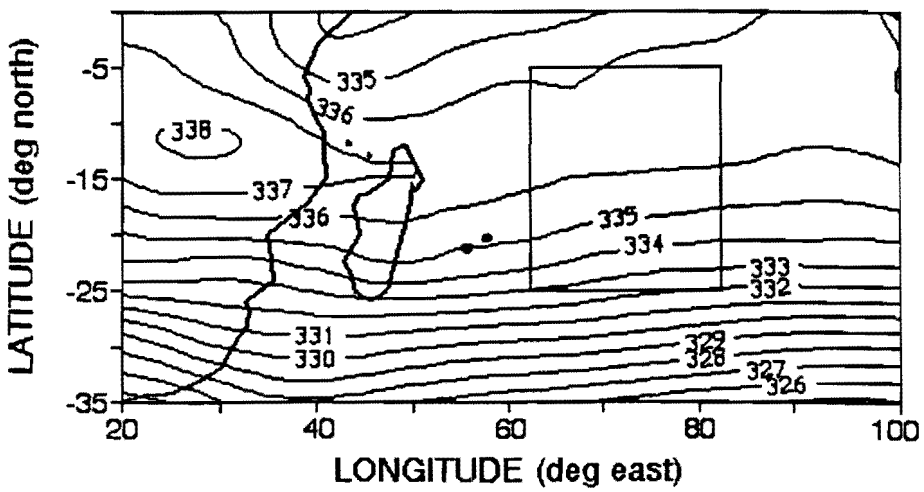

Figure 3-11b : MSC equivalent potential temperature field @ 500 hPa.

Contour interval is 1 °K.

Chapter 4

MEAN TC COMPOSITE ANALYSES

This chapter will be divided into two main sections, each of which will focus on the analyses of the westward moving (WM) and recurving (REC) tropical cyclones in the SW Indian Ocean. For the composite cases mean horizontal and vertical sections will be used to analyse the various ECMWF observed and derived parameters, each with their individual results. Where applicable, comparisons between the WM TC composite and TC Firinga will be made to assess the operational relevance of the mean composite. This is done to determine which parameters are reliable predictors of short-term TC intensity and track. TC Firinga horizontal maps and vertical sections are presented in **Appendix B**.

Six SW Indian Ocean TC's having tracks oriented towards the west and southwest were formed into the WM composite (see **Table 2-3a**) one of which was Firinga. Four TC's which initially had southwest tracks, but which changed direction to the southeast were used to form the REC composite (see **Table 2-3b**). Although a full description of the method used to align the individual TC centres to form the composites were given in Chapter 2, a brief summary of the procedure follows. Individual TC data was extracted in a 20° by 20° grid with the centre of the grid corresponding to the TC centre as recorded by the weather offices of Mauritius and Reunion. The data for each TC, day, level and parameter were then averaged to form the composites. Hence the composite centre is a resultant of the centre of each TC used in the composite.

The mean tropical cyclone composites (MTCC) will be used to analyse the changes occurring between D-3, D-1 and D+1, which will allow for the recognition of changes occurring as each TC progresses towards and past the day of maximum intensity. Comparisons between WM and REC TC's will be carried out in chapter five using anomalies.

4.1 Westward Moving TC Analyses

4.1.1 Horizontal Kinematics, Moisture and Thermodynamics

4.1.1.1 Geopotential

850 hPa

A weak geopotential minimum at P_{850} shifts from the composite centre (C_{cen}) on D-3, 2.5° northward by D+1 (**Figures 4-1a, b** and **c**). An accompanying increase in geopotential from 1465 gpm to 1470 gpm reveals a decrease in TC intensity. Due to the relative northwestward displacement of the low from C_{cen}, increases of approximately 50 gpm occur from D-3 to D+1.

200 hPa

At P_{200} the geopotential high is observed to shift from south of C_{cen} on D-3, to the northeast on D+1 (**Figures 4-2a, b** and **c**). An increase of the geopotential centre from 12440 gpm at D-3 to 12450 gpm at D+1 accompanies this shift. Shifting of the geopotential maxima results in an increase in the geopotential gradient to the south with a resultant increase in the asymmetry of the geopotential field.

The MTCC geopotential field for D-3, D-1 and D+1 show relatively minor differences between the various composite days. Subtle changes in the geopotential fields at P_{850} and P_{200} indicate a relative northward shift of the circulatory features. The increase in the geopotential gradient to the south at P_{850} is attributed to TC interaction with the midlatitude ridge of the SW Indian Ocean. The upper level trough at P_{200} extending from the southwest towards C_{cen} on D+1 has been found to be an effective mechanism for weakening TC's near the latitude of Mauritius (Padya, 1989).

4.1.1.2 Horizontal Wind

850 hPa

The wind vectors at P_{850} show the typical cyclonic structure expected close to the surface of TC's (**Figure 4-3a, b** and **c**). Although the relatively symmetric structure is maintained from D-3 to D+1, the quadrant in which the highest wind velocities are observed shifts from the rear, northeast to the front, southwest. This is mainly due to the wind in the northern half of the composite reducing considerably in strength by D+1 (< 10 m s^{-1}), while winds in the southern half have remained relatively constant ($\pm$ 10 m s^{-1}).

500 hPa

The cyclonic rotation seen at P_{850} is present at P_{500}, with a slight reduction in average speed (**Figure 4-4a, b** and **c**). On D-3 a region of high wind velocities > 10 m s^{-1} is located in the northeast quadrant. On D-1 an apparent weakening in the cyclonic symmetry begins to show when north of +5° latitude vectors having strong westerly components are observed, while in the southwest quadrant an easterly component is

dominant south of -5° latitude. On D+1 a severe disintegration of the cyclonic structure is observed when northwesterly winds replace the easterlies present on D-1 in the southwest quadrant of the composite.

200 hPa

The wind at P_{200} exhibits the most change in time with regard to the wind directions and their magnitudes. On D-3 a strong easterly flow is maintained to the north of -2.5° latitude (> 10 m s^{-1}), while north-northwesterly flow is observed in the extreme southwest quadrant (**Figure 4-5a**). The same structure is observed on D-1, but with the winds in the southwest quadrant having increased in magnitude to > 15 m s^{-1} as well as becoming westerly (**Figure 4-5b**). The most dramatic change is seen on D+1, where the magnitude of northwesterly winds in the southwestern half of the composite has increased and extended northward to C_{cen} (**Figure 4-5c**).

The horizontal wind field shows a steady structure at P_{850} throughout the sequence, while at P_{200} changes in the structural flow patterns are pronounced. The presence on D-3 of easterly flow in the northern quadrant at P_{200} aids the growth of the TC by creating an effective evacuation mechanism for the ascending air by increasing the outflow channel (Holland and Merrill, 1984; Padya, 1989). This effect is however negated on D+1 when the upper level trough producing the northwesterly flow has encroached on the C_{cen} to such an extent that momentum dissipation between the TC and the northwesterlies occurs at levels where the TC circulation is southeasterly (D+1, P_{500}). Weakening of the circulation occurs rapidly even before invasion of colder air from the trough system can take place as observed by Padya (1989). While

the trough may 'decay' the TC when it interacts with C_{cen}, it also serves as an 'attractor' before it impinges on C_{cen}. Since the trough remains in the southwest quadrant throughout the sequence it may aid in the westerly track of the TC.

4.1.1.3 Kinetic Energy

850 hPa

At P_{850} propagation of the highest kinetic energy values (> 70 J kg^{-1}) is observed to follow a southerly path east of the C_{cen}, while west of -5° longitude kinetic energy values average < 30 J kg^{-1} (**Figures 4-6a, b** and **c**). On D-3 the kinetic energy values > 50 J kg^{-1} are in the rear of the TC at +2.5° longitude, +5° latitude, with a tongue of kinetic energy values between 40 - 50 J kg^{-1} occurring south of the C_{cen}. The intrusion of kinetic energy values > 40 J kg^{-1} to the south of the C_{cen} (D-3) results in the formation of an arc of high kinetic energy values (> 50 J kg^{-1}) around the east C_{cen} on D-1. By D+1 the region of high values has consolidated to cover most of the southeast of the composite. The presence of an area of high kinetic energy values > 40 J kg^{-1} north of +7.5° latitude separated from that east of the C_{cen} by a region of low kinetic energy values (< 30 J kg^{-1}) can be traced back to the horizontal wind velocities being weak north of the C_{cen} (see **Figure 4-3c**).

200 hPa

The kinetic energy field at P_{200} is observed to increase in strength 4-fold in the southwest from a maximum of 60 J kg^{-1} on D-3 to > 280 J kg^{-1} on D+1. On D-3 the kinetic energy values > 60 J kg^{-1} in the northwest quadrant are observed to be west of -5° longitude, while a zonal distribution of the kinetic energy values > 40 J kg^{-1} occurs

south of -5° latitude (**Figure 4-7a**). In **Figure 4-7b** (D-1) increased kinetic energy is found in a zonal band south of -2.5° latitude, while within a radius 2.5° of the C_{cen} values of < 20 J kg^{-1} are distributed. On D+1 kinetic energy values to the south and southwest produce a very steep gradient as they increase from 40 J kg^{-1} at the C_{cen} to > 250 J kg^{-1} at a radius of 10° (**Figure 4-7c**). This rapid change in gradient from D-3 to D+1 is not reflected on the equatorward side of the C_{cen}, where it remains relatively constant throughout the period.

From the analysis of kinetic energy, location of the horizontal wind maxima at P_{850} is observed to rotate from behind the TC on D-3, to the left of the direction of movement by D+1. At P_{200} the highest values congregate in the front of the TC composite, consistent with previous TC studies (Padya, 1989). The decrease in kinetic energy at P_{850} and the increase at P_{200} reflects a breakdown of warm cored structure and vertical transport of mass to upper tropospheric levels.

4.1.1.4 Vertical Movement

500 hPa

The area of maximum uplift at P_{500} is observed to remain in the southeast quadrant from D-3 through to D+1 (**Figure 4-8a, b** and **c**). On D-3 the maximum uplift of < -1.2 Pa s^{-1} is situated south of the C_{cen} with weaker uplift of < -0.4 Pa s^{-1} dominating the eastern half of the composite. The strongest uplift on D-1 is -1.0 Pa s^{-1} with the area of < -0.4 Pa s^{-1} in the northeast replaced by a centre of subsidence east of the C_{cen}. On D+1 reinstatement of the northeast region of uplift of < -0.4 Pa s^{-1} is observed with two centres of uplift of < -1.0 Pa s^{-1} occurring along the +5° meridian at

+10° latitude and -5° latitude, while a uniform area of subsidence is established to the west of +5° longitudinal.

The commonly recognised feature of a weak central subsidence region (i.e. the eye) surrounded by an area of strong vertical updraft at a radius of > 1.0° (Simpson and Riehl, 1981; Anthes, 1982; Padya, 1989; Asnani, 1993) is only discernible on D-1. Vertical uplift greater than the environmental mean of -0.4 Pa s^{-1}, is well developed to the left of the direction of motion where surface convergence and moisture is at a maximum.

4.1.1.5 Divergence

200 hPa

Figures 4-9a, b and **c** show no intensification in the strength of the divergence maxima in the D-3, D-1 and D+1 sequence, but they do show changes in the positions of these maxima. On D-3 a maximum divergence of > 8 x 10^{-5} s^{-1} is situated to the south of the C_{cen}, while a centre of negative divergence (convergence) is situated to the north (-4 x 10^{-5} s^{-1}). On D-1 three centres of divergence > 6 x 10^{-5} s^{-1} occur along the points of a V having its vertex southeast of the C_{cen}, while the centre of convergence has moved to the east of its previous position. Convergence of < -2 x 10^{-5} s^{-1} is found to the southwest of the C_{cen} along a northwest-southeast band. On D+1 the V structure has disintegrated with only the eastern two divergence centres still present, separated however by low divergence values of less than 2 x 10^{-5} s^{-1}. A centre of divergence (> 4 x 10^{-5} s^{-1}) in the southwest quadrant is separated from the divergence

in the southeast quadrant by a tongue of convergence values of < -2 x 10^{-5} s^{-1} along -2.5° longitude.

When comparing the divergence and the vertical movement composites it is evident that the position of maximum uplift at P_{500} always occurs under a region of maximum divergence at P_{200}, but with the reverse not necessarily true. A notable feature is that the vertical motion at P_{500} and the divergence at P_{200} are only well correlated spatially on D-1 suggesting that the deep convective updrafts of the TC are directly channelled to outflow for a short period.

4.1.1.6 Vorticity

850 hPa

Cyclonic vorticity dominates the region around the C_{cen} from D-3 to D+1 with very little change in intensity. On D-3 a cyclonic vorticity maxima of -30 x 10^{-5} s^{-1} is situated southeast of the C_{cen}, with an area of anticyclonic vorticity (+15 x 10^{-5} s^{-1}) situated to the northeast (**Figure 4-10a**). On D-1 the cyclonic vorticity maxima is situated across the C_{cen}, with the small area of anticyclonic vorticity in the northeast quadrant having increased to > +20 x 10^{-5} s^{-1} (**Figure 4-10b**). On D+1 the cyclonic vorticity maximum has decreased to -25 x 10^{-5} s^{-1} accompanied by a minor northeast shift of the pattern. The anticyclonic vorticity region to the north has been eliminated, with only a region to the extreme east and south of the C_{cen} exhibiting anticyclonic vorticity (**Figure 4-10c**).

500 hPa

At P_{500} a decrease in spatial extent is observed from D-3 to D+1 (**Figures 4-11a, b** and **c**). On D-3 cyclonic vorticity having a northwest-southeast orientation, is observed across C_{cen} with values of $< -20 \times 10^{-5}$ s^{-1}. The area under the influence of the cyclonic vorticity region on D-1 is reduced in response to the retreat of the northwest limb of negative vorticity. Anticyclonic vorticity is observed to intrude to a greater extent on D+1 from the south than previously (D-3, D-1). The result is that cyclonic vorticity is reduced ($< -15 \times 10^{-5}$ s^{-1}) and also retreats north of C_{cen}.

200 hPa

On D-3 a band of cyclonic vorticity stretching from the northwest to the southeast is situated across the C_{cen}, with regions of anticyclonic vorticity on either side of it. The strongest cyclonic vorticity is -10×10^{-5} s^{-1} (C_{cen} and -2.5° longitude +7.5° latitude) and the strongest anticyclonic vorticity is $> +20 \times 10^{-5}$ s^{-1} south of the C_{cen} (**Figure 4-12a**). D-1 sees the cyclonic vorticity band break up into smaller pockets of cyclonic vorticity with one situated over the C_{cen}, while the region of anticyclonic vorticity to the south has moved westward and intensified to $> +30 \times 10^{-5}$ s^{-1} (**Figure 4-12b**). On D+1 (**Figure 4-12c**) only anticyclonic vorticity regions are observed with a maxima of $> +35 \times 10^{-5}$ s^{-1} to the southeast and a region having values $> +25 \times 10^{-5}$ s^{-1} to the northwest of the C_{cen}.

As expected the region of cyclonic vorticity remains the dominant feature at P_{850} and P_{500} throughout the sequence, while a progression from cyclonic to anticyclonic vorticity across the C_{cen} is observed at P_{200}. The minimal decrease in cyclonic vorticity

values between P_{850} and P_{500} gives an indication of the strength and depth of circulation. The change from cyclonic to anticyclonic vorticity at P_{200} is an indication of increasing diffluence in the northwest quadrant of the composite. In essence, the upper anticyclonic outflow is disorganised at P_{200}, with maximum in 'front' of the TC. Observation of the shape of the cyclonic vorticity region at P_{850}, and to a lesser extent at P_{500}, reveals a change from zonal on D-3 to meridional on D-1 and D+1.

4.1.1.7 Temperature

850 hPa

The maximum temperature attained during the sequence at P_{850} is just over 18.5 °C (**Figure 4-13a, b** and **c**). On D-3 an area of less than 18 °C occurs northeast of the C_{cen} within a large area having temperatures above 18 °C. On D-1 a latitudinal band of temperatures between 17.5 °C and 18 °C extends along +7.5° longitude. The highest temperatures of > 18.5 °C are found to occur on D+1 in two areas, one northeast and the other west of the C_{cen}. Temperatures south of the 17.5 °C isotherm exhibit the expected decrease away from the equator also observed for the MSC. A noteworthy feature is that the temperature gradient in the south increases during the sequence as cooler air skirts the southern edge of the TC.

200 hPa

At P_{200} a dramatic reduction in the area of maximum temperature (greater than -52 °C) is observed (**Figure 4-14a, b** and **c**). From D-3 to D-1 the area, initially covering most of the southern half of the composite, is reduced to a circular region of approximately 2.5° radius. On D+1 the circular region has spread out into an elliptical region

extending from the C_{cen} to the southeast. Unlike the temperatures at P_{850} a uniform poleward decrease in temperature is not observed.

4.1.1.8 Relative Humidity

850 hPa

On D-3 relative humidity values of > 80 % dominate the composite with only the northwest quadrant having values below 75 % (**Figure 4-15a**). The highest humidity values of > 85 % are found in three areas along the -5° latitude. On D-1 a maximum relative humidity of > 90 % is observed southeast of the C_{cen}, while a relatively large area < 80 % occurs to the west of it (**Figure 4-15b**). On D+1 a broad band (10° longitude in width) of relative humidity above 80% extends meridionally along +5° longitude, with values to the west of it dipping below 70% (**Figure 4-15c**). The clockwise intrusion of dry air from the southwest quadrant is clear.

500 hPa

The relative humidity structure at P_{500} shows a much more coherent change in the areas of high values than was evident at P_{850} (**Figure 4-16a, b** and **c**). On D-3 an area of minima (less than 40%) is observed along 0° longitude, with values > 50 % occurring only on the extreme east of the composite. The meridional band is replaced by an smaller region of < 40 % at the C_{cen} on D-1, with the influx of relative humidity values > 50 % south of the C_{cen} separating it from a region of low relative humidities (< 30 %) to the southwest. A retreat of high relative humidity values is observed on D+1 by the presence of a small area to the east of the C_{cen} having values > 50 %. To the west of the 0° longitude relative humidity values of < 40 % are predominant.

Changes in the relative humidity structure at P_{850} are less coherent than at the P_{500}, as observed by the intrusion and later retreat of relatively high humidities to the southeast of the C_{cen}. At P_{850} the most noticeable change is the evolution of predominantly high values on D-3 (> 80 %) to relatively low humidity values of < 80 % on D+1. At both P_{850} and P_{500} it is found that the introduction of low relative humidity values occurs from the west, likely in response to the TC entering the subtropical regions.

4.1.1.9 Precipitable Water

Surface - 300 hPa

Figure 4-17a (D-3) reveals that precipitable water values > 53 mm are situated north of -5° latitude, but with a low axis (< 50 mm) along the -5° longitude. To the south of -5° latitude the precipitable water contours are arranged zonally with a steep gradient to the lowest value of < 45 mm. Highest values of > 56 mm are found east of the C_{cen}. On D-1 the areas of minimum and maximum precipitable water are still located in similar positions (**Figure 4-17b**). The region of high values to the east of C_{cen} has increased to > 57 mm while the region of minimum values in the south has reduced to < 40 mm. A region of lower values is still found northwest of the C_{cen} but does not drop below 54 mm. On D+1 (**Figure 4-17c**) the highest precipitable water of > 56 mm is found east of the C_{cen}, while values < 38 mm are found to the southwest of the C_{cen}. Precipitable water values < 53 mm dominate the composite following peak intensity resulting in very steep gradients to the south. The whole pattern rotates clockwise from D-3 to D+1.

The precipitable water field shows a steep gradient for values < 52 mm throughout the sequence. As would be expected the precipitable water sequence has a similar structure to the relative humidity sequence at P_{850} (see **Figures 4-16a, b** and **c**).

4.1.1.10 Equivalent Potential Temperature

850 hPa

On D-3 a maximum θ_e value of > 344 °K is situated across and south of the C_{cen}, with values to the south decreasing to < 335 °K, and those in the northwest quadrant to < 340 °K (**Figure 4-18a**). The contour gradient south of the θ_e maximum is steeper and more zonal than that in the north. On D-1 the θ_e maximum intensifies to > 346 °K at C_{cen}, with the 344 °K contour reaching as far south as -5° latitude (**Figure 4-18b**). The centre of low θ_e values in the north has been displaced while the values in the south have decreased to < 330 °K. In **Figure 4-18c** for D+1 it is observed that the contours in the vicinity of the θ_e maximum (> 346 K) have rotated from the southeast-northwest orientation to a southwest-northeast orientation. Although the gradient south of the C_{cen} has not increased, the northward movement of the θ_e maximum has resulted in a decrease in the θ_e minimum to < 328 °K in the southwest.

500 hPa

The θ_e field at P_{500} exhibits a progressive intrusion of high values (> 336 °K) from the east as well as a steady decrease in the θ_e values south of the C_{cen}. On D-3 an area of low θ_e values(< 335 °K) is situated across the C_{cen}, but is cut off from the low values (< 333 °K) to the south by an intrusion of the higher values from the east at -5°

latitude (**Figure 4-19a**). On D-1 the intrusion of high θ_e values has progressed, in a shift to west of C_{cen}, with an accompanying decrease in the θ_e values to the south (**Figure 4-19b**). The area of high θ_e values has moved across the C_{cen} on D+1 (**Figure 4-19c**) causing the low θ_e values in the north to retreat, while the low θ_e values in the south have reduced to < 331 °K.

The θ_e gradient at P_{850} on the poleward side of the TC is very steep throughout the sequence, while it is slacker on the equatorward side. The strength of the θ_e maximum is considerably lower than recorded by Anthes (1982) for a mean hurricane using near surface radiosonde data. Minimum values at a radius of 10° are also lower. At P_{500}, low θ_e near C_{cen} are circled by higher θ_e values, a pattern consistent with previously recorded TC structures (Anthes, 1982; Jury, 1993).

4.1.2 Vertical Section Analyses

4.1.2.1 Horizontal Kinetic Energy

Zonal Section

A progressive increase in horizontal kinetic energy below P_{700} in the east, and at P_{200} in the west is observed through the sequence (**Figure 4-20a, b** and **c**). On D-3 at the C_{cen}, between P_{300} and P_{850}, light winds are prevalent with strong winds present only above P_{200}. On D-1 a region of horizontal kinetic energy of > 50 J kg^{-1} is situated at P_{850} east of the C_{cen}. Horizontal kinetic energy values have decreased in intensity above P_{200} compared to D-3. On D+1 strengthening of the lower tropospheric horizontal kinetic energy maxima continues. At P_{200}, west of the C_{cen} a region of increased values of > 140 J kg^{-1} are found.

Meridional Section

On D-3 a region of low horizontal kinetic energy values (< 40 J kg^{-1}) between the surface and P_{200} is situated within 5° of the C_{cen} (**Figure 4-21a**). North of the C_{cen} at P_{700} a region of horizontal kinetic energy values > 70 J kg^{-1} is observed. As for the zonal section, kinetic energy values > 40 J kg^{-1} are prevalent above P_{300} on D-3. On D-1 (**Figure 4-21b**) the region of low horizontal kinetic energy at the C_{cen} is reduced to the P_{700} and P_{200} layer, while a region of horizontal kinetic energy > 100 J kg^{-1} is established in the south at P_{200}. Below P_{850} values of between 30 and 50 J kg^{-1} are prevalent. In **Figure 4-21c** (D+1) it is observed that the area of high horizontal kinetic energy north of the C_{cen} below P_{500} is replaced by values of < 40 J kg^{-1}. In the south the region of high horizontal kinetic energy below P_{700} has intensified to > 60 J kg^{-1}

with an accompanying increase in the upper tropospheric values (> 150 J kg^{-1}) in the southern sector.

On D-3 both the zonal and meridional sections contain regions of relatively low horizontal kinetic energy at the C_{cen}, corresponding to the low wind speeds at the TC centre observed in **Figures 4-3, 4-4** and **4-5**. It is notable that on D-1 and D+1 the region of low mid-level horizontal kinetic energy becomes increasingly tilted in the west.

4.1.2.2 Vertical Movement

Zonal Section

The vertical section sequence of vertical movement shows the strongest uplift of < -1.2 Pa s^{-1} occurs at P_{700}, +5° west of the C_{cen}. A progressive increase in the depth of the downward motion at the C_{cen} is noted (**Figures 4-22a, b** and **c**). On D-3 the dominant upward movement is interrupted at the surface by downward motion +7.5° west of the C_{cen}, and downward motion in the upper troposphere east of the C_{cen} of > 0.4 Pa s^{-1}. On D-1 the strength of the uplift decreases to 0.6 Pa s^{-1} in the mid-troposphere west and east of the C_{cen}. The region of downward motion near the surface extends 5° west and east of the C_{cen}, while the upper tropospheric downward motion extends down to P_{500}. On D+1 a region of downward motion (> 0.4 Pa s^{-1}) is situated on the C_{cen} with strong uplift to the east between P_{500} and P_{850}. The region of downward motion in the upper troposphere is displaced to the east while a region of strong downward motion (> 0.4 Pa s^{-1}) is established in the west from the surface to P_{700}.

Meridional Section

The sequence of vertical movement diagrams shows a dramatic reduction in the strength of the uplift occurring within the composite TC (**Figure 4-23a, b** and **c**). The core of downward motion on D-3 is situated in the northern sector of the diagram with an area from the surface to P_{100} experiencing maximum uplift of < -0.4 Pa s^{-1}. The area of strongest uplift of < -1.4 Pa s^{-1} is found near 400 hPa south of the C_{cen}. The southern edge of the uplift zone stretches from the surface to P_{100} along the +7.5 ° latitude. On D-1 strengthening of the downward motion at P_{300} (> 0.4 Pa s^{-1}) as well as a reduction in the uplift to < -0.2 Pa s^{-1} is observed. Disintegration of the southern convective area is evidenced by reduction in the highest uplift to -0.8 Pa s^{-1}. On D+1 a dramatic change is observed when the strongest uplift of < -0.4 Pa s^{-1} is found at P_{850}, while the region of downward motion to the north has lost its coherence.

From the sequence of zonal and meridional vertical sections a clear area of uplift and downward motion is recognisable on D-3 and D-1, but this structure disintegrates by D+1. Although the change in the vertical movement structure from D-1 to D+1 is dramatic, this phenomenon is often recorded once TC's have attained their maximum intensity and start to decay. On D-3 it is noted that no tilt occurs in the uplift core in the meridional section, while on D-1 tilt is observed to the south below P_{500}. The maintenance of the vertical coherence and shape of the uplift core is better represented in the meridional sections than the zonal sections. The lack of coherence of the uplift core in the zonal sections may be a function of the offset of the C_{cen} and the vertical uplift core (see **Figure 4-8**).

4.1.2.3 Divergence

Zonal Section

A region of strong divergence on D-3 is situated at P_{200} to the east of the C_{cen}, where values of > +5 x 10^{-5} s^{-1} are distributed (**Figure 4-24a**). Between P_{850} and P_{300} convergence and divergence regions are distributed alternately from east to west with the former < -1 x 10^{-5} s^{-1} and the latter > +2 x 10^{-5} s^{-1}. At the surface convergent values of < -2 x 10^{-5} s^{-1} are distributed up to P_{850}. On D-1 strengthening of the P_{200} divergence is accompanied by a downward extension of the +1 x 10^{-5} s^{-1} divergence contour west of the C_{cen} (**Figure 4-24b**). The surface layer of convergence has retained its vertical expression and is linked to a region of convergence < -3 x 10^{-5} s^{-1} between P_{500} and P_{300}. The downward extension of the upper level divergence reaches P_{850} on D+1 even though it is reduced in intensity to approximately 2 x 10^{-5} s^{-1}, while the surface convergence reaches up P_{700} at C_{cen} (**Figure 4-24c**).

Meridional Section

The meridional divergence section shows a progressive decrease in strength of the upper level divergence, a parameter which needs to be sustained to ensure TC development (**Figures 4-25a, b** and **c**). On D-3 the maximum divergence of 6 x 10^{-5} s^{-1} is located in the southern sector at P_{200}, while at the surface convergent flow reaches a maximum of -9 x 10^{-5} s^{-1}. The area of convergence at P_{200} of 3 x 10^{-5} s^{-1} north of the C_{cen}, corresponding to downward motion in the vertical wind section, is an indicator of the position of the TC eye (see **Figure 4-23a**). The maximum divergence on D-1 is maintained at P_{200}, but the strength of the surface convergence as well as that at P_{200} has diminished by 2 x 10^{-5} s^{-1}. Although the surface convergence is still present on

D+1, the upper level divergence has decreased to 2 x 10^{-5} s^{-1}. Most significant is the shallowness of the surface convergence, values < -2 x 10^{-5} s^{-1} are confined below P_{850} throughout.

From the zonal and meridional vertical sections for divergence, persistence of the surface (1000 hPa) convergence is evident all around and to the southeast of C_{cen} from D-3 to D+1. The upper tropospheric divergence is located above the region of maximum uplift, while little surface divergence is evident in the regions of downward motion (**Figures 4-22 and 4-23**). Upper divergence collapses after D-1.

4.1.2.4 Vorticity

Zonal Section

The zonal vertical section of vorticity shows a sequential decrease in depth of the cyclonic vorticity areas together with a simultaneous decrease in its radial extent about the C_{cen} (**Figure 4-26a, b c**). On D-3 the cyclonic vorticity area extends from the surface to P_{200} with a value of < -25 x 10^{-5} s^{-1} at P_{850} at the C_{cen}. Anticyclonic vorticity of > 15 x 10^{-5} s^{-1} is found at P_{200} in the west of the composite. A decrease in the depth of the cyclonic vorticity is observed on D-1 in the east with anticyclonic vorticity increasing to > 20 x 10^{-5} s^{-1} at P_{200}, while the highest cyclonic vorticity is still present at P_{850}. D+1 sees the cyclonic vorticity depth decreasing to P_{300}, while the east-west distance covered decreases to < 20°.

Meridional Section

Throughout the sequence of vorticity sections the area of cyclonic vorticity is dominant as expected for southern hemisphere TC's (**Figures 4-27a, b** and **c**). On D-3 the region of cyclonic vorticity reaches from the surface to P_{100}, with a maximum of -25 x 10^{-5} s^{-1} occurring below P_{700}. The area of cyclonic vorticity < -30 x 10^{-5} s^{-1} reaches up to P_{500} on D-1, with lower values at P_{850}. On D+1 anticyclonic vorticity is observed to dominate the sector east of the C_{cen} with a value of > 20 x 10^{-5} s^{-1} occurring between P_{500} and P_{200}. A pronounced equatorward tilt is evidenced in the cyclonic vorticity minima.

For both the zonal and meridional sections a decrease in the depth of the cyclonic vorticity region is apparent. Gradual decay of the TC is evidenced on D+1 by the reduction in the vertical extent of the cyclonic vorticity, a reduction in the height of the maximum cyclonic vorticity to below P_{850}, and the increased anticyclonic vorticity in the south at the higher levels resulting in a tilt of the system.

4.1.2.5 Relative Humidity

Zonal Section

The zonal section of relative humidity reveals that a steady intrusion of low values occurs from the west between P_{700} and P_{200}, while values to the east are relatively constant (**Figures 4-28a, b** and **c**). On D-3 a steady decrease in relative humidity values from the surface to P_{700} is observed while above P_{200} a steady decrease is observed. A region of relative humidity values < 40 % is situated near C_{cen} and to the west between P_{700} and P_{500}. A decrease in vertical extent of the low relative

humidity over the C_{cen} is observed on D-1, while an increase in its vertical extent is seen west of -5° longitude. A region of relative humidity > 90 % occurs east of the C_{cen} close to the surface. Very low relative humidity values (< 30 %) have penetrated along P_{300} west of the C_{cen} on D+1, while the relative humidity values at the surface have decreased to < 80 %.

Meridional Section

A consistent feature of the vertical section of relative humidity is the steady increase in values below P_{700} and above P_{200} respectively (**Figures 4-29a, b** and **c**). Areas containing relative humidity values less < 50 % are the only regions in which changes in the vertical structure of the relative humidity is observed. On D-3 a large region of low relative humidity values in the mid-troposphere intrudes from the south. D-1 sees the northward elongation of the relative humidity region < 40%. On D+1 re-establishment of the link between the southern and the northern areas of relative humidity less than 40% is observed to have taken place at P_{300} at the C_{cen}.

4.1.2.6 Equivalent Potential Temperature

Zonal Section

The vertical distribution of θ_e undergoes very little change from D-3 to D+1, especially at the upper tropospheric levels where values > 350 °K increase uniformly towards the tropopause (**Figures 4-30a, b** and **c**). On D-3 the θ_e values from the surface up to P_{100} has the same structure on both sides of the C_{cen}, with only values at P_{700} decreasing to < 330 °K. The extent of the 350 °K contour at the surface is restricted to the east of the C_{cen}, while the θ_e minimum at P_{700} has decreased in extent.

On D+1 the surface θ_e maximum is restricted to approximately 5° west and east of the C_{cen} with the 350 °K area deepening to P_{850}. The low θ_e values (< 330 °K) at P_{700} are observed to extend both west and east of the C_{cen} for approximately 7.5°.

Meridional Section

From **Figures 4-31a, b** and **c** it is clearly evident that the region of maximum change in the θ_e vertical field occurs on the poleward side of the TC, while the northern sector of the vertical contour plot remains relatively stable through the sequence. The θ_e contours above P_{200} retain their structure and intensity throughout the sequence due to the dryness of the atmosphere. On D-3 a minimum area of < 330 °K is situated across the C_{cen} above P_{700}, with a maximum of > 350 °K occurring at the surface. On D-1 the 330 °K minimum has shifted towards the south while at the surface the 350 °K maximum is maintained. On D+1 very little change is observed to have occurred from the previous day.

Throughout the meridional sequence the θ_e value at the surface in the southern sector (+5° latitude) becomes progressively lower, going from 350 °K (D-3) to 345 °K (D+1). A similar pattern is observed to the west in the zonal sections. This change is significant as it occurs in the direction of TC movement, while in the north, and to a lesser extent in the east (the TC origin). The θ_e vertical profile has already been modified and is thus relatively stable. Jury (1993) showed that at the surface θ_e values initially increased as the TC approached and then decreased after the TC passed, similar to evidence in the zonal section at +5° longitude. TC convective 'erosion' occurs on the poleward side in the 700 - 600 hPa layer.

Westward Moving TC Synthesis

The WM TC is seen to retain a strong cyclonic wind structure at the 850 hPa and the 500 hPa surfaces throughout the sequence while a growth of anticyclonic structure is observed at the 200 hPa surface. The vorticity diagrams at the 850 hPa and the 200 hPa surfaces quantify the rotation observed in the horizontal wind diagrams, while the kinetic energy gives an indication of the strength of the winds at these levels. TC Firinga has a wind maxima of > 20 m s^{-1} near the surface, while the WM TC has a maxima of approximately 10 m s^{-1}. Observations of vertical movement and divergence combine to give a good representation of the strength and depth of the synoptic uplift associated with the TC composite as well as showing the strength of the mass and energy evacuation in the upper troposphere. Maximum uplift of -6 Pa s^{-1} is observed for TC Firinga, 3-times that observed for the WM TC with the upper level divergence exhibiting similar changes. These parameters are seen to be less organised than what is found for TC Firinga suggesting that the compositing procedure not only reduces the intensity but also the spatial agreement. When it is considered that uplift cores often have a spatial resolution of less than 2.5° (ECMWF data grid) the resultant 'smearing' should be expected as these cores may not locate themselves in the same position relative to the TC centre in each cyclone. Kinetic energy increases to 280 J kg^{-1}, similar to TC Firinga at the 200 hPa level, as the WM TC interacts with a subtropical trough. The upper level anticyclonic vorticity for the WM composite and TC Firinga is observed to be very similar at +35 x 10^{-5} s^{-1}.

From the thermodynamic and moisture variables interaction with the midlatitude systems are evidenced by steep temperature gradients, decreasing relative humidity values and low precipitable water values south of the C_{cen} in the lower troposphere. Equivalent potential temperatures calculated for the WM TC decreased significantly in the mid-troposphere. For this study values of ± 330 °K were recorded compared to values of > 340 °K in TC Danielle 1964 (Jury, 1993), note the main difference is the composite versus single case. At 850 hPa a differences of 14 °K exists between the WM composite and TC Firinga, while at the 200 hPa level a difference of only 2 °K is observed. It appears that the composite 'smears out' the saturated TC profile, hence uplift should not be readily sustained above 500 hPa. As for the kinematic analysis, spatial agreement with TC Firinga's thermodynamic and moisture fields is noted for parameters that possess circulation structures bigger than the 2.5° data resolution. It is for this reason that the composite vertical movement sections show very poor agreement with TC Firinga both zonally and meridionally, i.e. Firinga's maximum uplift is five times greater than the westward moving composite.

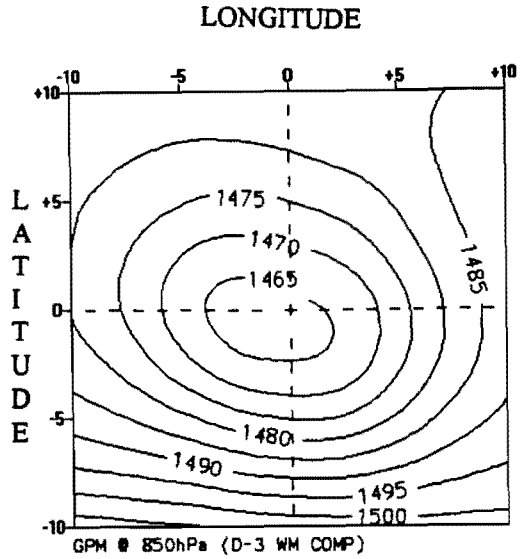

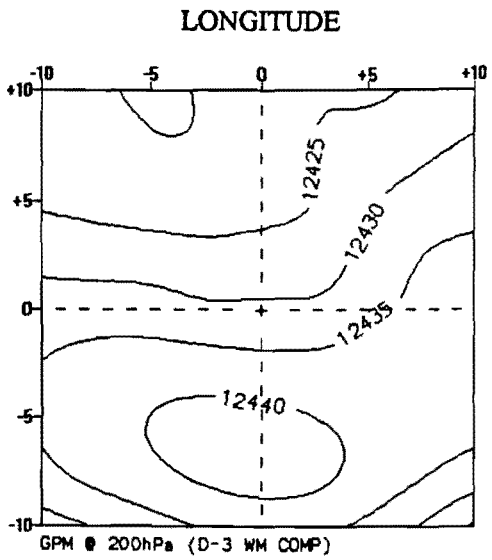

D-3

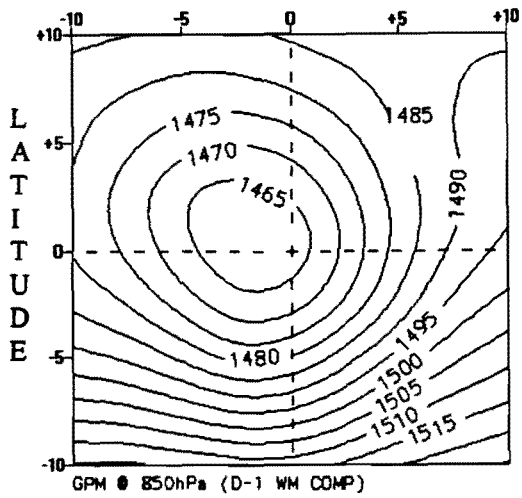

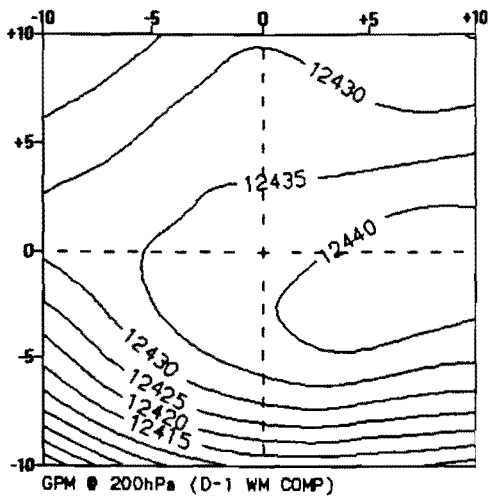

D-1

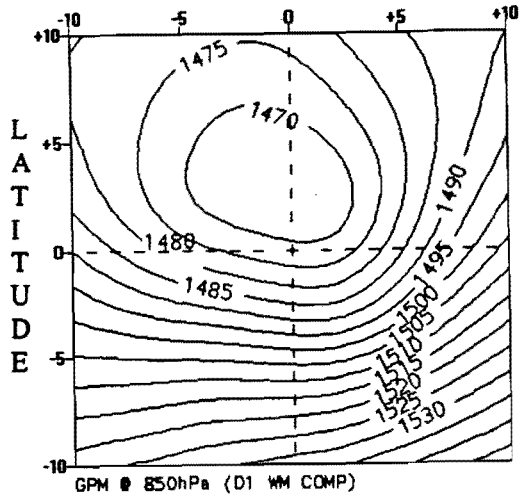

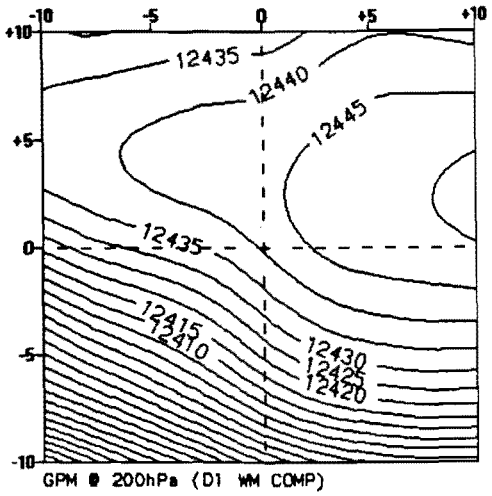

D+1

Figure 4-1a,b and c : WM geopotential @ 850 hPa. Contour interval 5 gpm.

Figure 4-2a,b and c : WM geopotential @ 200 hPa. Contour interval 5 gpm.

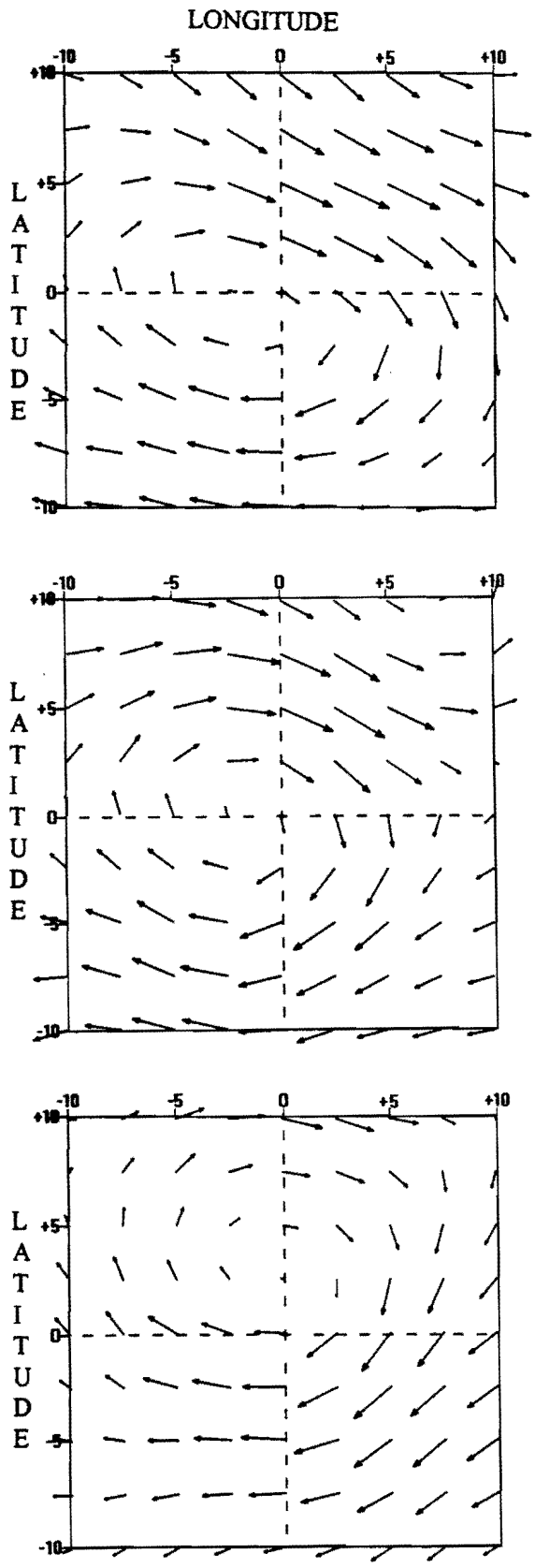

Figure 4-3a,b and c : WM horizontal wind @ 850 hPa.
Vector scale : ⟶ = 10 ms^{-1}.

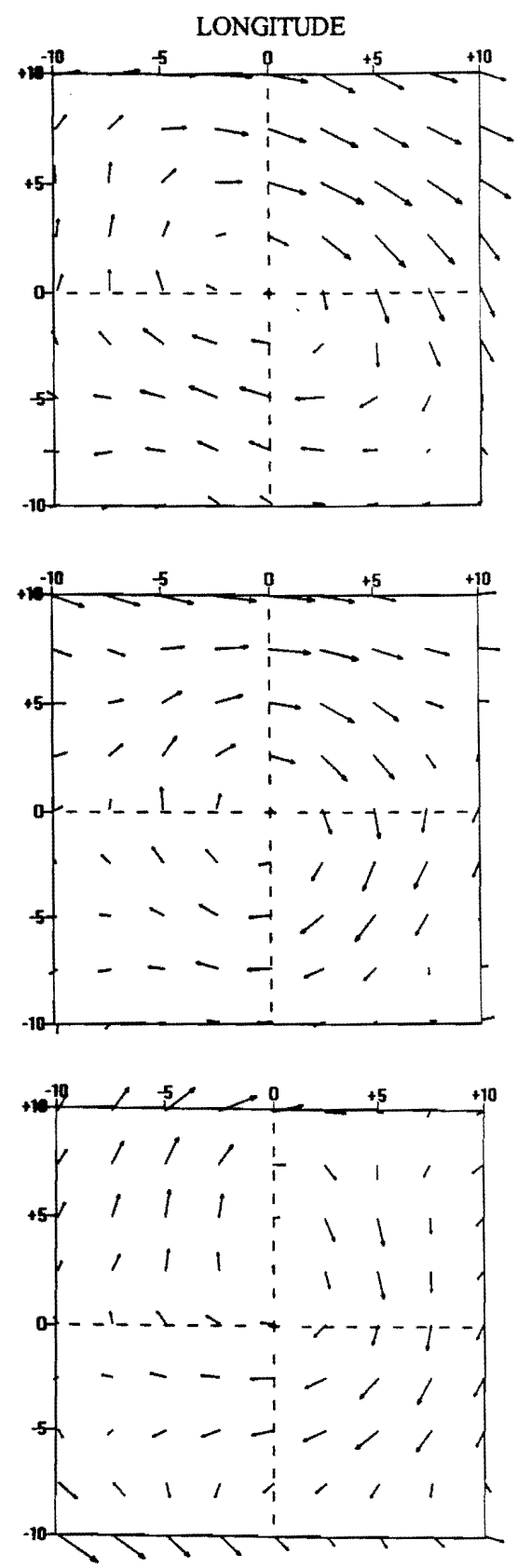

Figure 4-4a,b and c : WM horizontal wind @ 500 hPa.
Vector scale : ⟶ = 10 ms^{-1}.

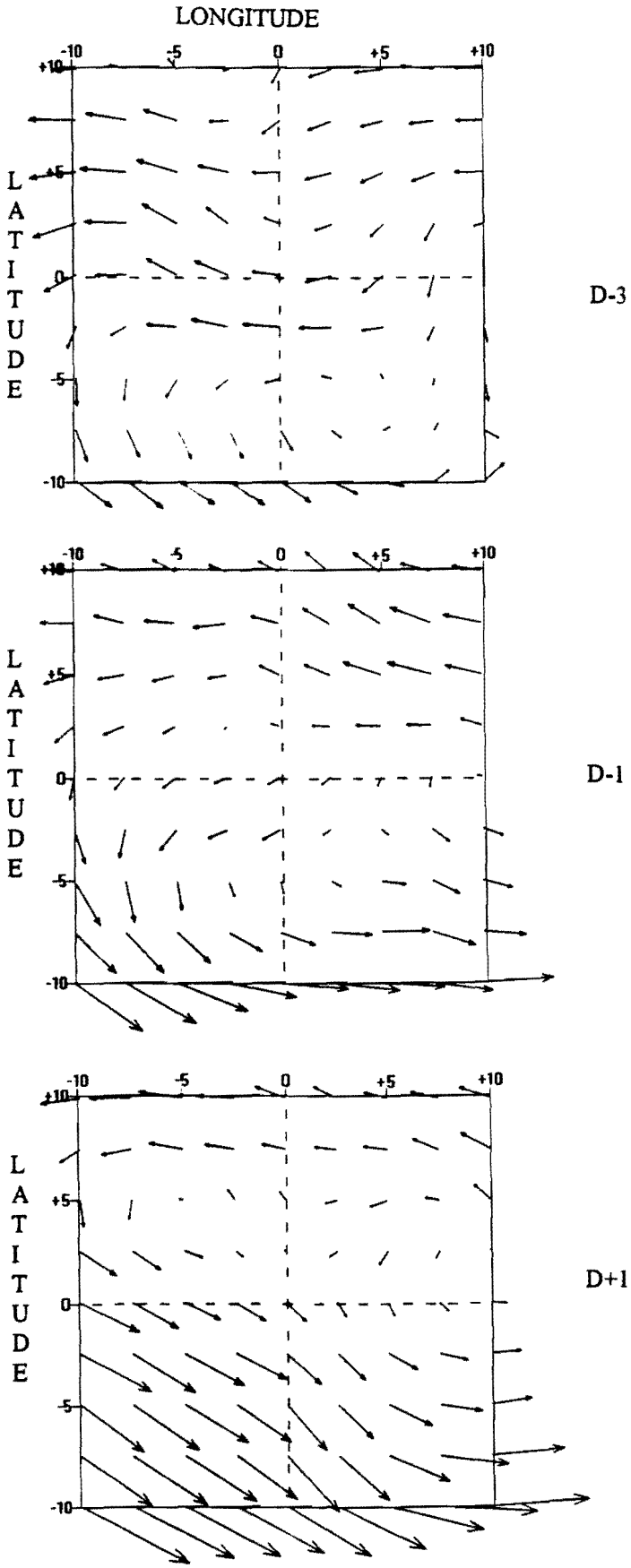

Figure 4-5a,b and c : WM horizontal wind @ 200 hPa.
Vector scale : ⟶ = 10 ms^{-1}.

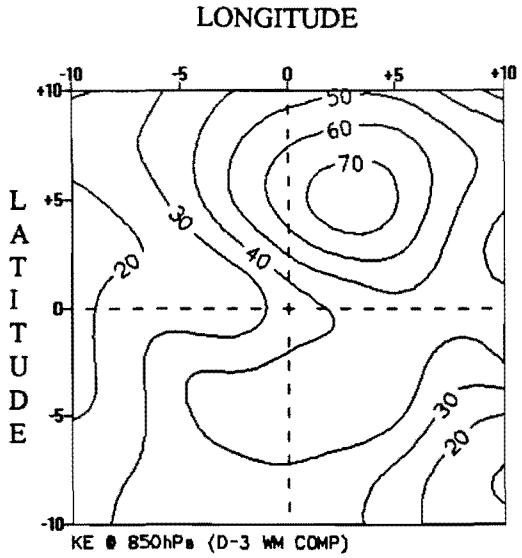

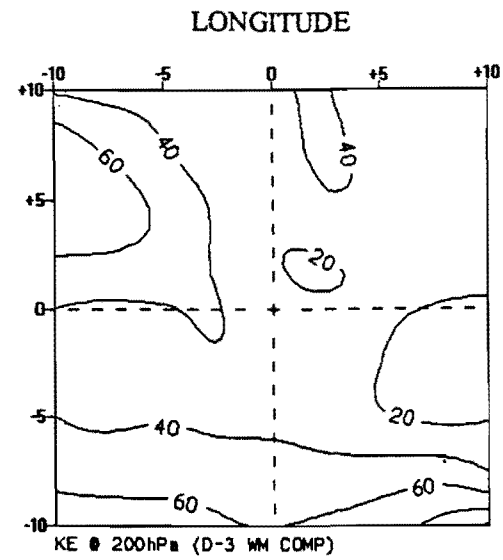

D-3

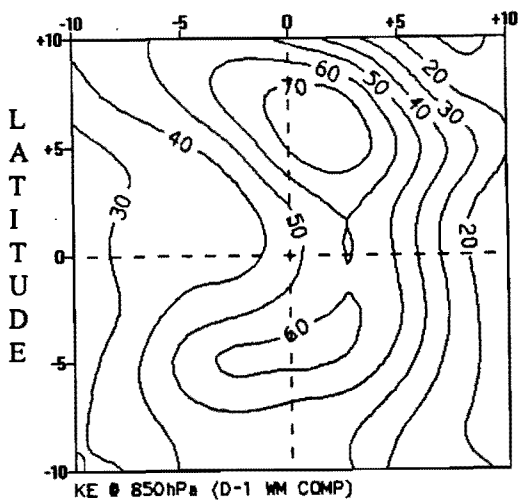

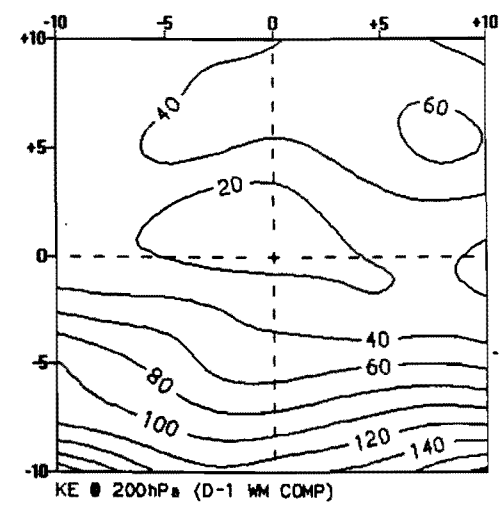

D-1

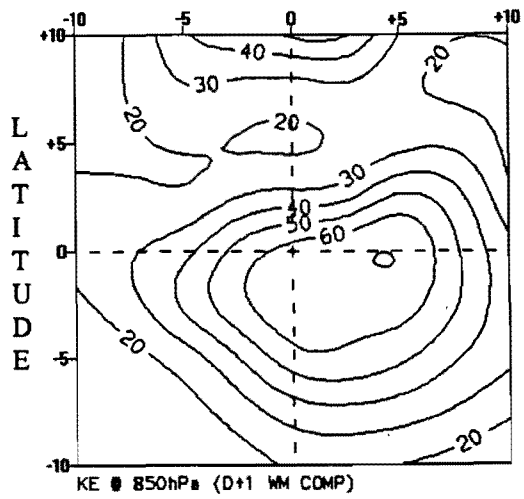

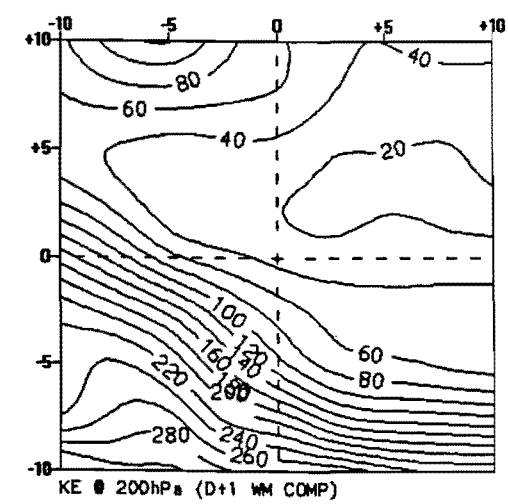

D+1

Figure 4-6a,b and c : WM kinetic energy @ 850 hPa. Contour interval is 10 J kg^{-1}.

Figure 4-7a,b and c : WM kinetic energy @ 200 hPa. Contour interval is 20 J kg^{-1}.

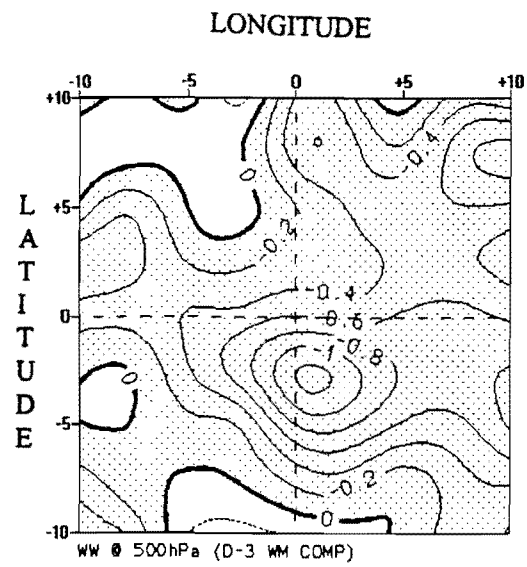

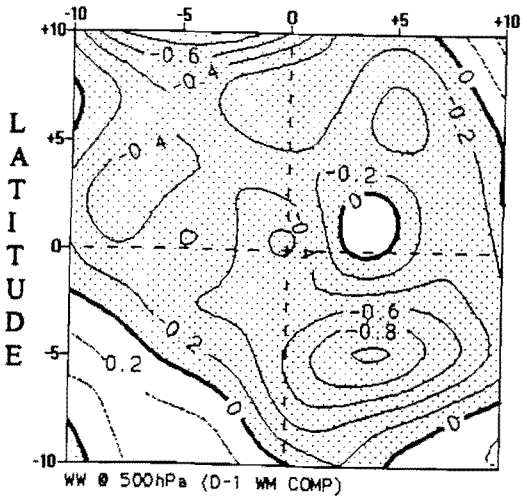

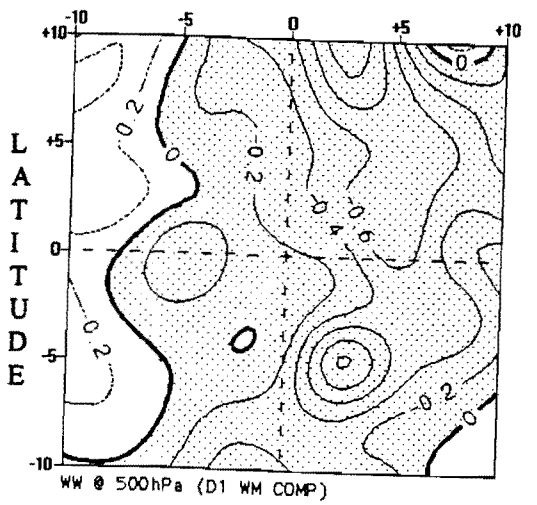

D-3

D-1

D+1

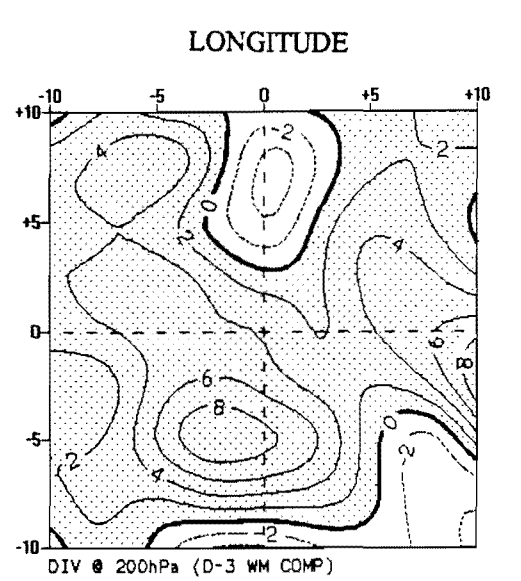

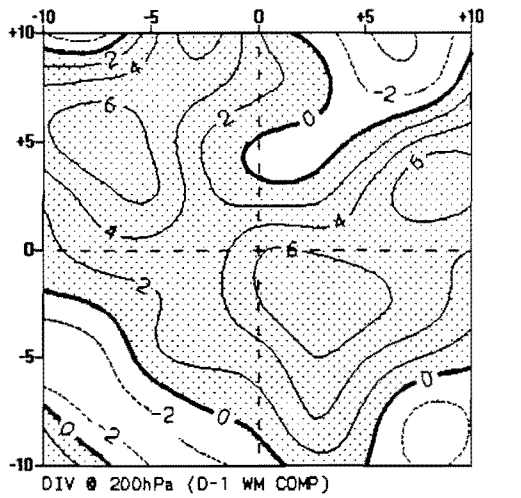

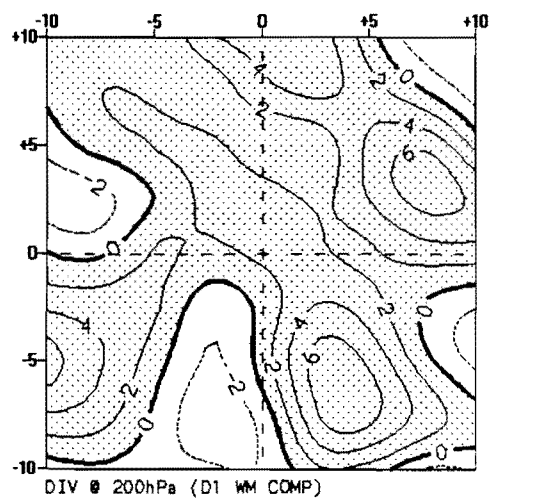

Figure 4-8a,b and c : WM vertical motion @ 500 hPa. Contour interval is 0.2 Pa s^{-1}.

Figure 4-9a,b and c : WM divergence @ 200 hPa. Contour interval is 2 x 10^{-5} s^{-1}.

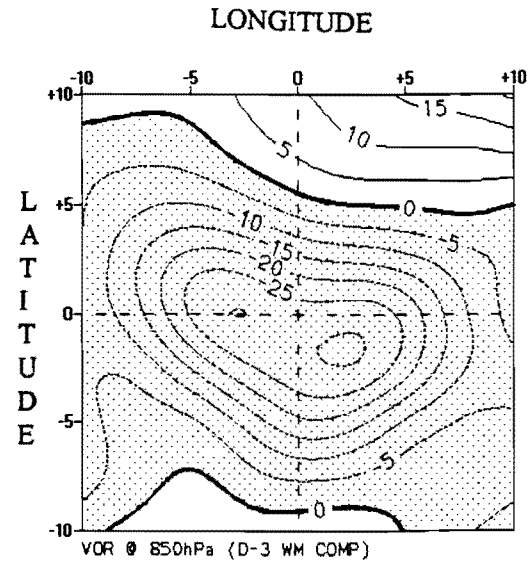

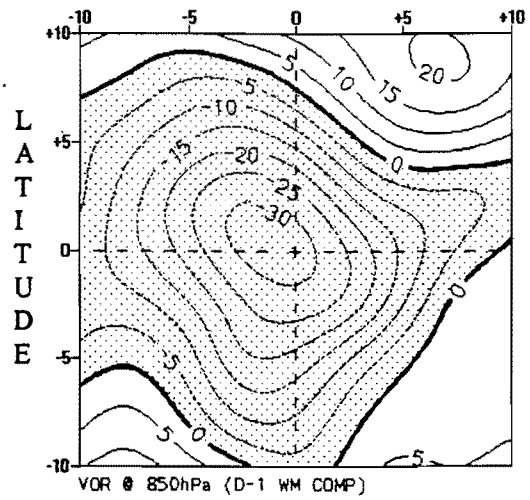

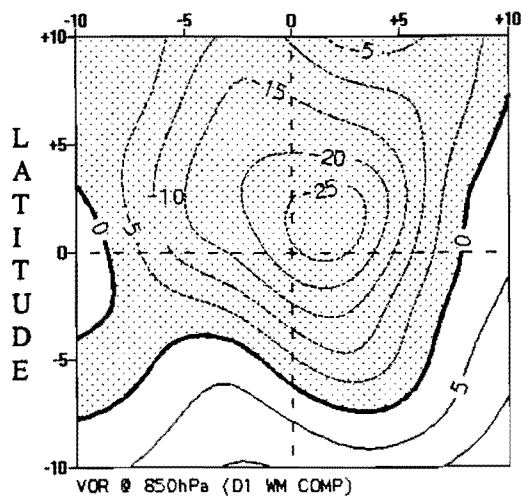

Figure 4-10a,b and c : WM vorticity @ 850 hPa.
Contour interval is 5 x 10^{-5} s^{-1}.

D-3

D-1

D+1

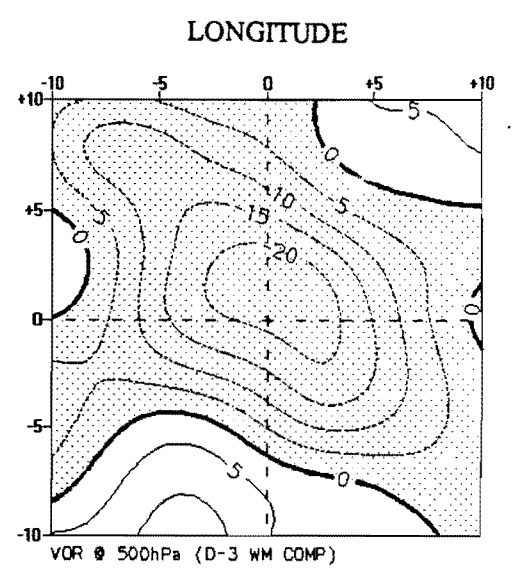

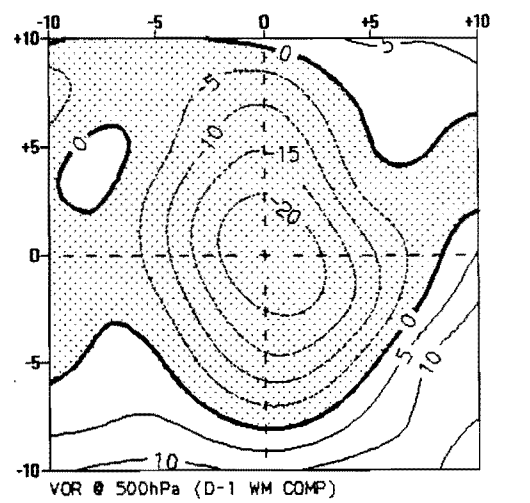

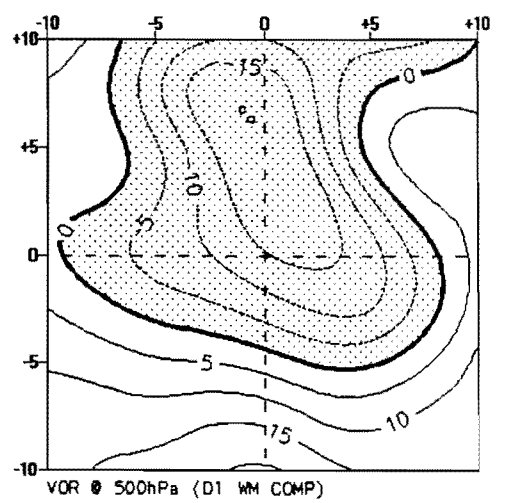

Figure 4-11a,b and c : WM vorticity @ 500 hPa.
Contour interval is 5 x 10^{-5} s^{-1}.

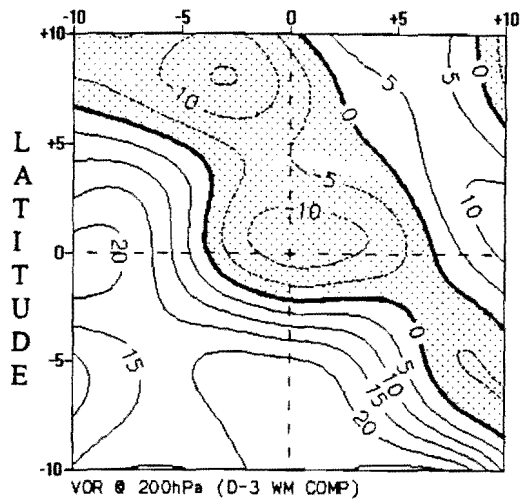

D-3

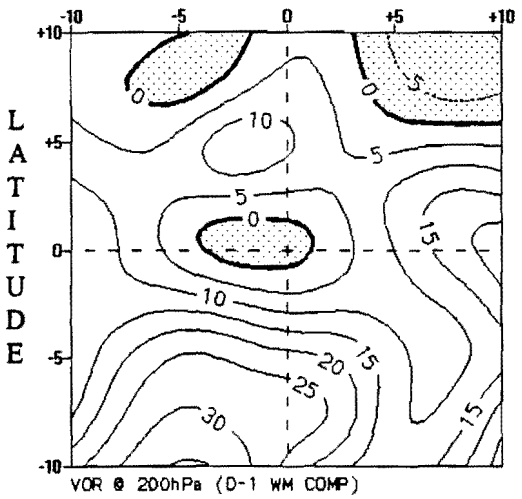

D-1

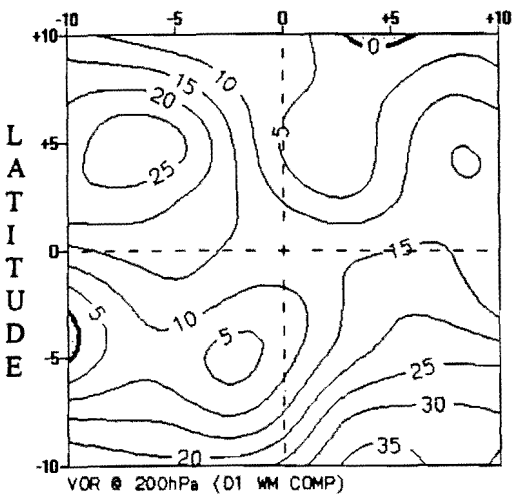

D+1

Figure 4-12a,b and c : WM vorticity @ 200 hPa. Contour interval is 5 x 10^{-5} s^{-1}.

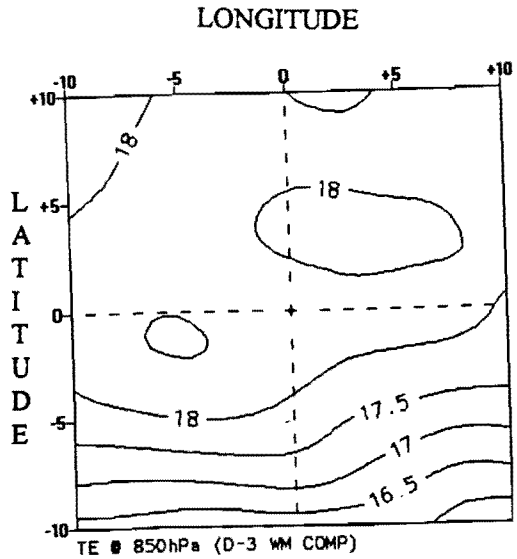

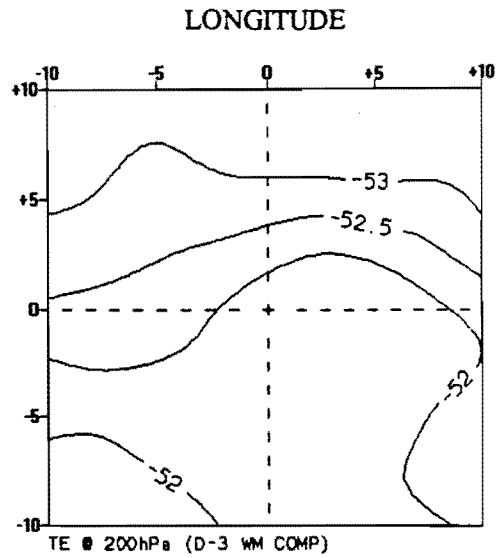

D-3

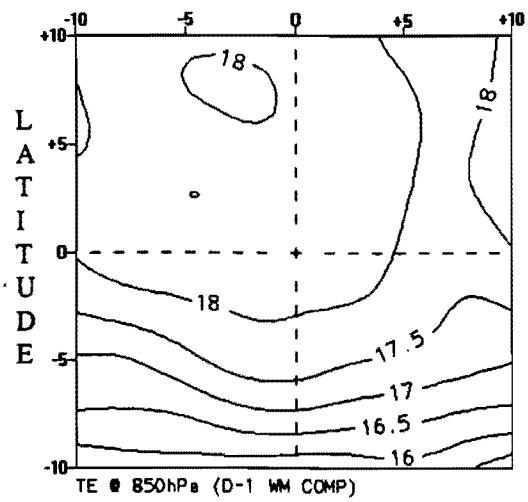

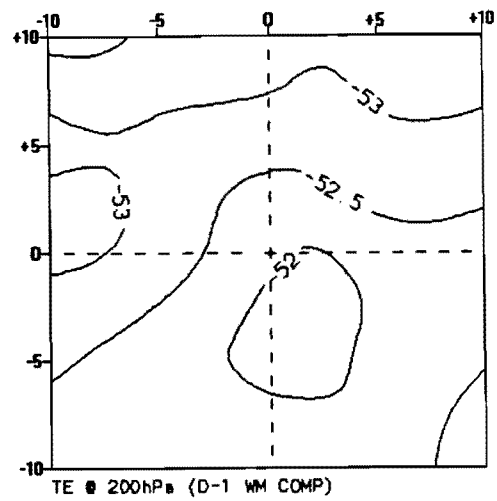

D-1

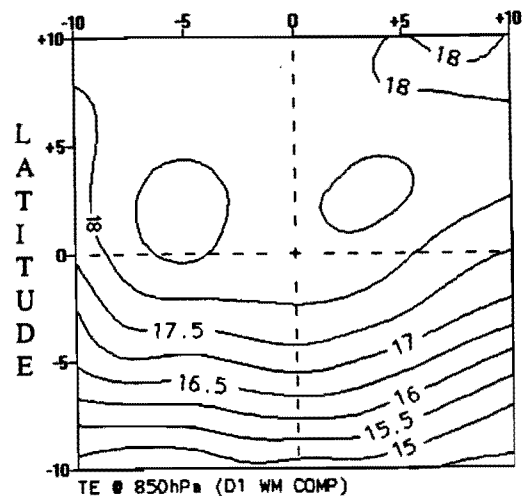

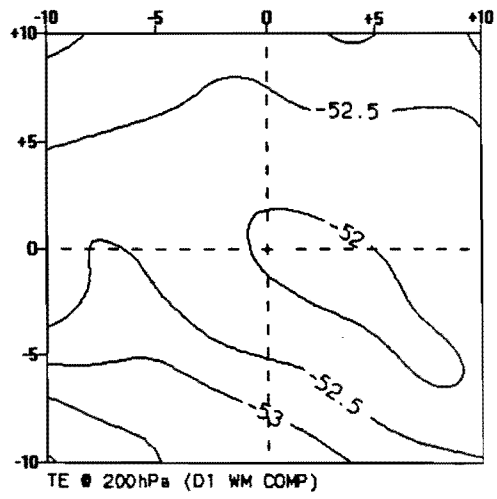

D+1

Figure 4-13a,b and c : WM temperature @ 850 hPa. Contour interval is 0.5 °C.

Figure 4-14a,b and c : WM temperature @ 200 hPa. Contour interval is 0.5 °C.

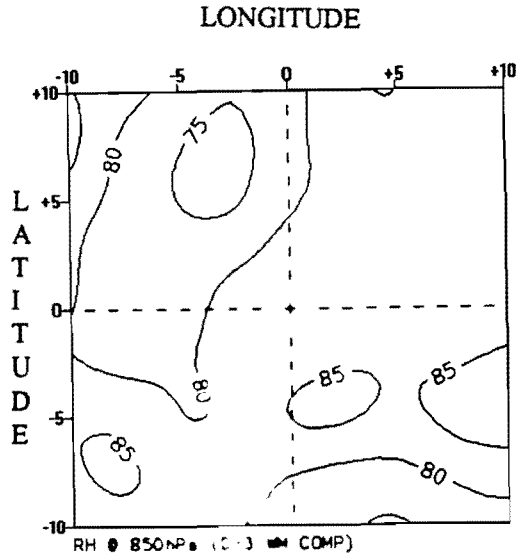

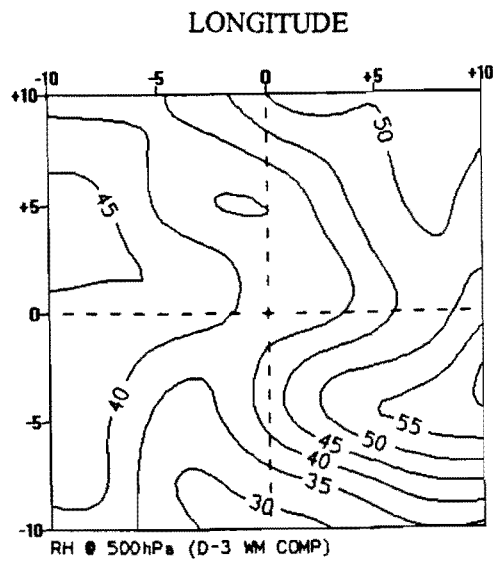

D-3

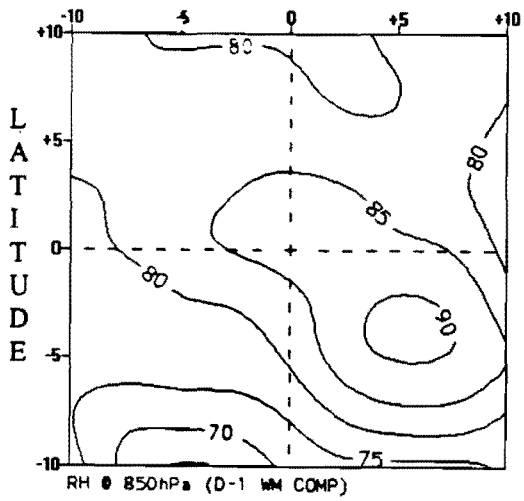

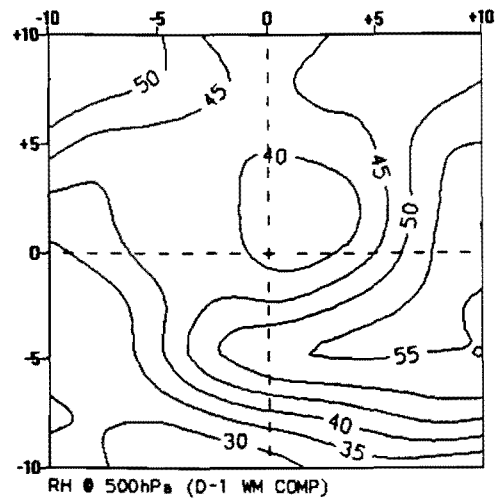

D-1

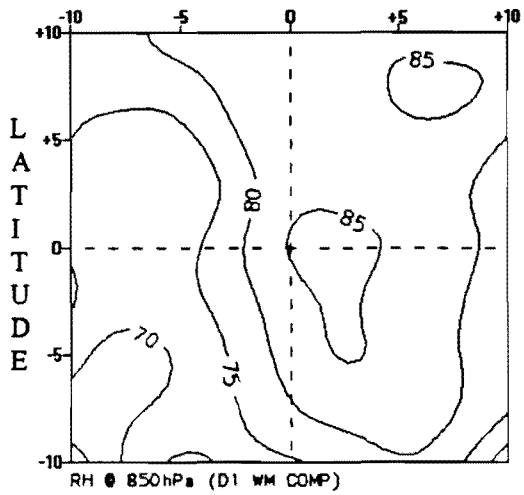

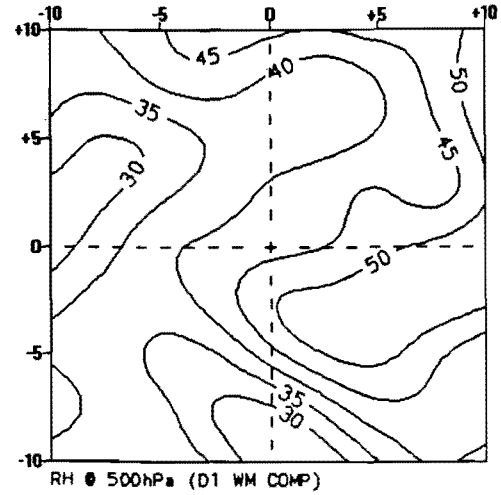

D+1

Figure 4-15a,b and c : WM relative humidity @ 850 hPa. Contour interval is 5 %.

Figure 4-16a,b and c : WM relative humidity @ 500 hPa. Contour interval is 5 %.

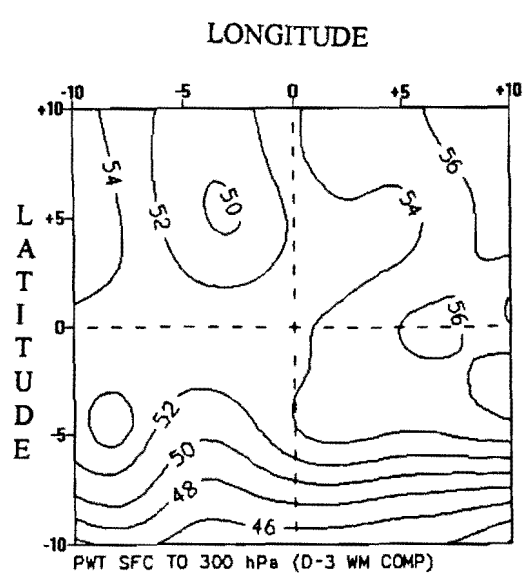

D-3

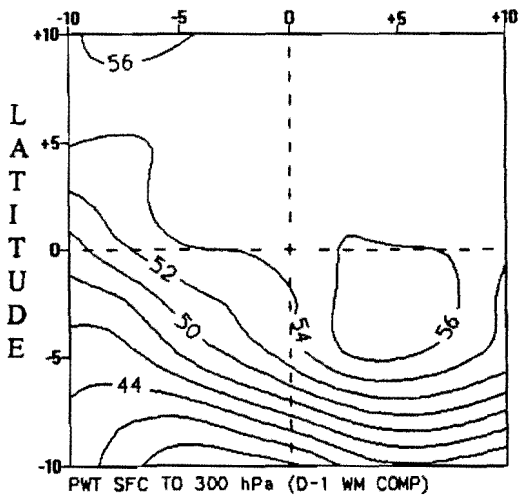

D-1

Figure 4-17a,b and c : WM precipitable water between the surface and 300 hPa.
Contour interval is 2 mm.

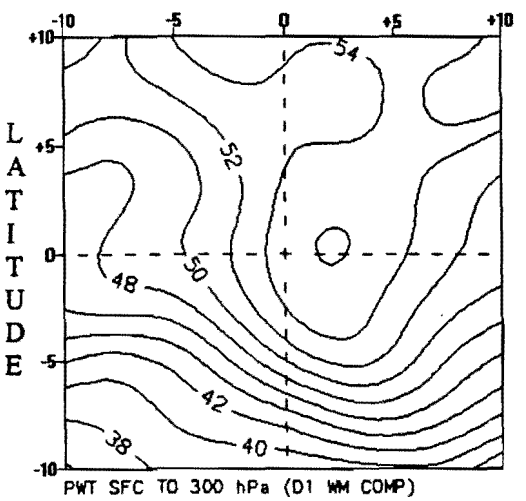

D+1

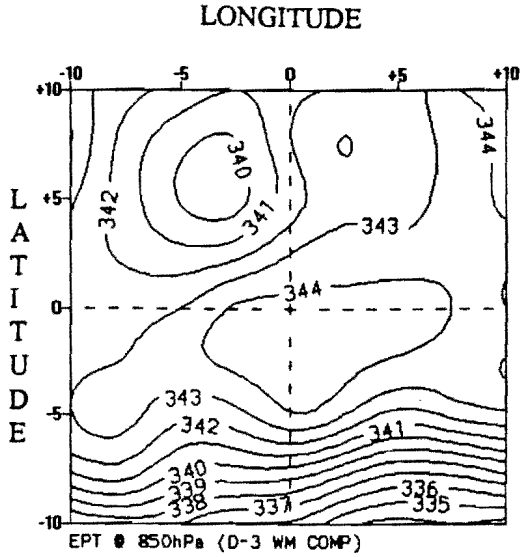

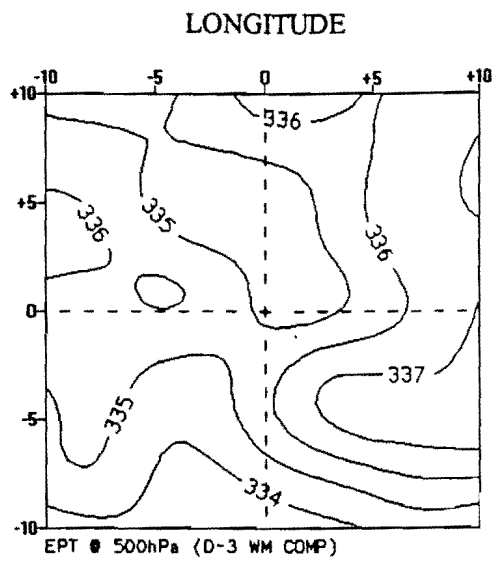

D-3

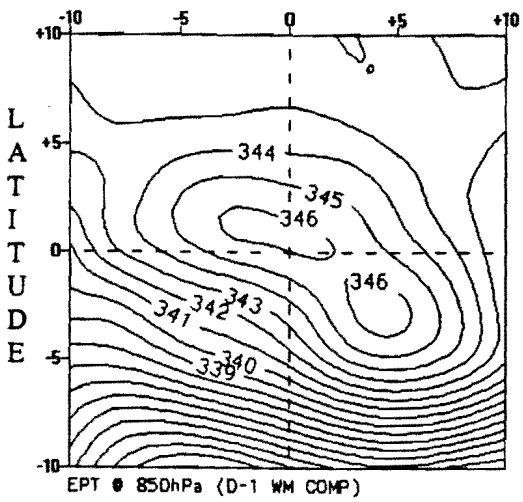

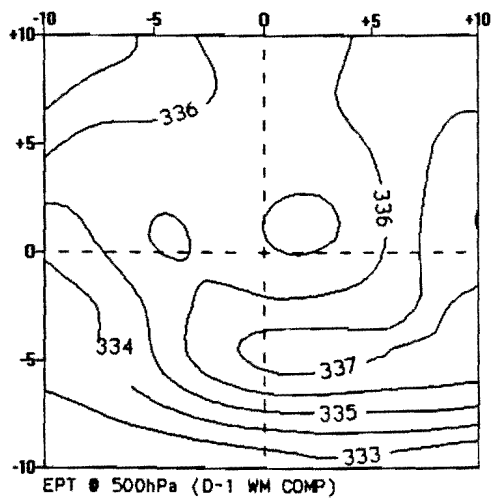

D-1

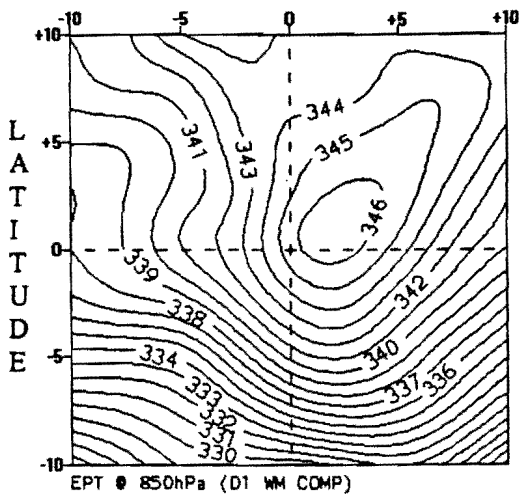

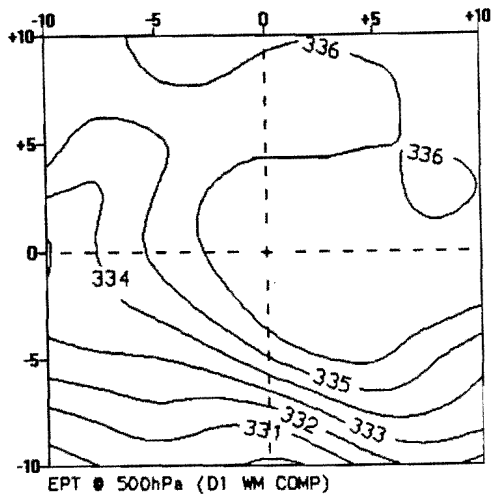

D+1

Figure 4-18a,b and **c** : WM equivalent potential temperature @ 850 hPa.
Contour interval is 1 °K.

Figure 4-19a,b and **c** : WM equivalent potential temperature @ 200 hPa.
Contour interval is 1 °K.

LONGITUDE

LATITUDE

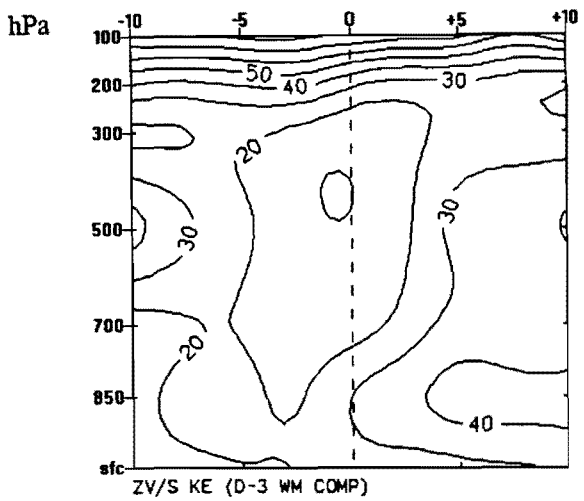

D-3

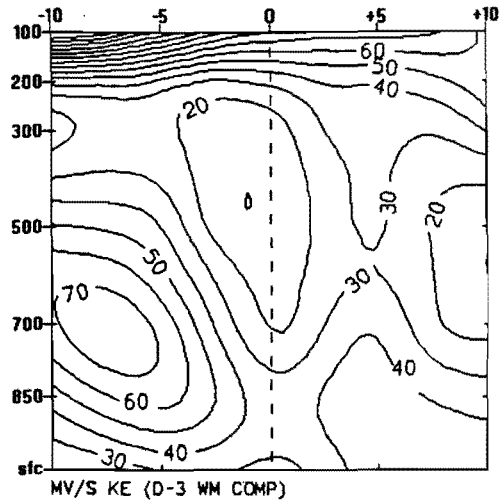

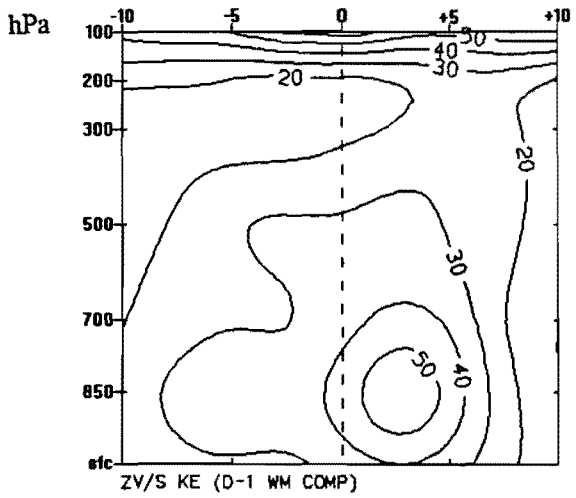

D-1

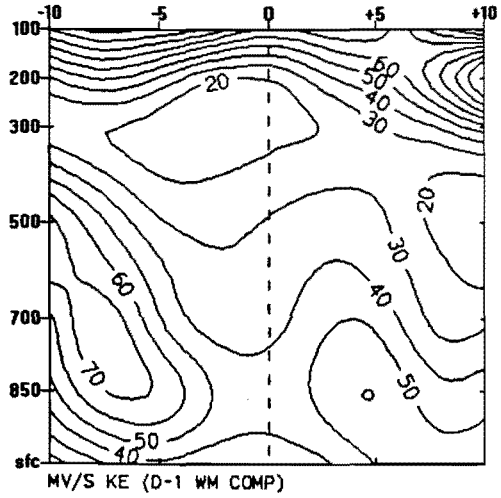

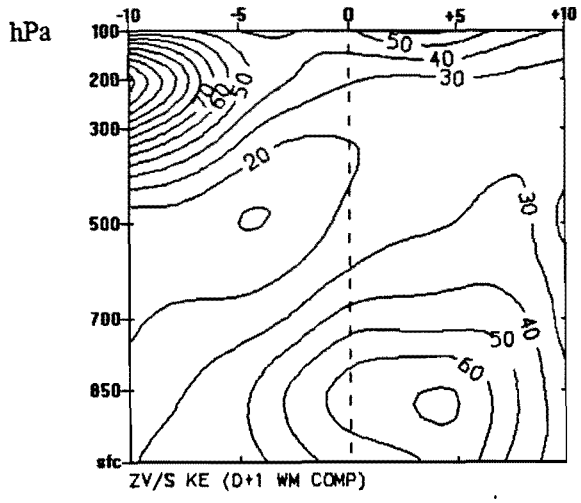

D+1

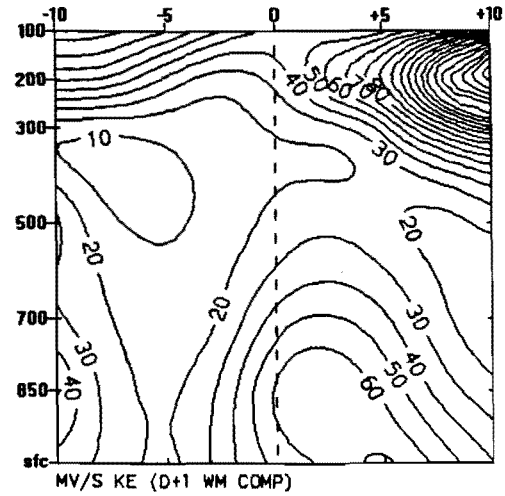

Figure 4-20a,b and c : WM zonal kinetic energy. Contour interval is 10 J kg^{-1}.

Figure 4-21a,b and c : WM meridional kinetic energy. Contour interval is 10 J kg^{-1}.

LONGITUDE

LATITUDE

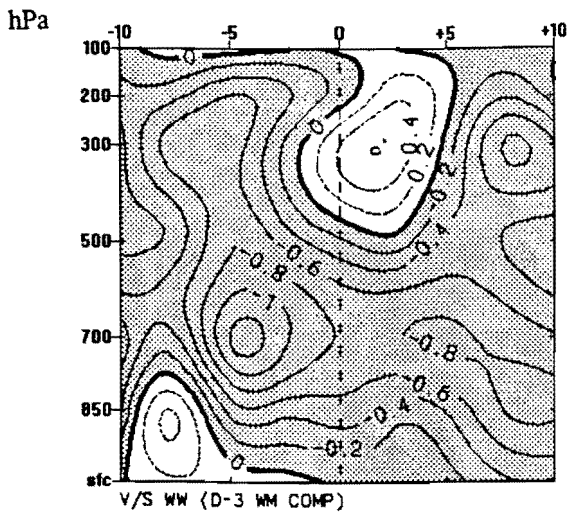

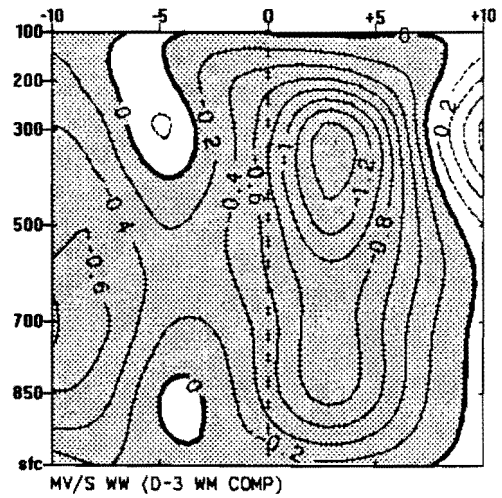

D-3

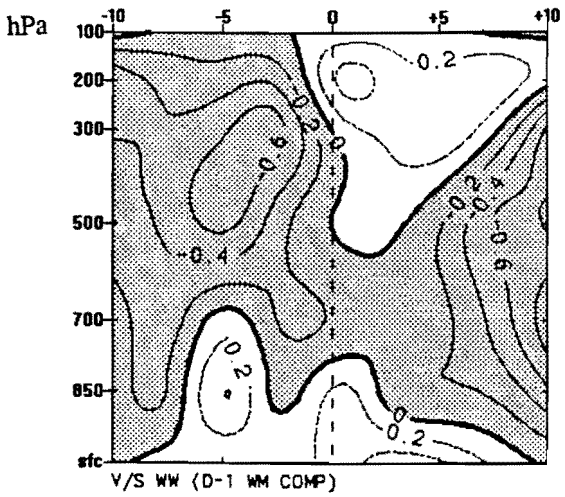

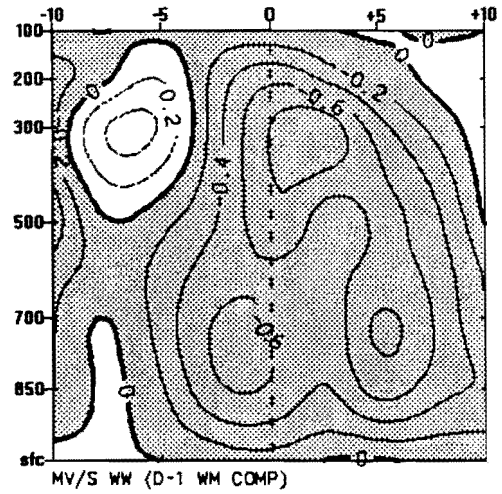

D-1

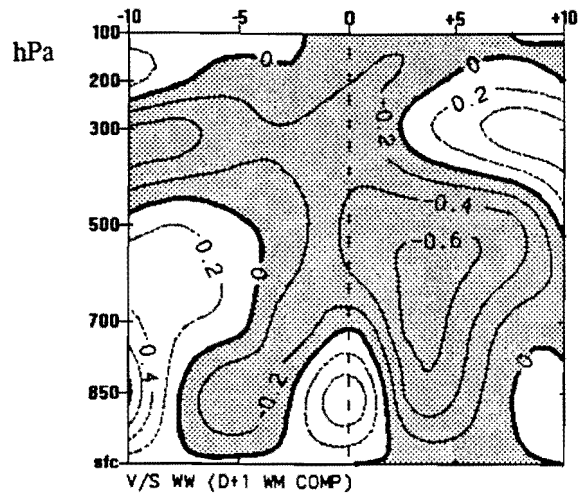

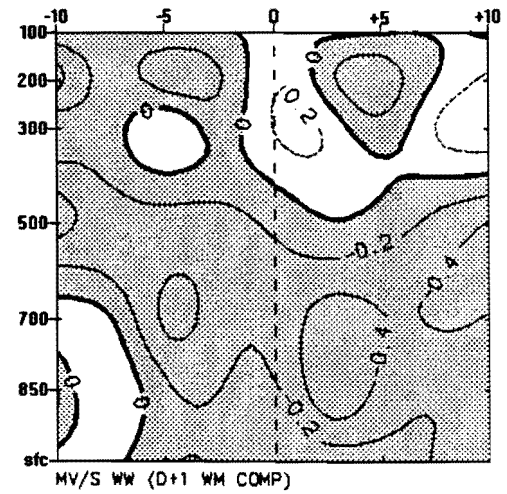

D+1

Figure 4-22a,b and c : WM zonal vertical motion. Contour interval is 0.2 Pa s^{-1}.

Figure 4-23a,b and c : WM meridional vertical motion. Contour interval is 0.2 Pa s^{-1}.

LONGITUDE

LATITUDE

hPa

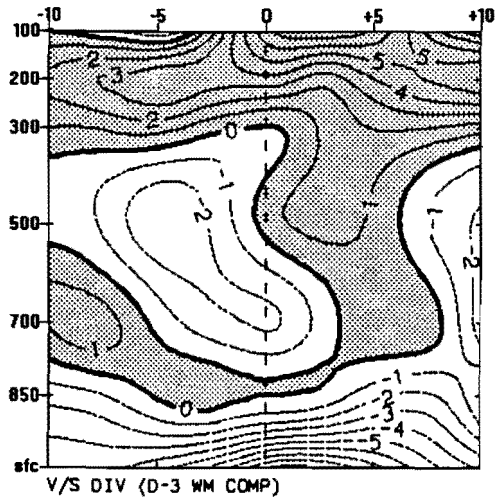

D-3

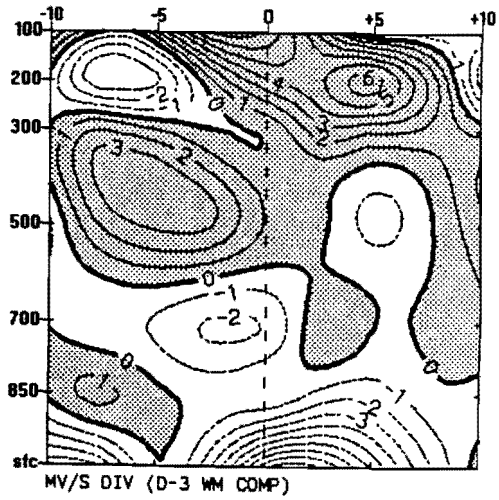

hPa

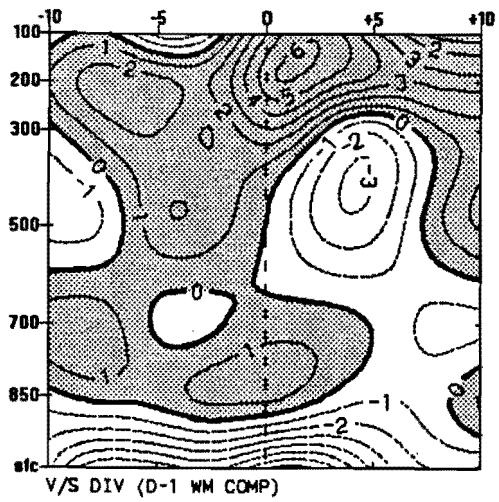

D-1

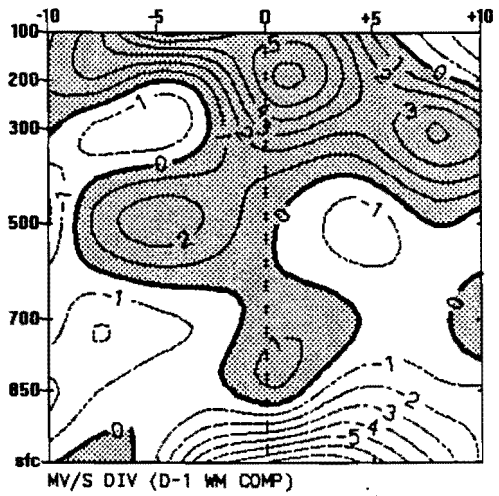

hPa

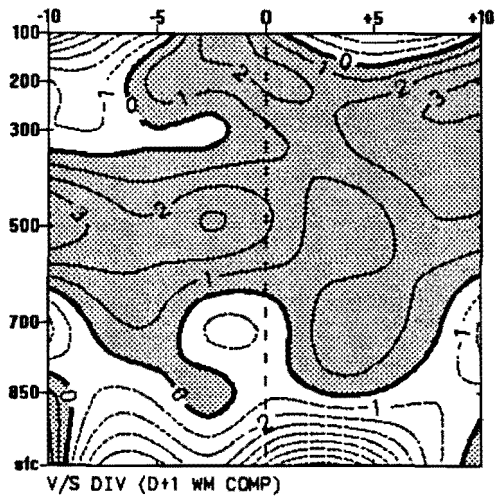

D+1

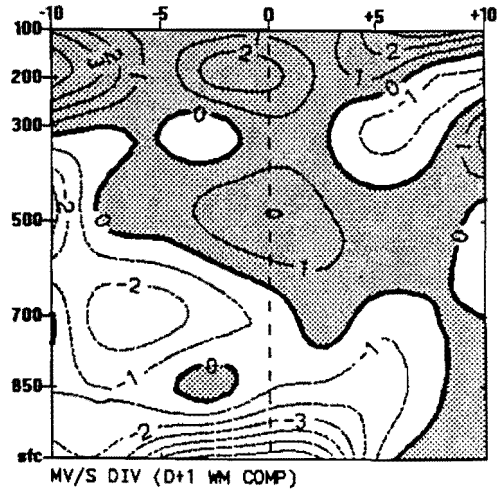

Figure 4-24a,b and c : WM zonal divergence. Contour interval is 1 x 10^{-5} s^{-1}.

Figure 4-25a,b and c : WM meridional divergence. Contour interval is 1 x 10^{-5} s^{-1}.

LONGITUDE

LATITUDE

hPa

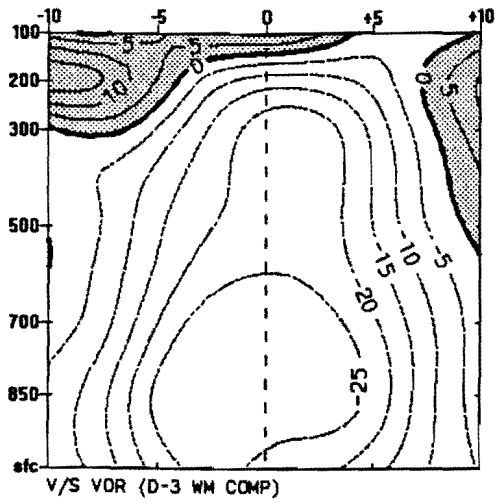

D-3

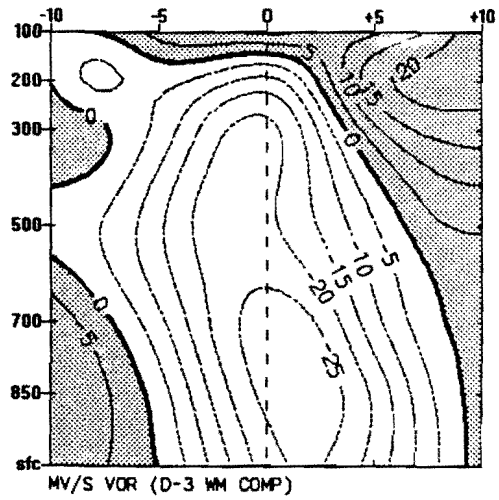

hPa

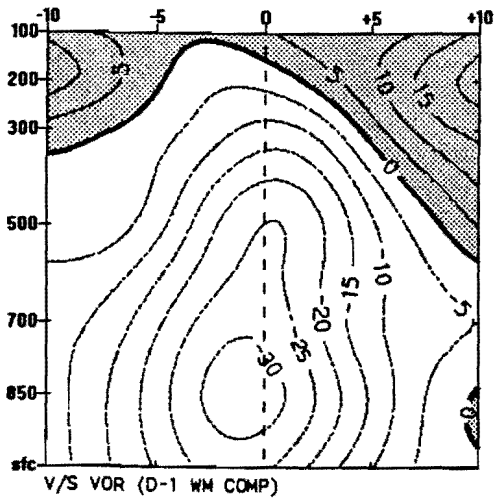

D-1

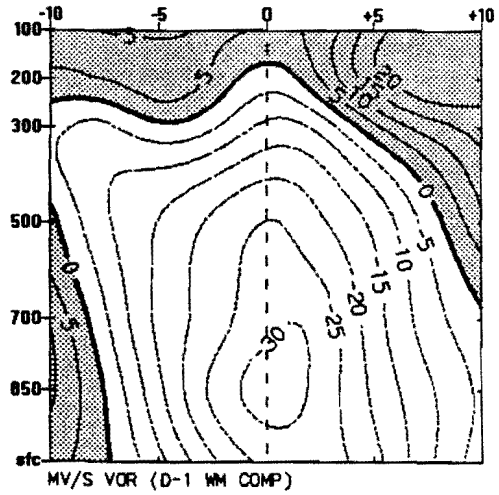

hPa

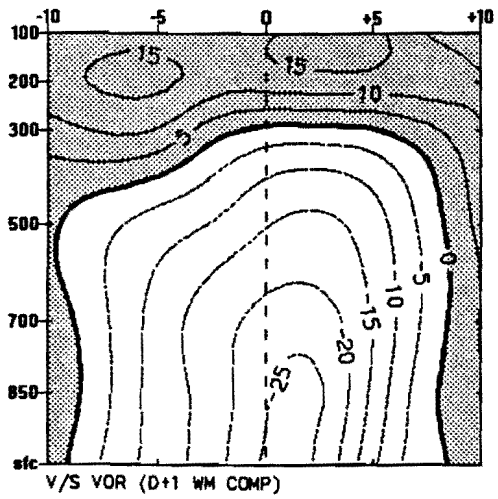

D+1

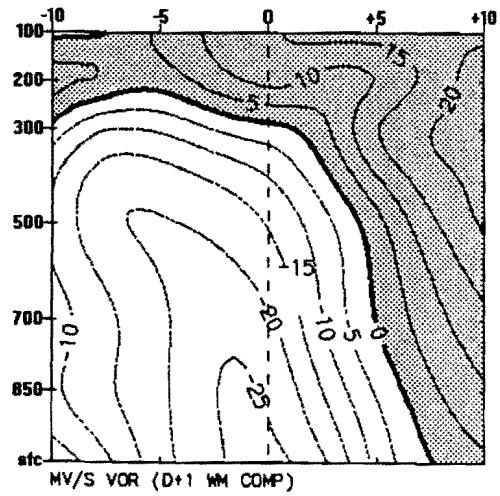

Figure 4-26a,b and c : WM zonal vorticity. Contour interval is 5 x 10^{-5} s^{-1}.

Figure 4-27a,b and c : WM meridional vorticity. Contour interval is 5 x 10^{-5} s^{-1}.

LONGITUDE

LATITUDE

hPa

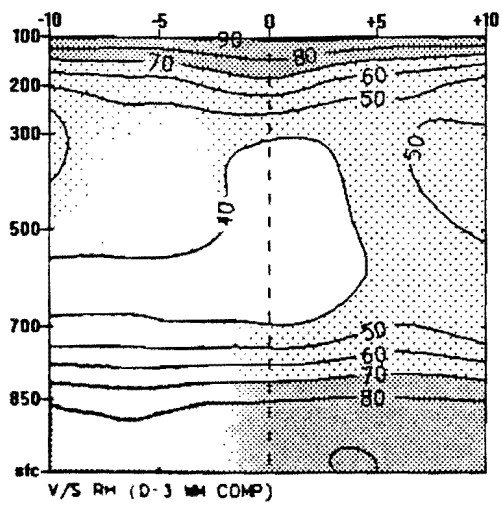

D-3

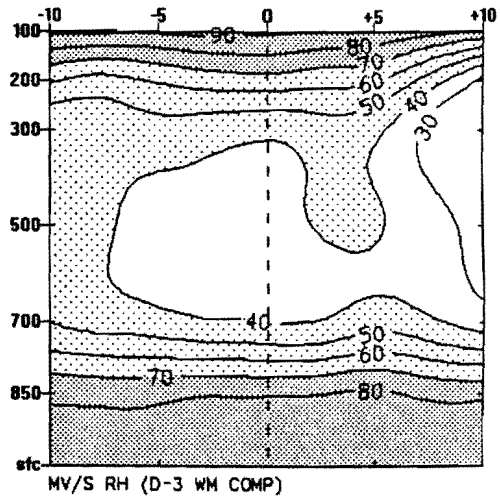

hPa

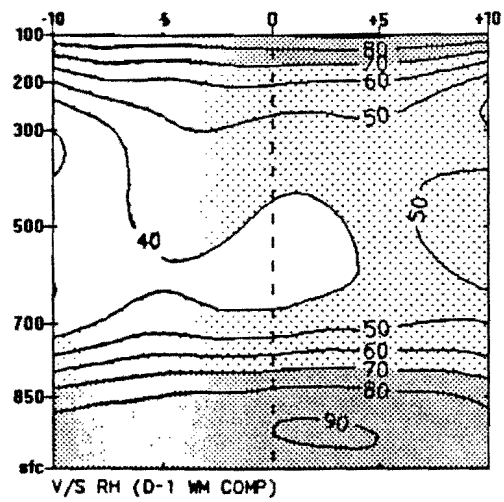

D-1

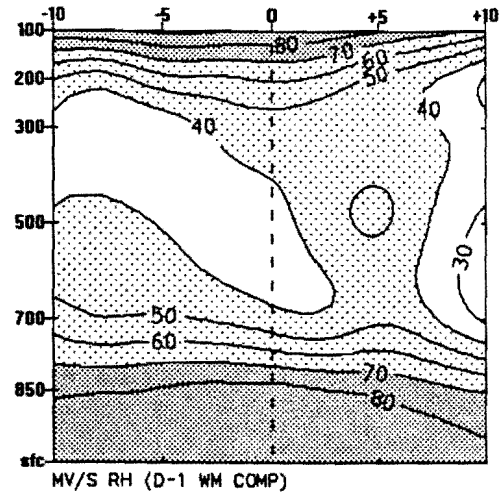

hPa

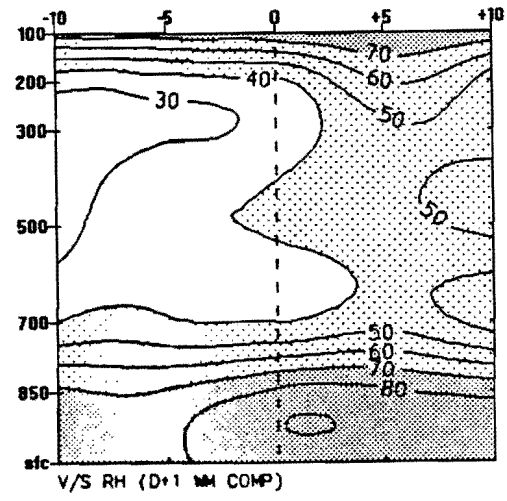

D+1

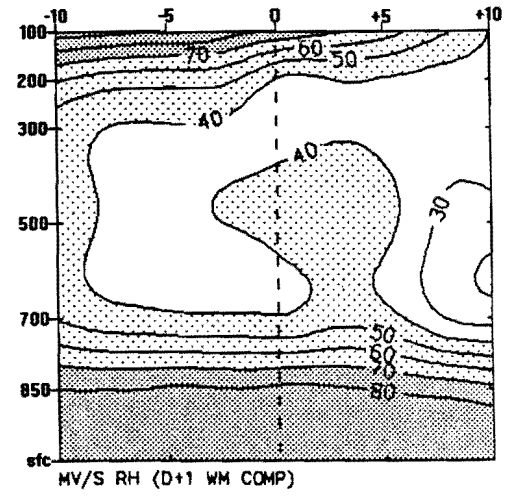

Figure 4-28a,b and c : WM zonal relative humidity. Contour interval is 10 %.

Figure 4-29a,b and c : WM meridional relative humidity. Contour interval is 10 %.

LONGITUDE

LATITUDE

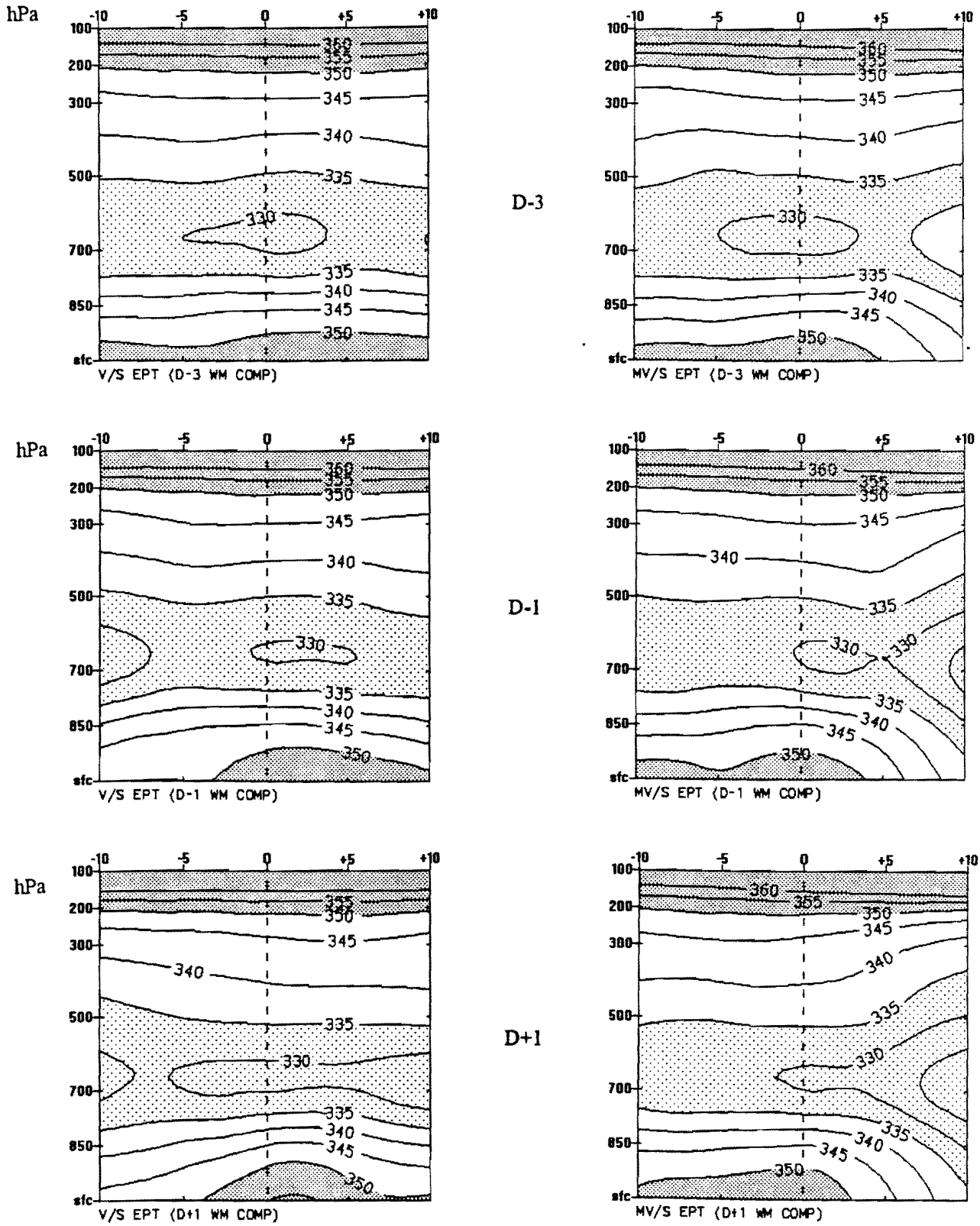

Figure 4-30a,b and c : WM zonal equivalent potential temperature.
Contour interval is 5 °K.

Figure 4-31a,b and c : WM meridional equivalent potential temperature.
Contour interval is 5 °K.

4.2 Recurving TC Analyses

4.2.1 Horizontal Kinematics, Moisture and Thermodynamics

4.2.1.1 Geopotential

850 hPa

At P_{850} the geopotential minima is observed to constantly decrease during the sequence to a sharp low by D+1 (**Figure 4-32a, b** and **c**). On D-3 the minimum geopotential of 1485 gpm is located at the C_{cen} with a steeper gradient to the south than to the north. The minimum has decreased to below 1465 gpm on D-1 with an accompanying increase in the gradient to the north of the cyclone centre. On D+1, still situated over the C_{cen}, the geopotential has decreased to 1450 gpm. The change of the geopotential field to the south is found to be almost twice that to the north. The sharp geopotential gradient in the southeast is likely a result of the direction of TC propagation.

200 hPa

At P_{200} a progressive northward movement of the anticyclonic maxima occurs with an accompanying increase in the geopotential gradient field from the south (**Figure 4-33a, b** and **c**). On D-3 the geopotential maximum (12455 gpm) is situated across the C_{cen} with the geopotential gradient to the north being noticeable less than that in the south. The position of the geopotential maximum (12445 gpm) has shifted to the northwest on D-1, but the area in which the closely packed contours are situated is still to the south of the C_{cen}. On D+1 a further northward encroachment of these contours is observed with contours which had previously congregated around the anticyclone centre (12445 gpm and 12440 gpm) having a zonal distribution.

4.2.1.2 Horizontal Wind

850 hPa

The wind vectors at P_{850} do not show the strong cyclonic rotation as was seen for the WM TC and which would be expected for a TC composite (**Figure 4-34a, b** and **c**). On D-3 a distinct pattern of high wind speeds ($\pm$ 10 m s^{-1}) is found in the southern sector with a contrasting northern sector of low wind speeds (< 5 m s^{-1}). A peculiar northeastward flow is observed in the eastern quadrant of the composite, inhibiting the enhancement of cyclonic flow around the C_{cen}. On D-1 the zonal pattern of the wind is still prevalent, but an increase of the wind speeds to > 5 m s^{-1} in the northern half of the composite is observed. A strong cyclonic rotation is only evident on D+1 when the winds in the southeastern quadrant exhibit a marked northeasterly component with winds in excess of 10 m s^{-1}.

500 hPa

At P_{500} the absence of any major cyclonic structure in the sequence is immediately evident and is expected due to the weak cyclonic structure at P_{850}. On D-3 a relatively weak cyclonic rotation is observed (**Figure 4-35a**) with only the southeast quadrant showing wind speeds in excess of 5 m s^{-1}. A strong westerly wind of magnitude $\pm$ 10 m s^{-1} is observed in the northern sector of the composite on D-1, while a weak easterly wind of magnitude < 5 m s^{-1} dominates the wind field in the southwestern quadrant (**Figure 4-35b**). A weak westerly wind of < 5 m s^{-1} is maintained in the extreme southeast. On D+1 (**Figure 4-35c**) the strongest cyclonic structure is observed with westerly wind speeds of $\pm$ 10 m s^{-1} occurring north of the C_{cen}, and also in the extreme south and southeastern quadrants.

200 hPa

At P_{200} a consistent pattern of westerly winds in the southern sector is observed through the sequence (**Figure 4-36a, b** and **c**), with an initial tropical easterly flow in the northern sector changing into a strong westerly of magnitude > 12 m s^{-1}. On D-3 the easterly and westerly flows are situated north and south of C_{cen} respectively. On D-1 the pattern has shifted slightly to the north, with an accompanying decrease in the strength of the easterly flow and an increase in the strength of the westerly flow to > 20 m s^{-1} in the southeast. The structure has change markedly on D+1 with westerly winds present throughout, and with the southeast quadrant containing the highest winds of magnitude > 20 m s^{-1}.

The structure and intensity of the horizontal wind field at P_{850} and P_{500} is weaker than what had previously been encountered (Anthes, 1982; Padya, 1989; Bannister and Smith, 1993; Jury, 1993; Tuleya, 1994) while the increase in intensity of the westerly wind at P_{200} is large. From the wind structure at P_{500} where westerly winds are dominant after D-1, the concept that TC's in the SW Indian Ocean are steered by winds at P_{500}, according to Padya (1989) and Jury (1993) is reinforced when one considers that this composite represents the southeastward recurving TC.

4.2.1.3 Kinetic Energy

850 hPa

At P_{850} changes in the kinetic energy field from D-3 to D-1 are minimal, while that occurring from D-1 to D+1 is very marked. The changes in the latter stages are not so much in the positions of maxima and minima but rather in the kinetic energy

intensity (**Figure 4-37a, b** and **c**). On D-3 a maximum of > 50 J kg^{-1} is found in the southeast quadrant, with a zonal band of values < 20 J kg^{-1} situated between +2.5° and +5° latitude. On D-1 an intrusion of kinetic energy values < 40 J kg^{-1} from the northwest has reached the C_{cen} resulting in an arc of higher values surrounding it from the north to the west. The explosive growth in the southeast quadrant of the maximum kinetic energy from 50 J kg^{-1} to 100 J kg^{-1} on D+1 has resulted in the region of minimum values present at the C_{cen}, on D-1, to be displaced.

200 hPa

In **Figure 4-38a, b** and **c** a clearly demarcated region between the areas containing steep gradients and that containing slacker gradients is observed along the 0° latitude line. The centre of minimum kinetic energy (< 20 J kg^{-1}) is situated in a zonal band across the C_{cen} on D-3, north of it on D-1 and northeast of it on D+1. An increase in the gradient to the south of the C_{cen} occurs during the sequence, but is found to be rather less than what was observed in the WM TC case.

The sequence of kinetic energy diagrams reveals that the horizontal wind vortex only reaches its maximum on D+1 at both P_{850} and P_{200}. At P_{850} a rotation or coalescing of the region of high kinetic energy in the north is observed to shift towards the south. Although the day of maximum surface wind was recorded on D-0, from these kinetic energy fields it is evident that the horizontal winds at P_{850} and P_{200} continued to increase on D+1 (see **Figures 4-34** and **4-36**).

4.2.1.4 Vertical Movement

500 hPa

In **Figures 4-39a, b** and **c**, a coalescing of two areas of vertical uplift of < -0.8 Pa s^{-1} is observed. On D-3 the two regions of maximum uplift are situated approximately 5° longitude either side of the C_{cen}, while an area of downward motion of +0.4 Pa s^{-1} dominates the northwest quadrant. The size and strength of the two uplift areas increases to < -1.4 Pa s^{-1} on D-1, resulting in the area of downward motion being displaced to the north. The coalescing of the two maximum uplift regions is completed on D+1 with an increase in the intensity to < -3 Pa s^{-1} on the 'front' side of the TC. The re-establishment of an area of strong downward motion of +0.6 Pa s^{-1} in the northwest quadrant is observed.

Strong uplift areas normally observed on the perimeter of the eye region dominate throughout the composite sequence. The presence of weak downward movement close to the C_{cen} on D-3 and D-1 is the main area of overturning and suppressed convection.

4.2.1.5 Divergence

200 hPa

The REC TC divergence composite field shows a steady increase in the area of maximum from +10 x 10^{-5} s^{-1} on D-3 to > +16 x 10^{-5} s^{-1} on D+1 (**Figure 4-40a, b** and **c**). On D-3 the comparatively uniform presence of divergence values > +2 x 10^{-5} s^{-1} in the northern sector is only interrupted by a small region of convergence near the C_{cen}, possibly the eye when considering the vertical movement results (see **Figures 4-39a, b**

and **c**). It is notable that two regions of high upper divergence occur either side of this convergence point. On D-1 the small area in which convergence was observed on D-3 is displaced by the coalescing of the two areas of divergence. A centre of convergence of $< -4 \times 10^{-5}$ s^{-1} has however developed south of the C_{cen}. On D+1 the region of divergence $> +8 \times 10^{-5}$ s^{-1} covers a large area south and east of the C_{cen}, once again displacing a region of convergence in the southwest.

4.2.1.6 Vorticity

850 hPa

The area of cyclonic vorticity at P_{850} is observed to increase in intensity during the composite sequence, although the area over which it occurs as well as the position of the maximum remains constant (**Figure 4-41a, b** and **c**). On D-3 a maximum cyclonic vorticity of -20×10^{-5} s^{-1} occurs across the C_{cen}, increasing to -25×10^{-5} s^{-1} on D-1 with a slight expansion in radius. On D+1 the cyclonic vorticity maximum has increased to $< -30 \times 10^{-5}$ s^{-1} and is no longer a zonally oriented structure along the 0° latitude. It is notable that throughout the composite sequence the areas of anticyclonic vorticity have maintained a slack gradient in contrast to what is observed for the area of cyclonic vorticity .

500 hPa

At P_{500} an increase in cyclonic vorticity and change from strongly zonal to circular structure is observed (**Figures 4-42a, b** and **c**). On D-3 a weak zone of cyclonic vorticity is observed across C_{cen}. Cyclonic vorticity increases to $< -20 \times 10^{-5}$ s^{-1} on D-1

along a zonal band across C_{cen}. On D+1 cyclonic vorticity < -35 x 10^{-5} s^{-1} is found at C_{cen} with a weak meridional band in the west.

200 hPa

At P_{200} we observe the emergence of an area of cyclonic vorticity at the C_{cen}, surrounded by predominantly anticyclonic vorticity (**Figure 4-43a, b** and **c**). Two areas of high anticyclonic vorticity of +20 x 10^{-5} s^{-1} are observed on D-3, one situated to the northwest of the C_{cen} and the other in the southeast quadrant. At this time there is no anticyclonic region near the C_{cen}, although low values of anticyclonic vorticity occur in the northeast quadrant. On D-1 the high anticyclonic vorticity to the northwest has coalesced with those to the south of the C_{cen} increasing the area of anticyclonic vorticity > +20 x 10^{-5} s^{-1}, while an area of cyclonic vorticity is found across the C_{cen}. On D+1 the cyclonic vorticity centre has increased to < -5 x 10^{-5} s^{-1} and the area of anticyclonic vorticity to the southeast has retreated. A region of high anticyclonic values (+20 x 10^{-5} s^{-1}) has established itself to the northeast, while cyclonic vorticity to the south of the C_{cen} has attained values of -10 x 10^{-5} s^{-1}.

Cyclonic vorticity at P_{850} and P_{500} are observed to increase in intensity from D-3 to D+1. This is contrary to what was observed for the WM composite where a reduction and northward propagation relative to C_{cen} was observed. At P_{200} a change from anticyclonic vorticity to cyclonic vorticity is observed at C_{cen}, with the strongest anticyclonic values in the southeast.

4.2.1.7 Temperature

850 hPa

The temperature field at P_{850} shows a progressive decrease in size of the region containing temperatures > 18 °C (**Figure 4-44a, b** and **c**). On D-3 the 18 °C isotherm is situated approximately along the -6° latitude, with the lowest temperature of < 16.5°C occurring in the extreme southeast and the highest temperature of >19 °C occurring in the northwest. Another feature is the slack temperature gradient to the north of the 18 °C isotherm compared to that to the south. On D-1 the 18 °C isotherm is maintained at -5° longitude, resulting in a northward encroachment of the isotherms < 17 °C. An accompanying increase in the temperature gradient to the south of the C_{cen} results in the lowest isotherm of 15.5 °C being introduced. An intrusion of air, of temperature less than 18 °C, is observed on D+1 to the northwest of the C_{cen}, resulting in a region of high temperatures (> 18.5 °C) being cut off from the area of similar temperatures to the west. The zonal temperature gradient in the south has increased resulting in a minimum temperature of < 14 °C in the southeast.

200 hPa

At P_{200} a region of high temperatures (> -52.5 °C) is observed to grow along a zonal band from the west on D-3 to an elliptical region situated across the C_{cen} on D+1 (**Figure 4-45a, b** and **c**). On D-3 a tongue of high temperatures is observed to extend eastward, toward the C_{cen}, while temperatures on either side of this region drop to < -53 °C. On D-1 the band has transformed into a circular region situated across and east of the C_{cen}, with the temperature gradient on the poleward side of the maxima steeper and more zonal in structure than the gradient on the equatorward side. On

D+1 the temperature maximum has increased to > -52 °C across the C_{cen}, with the temperature gradient taking on a uniform pattern around this maxima.

4.2.1.8 Relative Humidity

850 hPa

Although the region of maximum relative humidity (> 80 %) oscillates with regard to size, the structure of the relative humidity field at P_{850} remains fairly consistent with regard to the position and location of the 75 % relative humidity contour (**Figure 4-46a, b** and **c**). On D-3 the highest values are located across the C_{cen} with relative humidity values decreasing at a constant rate towards the north and the south. The region of relative humidity values > 80 % decreases by more than 50 % on D-1 while the region > 75% has remained relatively constant. The lowest relative humidity values of < 65 % are located in the southeast. On D+1 the area of relative humidity values > 80 % increases, while the region of low values (< 65 %) observed on D-1 has been displaced. The low level moisture distribution is relatively symmetrical and stable with regard to the TC.

500 hPa

A remarkable feature of the relative humidity field at P_{500} is the strong oscillation of the maximum values from > 60 % on D-3 to 45 % on D-1 and then back to > 65 % on D+1 (**Figures 4-47a, b** and **c**). On D-3 a region of relative humidity values > 50 % extends in a band roughly from the northeast to south of the C_{cen}, with values either side of it decreasing to < 35 %. A sharp drop in relative humidity values is observed on D-1 across the region where values of > 45 % are observed. On D+1 a re-emergence

of relative humidity values > 60 % is observed to the east of the C_{cen}, while to the west very little increase occurs. The difference in the highest and lowest relative humidity values are of the order of 35 %. The small moist region remains relatively unchanged throughout the TC sequence.

4.2.1.9 Precipitable Water

Surface - 300 hPa

The precipitable water field is seen to exhibit a similar reduction (D-3 to D-1) and increase (D-1 to D+1) in maximum values as was observed for the relative humidity. On D-3 (**Figure 4-48a**) a region of high precipitable water (> 60 mm) is situated east of the C_{cen}. Although the precipitable water values decrease away from this region, the gradient in the south is steeper than the gradient in the north. A minimum of < 44 mm is located in the southeast. D-1 (**Figure 4-48b**) exhibits a decrease of 2 mm in the maximum precipitable water value from D-3 and a shift towards the northeast. The minimum precipitable water value has decreased to < 40 mm in the south while remaining constant in the north. **Figure 4-48c** shows an increase in the precipitable water maxima from > 58 mm on D-1 to > 62 mm on D+1. A noticeable increase is observed in the gradient of precipitable water in the southern sector of the composite, resulting in values decreasing to < 36 mm in this region.

4.2.1.10 Equivalent Potential Temperature

850 hPa

The equivalent potential temperature maximum (> 345 °K) at P_{850} is observed to remain relatively stable in position through the sequence, while the equivalent potential temperature minimum decreases by more than 10 °K (**Figure 4-49a, b** and **c**). On D-3 the equivalent potential temperature maximum is situated across the C_{cen} with a steeper contour gradient in the south than in the north, with a noticeably zonal structure to the contours < 341 °K. The slope of the contours are compressed even further in the south on D-1, while a slackening of the gradient is observed in the northeast where equivalent potential temperature values > 342 °K occur. On D+1 the gradient southeast of the C_{cen} is found to be even greater than on D-1, with the gradient to the northwest decreasing still further. Overall a fairly stable pattern is seen with the expected dry air to the south.

500 hPa

The equivalent potential temperature field at P_{500} shows a decrease from D-3 to D-1 and then an increase in the maximum equivalent potential temperature from D-1 to D+1 (**Figures 4-50a, b** and **c**), reflecting the oscillation of the equivalent potential temperature maximum observed at P_{850}. On D-3 a maximum of > 340 °K occurs at the C_{cen} with values decreasing to the northwest and the south at almost the same rate. A reduction in the equivalent potential temperature maximum occurs on D-1 (> 338 °K), with values south of the C_{cen} decreasing to < 332 °K and those in the northwest to < 336 °K. An increase in the contour gradient to the south accompanies the decrease in equivalent potential temperature. On D+1 re-establishment of a high

equivalent potential temperature centre (> 340 °K) is observed to the east of the C_{cen}. The growth of the high values to the north and west results in an even bigger difference in gradient between the contours south of the maximum centre compared to that in the north. The main unstable convective area seems to be in the east, as in the WM composite.

4.2.2 Vertical Section Analyses

4.2.2.1 Horizontal Kinetic Energy

Zonal Section

In **Figure 4-51a, b** and **c** a progressive increase in the horizontal kinetic energy east of the C_{cen} is observed throughout the sequence, while very little change occurs in the west. On D-3 the highest horizontal kinetic energy value (> 40 J kg^{-1}) is situated in the west below P_{700}, while the rest of the section contains values of < 30 J kg^{-1}. Between P_{200} and P_{700} values of < 10 J kg^{-1} are present at the C_{cen}. On D-1 a region of horizontal kinetic energy values < 20 J kg^{-1} is situated within 5° of the C_{cen} between the surface and P_{200}. The region of high kinetic energy in the west is still present, while in the east values have increased in the lower and upper troposphere. On D+1 it is observed that kinetic energy values have increased to > 90 J kg^{-1} east of the C_{cen} at P_{850} and above P_{300}.

Meridional Section

The meridional vertical section of horizontal kinetic energy shows intensification at the upper tropospheric level in the south (**Figure 4-52a, b** and **c**). Values of the upper level high kinetic energy region exceeds 100 J kg^{-1} on D-3. Below P_{300} the highest kinetic energy value attained is > 40 J kg^{-1} in the south, with values seldom > 20 J kg^{-1} across the rest of the section. On D-1 the kinetic energy at the upper tropospheric level increases to > 150 J kg^{-1}, while to the north in the P_{400} and surface layer, kinetic energy values > 40 J kg^{-1} are established. A region of kinetic energy values > 100 J kg^{-1} is observed below P_{850} in the south, with the upper tropospheric values increasing to > 200 J kg^{-1}. It is noticeable that values either side of

the C_{cen} exceed 60 J kg^{-1} while at the C_{cen} it is < 50 J kg^{-1} from the surface to the upper troposphere.

The zonal and meridional vertical sections show dramatic increases in the horizontal kinetic energy values in the middle and lower troposphere through the sequence. Values not exceeding 50 J kg^{-1} are found below P_{300} for both sections on D-3. Kinetic energy values are seen to increase slightly on D-1, but it is on D+1 that the most change is noticeable. This increase is especially evident in the east (zonal section) and south (meridional section), corresponding to the increase in the horizontal winds seen in **Figures 4-34, 4-35** and **4-36**.

4.2.2.2 Vertical Movement

Zonal Section

The zonal section of vertical movement shows a dramatic change in intensity for descent and uplift as well as the regions in which these vertical movements are established. D-3 represents a dominant upward movement structure with only a small region at P_{500}, across the C_{cen}, containing downward motion (**Figure 4-53a**). Two regions of high uplift are found, one at P_{850} of < -1 Pa s^{-1} and one between P_{200} and P_{300} of < -0.8 Pa s^{-1}, both to the east. **Figure 4-53b**, representing D-1, contains a deep layer (surface to P_{200}) of weak downward movement 5° east of the C_{cen} with regions of uplift on either side. The magnitude of the strongest uplift and the strongest downward motion region is > +0.4 Pa s^{-1}. The region of uplift across the C_{cen} on D-1 has intensified to < -0.6 Pa s^{-1} and deepened (P_{850} to P_{200}) to cover most of the eastern part

of the composite, while a region of strong downward movement (> +0.8 Pa s^{-1}) is observed west of the C_{cen} below P_{500} in the 'rear' of the TC (**Figure 4-53c**).

Meridional Section

The dominant feature of the vertical wind field is the growth observed in the uplift region south of the C_{cen} from -1 Pa s^{-1} on D-3 to -2.6 Pa s^{-1} on D+1 (**Figures 4-54a, b** and **c**). Not only is the growth rate very high but it reaches a maximum one day after maximum wind. On D-3 two areas of high uplift (< -0.6 Pa s^{-1}) are found on either side of the C_{cen}. At the C_{cen} a region of low uplift values (< -0.2 Pa s^{-1}) occur coinciding well with data often observed in the eye of TC's. The region of low uplift has disintegrated on D-1 forming an area from P_{850} to P_{400} where values of < -0.8 Pa s^{-1} are concentrated. From D-1 to D+1 the uplift region over the C_{cen} increases by -2 Pa s^{-1} resulting in a steep gradient in the vertical uplift to the -0.6 Pa s^{-1} contour.

4.2.2.3 Divergence

Zonal Section

A strengthening and consolidation of both the convergence (surface) and divergence (P_{200}) maxima are observed in the sequence of zonal divergence sections (**Figures 4-55a, b** and **c**). On D-3 a strong divergence centre is located west of the C_{cen} at P_{200} (> +10 x 10^{-5} s^{-1}), while east of the C_{cen} at the surface, convergence exceeds -6 x 10^{-5} s^{-1}. A region of high convergence is found at P_{500} adjacent to an area of strong divergence at P_{300}. On D-1 demarcation between the regions of divergence and convergence occurs at P_{500}, with divergence values > +14 x 10^{-5} s^{-1} west of the C_{cen} (P_{200}) and convergence values of < -8 x 10^{-5} s^{-1} at the surface. The intensification

of the divergent and convergent regions continues on D+1 where values of > +17 x 10^{-5} s^{-1} are found at P_{200} east of the C_{cen}, and convergent values of < -12 x 10^{-5} s^{-1} are found at the surface. A region of strong divergence is established west of the C_{cen} up to P_{500} above which a region of divergence occurs.

Meridional Section

The divergence field shows most changes in spatial structure at P_{200} and at the surface, with an increase in the divergence values (positive and negative) occurring with increasing time (**Figure 4-56a, b** and **c**). On D-3 two regions of divergence > +4 x 10^{-5} s^{-1} are found either side of the C_{cen} at P_{200}. A region of convergence (-4 x 10^{-5} s^{-1}) is located below P_{300} in the northern sector, while at the surface the convergence attains a strength of < -6 x 10^{-5} s^{-1}. On D-1 a single region of divergence has formed at P_{200} (+6 x 10^{-5} s^{-1}), as well as contracting in the vertical to reach P_{500}. The surface convergence, although still > 6 s^{-1} has decreased in meridional extent by approximately 2.5° in the north. A significant increase in surface convergence (-4 x 10^{-5} s^{-1}), and upper divergence (+8 x 10^{-5} s^{-1}), occurs from D-1 to D+1 resulting in a steep divergence gradient forming between the surface and the upper pressure levels across the C_{cen}.

4.2.2.4 Vorticity

Zonal Section

The zonal sequence of vorticity sections shows the establishment of a region of strong cyclonic vorticity with well defined borders, beyond which weak anticyclonic vorticity is dominant (**Figures 4-57a, b** and **c**). A horizontal demarcation between the

upper level anticyclonic vorticity and the middle and lower level cyclonic vorticity is observed at P_{300} on D-3. The strongest cyclonic vorticity of $< -25 \times 10^{-5}$ s^{-1} occurs at P_{850} over the C_{cen}, while the anticyclonic region above P_{200} has a uniform value of approximately $+10 \times 10^{-5}$ s^{-1}. On D-1 the strengthening of the cyclonic vorticity region has resulted in it deepening across the C_{cen} to P_{200}. The surface cyclonic maximum has intensified to $< -30 \times 10^{-5}$ s^{-1} magnitude and the upper level anticyclonic maximum east of the C_{cen} has increased to $> +15 \times 10^{-5}$ s^{-1} magnitude. A doubling of the highest cyclonic vorticity to -30×10^{-5} s^{-1} (D-1) to $< -60 \times 10^{-5}$ s^{-1} is observed on D+1. Since the horizontal extent of the cyclonic vorticity is approximately 7.5° east and west of the C_{cen} throughout the sequence this dramatic increase in strength results in a very steep gradient about the C_{cen}. The REC TC appears to 'spin-up' rapidly at D+1 similar to Mozambique Channel TC's.

Meridional Section

It is immediately apparent that very little tilting in the vertical occurs when viewing the structure of cyclonic vorticity around the C_{cen}. Penetration of the cyclonic vorticity above P_{200} and a two-fold increase in the gradient between the cyclonic and the anticyclonic vorticity regions occurs on from D-3 to D+1 (**Figure 4-58a, b** and **c**). The area of maximum cyclonic vorticity over the C_{cen} remains at P_{850} throughout the sequence while going from approximately -25×10^{-5} s^{-1} magnitude on D-3 to $< -55 \times 10^{-5}$ s^{-1} magnitude on D+1. The region of anticyclonic vorticity at P_{200} south of the C_{cen} maintains a value $> +10 \times 10^{-5}$ s^{-1} from D-3 to D+1.

4.2.2.5 Relative Humidity

Zonal Section

The zonal section of relative humidity on D-3 shows two distinct cells of low values (< 50 %) either side of the C_{cen} (**Figure 4-59a**). The 70 % relative humidity contour in the lower troposphere shows an increase in height at the C_{cen}, while in the upper troposphere a decrease in height is observed. East of -5° longitude, in the TC 'wake', relative humidity values > 80 % are seen to penetrate to P_{850}. On D-1 (**Figure 4-59b**) only the western cell of low relative humidity values < 50 % is observed, while to the east a well stratified structure is observed. As on D-3, the surface relative humidity to the east of the TC is higher although in the mid-troposphere lowest values are in the rear (west). On D+1 (**Figure 4-59c**) a dramatic change in the relative humidity structure in the east is observed, with a region of relative humidity values > 70 % extending from the surface to the upper troposphere along +5° longitude. An increase in the cell of relative humidity values < 50 % in the mid-troposphere west of the C_{cen} is accompanied by an increase in the surface relative humidity as well.

Meridional Section

Similar to the zonal relative humidity section, two regions of low relative humidity (< 50 %) occur on either side of the C_{cen} (**Figures 4-60a, b** and **c**), but unlike the zonal section, the meridional section exhibits growth of these regions. On D-3 the northern and the southern mid-tropospheric low relative humidity cells are separated by a region of relative humidity > 60 % extending from P_{700} to P_{300} south of the C_{cen}. The lower tropospheric high relative humidity of > 70 % extends from the surface to P_{850}, while the upper tropospheric high values are congregated in the northern sector

of the composite down to P_{300}. A growth in the regions of low relative humidity is observed on D-1, with a downward intrusion of relative humidity of > 60 % along the C_{cen}, and a slight reduction in the depth of the lower tropospheric relative humidity > 70 % observed. On D+1 the northern cell of low relative humidity < 50 % is diminished in extent, while the southern cell is observed to stretch from P_{700} to P_{100} with values as low as 30 % observed. Driest air is in the southern mid-troposphere, and may 'subdue' the REC TC as it moves over cooler water after D+1.

4.2.2.6 Equivalent Potential Temperature

Zonal Section

Very little structural change is observed for the equivalent potential temperature zonal sections where values decrease to P_{500} and increasing to P_{100} (**Figures 4-61a, b** and **c**). Above P_{700} the increase in the equivalent potential temperature values is maintained from D-3 to D+1 with only a slight fluctuation (increase in height) in the 340 °K contour across the C_{cen} on D-1. The regions of minimum equivalent potential temperature(< 335 °K) are situated on the eastern and western edges of the composite throughout the sequence with a slight retreat in area with time. On D-3 the surface maximum of > 350 °K extends east-west across the composite, while on D-1 it is displaced to the east, and on D+1 it increases to > 355 °K east of the C_{cen}.

Meridional Section

As was found for the WM TC composite very little change in equivalent potential temperature occurs on the equatorward side of the TC, while a definite

reduction in equivalent potential temperature occurs on the southern side of the TC (**Figure 4-62a, b** and **c**). The contour structure above P_{200} shows no change with time and increases towards the tropopause as is expected in the mean atmosphere. The minimum equivalent potential temperature values (> 330 °K) are located in the southern sector at approximately P_{200}. An upward trend at P_{850} of the 340 °K contour and a downward trend of the same contour at P_{400} shows the saturation and convective mixing occurring in the atmospheric equivalent potential temperature values when TC's traverse a region. This pattern is unlike the WM composite, where relatively low equivalent potential temperature remained over the C_{cen}.

Recurving TC Synthesis

A peculiarity of the REC TC is the very low wind speeds observed at the 850 and 500 hPa surfaces compared to the 200 hPa surface. When it is noted that at the 200 hPa surface the strong westerly winds are initially situated south of the C_{cen}, and that recurving of the TC towards the southeast occurs after D-1, penetration of these winds into the mid-troposphere likely play a role in the track change, even though steering is considered to occur near the 500 hPa surface (Padya, 1989; Jury, 1993). The REC TC is observed to exhibit a sharp increase in the regions of uplift at the 500 hPa surface as well as divergence at the 200 hPa surface. Evacuation of mass and energy in the upper troposphere by the strong westerlies south of the C_{cen} aids in the strengthening of the convective updrafts (Anthes, 1982; Padya, 1989; Asnani, 1993).

TC's are enhanced by mid-tropospheric moisture (Anthes, 1982; Asnani, 1993) and increased latent heat release with the formation of strong convective columns. The ability of the system to be sustained through recurvature could be enhanced by re-entrainment of moist air in the lee of the TC, increased low level cyclonic vorticity and convergence as encountered in this study. For the REC TC, equivalent potential temperatures are observed to be > 335 °K in the 700 to 500 hPa layer, similar to that recorded by Jury (1993).

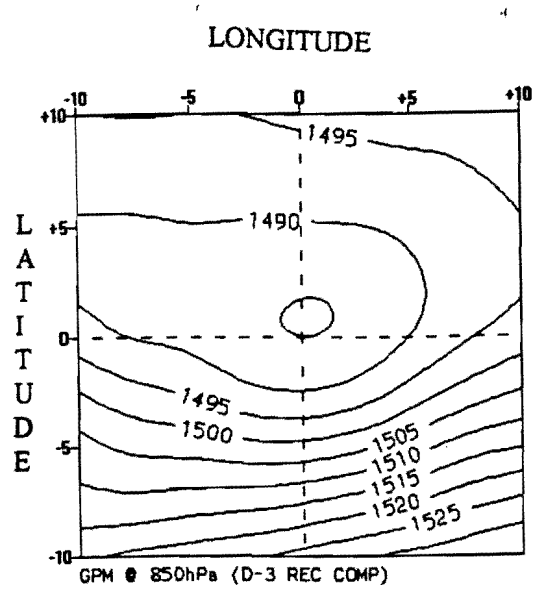

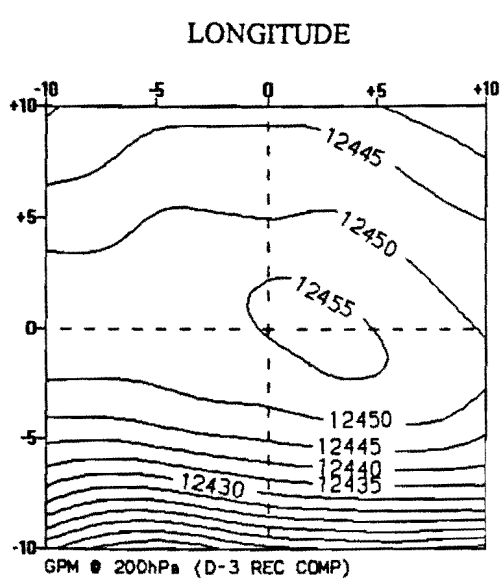

D-3

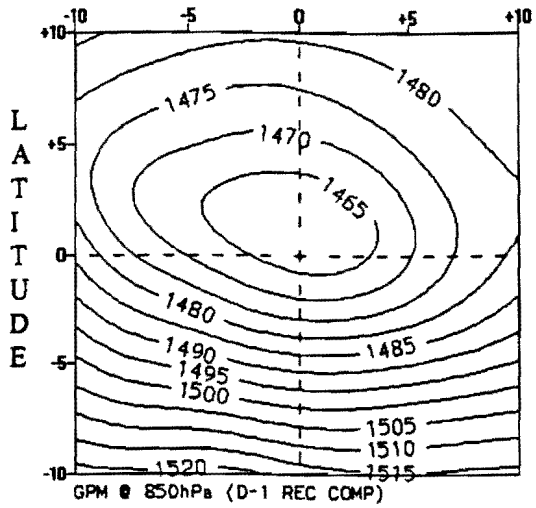

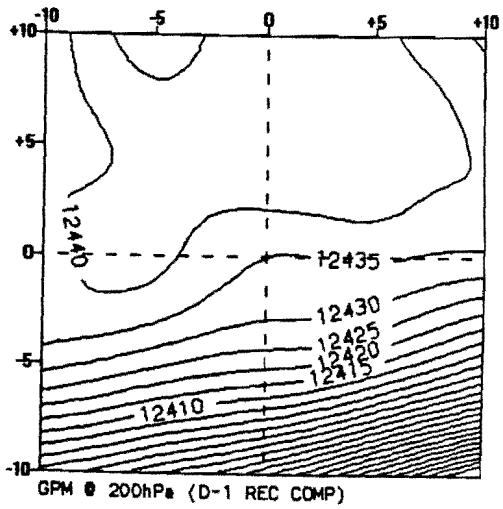

D-1

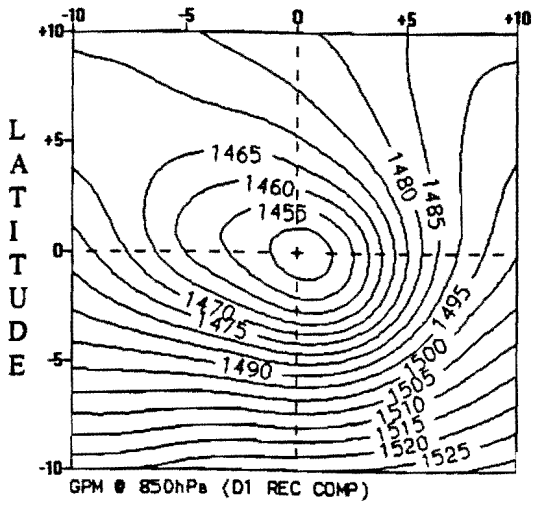

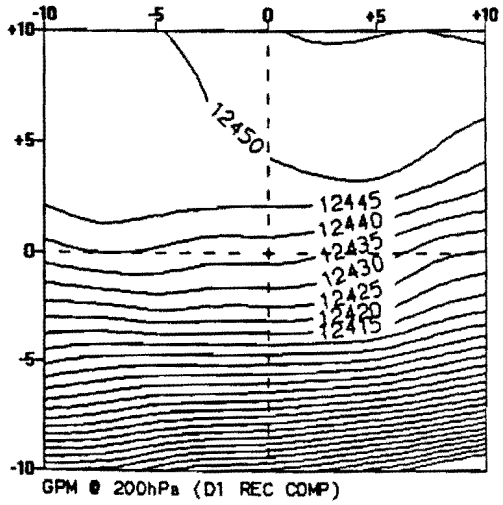

D+1

Figure 4-32a,b and c : REC geopotential @ 850 hPa. Contour interval is 5 gpm.

Figure 4-33a,b and c : REC geopotential @ 200 hPa. Contour interval is 5 gpm.

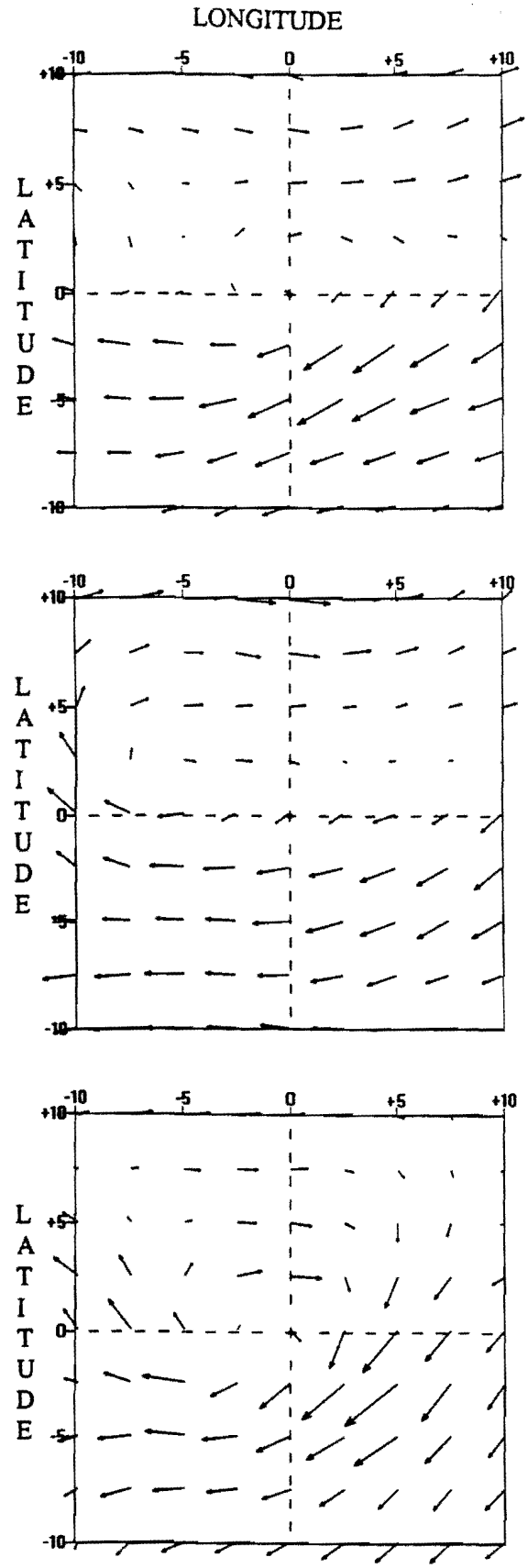

Figure 4-34a,b and c : REC horizontal wind @ 850 hPa.
Vector scale : ⟶ = 10 ms^{-1}.

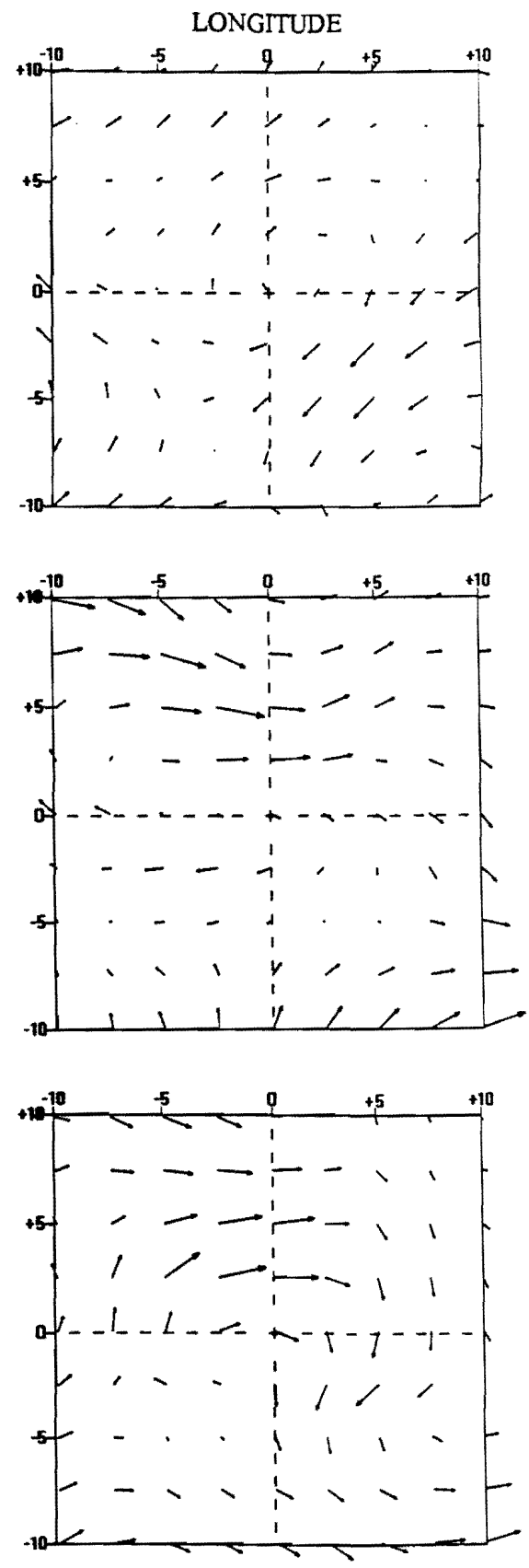

Figure 4-35a,b and c : REC horizontal wind @ 500 hPa.
Vector scale : ⟶ = 10 ms^{-1}.

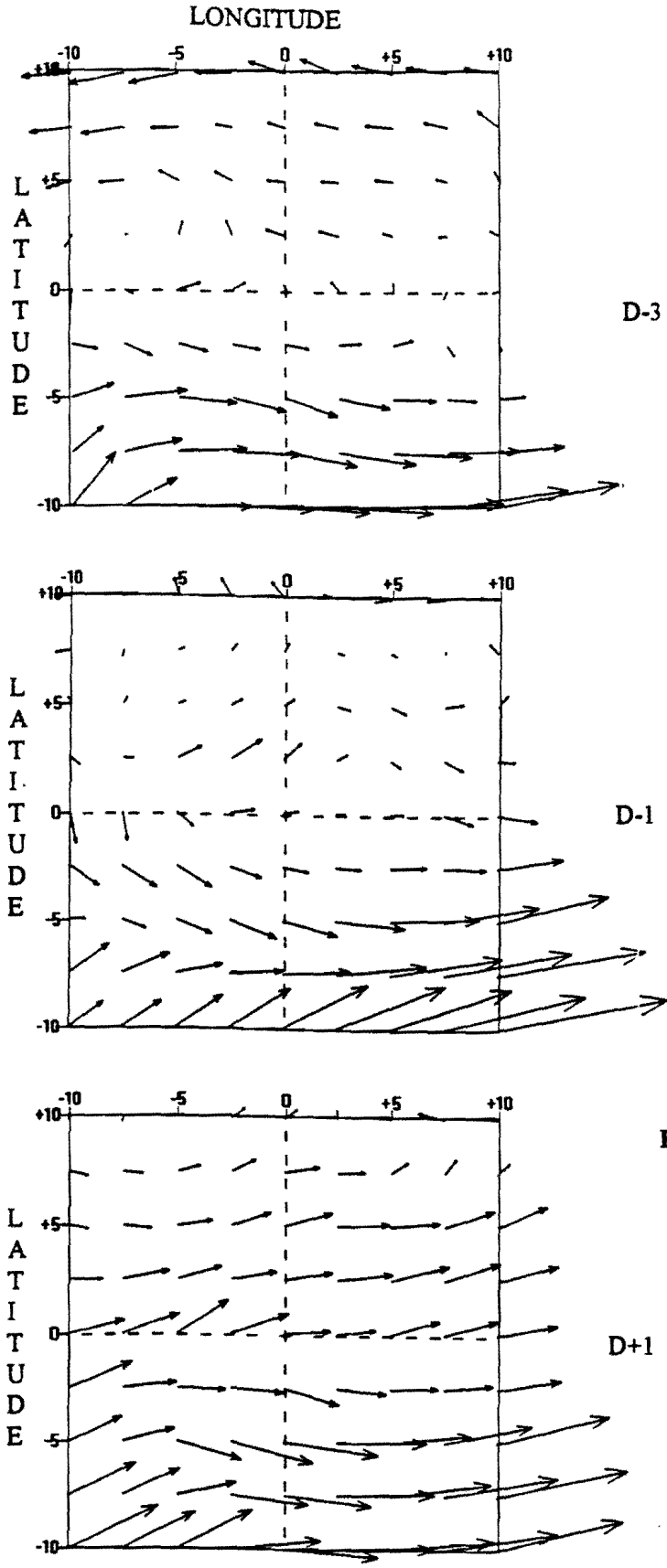

Figure 4-36a,b and c : REC horizontal wind @ 200 hPa.
Vector scale : ⟶ = 10 ms^{-1}.

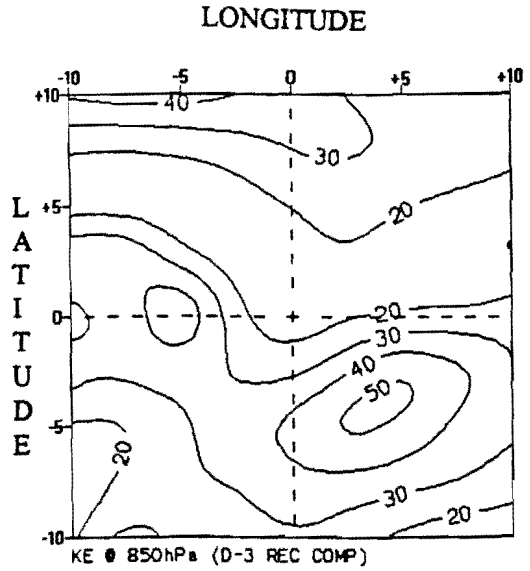

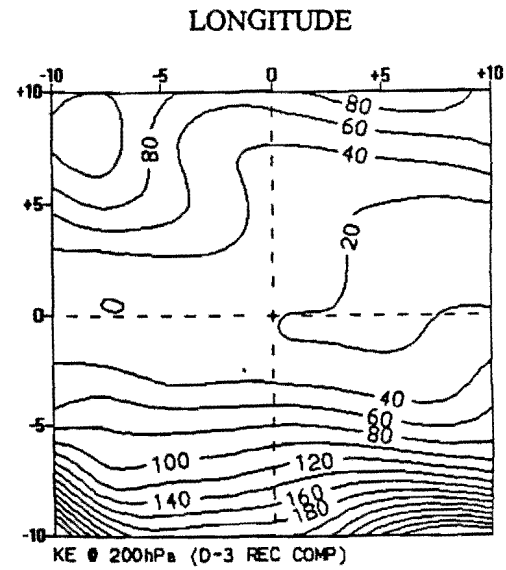

D-3

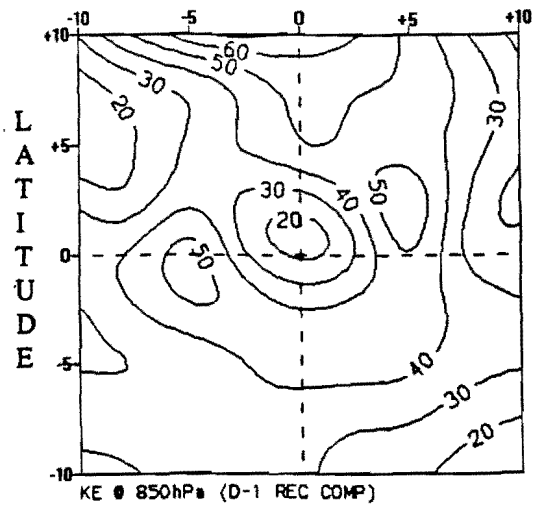

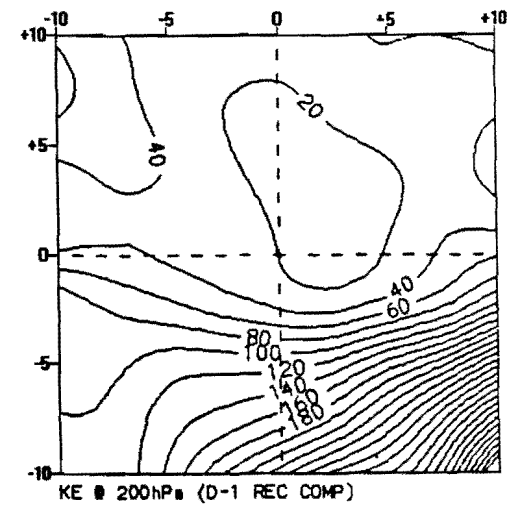

D-1

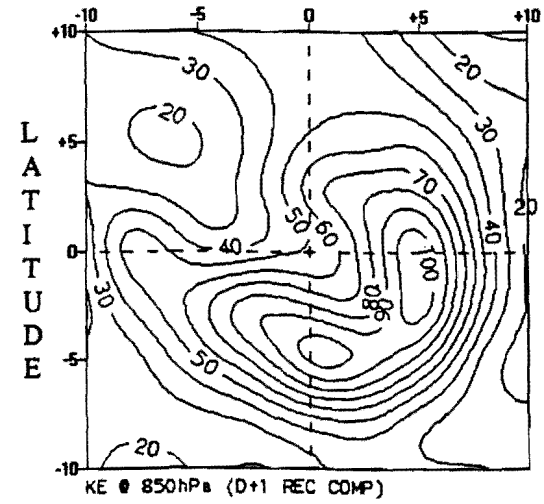

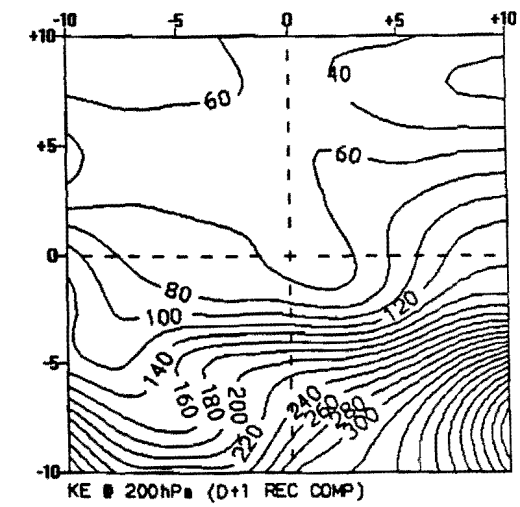

D+1

Figure 4-37a,b and c : REC kinetic energy @ 850 hPa. Contour interval is 10 J kg^{-1}.

Figure 4-38a,b and c : REC kinetic energy @ 200 hPa. Contour interval is 20 J kg^{-1}.

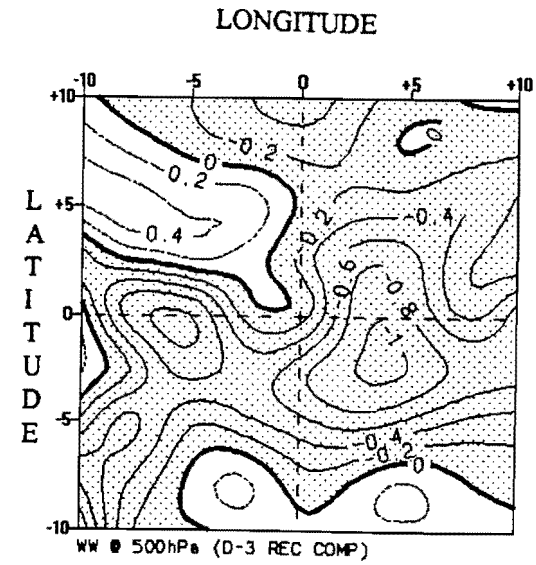

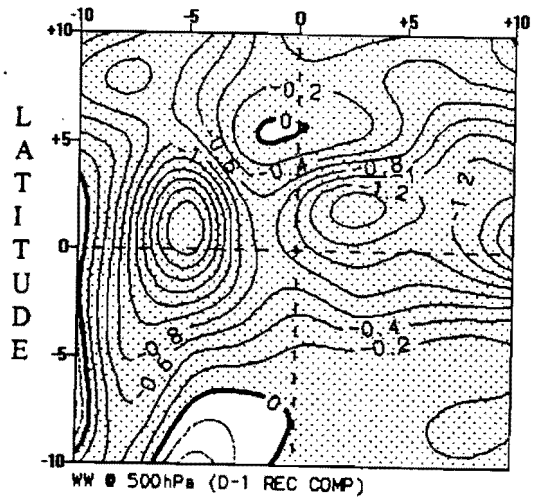

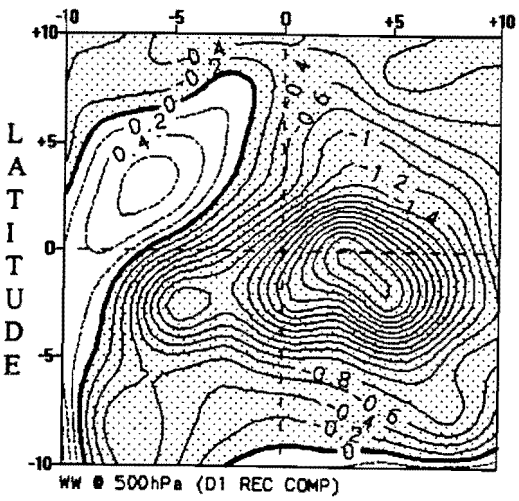

Figure 4-39a,b and c : REC vertical motion @ 500 hPa. Contour interval is 0.2 Pa s^{-1}.

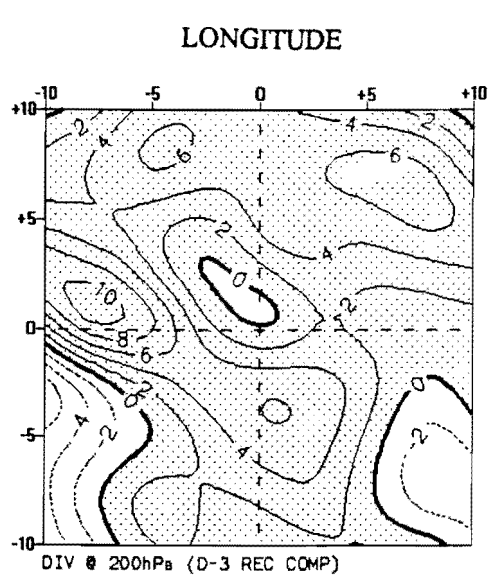

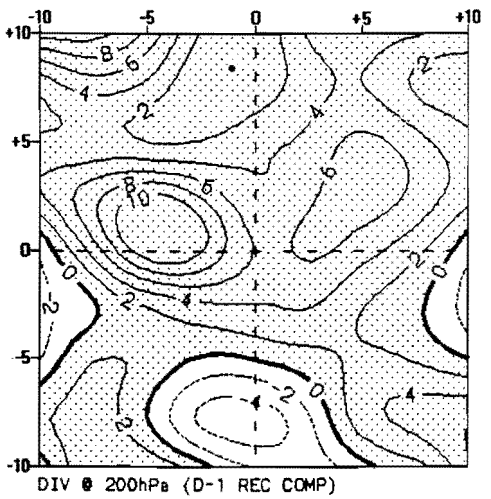

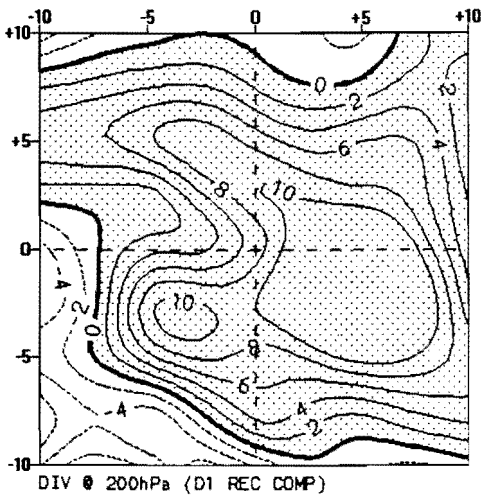

Figure 4-40a,b and c : REC divergence @ 200 hPa. Contour interval is 2 x 10^{-5} s^{-1}.

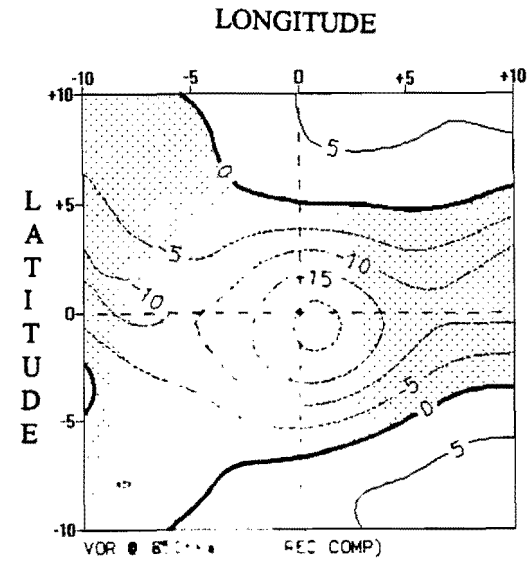

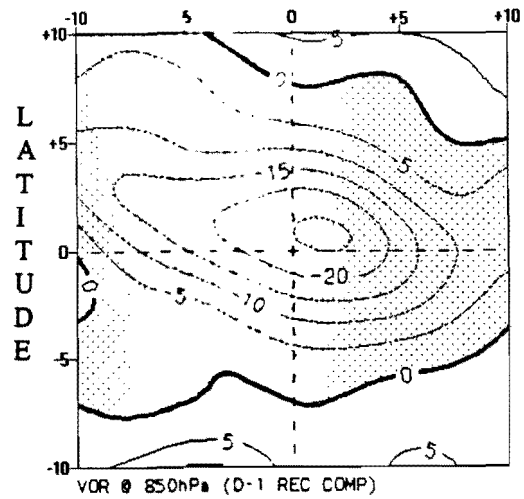

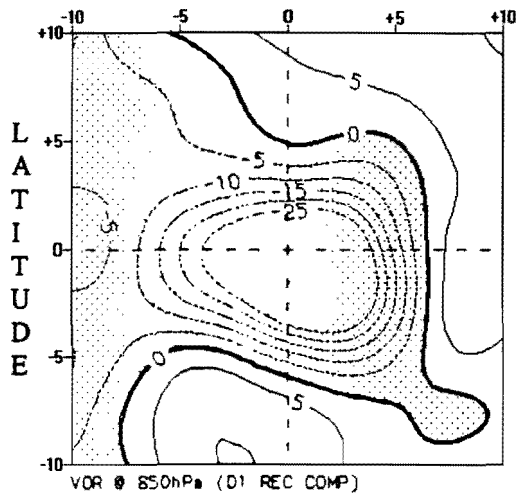

Figure 4-41a,b and c : REC vorticity @ 850 hPa.
Contour interval is 5 x 10^{-5} s^{-1}.

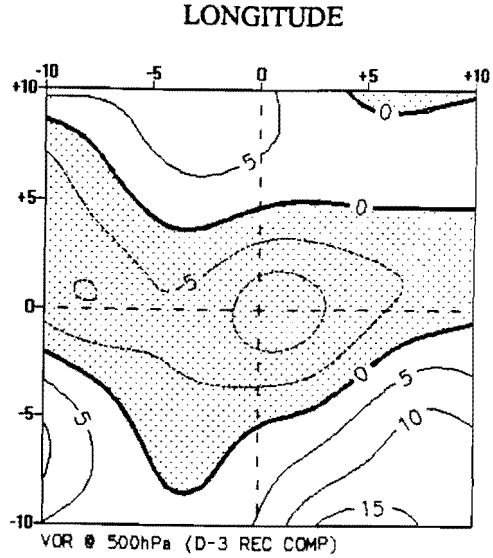

D-3

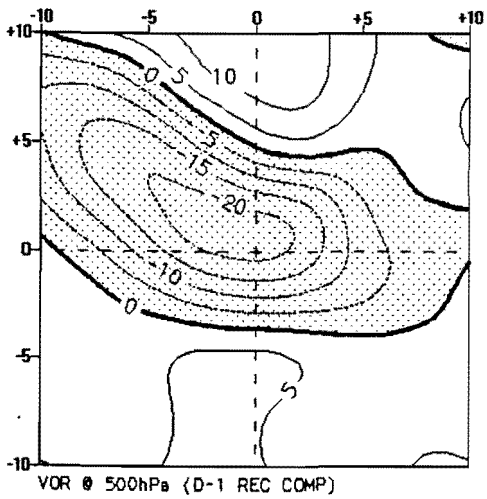

D-1

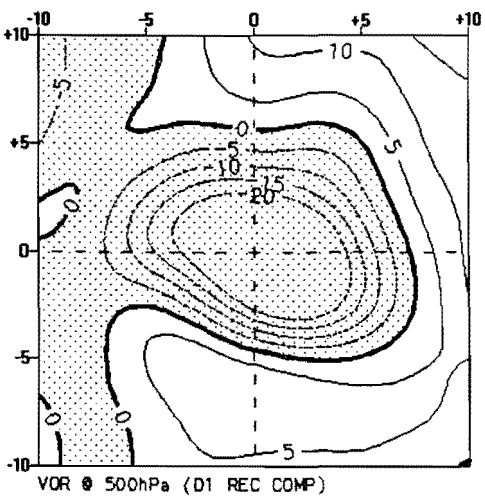

D+1

Figure 4-42a,b and c : REC vorticity @ 500 hPa.
Contour interval is 5 x 10^{-5} s^{-1}.

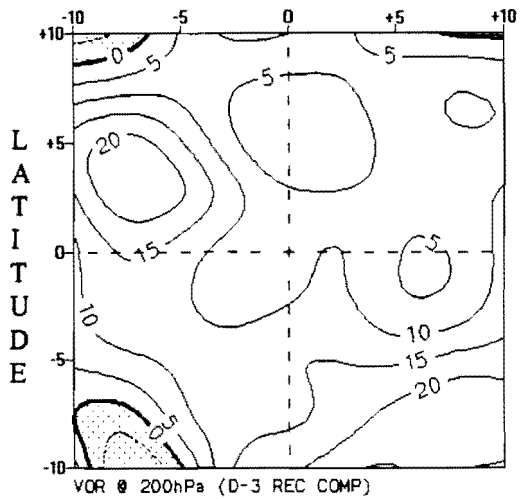

D-3

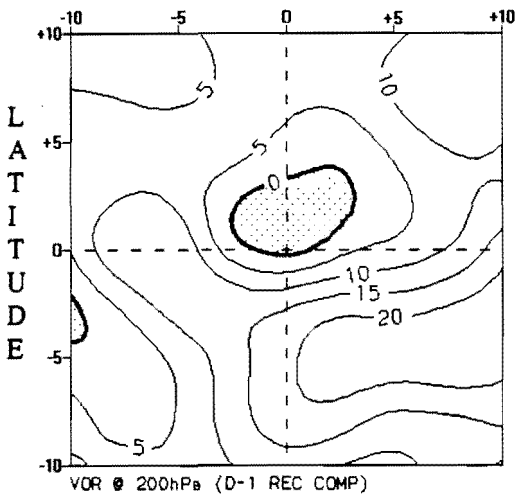

D-1

Figure 4-43a,b and c : REC vorticity @ 200 hPa. Contour interval is 5 x 10^{-5} s^{-1}.

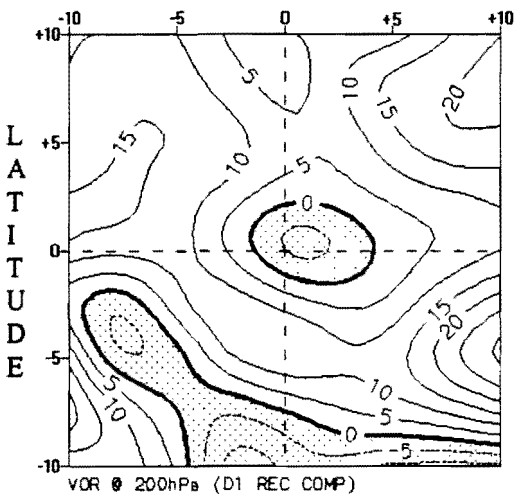

D+1

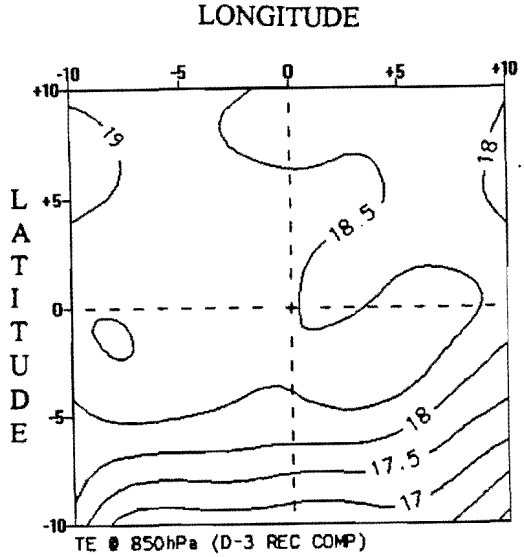

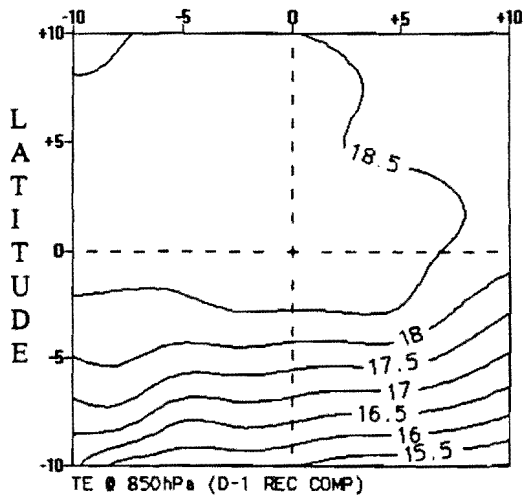

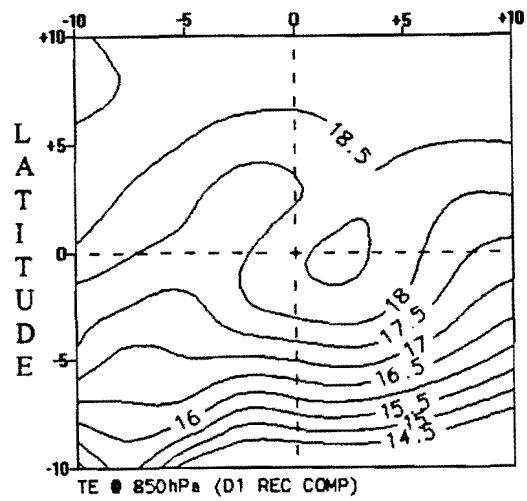

Figure 4-44a,b and c : REC temperature @ 850 hPa. Contour interval is 0.5 °C.

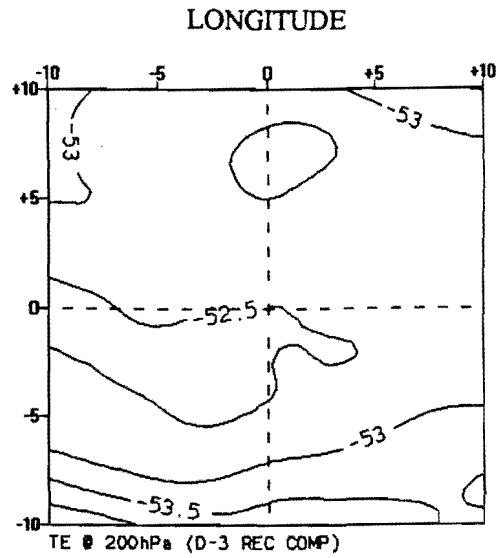

D-3

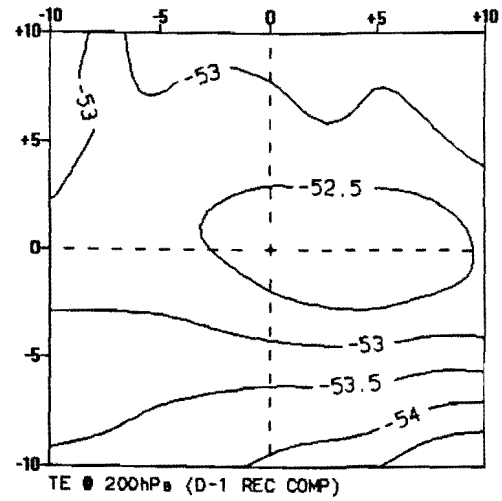

D-1

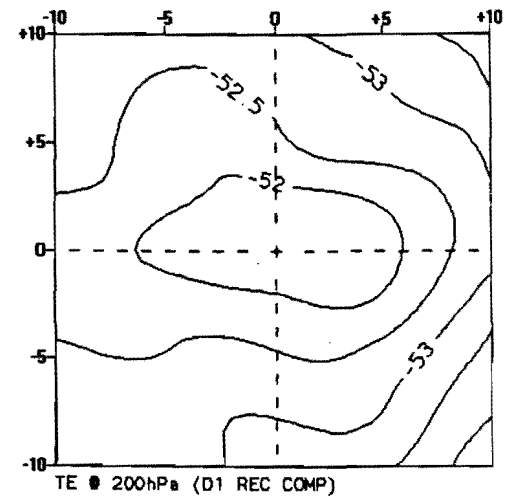

D+1

Figure 4-45a,b and c : REC temperature @ 200 hPa. Contour interval is 0.5 °C.

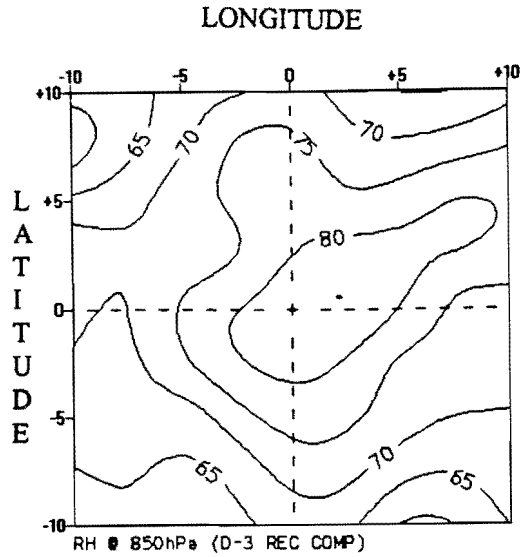

D-3

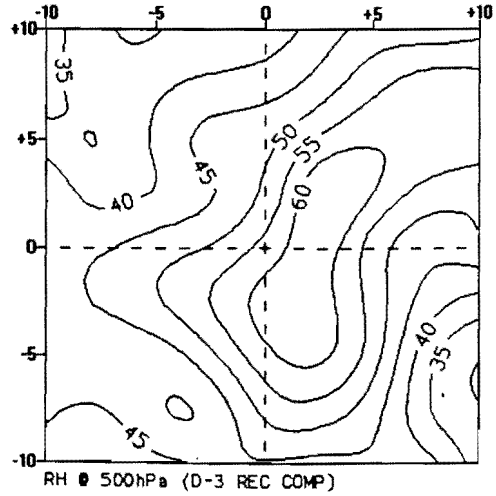

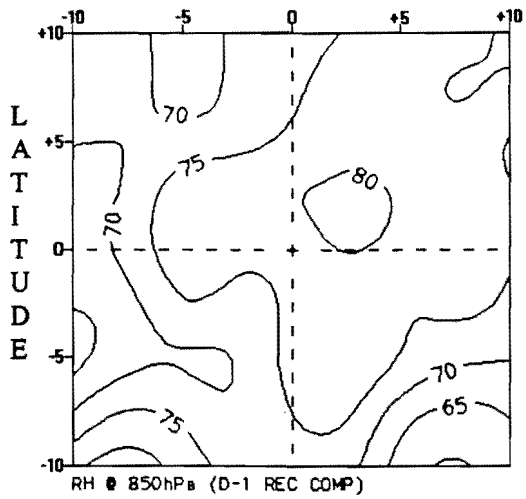

D-1

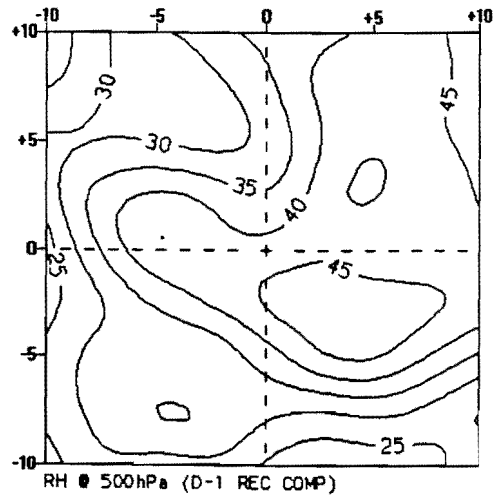

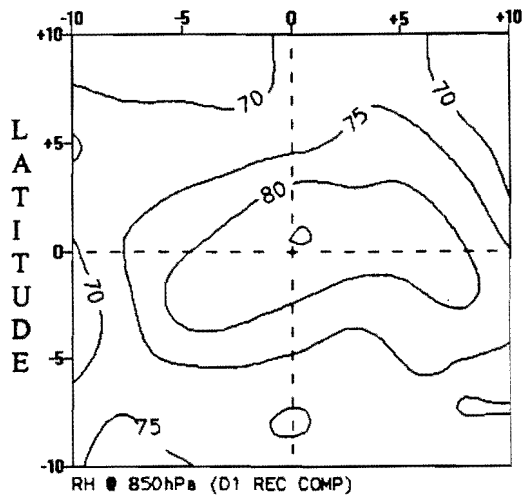

D+1

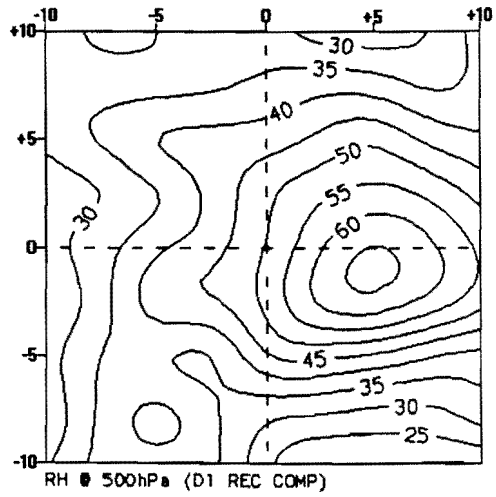

Figure 4-46a,b and **c** : REC relative humidity @ 850 hPa. Contour interval is 5 %.

Figure 4-47a,b and **c** : REC relative humidity @ 500 hPa. Contour interval is 5 %.

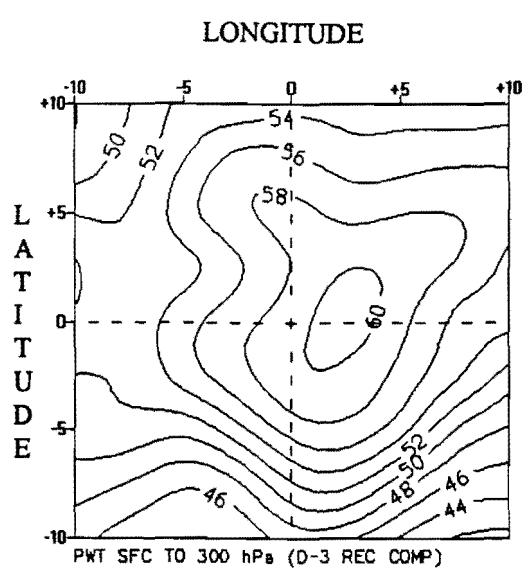

D-3

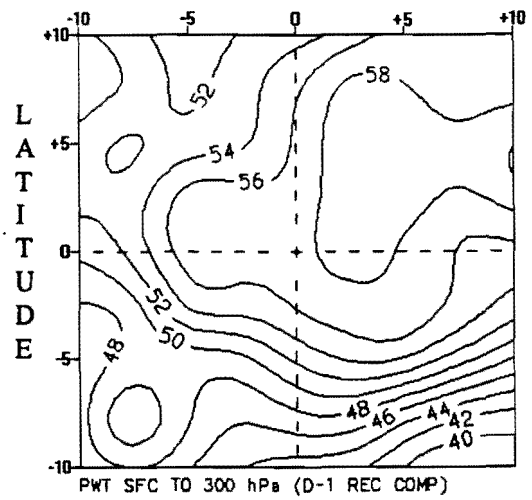

D-1

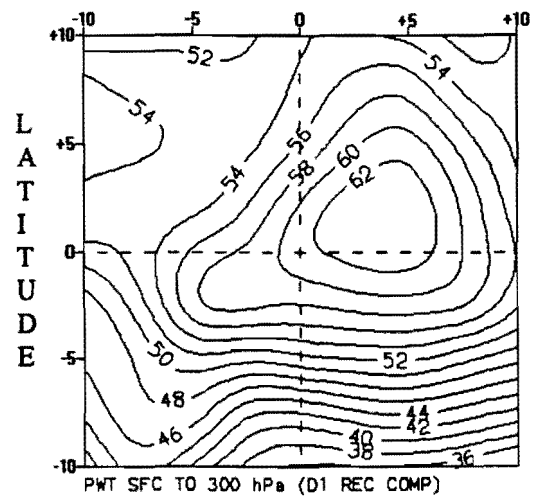

D+1

Figure 4-48a,b and c : REC precipitable water between the surface and 300 hPa.
Contour interval is 2 mm.

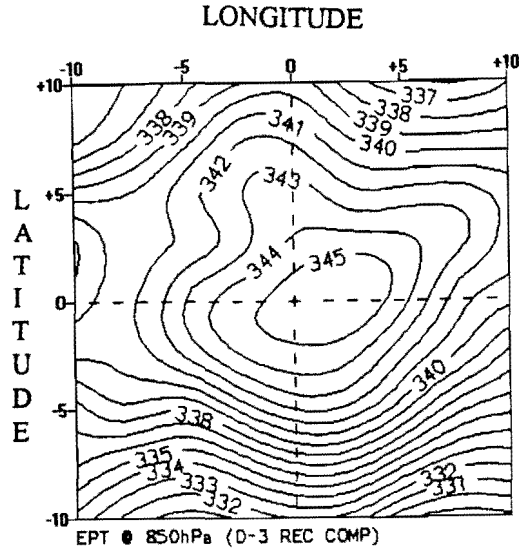

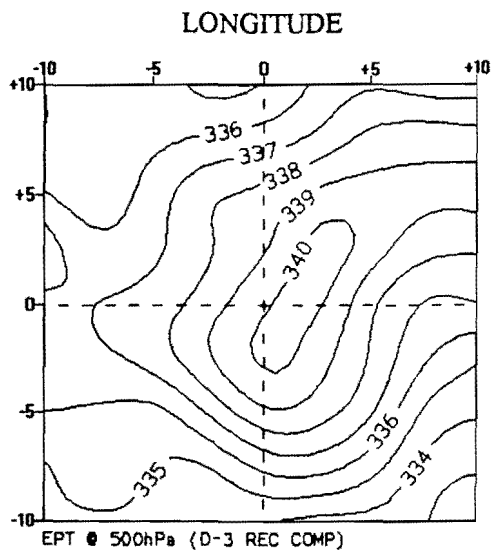

D-3

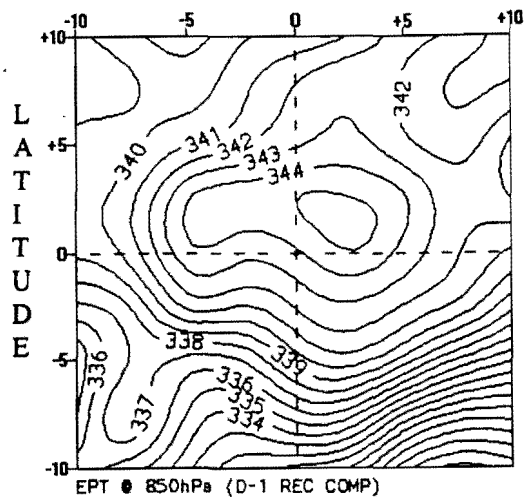

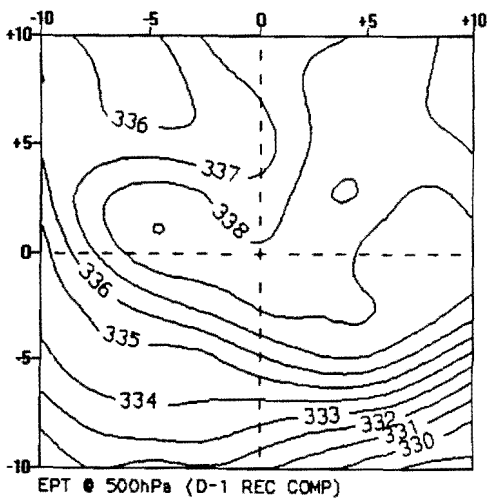

D-1

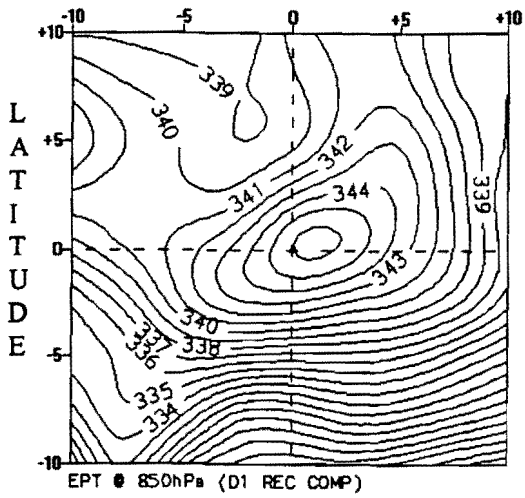

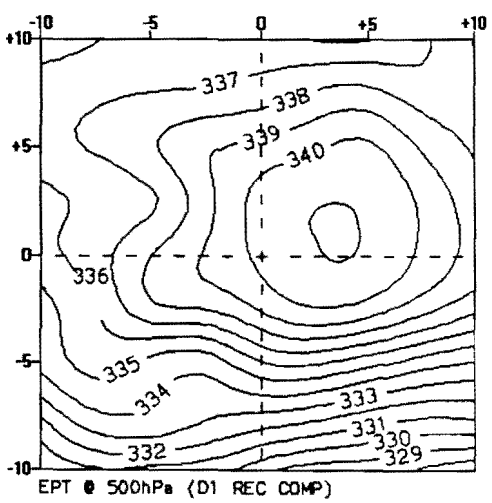

D+1

Figure 4-49a,b and c : REC equivalent potential temperature @ 850 hPa.
Contour interval is 1 °K.

Figure 4-50a,b and c : REC equivalent potential temperature @ 200 hPa.
Contour interval is 1 °K.

LONGITUDE

LATITUDE

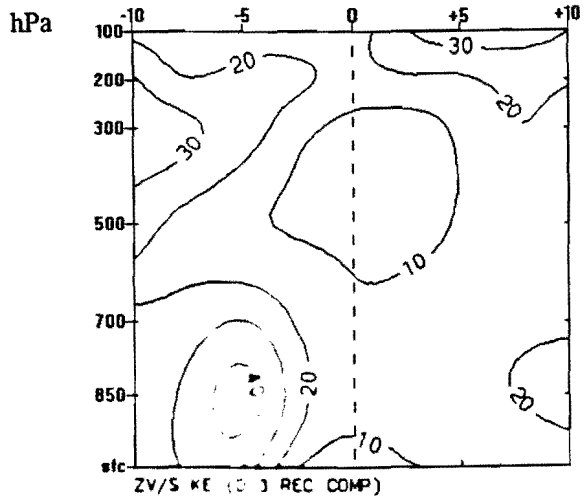

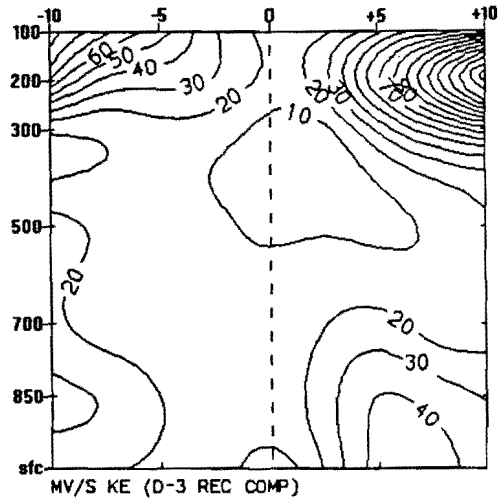

D-3

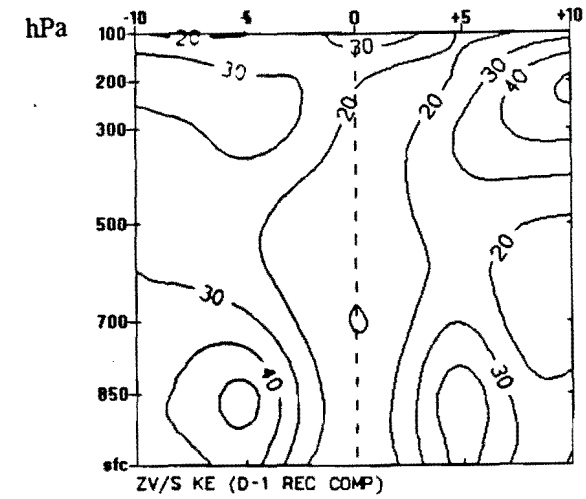

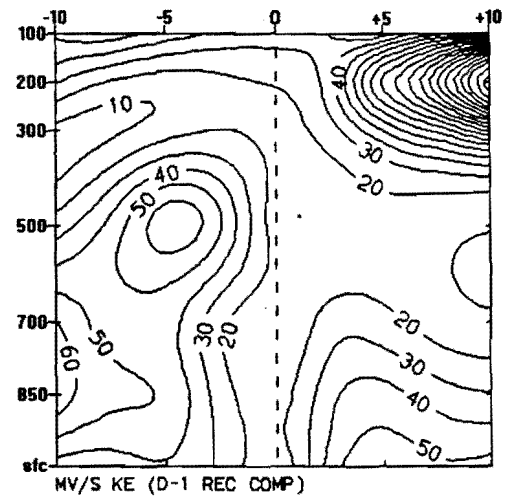

D-1

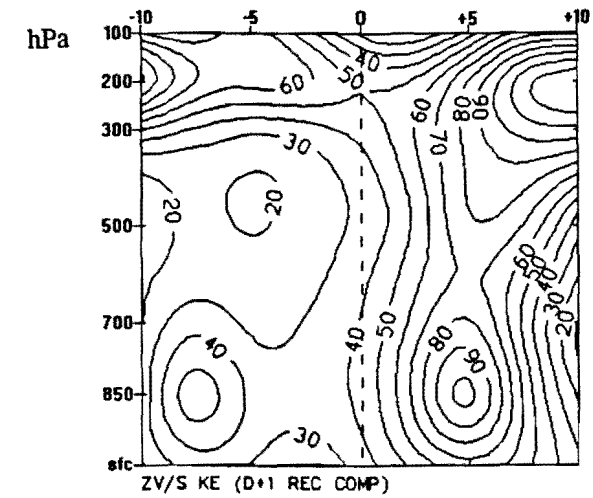

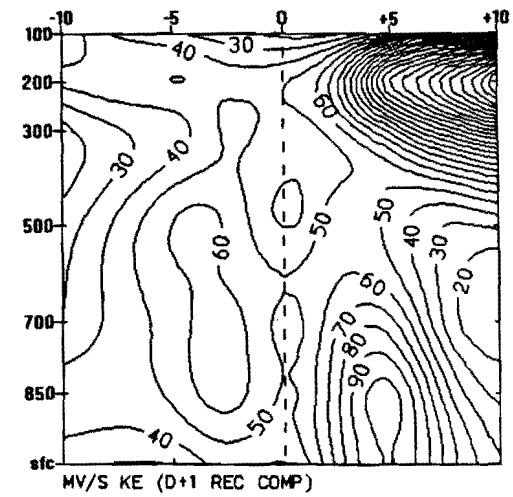

D+1

Figure 4-51a,b and c : REC zonal kinetic energy. Contour interval is 10 J kg^{-1}.

Figure 4-52a,b and c : REC meridional kinetic energy. Contour interval is 10 J kg^{-1}.

LONGITUDE

LATITUDE

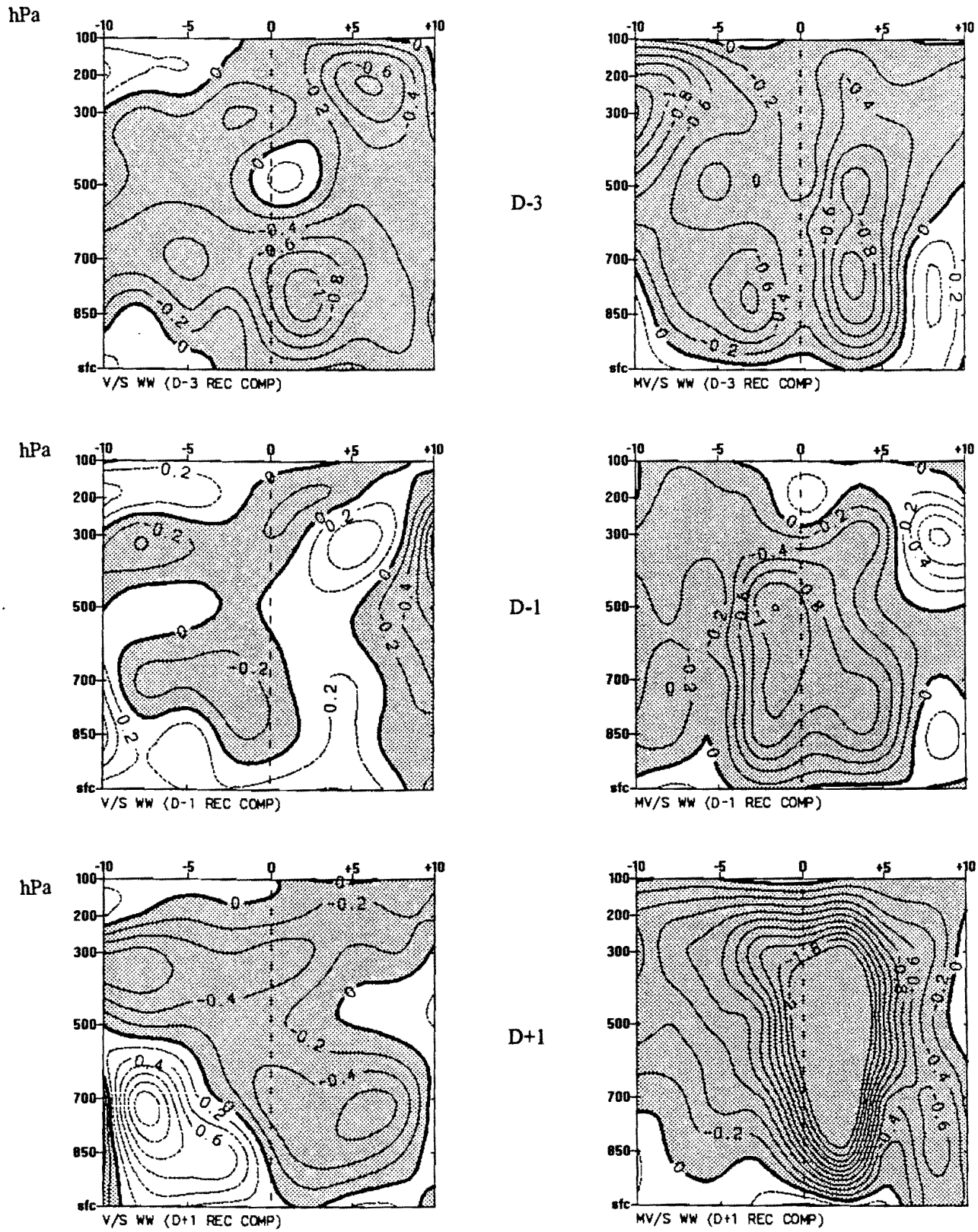

Figure 4-53a,b and c : REC zonal vertical motion. Contour interval is 0.2 Pa s^{-1}.

Figure 4-54a,b and c : REC meridional vertical motion. Contour interval is 0.2 Pa s^{-1}.

LONGITUDE

LATITUDE

hPa

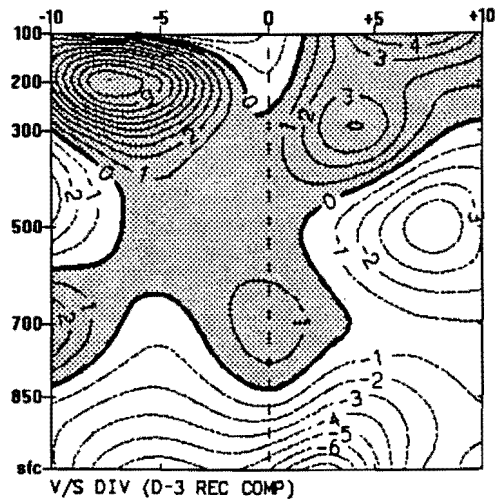

D-3

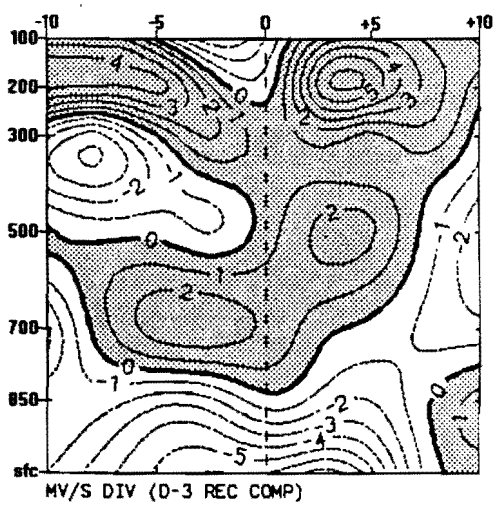

hPa

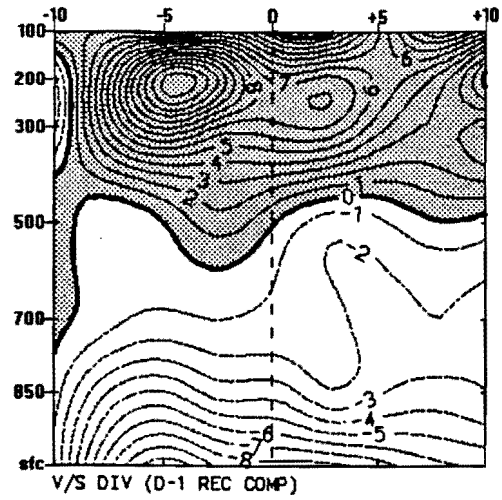

D-1

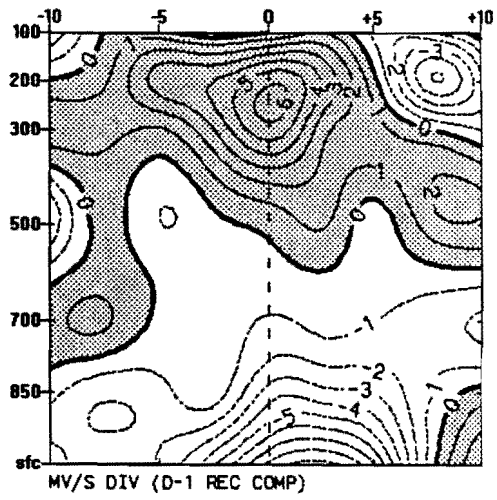

hPa

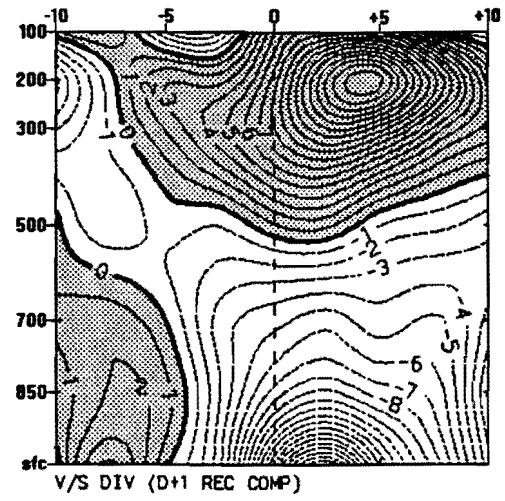

D+1

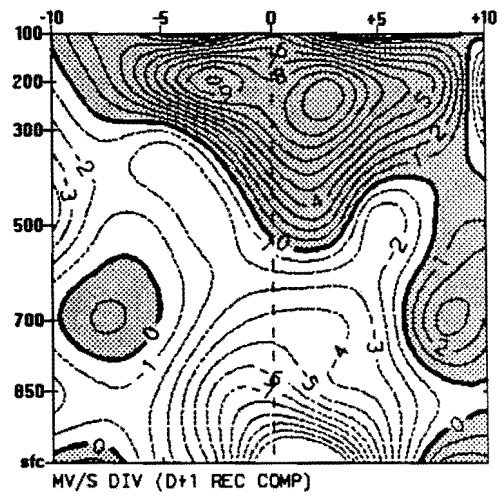

Figure 4-55a,b and c : REC zonal divergence. Contour interval is 1 x 10^{-5} s^{-1}.

Figure 4-56a,b and c : REC meridional divergence. Contour interval is 1 x 10^{-5} s^{-1}.

LONGITUDE

LATITUDE

hPa

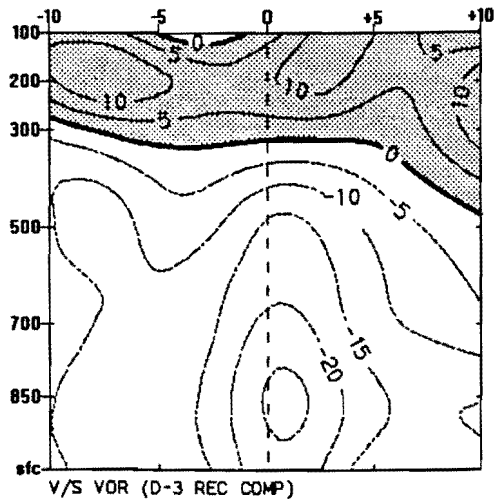

D-3

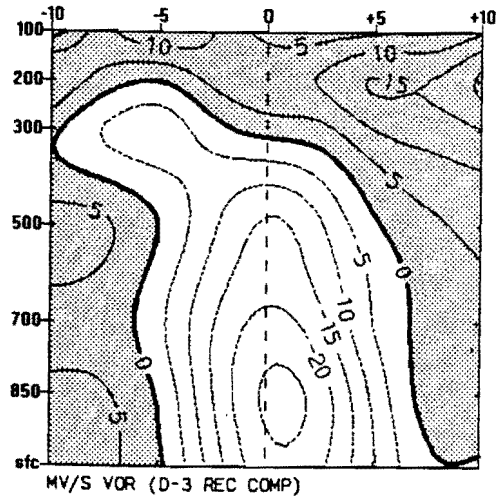

hPa

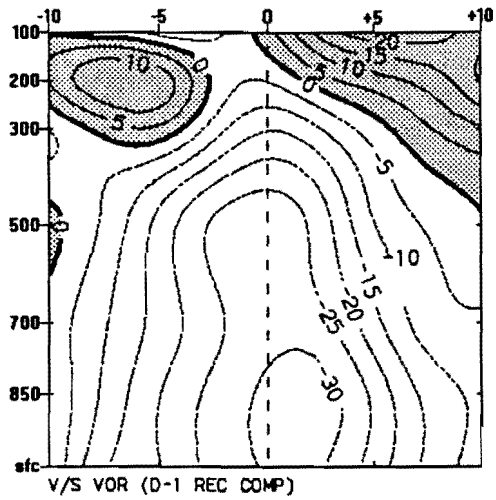

D-1

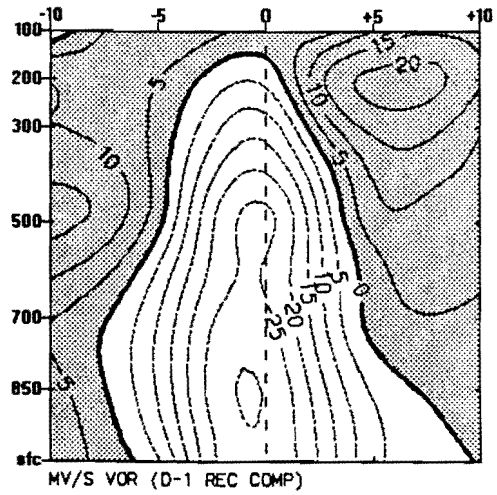

hPa

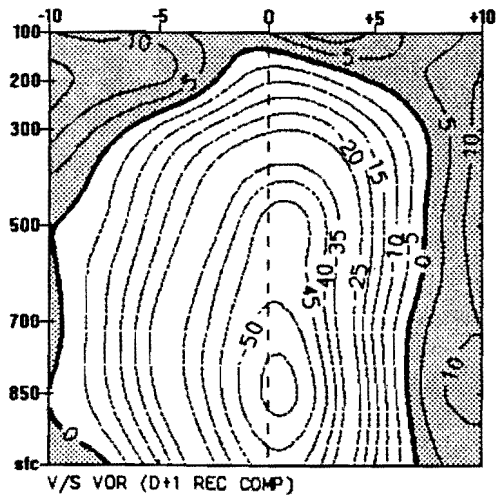

D+1

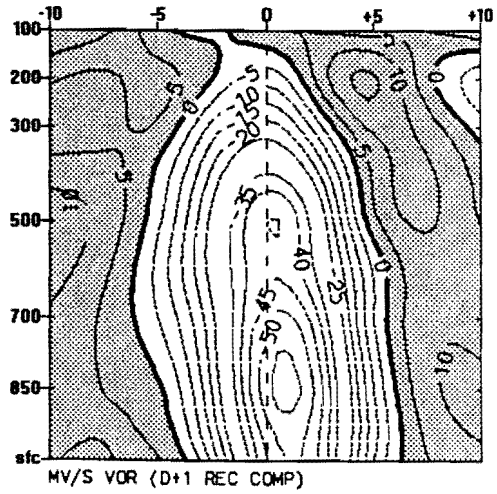

Figure 4-57a,b and c : REC zonal vorticity. Contour interval is 5 x 10^{-5} s^{-1}.

Figure 4-58a,b and c : REC meridional vorticity. Contour interval is 5 x 10^{-5} s^{-1}.

LONGITUDE

LATITUDE

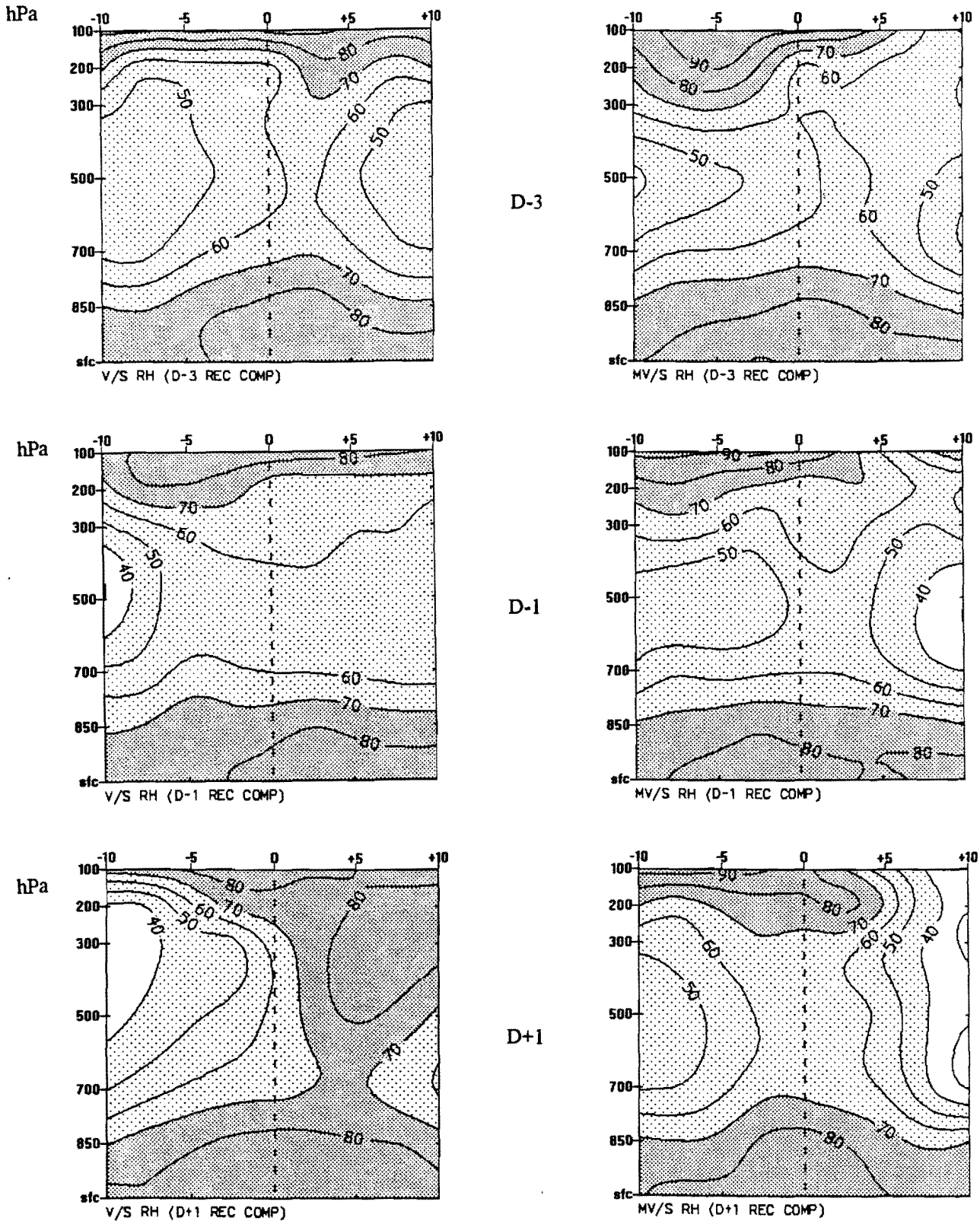

Figure 4-59a,b and c : REC zonal relative humidity. Contour interval is 10 %.

Figure 4-60a,b and c : REC meridional relative humidity. Contour interval is 10 %.

LONGITUDE

LATITUDE

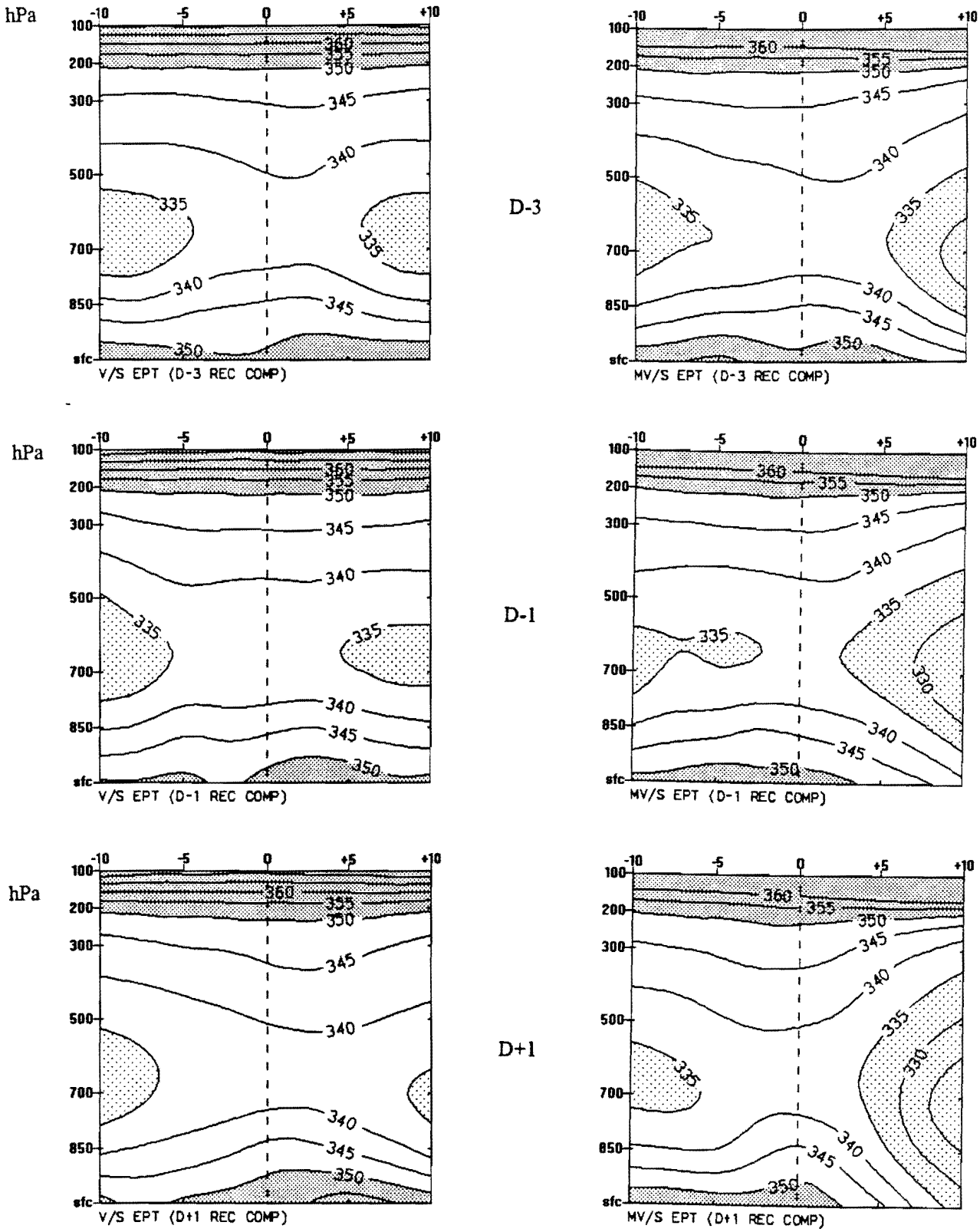

Figure 4-61a,b and c : REC zonal equivalent potential temperature.
Contour interval is 5 °K.

Figure 4-62a,b and c : REC meridional equivalent potential temperature.
Contour interval is 5 °K.

Chapter 5

TC ANOMALY ANALYSES

In this chapter comparisons between the WM and the REC TC composites are analysed with the aid of TC anomalies. These are obtained by removing the mean background structure (MSC, **Chapter 3**) from the TC composites (**Chapter 4**). This is done in recognition that anomaly patterns are better suited to be used in making comparisons between the WM and REC TC's. For the WM TC the anomaly centre is 82.5°E, 15.5°S on D-3, 80°E, 15°S on D-1, and 72.5°E, 20°S on D+1. For the REC TC it is 65°E, 12.5°S on D-3, 62.5°E, 15°S on D-1, and 75°E, 17.5°S on D+1. Vertical anomaly sections are not produced as these were found to be distorted primarily by meridional gradients. This 'smearing' effect is thought to be a result of the moving co-ordinate system employed in the composite TC grid.

Daily TC anomalies are used to analyse differences occurring between the WM and REC TC's on D-3, D-1 and D+1. Comparison of the WM and REC anomalies may result in the recognition of kinematic, moisture and thermodynamic patterns unique to each composite. The anomalies will thus be used to determine which parameters are linked to the non-recurving or recurving TC tracks.

5.1 Kinematic Analyses

5.1.1 Geopotential Height

850 hPa

On D-3 at P_{850} a much stronger negative anomaly is observed for the WM TC than for the REC TC case (**Figures 5-1a, 5-2a**). A negative anomaly of < -30 gpm is observed for the WM TC, while a value of -10 gpm is observed for the REC TC. Although the REC TC contains positive anomalies at a radius of > 5° from the C_{cen}, the anomaly range is only 15 gpm while for the WM TC the range is > 20 gpm. The larger range of anomaly values for the WM TC result in it having a steeper geopotential gradient compared to the REC TC and stronger P_{850} horizontal winds (see **Figures 5-5a** and **5-6a**).

On D-1 a similar anomaly structure is observed for both the WM and the REC TC, with both attaining negative geopotential anomaly values of < -30 gpm at the C_{cen} (**Figures 5-1b, 5-2b**). The gradient of the geopotential contours as well as the anomaly ranges are the same for both the WM and REC TC's. The contours are distributed in an ellipse for both TC's, the major axis oriented north-northwest in the case of the WM TC and northwest for the REC TC.

The most apparent difference between the WM and the REC TC anomalies on D+1 is continued intensification of the negative anomalies in the case of the latter compared to a decrease in intensity of the former (**Figures 5-1c, 5-2c**). The negative anomaly for the WM TC reduces to -25 gpm, while the negative anomaly for the REC TC intensifies to < -45 gpm at the C_{cen}. Positive anomalies are observed to reach as close

as 5° radius from the C_{cen} for the WM TC, but only as close as 7.5° for the REC TC east of the C_{cen}.

200 hPa

On D-3, very few similarities are observed between the WM and the REC anomalies, in fact the structural differences in the geopotential anomaly fields are very distinct even though both contain large areas of positive geopotential anomalies **(Figures 5-3a, 5-4a)**. For the WM TC the northwest quadrant and the adjacent half of the northeast quadrant contain negative geopotential anomalies, whereas south of the C_{cen} only positive geopotential anomalies are observed (> +50 gpm). For the REC TC the entire composite area contains positive geopotential anomalies, but with a maximum in the southeast quadrant of only half of that observed for the WM TC. Another difference is the strong zonal gradient observed for the WM TC, while a weak gradient, having no specific orientation is observed for the REC TC.

On D-1 the WM and REC TC's still exhibit more differences than similarities in the geopotential anomaly structure **(Figures 5-3b, 5-4b)**. The zonal gradient in the positive anomalies, although much reduced and only dominant in the southeast quadrant of the WM TC, is similar to that of D-3. For the REC TC an intrusion of intense negative anomalies, with a very steep gradient is observed in the southeast quadrant with an anomaly of < -50 gpm. The maximum anomaly for the WM TC is found in the south (> +25 gpm), and for the REC TC in the north (> +15 gpm).

In **Figures 5-3c** and **5-4c** (D+1), similar gradients are observed in the negative anomaly regions of both the WM and the REC TC. Intrusion of negative anomalies are only observed in the southwest quadrant of the WM TC. For the REC TC, negative anomalies are found to dominate the southern half of the composite, with negative anomaly values of < -60 gpm. The positive anomaly regions for both the WM and the REC TC's have much slacker gradients, with the maximum anomaly of the former occurring along a meridional band east of the C_{cen} (> +15 gpm), and a more zonally distributed band occurring in the north for the REC TC (> +20 gpm).

At P_{850} it is observed that the negative geopotential anomalies for the WM TC decrease after the day of maximum intensity. The REC TC is found to continue intensifying after D-0 at P_{850}. At P_{200} positive geopotential anomaly regions decrease in strength for the WM and the REC TC. The advancement of an upper level trough (P_{200}) in the southwest of the WM TC is evidenced by the rapid intensification of the negative anomalies to < -50 gpm on D+1. Comparison of P_{850}, suggest that WM TC's are sustained at a steady rate while REC TC's seem to have a more 'explosive' nature. The WM TC negative anomaly at P_{850} reduces by -5 gpm, while the REC TC anomaly intensifies from -10 gpm (D-3) to -45 gpm (D+1).

5.1.2 Horizontal Wind

850 hPa

Cyclonic anomaly wind patterns exist for both the WM and the REC TC's on D-3 (**Figures 5-5a, 5-6a**). The WM TC is however observed to have wind anomalies > +10 m s^{-1} east of the C_{cen}, while the maximum wind anomaly for the REC TC is < +7

m s^{-1}. The northeast, rear quadrant of the WM TC contains the highest anomalies, while the highest anomalies for the REC TC is found in the southeast, front quadrant. It is noticeable that the WM TC possesses a much more intense and organised cyclonic structure than the REC TC.

On D-1 very little change is observed from the D-3 structure for the WM and REC TC's. The maximum wind anomalies of > +10 m s^{-1} are still observed in the northeast quadrant of the WM TC (**Figure 5-5b**), whereas for the REC TC the only discernible feature is the uniformly lower anomalies (< +5 m s^{-1}) within 7.5° radius of the C_{cen} (**Figure 5-6b**). The strong cyclonic anomaly pattern present for the WM TC is almost absent for the REC TC, where an almost zonal anomaly pattern exists to the north of the C_{cen}.

On D+1 changes in the wind anomaly patterns are observed for both the WM and the REC TC (**Figures 5-5c, 5-6c**). The cyclonic circulation pattern is less symmetrical but broader for the WM TC, whereas for the REC TC this pattern is only evident within 5° radius of the C_{cen}. Outside of this radius anticyclonic flow is observed in the northwest quadrant and the extreme southwest of the REC TC. The strength of the anomalies has reduced to < +10 m s^{-1} for the WM TC, while an increase to a similar value is observed in the southeast quadrant of the REC TC.

500 hPa

On D-3 cyclonic wind anomalies are observed to be stronger for the WM TC (**Figure 5-7a**) than the REC TC (**Figure 5-8a**). Values of > +10 m s^{-1} observed for the WM TC while maximum values of +5 m s^{-1} are observed for the REC TC. Apart from the wind anomaly being stronger for the WM TC, the structure of the vortex is more cyclonic than for the REC TC.

Differences on D-1 are evident in the continued cyclonic anomaly present for the WM TC (**Figure 5-7b**), and a collapse of cyclonic rotation for the REC TC wind anomaly (**Figure 5-8b**). For the REC TC westerlies are observed in the northern half of the composite (< +10 m s^{-1}), while in the extreme south of the composite, northward anomalies are observed (< +5 m s^{-1}). The highest wind anomaly of the WM TC is found in the northeast quadrant (+8 m s^{-1}).

On D+1 a symmetrical cyclonic vortex anomaly is not evident for the WM nor the REC TC (**Figures 5-7c, 5-8c**). In the case of the WM TC a meridionally elongated cyclonic structure is apparent. The presence of northwesterly flow is however observed in the southwest quadrant of the WM TC. For the REC TC a wave-like structure with a cyclonic rotation around the C_{cen} is observed with highest wind anomalies in the north. South of -5° latitude weak westerly anomalies are present.

200 hPa

On D-3 strong easterly anomaly flow of > +13 m s^{-1} is observed for the WM TC (**Figure 5-9a**), while weak easterly anomaly is observed to the north of the C_{cen} of the REC TC, and a weak westerly anomaly to the south (**Figure 5-10a**). For the WM TC this represents increased easterly flow in the north, but a decreased westerly flow in the south when remembering the MSC horizontal wind field at P_{200} (see **Figure 3-2c**). The REC TC anomaly structure shows weak reinforcing of the easterly flow north of the C_{cen} and westerly flow south of the C_{cen}.

Figure 5-9b reveals that minimal change in the anomaly wind direction has occurred from D-3 to D-1 for the WM TC, except for a dramatic reduction in the easterly anomaly observed in the southeast quadrant (almost returns to westerly mean). The REC TC sees a change from a easterly anomaly on D-3, to a westerly anomaly on D-1, north of the C_{cen} (**Figure 5-10b**). In the southwest quadrant of the WM TC northerly winds are associated with the 'attractor' trough, while the southeast quadrant of the REC TC contains a similar 'attractor' mechanism associated with westerly winds.

The most noticeable difference on D+1 is the strong northwesterly anomaly in the southwest quadrant of the WM TC (**Figure 5-9c**), compared to the uniformly strong westerly anomaly of the whole REC TC composite (**Figure 5-10c**). The mean westerly wind south of the C_{cen} is being re-established and strengthened for the WM TC with the eastward advancement of a trough (see **Figure 5-3c**). The REC TC is observed to have westerly wind anomalies in excess of +10 m s^{-1} over most of the composite,

representing westerly flow re-establishment south of the C_{cen}, but easterly flow reversal north of the C_{cen}. The conditions of strong westerly flow at the C_{cen}, in the upper levels has been shown to be a phenomena present for recurving TC (Hodanish and Gray, 1993).

Comparison of the anomalies reveal that horizontal wind strengths at P_{850} and P_{500} are greater for the WM TC than the REC TC. The depth of the cyclonic vortex is apparent for the WM TC, as the P_{850} and P_{500} anomaly structures are similar throughout the sequence. This is not apparent for the REC TC except on day D+1. At P_{200} the wind anomalies exhibit very different directions south of the C_{cen} on D-3 and D-1 for the WM (easterly) and the REC (westerly) TC. D-3 of the WM TC is nearly the opposite of D+1 REC, suggesting an entirely different upper shear response for convective maintenance.

5.1.3 Kinetic Energy

850 hPa

The kinetic energy anomaly structures at D-3 for the WM and REC TC are dissimilar, except that both composites contain large regions of positive anomalies (**Figures 5-11a, 5-12a**). A striking difference is the distribution of a zonally oriented band of negative anomalies for the REC TC north of the C_{cen}. Orientated similar to the negative band, two regions of positive anomalies are situated north and south of this band, containing regions of maximum anomalies > +20 J kg^{-1}. For the WM TC a

region of positive kinetic energy anomalies is observed in the rear northeast quadrant with the maximum > +50 J kg^{-1}.

On D-1 similarities between the positive anomaly areas > +30 J kg^{-1} for the WM and the REC TC have appeared with both TC composites exhibiting clockwise movement of these areas around the C_{cen} in the east (**Figure 5-11b, 5-12b**). Although the WM TC has a maximum positive anomaly > +50 J kg^{-1} at 0° longitude, +5° latitude, the encompassing of the weak negative anomaly core is in a more advanced state for the REC TC

D+1 sees the intensification of the REC TC positive anomaly areas > +70 J kg^{-1} southeast of the C_{cen} (double that for D-1), while the positive anomaly region of the WM TC has consolidated itself into a circular region situated about +5° longitude, 0° latitude with no change in strength (**Figure 5-11c, 5-12c**). Because of the high positive kinetic energy anomalies situated to the southeast of the C_{cen} in the REC TC map, a shift of the region of negative anomalies previously situated at the C_{cen}, has occurred to the northwest.

200 hPa

On D-3 negative kinetic energy anomalies dominate the WM TC (**Figure 5-13a**), while for the REC TC a zonally situated negative anomaly across C_{cen} is bordered on both sides by areas of positive anomalies > +40 J kg^{-1} (**Figure 5-14a**). A region of positive anomaly > +20 J kg^{-1} is situated in the northwest quadrant of the

WM TC, with the negative anomaly region to the south reaching an intensity of < -100 J kg^{-1}. For the REC TC negative anomalies do not exceed -60 J kg^{-1}.

On D-1 it is observed that the region of positive anomalies previously situated in the north of the WM TC composite on D-3, has been replaced by a zonal band at +5° latitude, with a value > +20 J kg^{-1} northeast of the C_{cen} (**Figure 5-13b**). In the REC TC anomaly composite (**Figure 5-14b**) the previously negative anomaly along the 0° latitude is displaced almost entirely to the north of the 0° latitude. The incursion of strong positive anomalies to the south of the C_{cen} reaches values of > +200 J kg^{-1} in the southeast quadrant. The strongest negative anomalies for the WM TC are found in the southeast quadrant (< -60 J kg^{-1}) and for the REC TC north of the C_{cen} (< -20 J kg^{-1}).

Figures 5-13c and **5-14c** reveal that both the WM and the REC TC possess high positive kinetic energy anomalies of > +140 J kg^{-1} on D+1. The gradient of the positive anomaly contours above +40 J kg^{-1} contour are similar for both cases. The region in which these strong positive anomalies are located, although both in the southern half of the composite, are in the southwest for the WM TC (> +140 J kg^{-1}) and in the southeast for the REC TC (> +200 J kg^{-1}). A major difference in the anomaly composites is the large area of negative anomalies found in the eastern half of the WM TC (< -40 J kg^{-1}) which is absent for the REC TC anomaly composite.

From the kinetic energy it is seen that at P_{850} easterly flow dominates the REC TC on D+1, while westerly flow dominates the WM TC on D-1. At P_{200} strong negative anomalies (< -100 J kg^{-1}) on D-1 for the WM TC indicate a change in direction as well

as an intensification relative to the mean structure. The strong positive anomalies > +100 J kg^{-1} for both the WM and the REC TC on D+1 represents a re-establishment and intensification of the mean westerly flow.

5.1.4 Vertical Movement

500 hPa

On D-3 it is observed that the region of strong negative anomalies ('uplift') exceeding -0.5 Pa s^{-1} is distributed along the -2.5° latitude for both the WM and the REC TC anomaly composites (**Figures 5-15a** and **5-16a**). The regions of positive anomalies ('downward motion') are very weak for the WM TC, but for the REC TC a northwest-southeast band of positive anomalies dominate the northwest quadrant.

Shifting of the regions of strongest negative anomalies are evident for both the WM and the REC TC anomaly composites on D-1 (**Figures 5-15b** and **5-16b**). For the WM TC anomaly composite an elliptical area situated at +5° longitude, -5° latitude has replaced the zonal band of D-3, while stronger negative anomalies are observed for the REC TC anomaly having a high value of -2 Pa s^{-1} west of the C_{cen}. In the latter case the negative anomaly area has expanded while in the former case it has receded. Small areas of positive anomalies are found east of the C_{cen} for the WM TC, and to the north for the REC TC.

On D+1 very different scenarios are evident for the WM and the REC TC's when considering the strength of the negative anomalies. Similarities are found in the spatial extent of the negative and positive anomalies (**Figure 5-15c** and **5-16c**). For the WM

TC anomaly composite a meridional band between 0° and +5° longitude from the north to -5° latitude emerges for negative anomalies stronger than -0.5 Pa s^{-1}. Intensification of the negative anomaly values is observed for the REC TC anomaly composite with values stronger than -3 Pa s^{-1} occurring east of the C_{cen} around which a steep gradient is found.

The general trend in the vertical movement anomalies for the WM TC is a gradual reduction in strength of the uplift regions (negative anomalies), while an increase is observed for the REC TC from -1 Pa s^{-1} on D-3 to < -3 Pa s^{-1} on D+1. The negative anomalies of the WM TC attain maxima of < -1 Pa s^{-1}, whereas the REC TC attain maxima of < -3 Pa s^{-1}. This implies that air parcels are lifted from 850 to 200 hPa within 6 hours in a REC TC, a sign of efficient cumulus convection leading to enormous diabatic heat release and upper outflow.

5.1.5 Divergence

200 hPa

From **Figures 5-17a** and **5-18a** it is evident that on D-3 the strength of the positive divergence anomaly is the same for both the WM and REC TC (+8 x 10^{-5} s^{-1}). Apart from attaining similar strengths, the strongest positive anomaly values are situated south and west of the C_{cen} for the WM and REC TC respectively. For the WM TC a region of strong negative anomalies (-6 x 10^{-5} s^{-1}) is found north of C_{cen}, whereas in the REC TC anomaly composite a northwest-southeast band of negative anomalies is situated across and east of the C_{cen} with the highest value being -2 x 10^{-5} s^{-1}. A

notable feature is the presence of positive anomaly 'bands' having similar orientations in both the WM and REC TC anomaly composites.

A reduction in the strength of the negative anomalies areas are observed for the WM TC on D-1, while an increase occurs for the REC TC (**Figures 5-17b** and **5-18b**). The orientation of the bands as found on D-3 has remained relatively the same for the major positive anomaly regions for both composite anomalies. The difference in strength of the positive anomaly areas is more than double for the REC TC ($+10 \times 10^{-5}$ s^{-1}) than for the WM TC ($+4 \times 10^{-5}$ s^{-1}). A region of strong negative anomalies (-6×10^{-5} s^{-1}) occurs across the northeast quadrant of the WM TC, while the strongest negative anomaly of -4×10^{-5} s^{-1} is found south of the C_{cen} in the REC TC anomaly composite.

On D+1 re-intensification of the REC as well as the WM TC positive anomaly regions is observed, although to contrasting degrees (**Figures 5-17c** and **5-18c**). A region of positive anomalies is dominant for the REC TC, attaining values $> +16 \times 10^{-5}$ s^{-1} to the southeast of the C_{cen}. For the WM TC the positive anomalies are only dominant in the southeast quadrant where a high value of $+6 \times 10^{-5}$ s^{-1} is reached. It is notable that the positive anomaly region of the REC TC is concentrated around a single point, but that for the WM TC three regions containing positive anomalies $> +4 \times 10^{-5}$ s^{-1} are present.

As observed for the vertical movement anomalies, a decrease in the strength of the positive upper divergence anomaly region occurs for the WM TC, while an increase in strength occurs for the REC TC positive anomaly region through the sequence. The

WM TC is observed to have a number of positive anomaly regions, while the REC TC only exhibits one area of strong positive anomaly.

5.1.6 Vorticity

850 hPa

On D-3 negative anomaly (cyclonic) areas are observed to be located at the C_{cen} for both the WM (< -20 x 10^{-5} s^{-1}) and the REC TC (< -10 x 10^{-5} s^{-1}) vorticity anomaly composites (**Figures 5-19a** and **5-20a**). As well as having double the intensity of the cyclonic vorticity anomaly of the REC TC the WM TC has stronger positive anomalies in the northeast quadrant (+10 x 10^{-5} s^{-1}). The strong negative and positive anomaly values present for the WM TC anomaly composite results in a much steeper gradient around the C_{cen} than for the REC TC. The area around the C_{cen} having negative anomaly values stronger than -5 x 10^{-5} s^{-1} is much larger in the case of the WM than the REC TC composite.

The negative anomaly region on D-1 is oriented meridionally for the WM TC and zonally for the REC TC (**Figures 5-19b** and **5-20b**). In both cases the strongest positive anomalies are situated in the northeast quadrant of the composite with values of > +20 x 10^{-5} s^{-1} for the WM TC and values of > +5 x 10^{-5} s^{-1} for the REC TC. Due to the larger difference between the positive and negative anomalies in the WM TC case compared to the REC TC case, the gradient for the former is noticeably steeper than for the latter.

On D+1 a complete reversal in the strength of the vorticity anomaly structure between the WM TC and the REC TC is observed. Whereas on the previous days the WM TC contained the strongest positive and negative anomalies, on D+1 the situation has reversed such that the REC TC cyclonic anomaly maxima is almost double the value observed for the WM TC (**Figures 5-19c** and **5-20c**). For the WM TC the cyclonic anomalies are distributed in a northwest-southeast pattern with a comparatively gentle gradient. The cyclonic anomalies for the REC TC are observed to be concentrated within a radius of approximately 7.5° from the C_{cen}, with a strength of $-35 \times 10^{-5}\ s^{-1}$ at its centre and a gradient much steeper than for the WM TC. Strengthening of the cyclonic vorticity is observed for the REC TC, while a slight weakening is observed for the WM TC.

500 hPa

On D-3 the negative cyclonic vorticity anomaly for the WM TC exceeds $-20 \times 10^{-5}\ s^{-1}$, while for the REC TC a value of $-10 \times 10^{-5}\ s^{-1}$ is attained (**Figures 5-21a** and **5-22a**). The regions of positive anomalies, approximately $+5 \times 10^{-5}\ s^{-1}$, are situated at a radius of greater than 5° from the C_{cen} in both the WM and the REC TC anomaly composites. A marked northwest-southeast orientation of the negative anomalies is present in the WM TC anomaly composite.

Figures 5-21b and **5-22b** reveal an increase in the strength of the negative vorticity anomaly for the REC TC anomaly composite but not for the WM TC anomaly composite on D-1. Maximum cyclonic anomaly values of approximately $-20 \times 10^{-5}\ s^{-1}$ are recorded for both anomaly composites, with the WM TC having a strong

meridional axis, while the REC TC exhibits an axis oriented northwest-southeast across the C_{cen} as previously seen for the WM TC on D-3.

On D+1 continued strengthening of the cyclonic anomaly region is observed for the REC TC, while the centre of the WM TC cyclonic anomaly region is displaced to the north with no change in intensity from the previous anomaly composite (**Figures 5-21b** and **5-22b**). The steeper gradient present in the negative anomalies compared to the positive anomalies for the REC TC is not reflected for the WM TC, where a relatively constant gradient is observed throughout.

200 hPa

For the vorticity anomalies on D-3 very little structural similarities are observed between the WM and the REC TC composites. The WM TC vorticity anomaly contains a broad region of cyclonic anomaly values ($< -20 \times 10^{-5}$ s^{-1}) stretching from the northwest to the southeast (**Figure 5-23a**). The REC TC vorticity anomaly however contains a region of cyclonic anomalies situated north and east of the C_{cen} with a high value of -10×10^{-5} s^{-1} (**Figure 5-24a**). In both cases the regions containing the highest positive anomaly are situated to the west of the highest negative anomaly areas.

On D-1 the strength of the negative anomaly is approximately the same for both the WM and the REC TC (-10×10^{-5} s^{-1}), while the highest positive anomaly is double the maximum for the WM TC (**Figures 5-23b**) compared to the REC TC (**Figure 5-24b**).

The REC TC anomaly composite has retained the positive-negative anomaly distribution observed on D-3 more effectively than the WM TC anomaly composite.

For the D+1 composite positive anomalies are seen to dominate the WM TC composite, while roughly similar areas are observed for the positive and negative anomalies in the REC TC composite (**Figure 5-23c** and **5-24c**). A strong positive anomaly region is found in the northwest quadrant ($> +20 \times 10^{-5}$ s^{-1}), while the negative anomaly regions north and south of C_{cen} only attains values of $< -5 \times 10^{-5}$ s^{-1} in the WM TC anomaly composite. Strong positive anomalies ($> +15 \times 10^{-5}$ s^{-1}) are located to the east of the C_{cen} in the REC TC composite.

The lower tropospheric vorticity anomaly structure of the WM TC remains structurally intact at P_{850} and P_{500} throughout the sequence. For the REC TC pronounced cyclonic anomalies are only observed after D-1 at these levels. The WM TC is observed to possess a greater meridional extent than the REC TC which is observed to have a greater zonal extent. The negative anomalies across the C_{cen} for the WM and the REC TC's show a reduction in cyclonic vorticity for the former and a weak increase for the latter. At P_{200} vorticity anomaly values are still cyclonic, hence upper anticyclonic rotation may occur near the tropopause.

5.2 Moisture and Thermodynamics

5.2.1 Temperature

850 hPa

On D-3 positive anomalies dominate the temperature composites for both TC cases (**Figure 5-25a** and **5-26a**), although a large region of negative anomalies are observed to occur north of the C_{cen} in the WM TC. The strongest positive anomalies occur in the south of the REC TC, attaining values > +1.2 °C, while the WM TC attains half that value (+0.6 °C). The centre of the negative anomaly region situated to the north of the C_{cen} reaches a strength of -0.4 °C for the WM TC. While no negative anomaly area is found in this region for the REC TC, the positive anomalies in the northeast quadrant are < 0.4 °C.

On D-1 intrusion of negative anomalies are seen in the south of the REC TC anomaly (**Figure 5-26b**), while the region of negative anomalies for the WM TC, present on D-3 to the north of the C_{cen}, has shifted to the northeast (**Figure 5-25b**). A decrease in the strength of the positive anomaly region is observed for both the WM TC and the REC TC to values of +0.4 °C (south of the C_{cen}) and +0.8 °C (at the C_{cen} and north of it), respectively.

On D+1 a dramatic change in the area of negative anomalies, for both the WM and the REC TC from the D-1 map is observed. For the REC TC (**Figures 5-26c**) encircling of the central positive anomaly region is observed with negative anomalies attaining strengths of < -1 °C. Although the central positive anomaly region has not been encircled in the WM TC (**Figures 5-25c**) anomaly composite, a region of very low

positive anomalies is situated along +5° latitude combined with a negative anomaly region north of the C_{cen}.

200 hPa

Positive anomalies dominate both the WM and the REC TC anomaly composite on D-3 as observed in **Figures 5-27a** and **5-28a**. A maximum positive anomaly of > +1.6 °C is observed south of the C_{cen} for the WM TC, while a value of +1 °C is observed north of the C_{cen} for the REC TC composite. Intrusion of positive anomalies are from the south for the WM TC, and from the north for the REC TC.

On D-1 a concentration of high positive anomalies is found to the east of C_{cen} for the REC TC (**Figure 5-28b**), while the highest positive anomalies of the WM TC still occur south of C_{cen} (**Figure 5-27b**). The REC TC positive anomalies are situated in a zonal band, while the WM TC anomalies tend toward a meridional structure. Negative anomalies of < -0.8 °C are observed north of the C_{cen} in the REC TC.

Figure 5-27c reveals a banded structure to the positive temperature anomalies oriented northwest-southeast for WM TC composite, while a circular structure is present for the REC TC composite (**Figure 5-28c**). Values of > +1.2 °C and > +1.6 °C occur east of the C_{cen} for the WM and REC TC's respectively. The northward shift of the positive anomalies (WM TC) results in the displacement of the previously lower positive anomalies along +5° latitude.

At P_{850} it is observed that positive temperature anomalies dominate the REC TC on D-3 and D-1 but recede northward with the advancement of strong negative anomalies in the south. It should be noted that a positive anomaly region has however remained at the C_{cen} on D+1. For the WM TC a region of negative anomalies propagates north and then east of the C_{cen} on D-3 and D-1. P_{200} reveals a consistent positive anomaly structure for the WM TC as well as the REC TC throughout the sequence suggesting deep cumulus heating.

5.2.2 Relative Humidity

850 hPa

Differences in the relative humidity anomaly fields for the WM and the REC TC composites are evidenced by the dominant positive anomaly field across the WM TC (**Figure 5-29a**) and a smaller positive anomaly area across the C_{cen} surrounded by negative anomaly areas for the REC TC (**Figure 5-30a**). The strongest positive anomaly is situated in the southwest quadrant of the WM TC (> +15 %), even though a large region of anomalies > +10 % is found in the southeast quadrant. For the REC TC, positive anomalies (> +10 %) are found at the C_{cen}. A region of negative relative humidity anomalies is found in the north of the WM TC. For the REC TC the strongest negative anomalies are found equatorward of +5° latitude.

On D-1 the highest positive anomaly for the WM TC is observed to occur in the southeast quadrant (**Figure 5-29b**). For the REC TC a positive anomaly band having a northeast-southwest orientation is situated across and east of the C_{cen}, with negative anomalies stronger than -5 % occurring on either side of it (**Figure 5-30b**).

On D+1, for the WM TC, a meridional band of negative relative humidity anomalies is situated between -10° and -5° longitude (**Figure 5-29c**), while negative anomalies are situated to the north of +5° latitude for the REC TC (**Figure 5-30c**). The strength of the positive anomaly for both the WM and the REC TC anomaly composites attains values of > +10 %. Positive anomalies > +5 % are situated along a meridional band in the eastern half of the WM TC composite, while it has a more zonal structure in the REC TC anomaly composite.

500 hPa

On D-3 for the WM TC negative relative humidities situated along a meridional band across C_{cen} divides a region of high positive relative humidity anomalies in the east from positive values in the west (**Figure 5-31a**). Positive anomalies of > 20 % (east) and negative anomalies of < -10 % (north) are observed for the WM TC. Positive relative humidity anomalies dominate the REC TC case with values of > +20 % at the C_{cen} (**Figure 5-32a**).

On D-1 the region of positive relative humidity anomalies for the WM TC have shifted south of C_{cen}, while a reduction in the positive anomaly values and the areal coverage is observed for the REC TC (**Figures 5-31b** and **5-32b**). Negative anomalies are observed to be stronger (< -15 %) than positive anomalies (10 %) for the REC TC. For the WM TC positive anomalies of > +15 % occur southeast of the C_{cen}, while negative anomalies of < -5 % occur north of the C_{cen}.

Figures 5-31c and **5-32c** reveal that more than a doubling in intensity of the positive relative humidity anomalies occur for the REC TC, whereas a reduction in the region of strongest positive anomaly (> +15 %) is observed for the WM TC. Although the strength of the positive anomaly has increased for the REC TC the negative anomaly intensity and coverage have not decreased substantially. For the WM TC a decrease in the intensity of the positive anomaly region sees an increase in strength of the negative anomaly region north of the C_{cen}.

From the relative humidity anomalies at P_{850} it is apparent that the area covered by the positive anomaly is much greater for the WM TC than the REC TC, although the strength of the anomalies are similar. In both cases positive relative humidity anomalies are introduced from the eastern edge of the TC. At P_{500} it is noted that positive anomalies are dominant in the east of both the WM and the REC TC strengthening the idea that moisture is more abundant in the eastern sector of the TC.

5.2.3 Precipitable Water

Surface -300 hPa

The precipitable water anomaly field (D-3) for both the WM and the REC TC's contain high positive values south and southeast of the C_{cen} with a maximum of > +8 mm for the former and > +10 mm for the latter (**Figure 5-33a** and **5-34a**). Negative anomalies < -4 mm are found north of C_{cen} for both TC's. The precipitable water anomalies of the WM TC have a stronger zonal signature than the REC TC.

The dominance of the positive anomaly areas continue on D-1 for both the WM and the REC TC, but intrusion of negative anomalies is observed in the west for the former (**Figures 5-33b** and **5-34b**). The region of positive anomalies > +8 mm is situated southeast of the C_{cen} for both the WM and the REC TC.

On D+1 a marked reduction in the area of positive precipitable water anomaly values is observed for the WM TC, while an increase in the strength occurs for the REC TC (**Figures 5-33c** and **5-34c**). Negative anomalies dominate the WM TC west of C_{cen} with values of < -6 mm in the southwest. Values of this magnitude are found to the south of the region of high positive precipitable water anomalies for the REC TC.

Overall the precipitable water anomalies are observed to decrease for the WM TC and remain relatively constant for the REC TC throughout the sequence. It is peculiar that negative precipitable water anomalies are found north of positive values on D-3 for the WM TC as well as for the REC TC. This can possibly be explained by the extraction of moisture from out-lying regions to the TC core. For the WM TC the reduction in positive anomaly intensity is accompanied by a reduction in the area that it covers. Although a slight reduction in the area covered by the positive anomalies is observed, it is accompanied by an increase in intensity.

5.2.4 Equivalent Potential Temperature

850 hPa

The region of positive equivalent potential temperature anomalies attain maxima of approximately +7 °K for both the WM and the REC TC on D-3 (**Figure 5-**

35a and **5-36a**). A region of positive anomalies > +5 °K is observed along a zonal band south of the C_{cen} for the WM TC, while the maxima for the REC TC is located at the C_{cen}. A region of negative anomalies < -2 °K is found in the northwest quadrant of the WM TC, while values of the same magnitude occur across the north of the REC TC.

On D-1 the intensity of the WM TC (**Figure 5-35b**) positive equivalent potential temperature anomaly region reaches a maximum of > +9 °K southeast of the C_{cen} with a relatively steeper gradient than observed on D-3. A decrease in the intensity of the positive anomaly region is observed for the REC TC, but with minimal change in location (**Figure 5-36b**). Negative anomaly values of < -4 °K are found in the southeast quadrant of the REC TC while values of < -2 °K occur southwest of the C_{cen} for the WM TC.

On D+1 a dramatic change in spatial coverage is observed for the REC TC with the region of positive anomalies occupying the centre of the composite and negative anomalies situated at a radius of approximately 7.5 ° from the C_{cen} (**Figure 5-36c**). Although an increase in strength of the negative anomalies is observed for the WM TC, the positive anomaly maximum only decreases by 2 °K at the C_{cen}. An increase in the strength of the positive anomaly (> +6 °K) as well as the negative anomaly (< -5 °K) region is observed for the REC TC.

500 hPa

On D-3 a region of negative anomalies is observed equatorward of the C_{cen}, while positive anomalies of > 3 °K occur south of the C_{cen} for the WM TC (**Figure 5-37a**). For the REC TC positive anomalies are dominant, with anomalies of > +4 °K at the C_{cen} (**Figure 5-38a**).

On D-1 the region of highest positive anomalies is observed in a similar position to that observed on D-3 for the WM TC. A reduction in the strength of the positive and negative anomalies is however observed (**Figure 5-37b**). Although a decrease in the intensity of the positive anomaly region is observed for the REC TC it maintains its position at the C_{cen} with only an intrusion of negative anomalies observed in the south (**Figure 5-38b**).

A further decrease in the intensity and size of the positive anomaly region and an increase in the strength of the negative anomaly region is observed for the WM TC on D+1 (**Figure 5-37c**). For the REC TC re-intensification of the positive anomaly region leads to a doubling of the positive anomaly maximum to 5 °K, even though the negative anomalies are observed to increase in intensity (**Figure 5-38b**).

TC Anomaly Synthesis

Comparing the WM TC and the REC TC using the anomalies has highlighted certain peculiarities. Looking at the kinematics it is observed that the negative geopotential anomalies at 850 hPa remain at approximately -30 gpm for the WM TC

and increase rapidly for the REC TC to -45 gpm on D+1. At 200 hPa positive geopotential anomalies are observed to decrease for both the WM and REC TC's, sharply for the former but slowly for the latter. The increase in the strength of the negative geopotential anomalies to the south is associated with the interaction with a subtropical trough system. It is notable that at 850 hPa negative geopotential anomalies of < -100 gpm were recorded for TC Danielle, relative to the January 1964 mean (Jury, 1993), more than double the anomaly value found for either the WM or REC TC's. Wind anomalies of the WM TC are observed to have greater cyclonic persistence and structural integrity than the REC TC anomalies at the 850 and 500 hPa surfaces. At 200 hPa subtropical interaction with the WM TC is observed via an area of northwesterly anomalies in the southwest. For the REC TC the 200 hPa wind anomaly has strong westerly flow across the composite at D+1. The kinetic energy anomalies at the 850 hPa surface for both the WM and REC TC's show a dominance of high positive anomalies in the east, while at the 200 hPa level introduction of strong positive anomalies are observed to a greater extent for the REC TC. Comparing the vertical movement anomalies at the 500 hPa surface, it is observed that the REC TC attains strong negative (uplift) anomalies of < -3 Pa s^{-1}, while the WM TC never experiences values < -1.5 Pa s^{-1}. The areas of high positive vertical movement anomalies are situated above areas of high kinetic energy anomalies at the 850 hPa surface, indicating interaction of horizontal and vertical shear. The 200 hPa positive divergence anomaly for the REC TC is observed to reach its peak at D+1 similar to the previously discussed parameters. From the vorticity anomalies at the 850 and 500 hPa surfaces it is observed that the WM TC retains its cyclonic vorticity anomaly longer than the REC TC which only attains a maximum on D+1. Kinematically the

WM TC exhibits a much more gradual growth and decay compared to the REC TC which is observed to mature very rapidly.

Uniform and dominant positive temperature anomalies are observed for the WM TC as well as the REC TC at the 200 hPa surface, while at 850 hPa this structure is more dominant for the REC TC. Weak negative temperature anomalies were recorded at Mauritius two days prior to the arrival of TC Danielle in the 500 and 850 hPa layer (Jury, 1993) similar to the weak anomalies found north of the C_{cen} on D-3 for the WM TC. Relative humidity anomalies at the 850 hPa surface are seen to be positive across the whole area for the WM TC but not for the REC TC, where positive anomalies are dominant in the east. At the 500 hPa surface D-1 and D+1 relative humidity structures are very similar, while on D-3 greater positive anomalies are present in the REC than the WM TC. Unlike previous parameters the relative humidity at 850 hPa is very similar to that recorded by Jury (1993). As with most of the parameters the positive precipitable water anomalies decrease with time for the WM TC, while the REC TC anomalies increase slightly. The increase for the REC TC occurs despite the reduction in the positive anomaly area. At 850 hPa positive equivalent potential temperature anomalies show a high correlation to the areas of high positive anomalies found for the precipitable water for both the WM and the REC TCs. At 500 hPa a close correspondence exists with the relative humidity anomalies at the same level for both the WM and the REC TC.

From the anomalies it is observed that certain parameters exhibit structures and intensities unique to each composite, i.e. 200 hPa wind anomalies, 500 hPa vertical

movement anomalies, 200 hPa divergence anomalies, and the 850 hPa relative humidity anomalies. For the 850 hPa geopotential, kinetic energy and equivalent potential temperature anomalies, and the 850 and 500 hPa vorticity anomalies very similar structures are observed for the WM and the REC TC's.

Previous studies by George and Gray (1976), Gentry (1983) and Hodanish and Gray (1993) have shown that the introduction of strong westerlies at the 200 hPa level 8° - 20° poleward of the cyclone centre can induce recurving of westward moving TCs. The presence of these conditions at the 200 hPa level is observed for the REC but not for the WM TC anomalies. These differences are also evident for the kinetic energy anomalies with values increasing dramatically from D-1 to D+1.

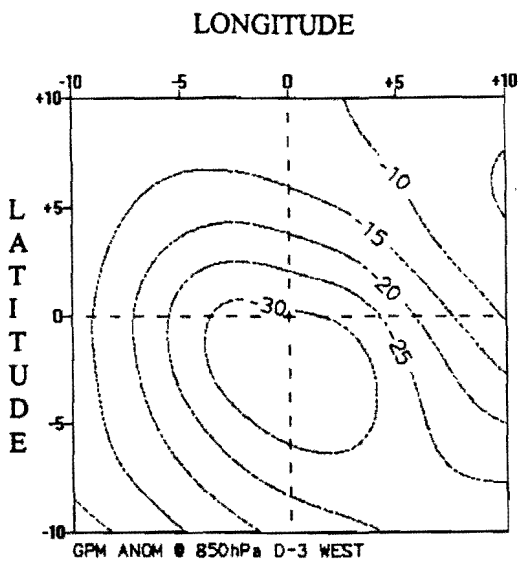

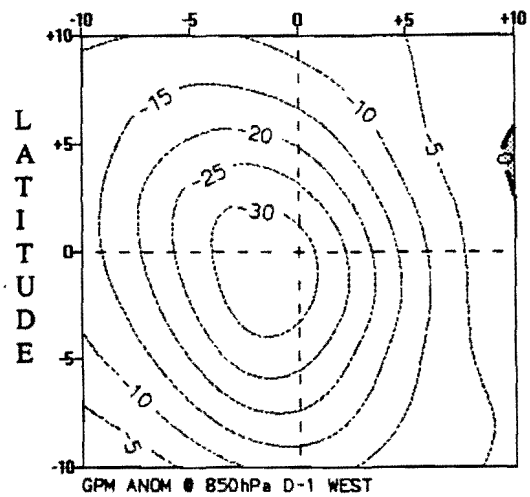

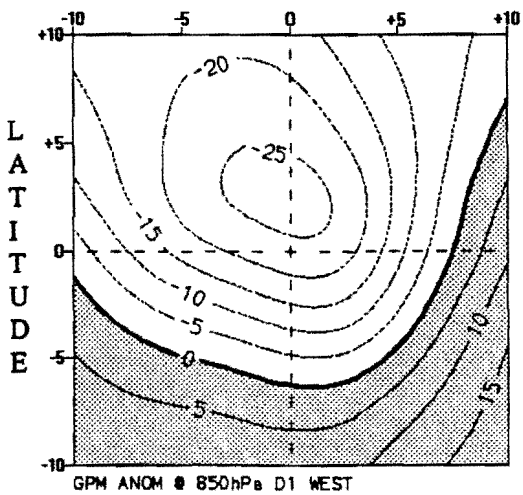

Figure 5-1a,b and c : WM geopotential anomaly @ 850 hPa. Contour interval is 5 gpm.

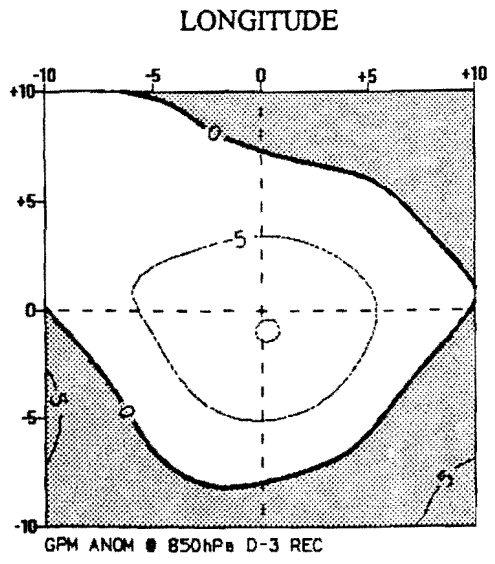

D-3

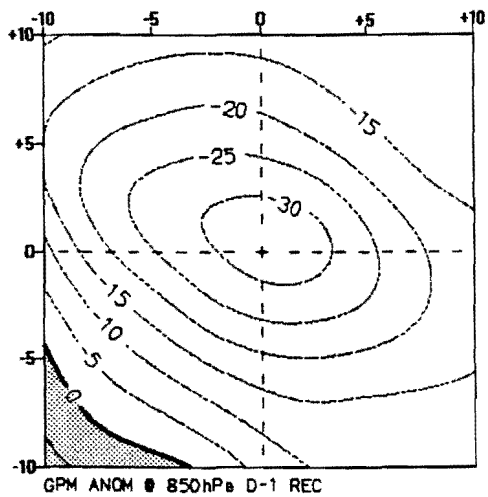

D-1

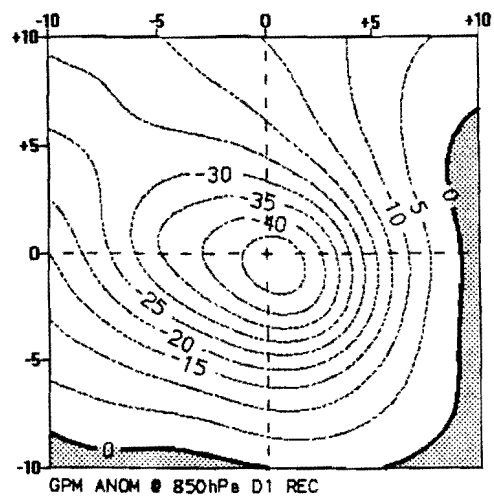

D+1

Figure 5-2a,b and c : REC geopotential anomaly @ 850 hPa. Contour interval is 5 gpm.

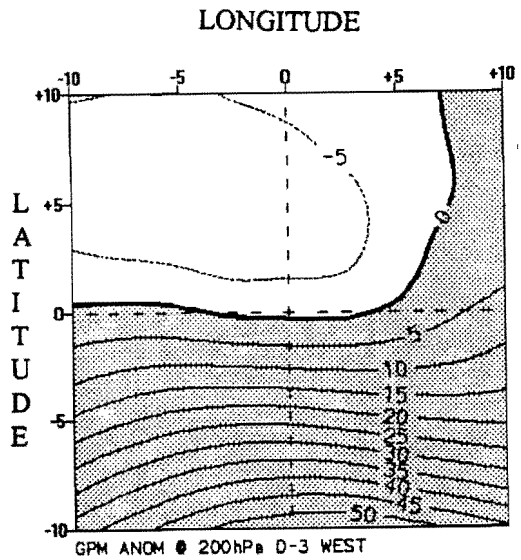

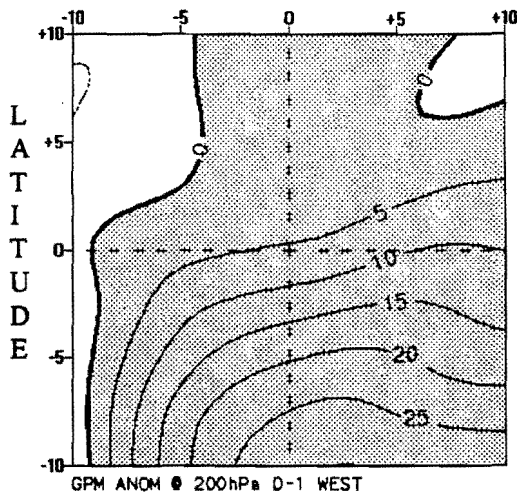

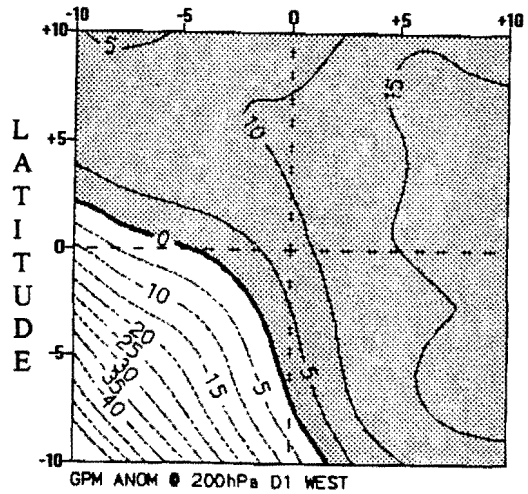

D-3

D-1

D+1

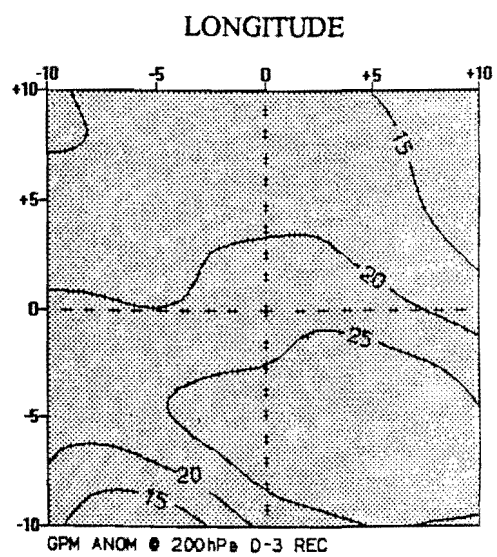

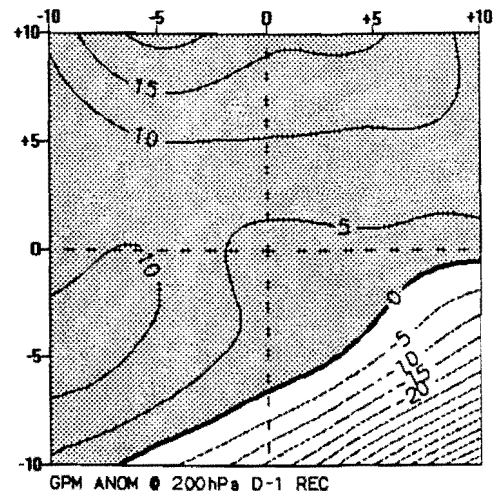

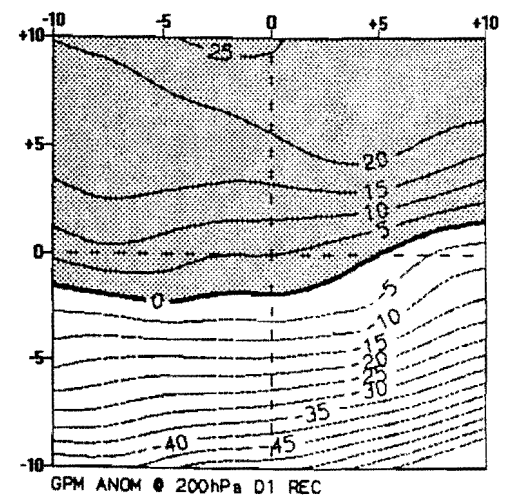

Figure 5-3a,b and c : WM geopotential anomaly @ 200 hPa. Contour interval is 5 gpm.

Figure 5-4a,b and c : REC geopotential anomaly @ 200 hPa. Contour interval is 5 gpm.

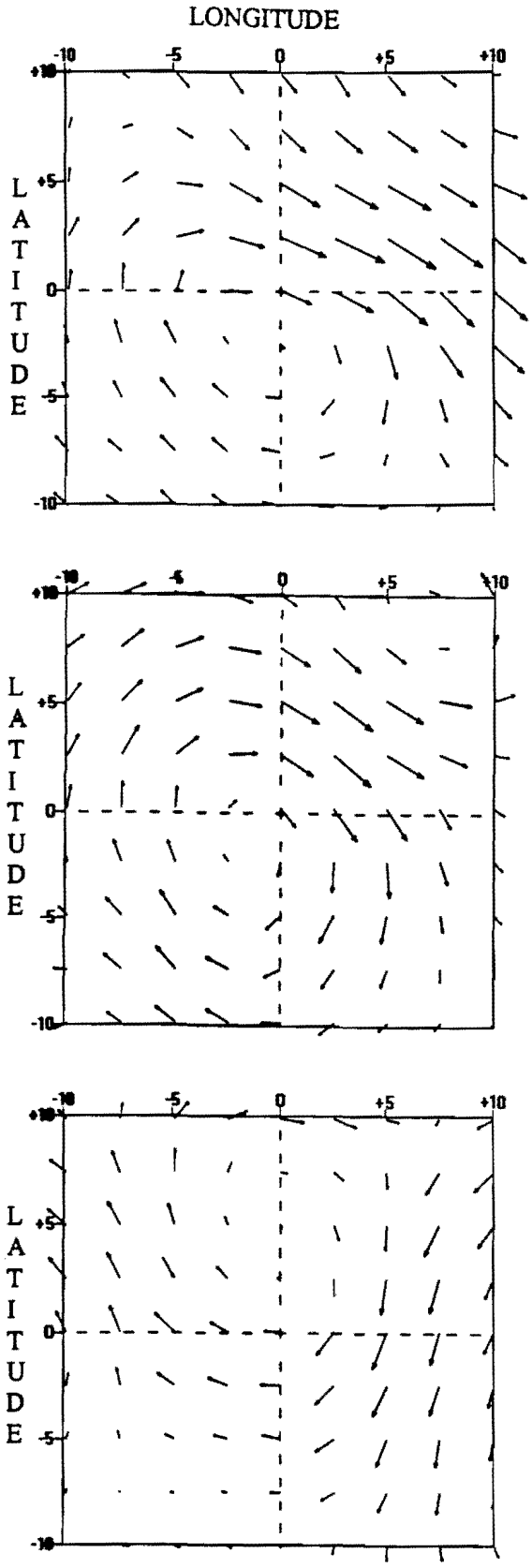

Figure 5-5a,b and c : WM horizontal wind anomaly @ 850 hPa. Vector scale : ⟶ = 10 ms^{-1}.

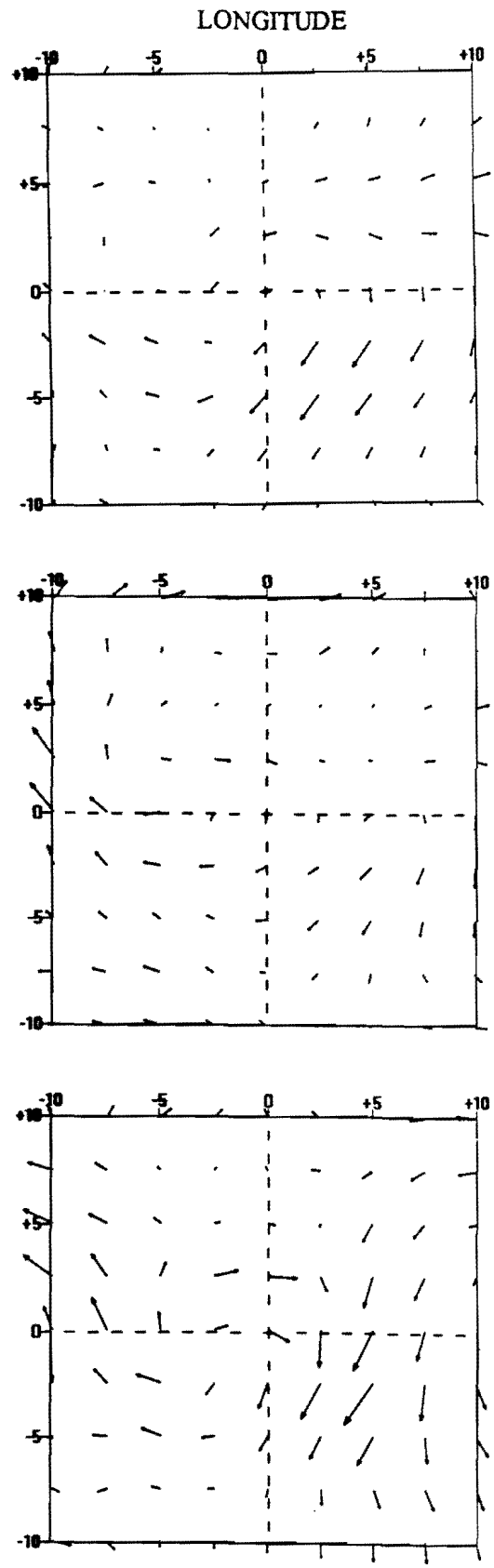

Figure 5-6a,b and c : REC horizontal wind anomaly @ 850 hPa. Vector scale : ⟶ = 10 ms^{-1}.

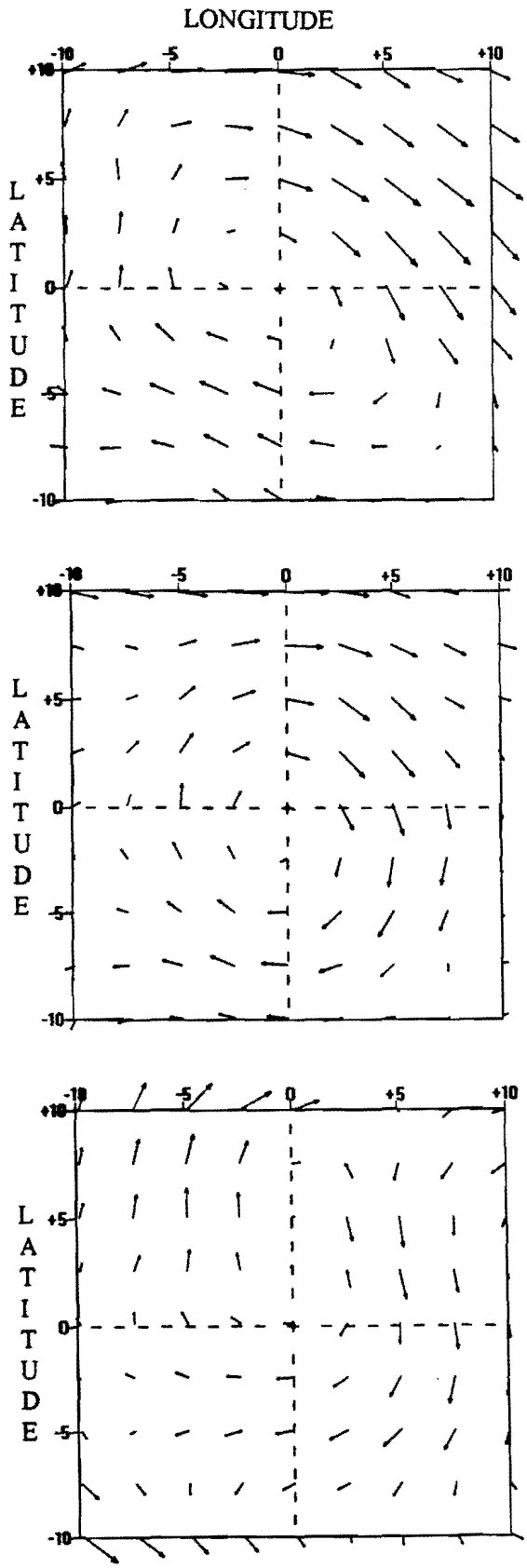

Figure 5-7a,b and c : WM horizontal wind anomaly @ 500 hPa. Vector scale : ⟶ = 10 ms^{-1}.

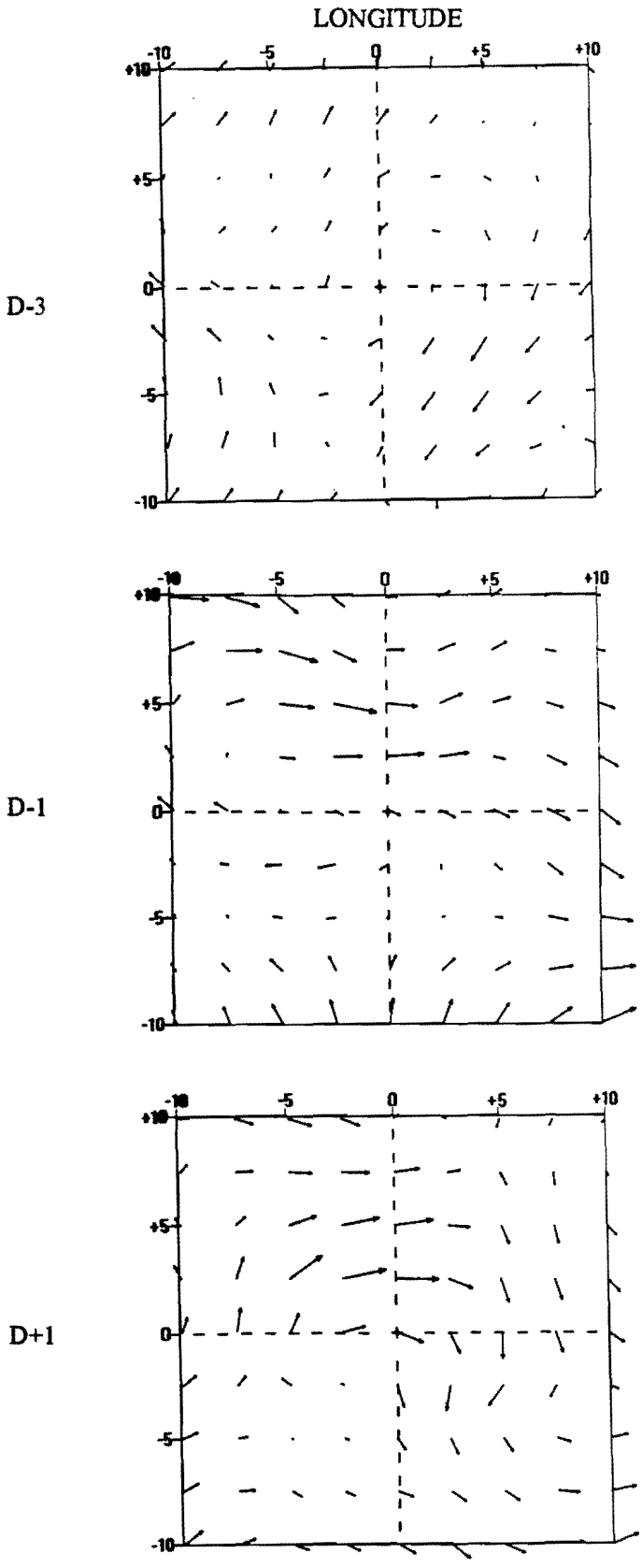

Figure 5-8a,b and c : REC horizontal wind anomaly @ 500 hPa. Vector scale : ⟶ = 10 ms^{-1}.

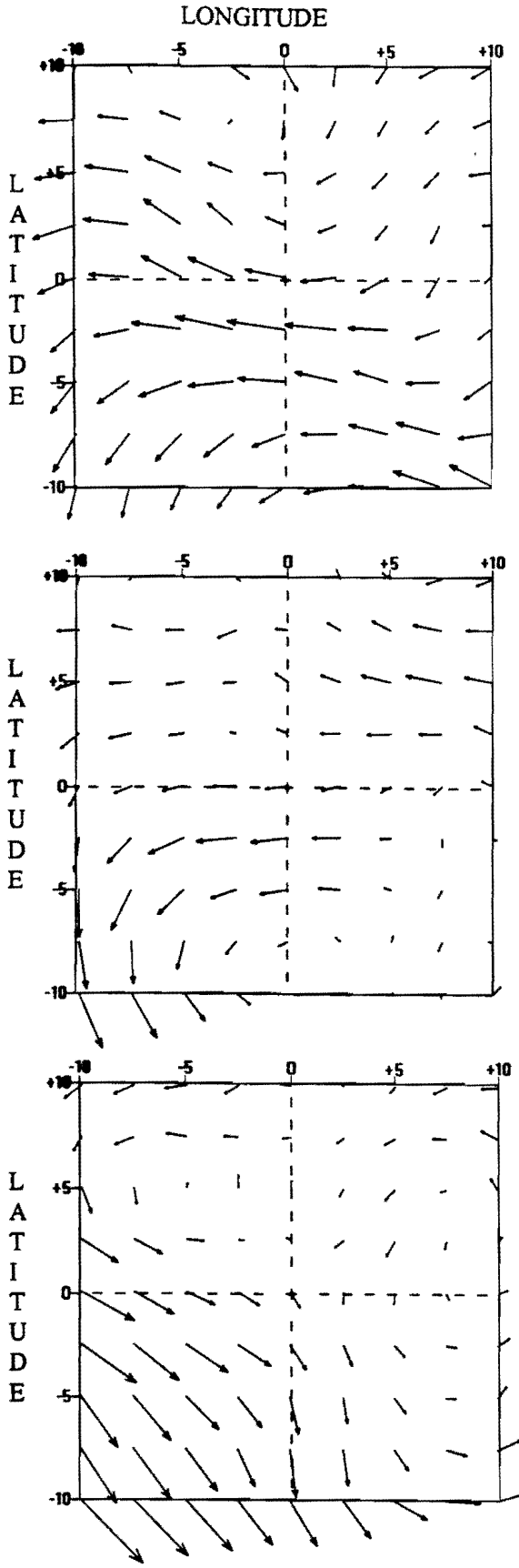

Figure 5-9a,b and c : WM horizontal wind anomaly @ 200 hPa. Vector scale : ⟶ = 10 ms^{-1}.

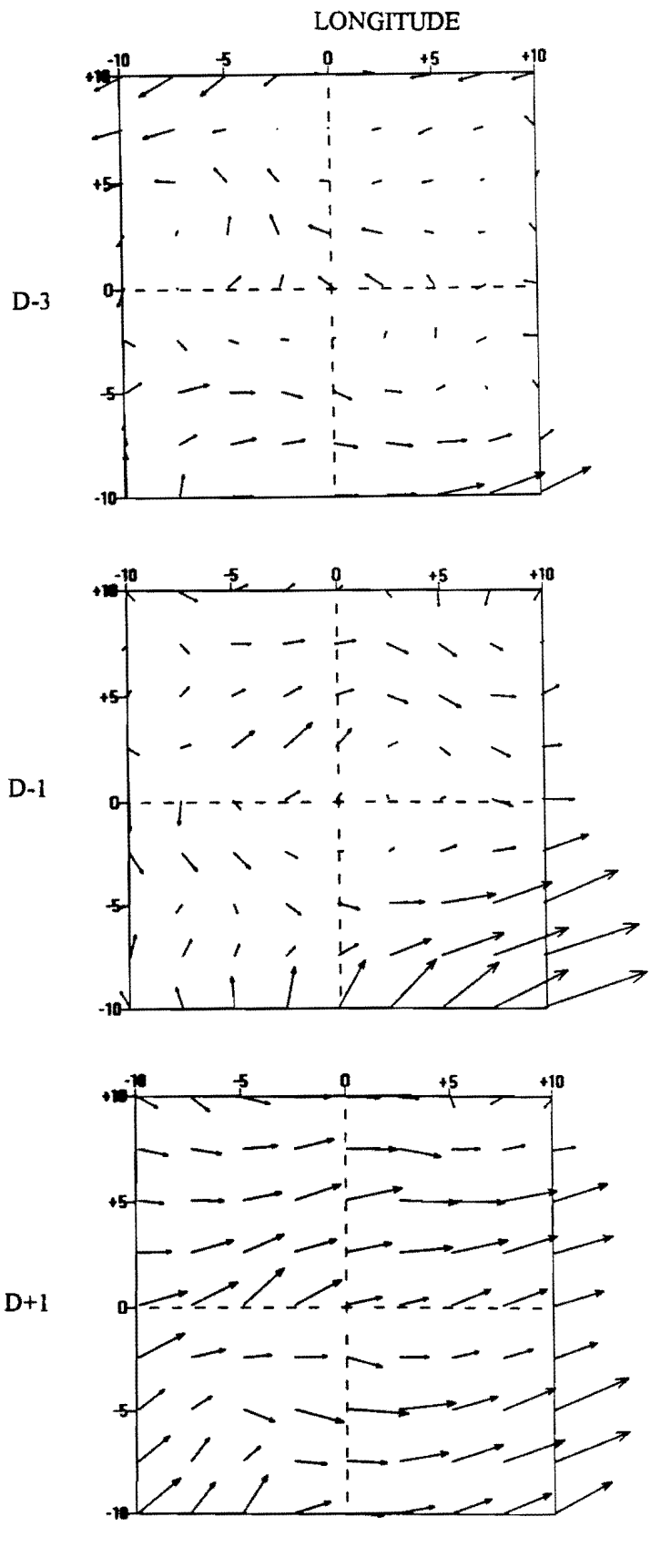

Figure 5-10a,b and c : REC horizontal wind anomaly @ 200 hPa. Vector scale : ⟶ = 10 ms^{-1}.

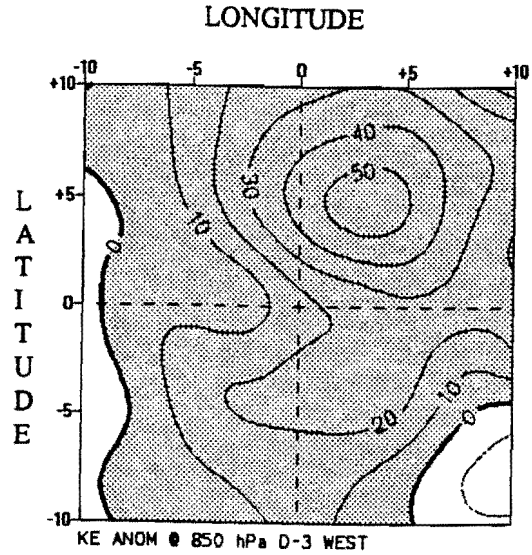

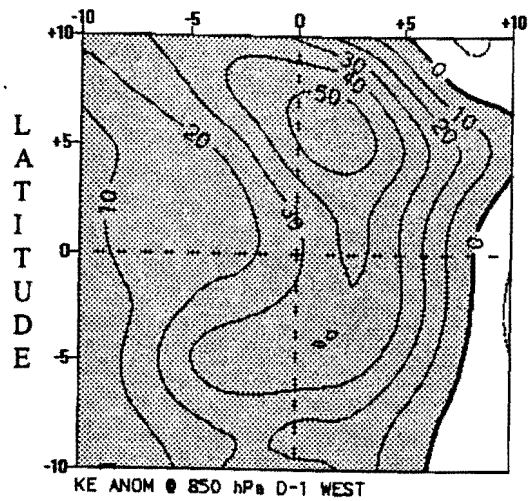

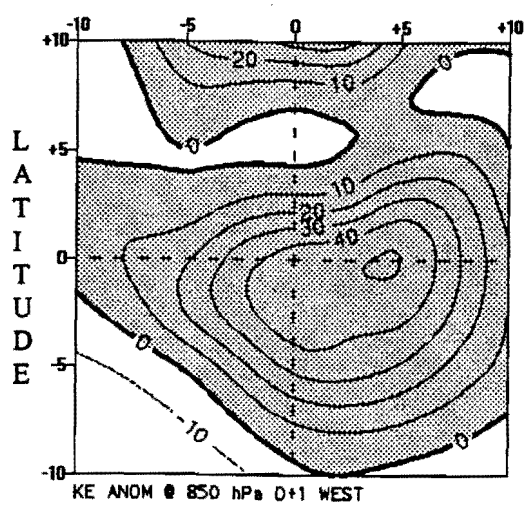

Figure 5-11a,b and c : WM kinetic energy anomaly @ 850 hPa. Contour interval is 10 J kg^{-1}.

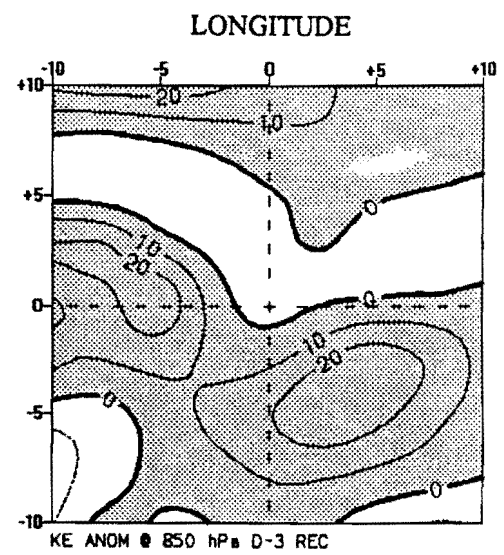

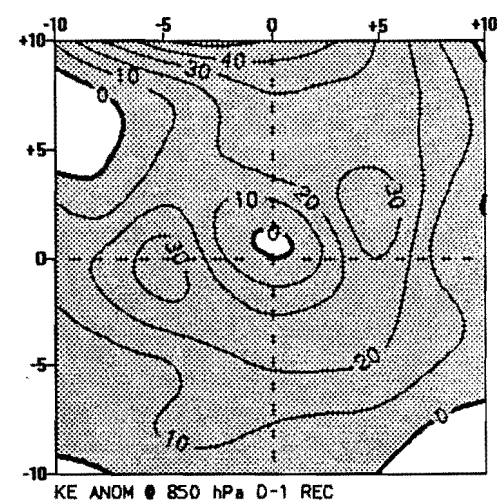

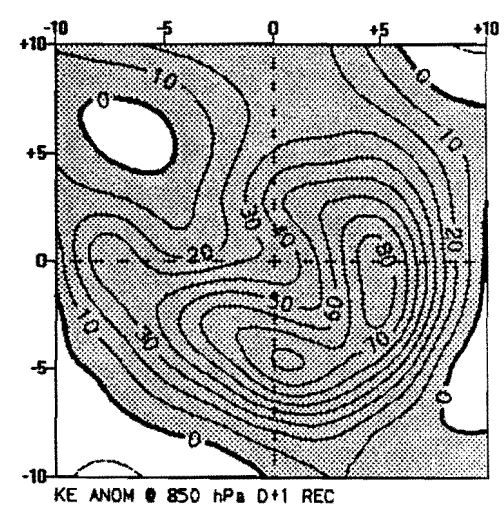

Figure 5-12a,b and c : REC kinetic energy anomaly @ 850 hPa. Contour interval is 10 J kg^{-1}.

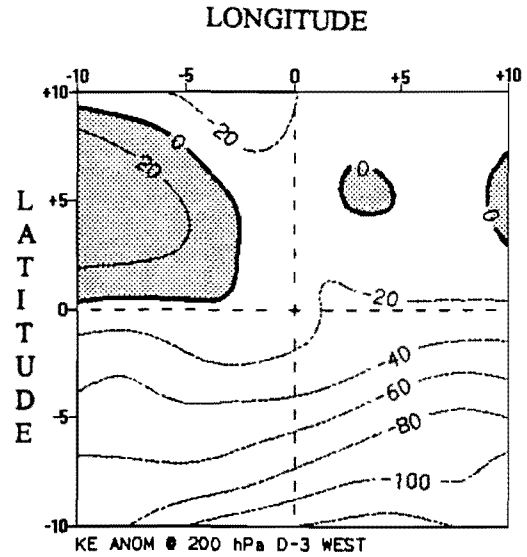

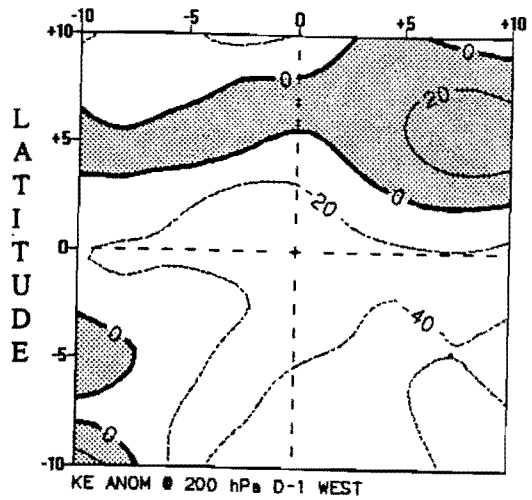

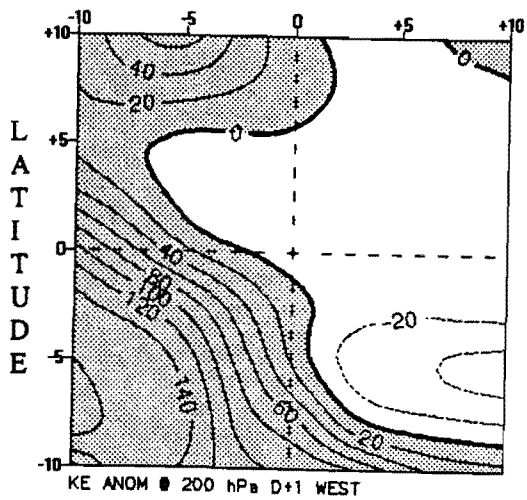

Figure 5-13a,b and c : WM kinetic energy anomaly @ 200 hPa. Contour interval is 20 J kg^{-1}.

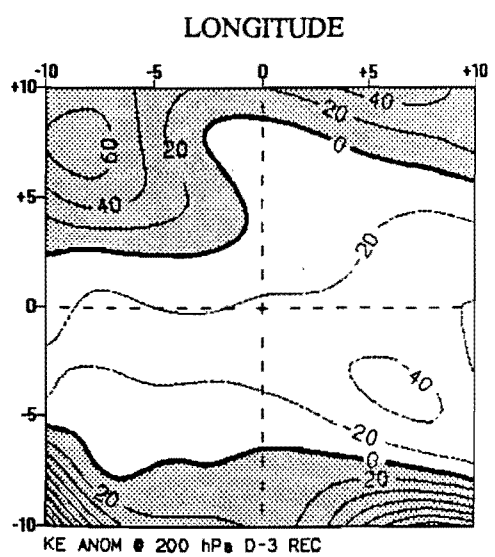

D-3

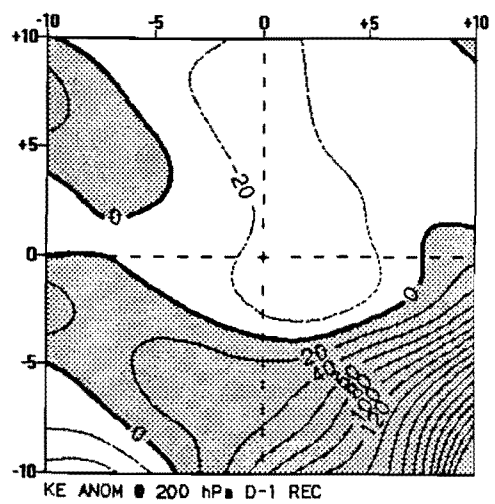

D-1

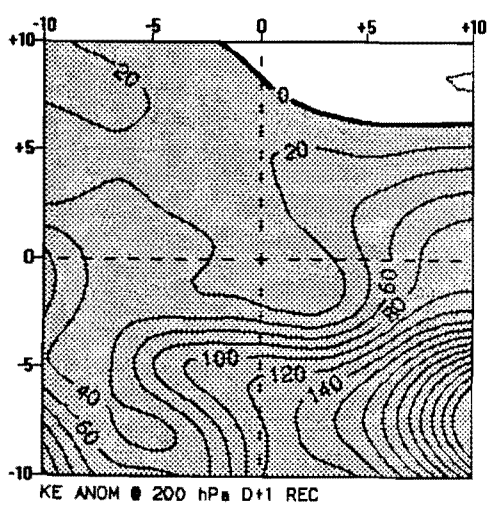

D+1

Figure 5-14a,b and c : REC kinetic energy anomaly @ 200 hPa. Contour interval is 20 J kg^{-1}.

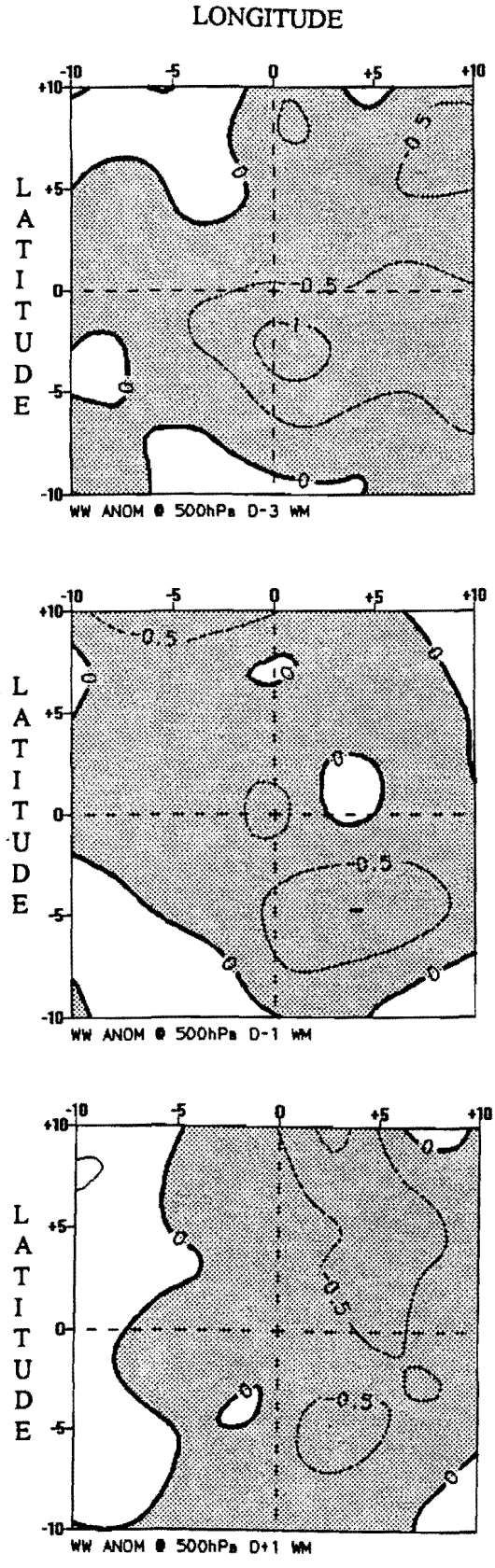

Figure 5-15a,b and c : WM vertical motion anomaly @ 500 hPa. Contour interval is 0.5 Pa s^{-1}.

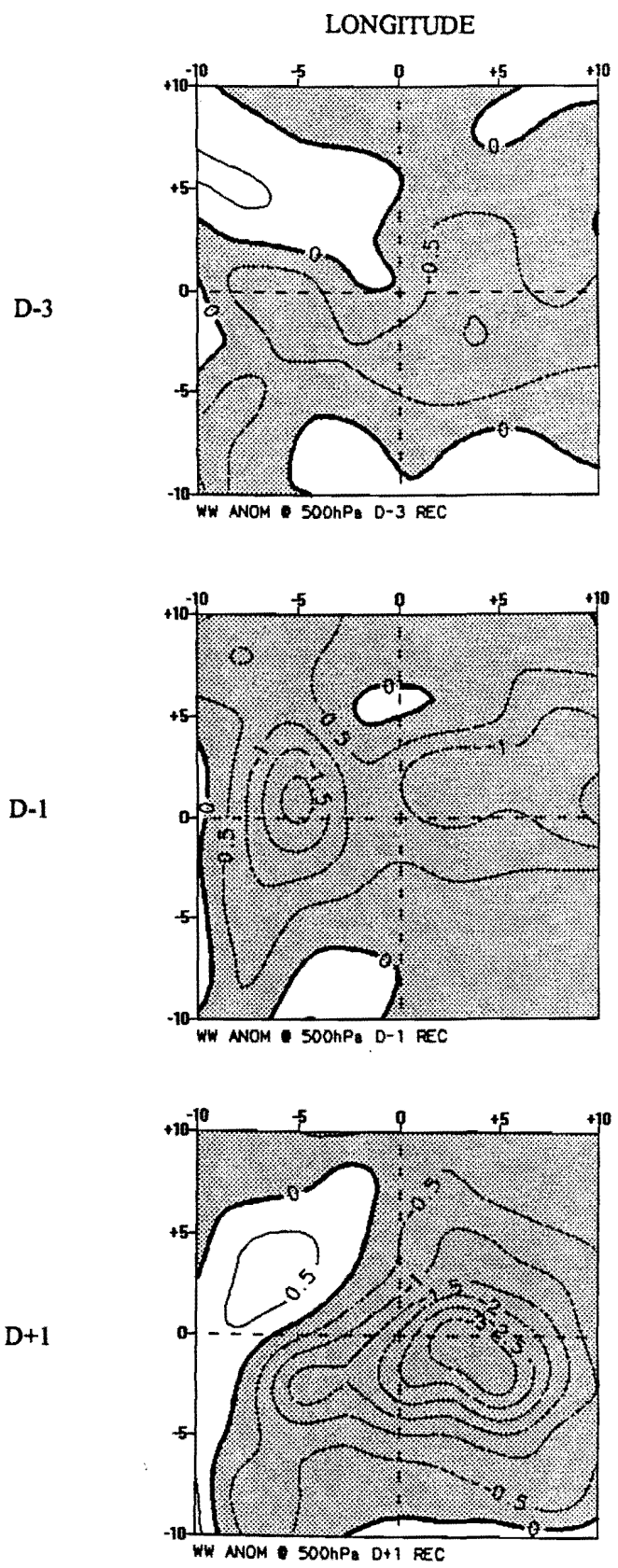

Figure 5-16a,b and c : REC vertical motion anomaly @ 500 hPa. Contour interval is 0.5 Pa s^{-1}.

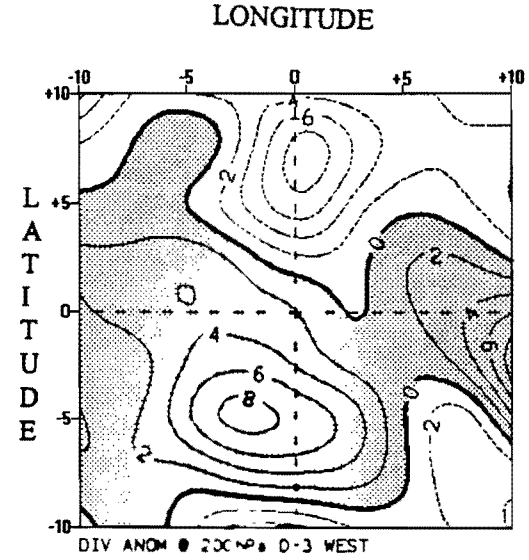

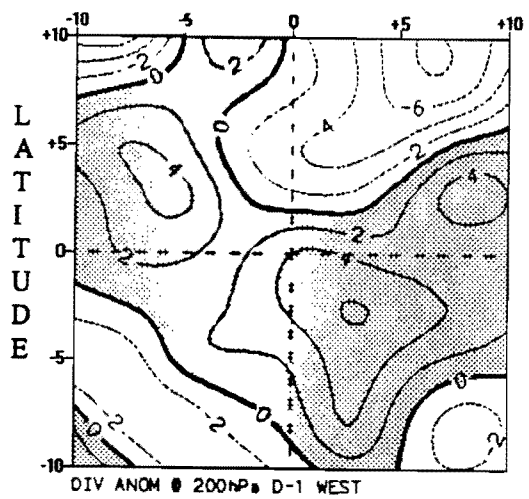

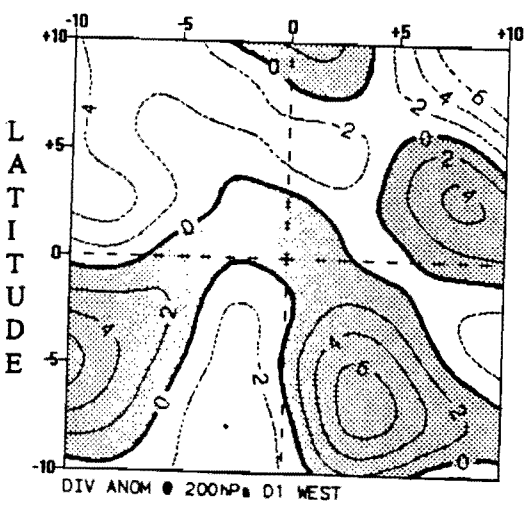

Figure 5-17a,b and c : WM divergence anomaly @ 200 hPa. Contour interval is 2 x 10^{-5} s^{-1}.

D-3

D-1

D+1

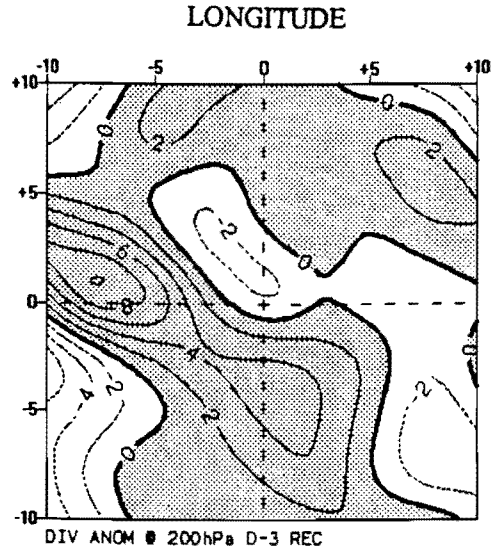

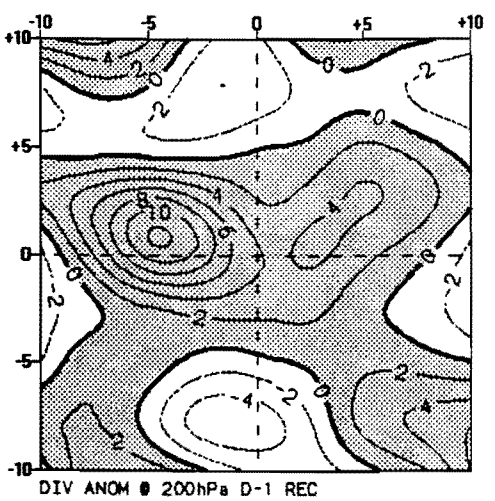

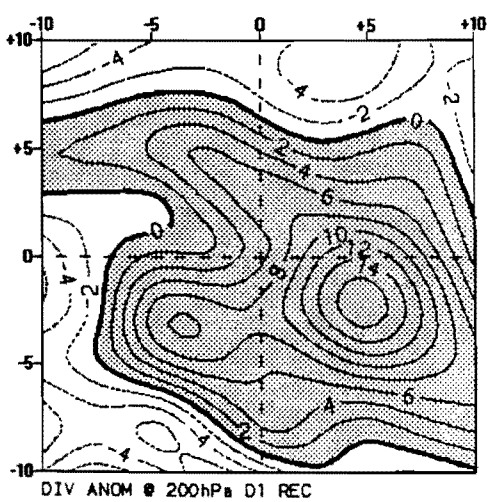

Figure 5-18a,b and c : REC divergence anomaly @ 200 hPa. Contour interval is 2 x 10^{-5} s^{-1}.

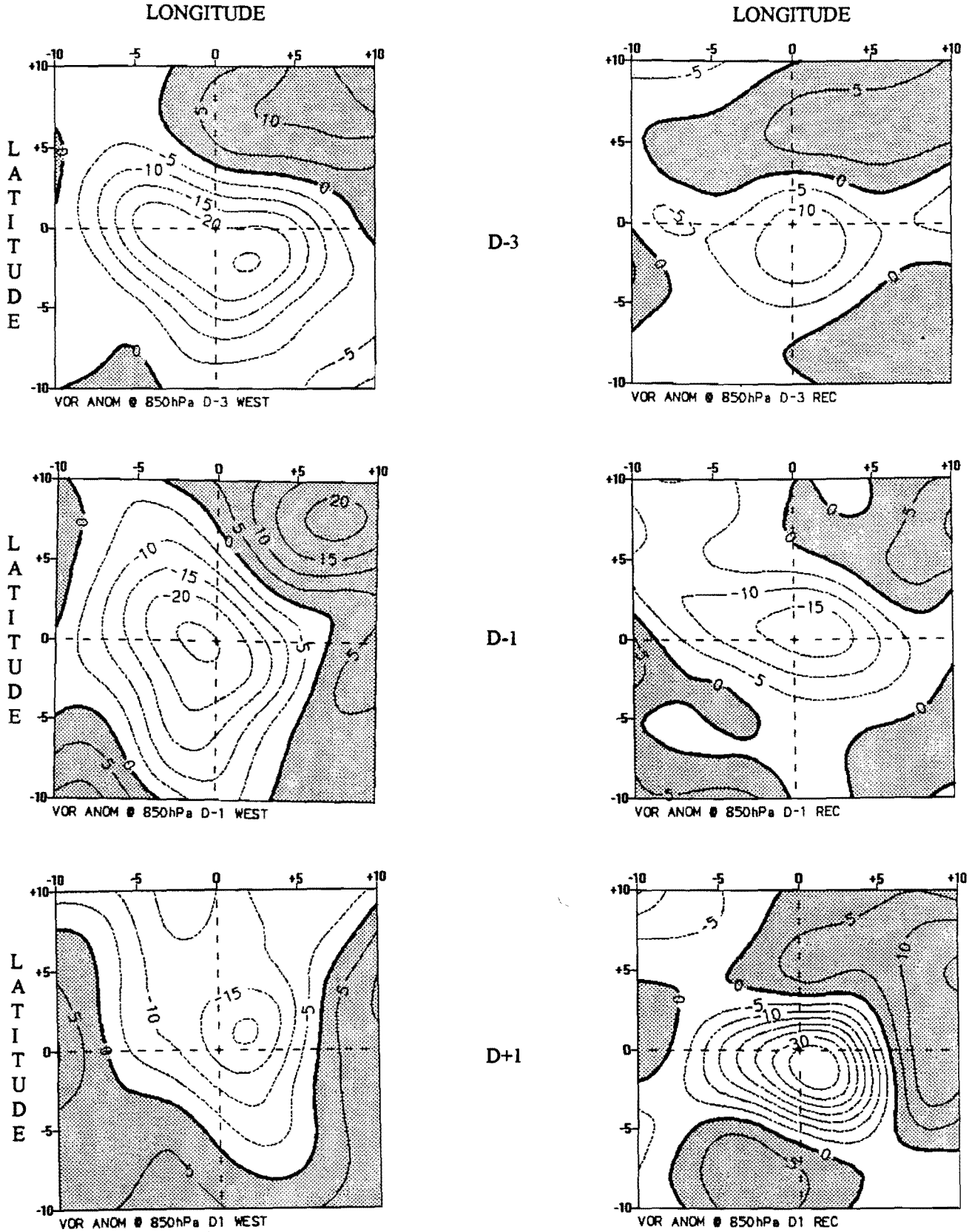

Figure 5-19a,b and c : WM vorticity anomaly @ 850 hPa. Contour interval is 5 x 10^{-5} s^{-1}.

Figure 5-20a,b and c : REC vorticity anomaly @ 850 hPa. Contour interval is 5 x 10^{-5} s^{-1}.

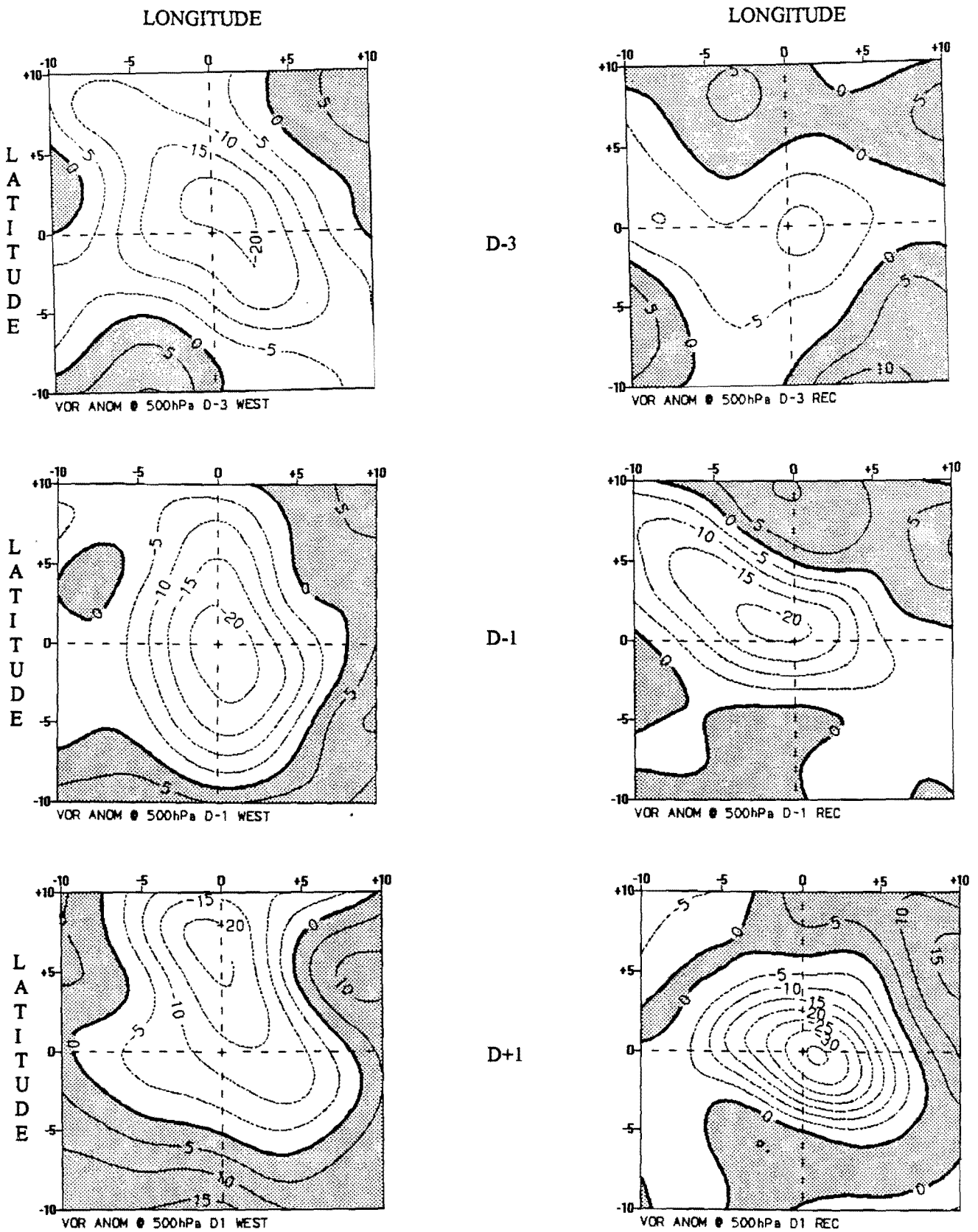

Figure 5-21a,b and c : WM vorticity anomaly @ 500 hPa. Contour interval is 5 x 10^{-5} s^{-1}.

Figure 5-22a,b and c : REC vorticity anomaly @ 500 hPa. Contour interval is 5 x 10^{-5} s^{-1}.

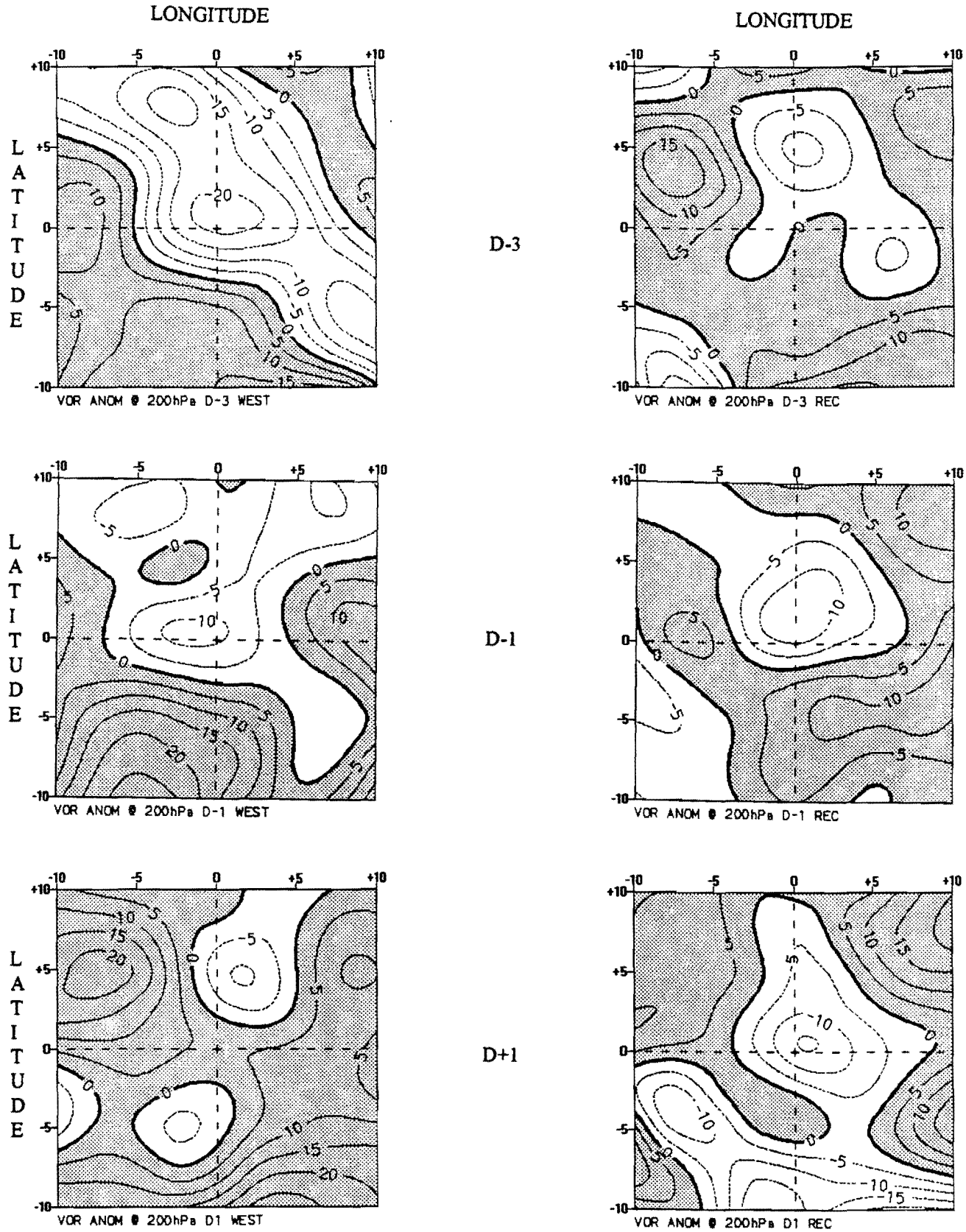

Figure 5-23a,b and c : WM vorticity anomaly @ 200 hPa. Contour interval is 5 x 10^{-5} s^{-1}.

Figure 5-24a,b and c : REC vorticity anomaly @ 200 hPa. Contour interval is 5 x 10^{-5} s^{-1}.

LONGITUDE

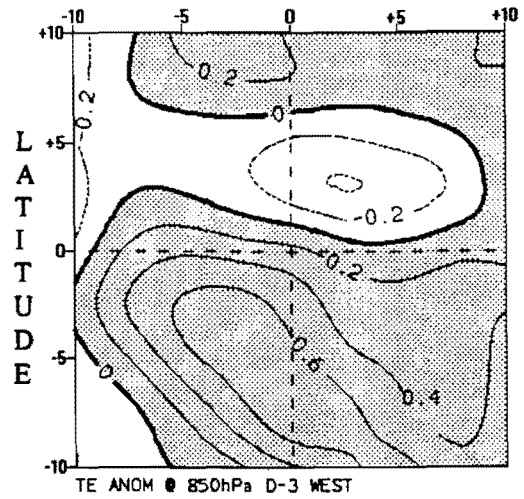

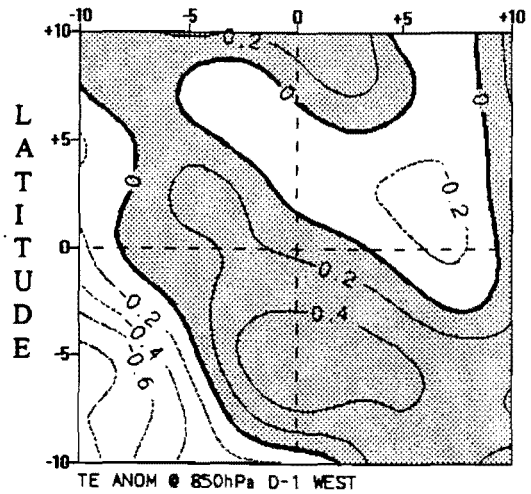

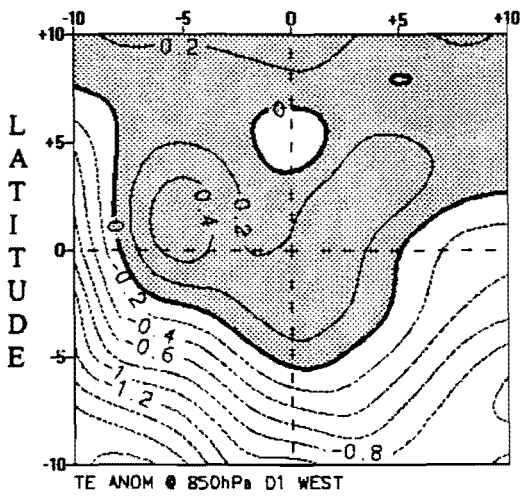

Figure 5-25a,b and c : WM temperature anomaly @ 850 hPa. Contour interval is 0.2 °C.

LONGITUDE

D-3

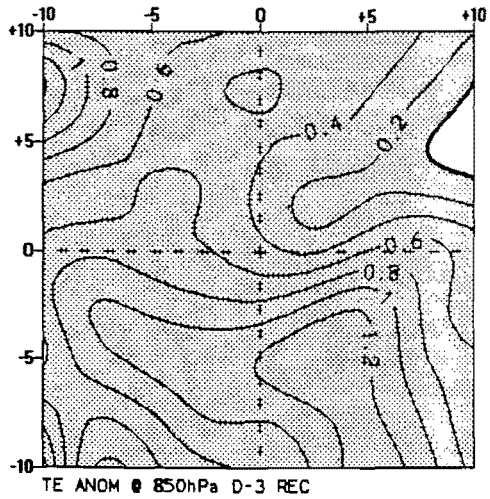

D-1

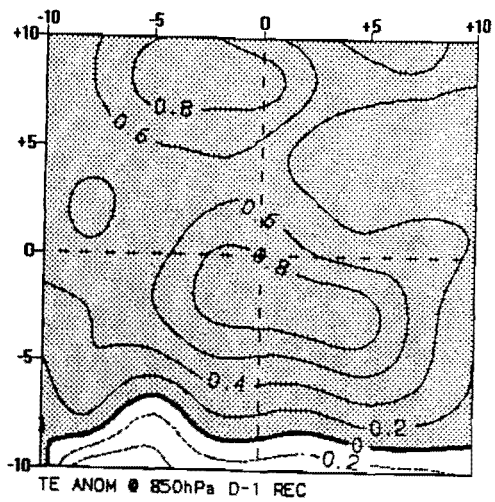

D+1

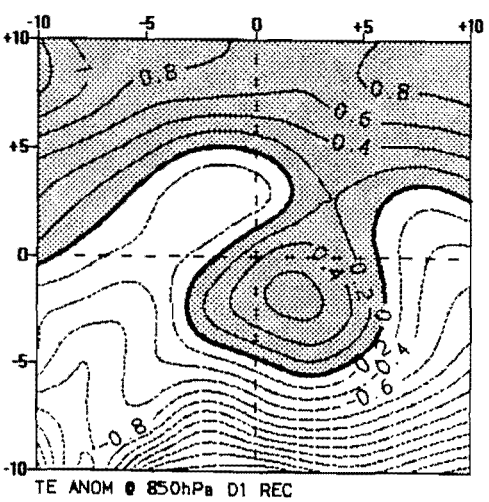

Figure 5-26a,b and c : REC temperature anomaly @ 850 hPa. Contour interval is 0.2 °C.

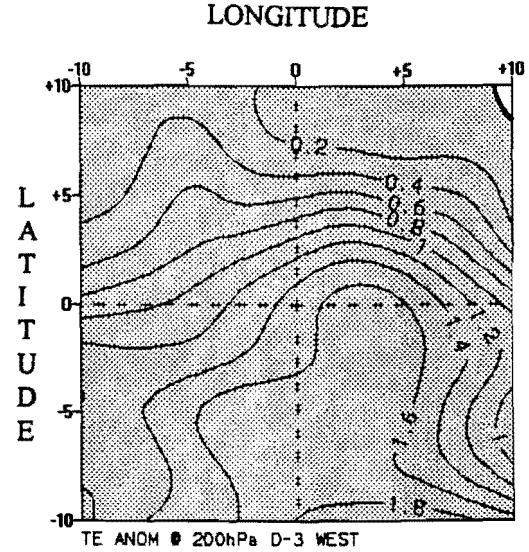

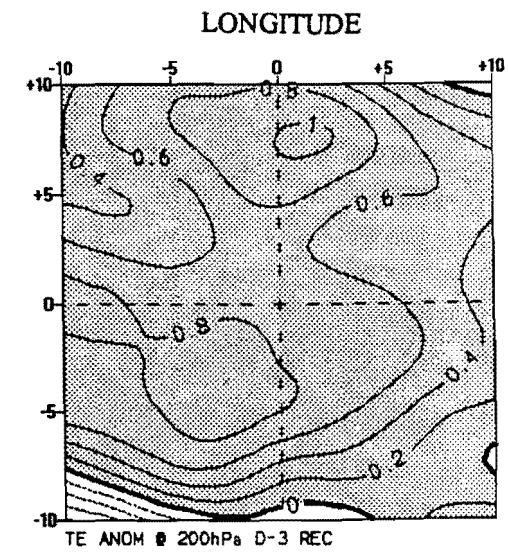

D-3

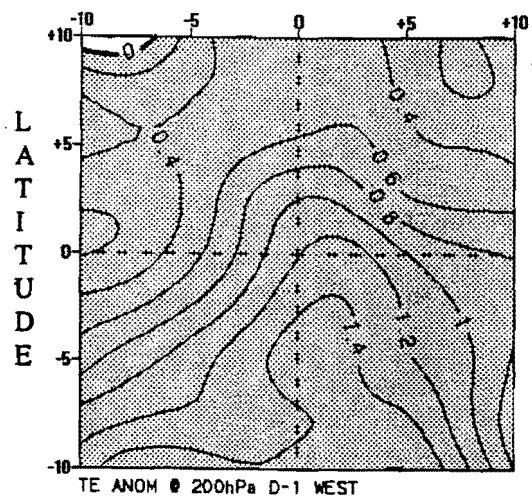

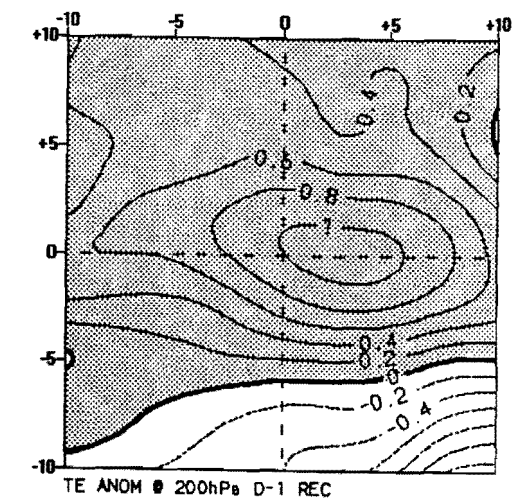

D-1

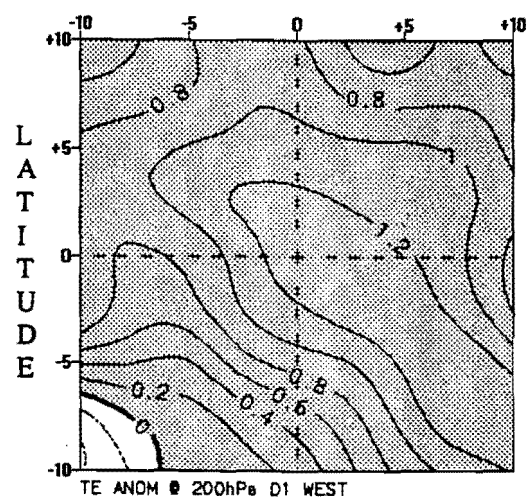

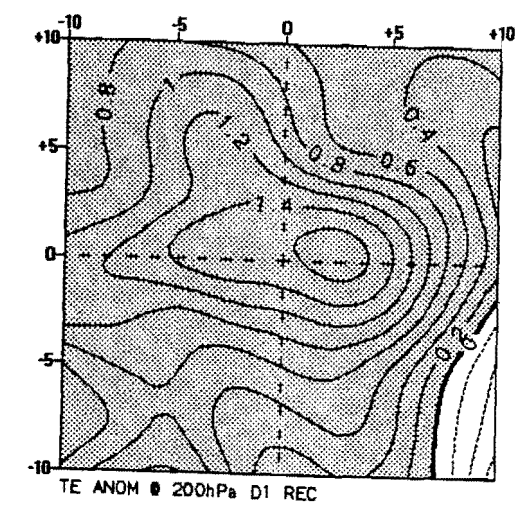

D+1

Figure 5-27a,b and c : WM temperature anomaly @ 200 hPa. Contour interval is 0.2 °C.

Figure 5-28a,b and c : REC temperature anomaly @ 200 hPa. Contour interval is 0.2 °C.

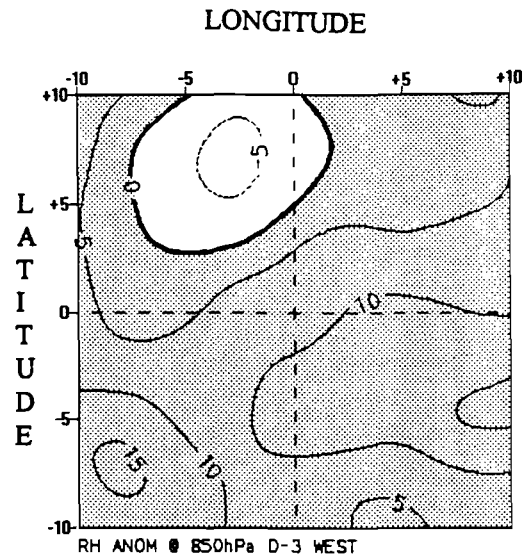

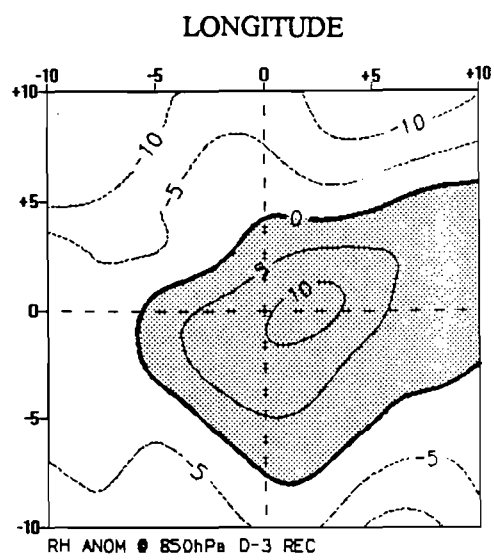

D-3

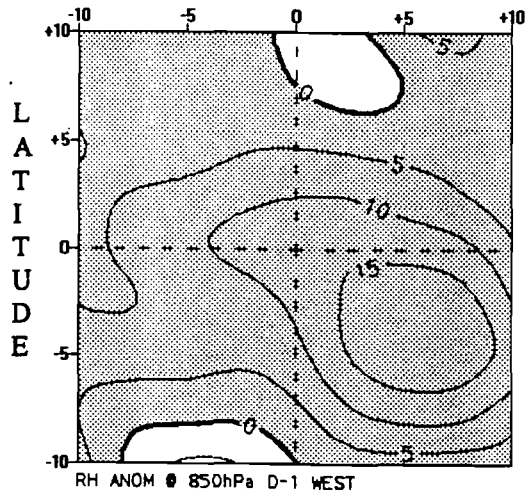

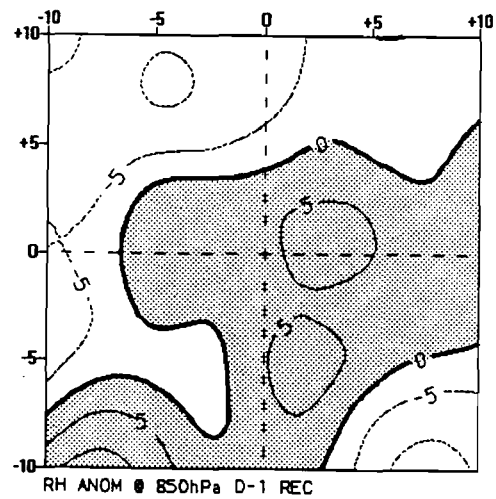

D-1

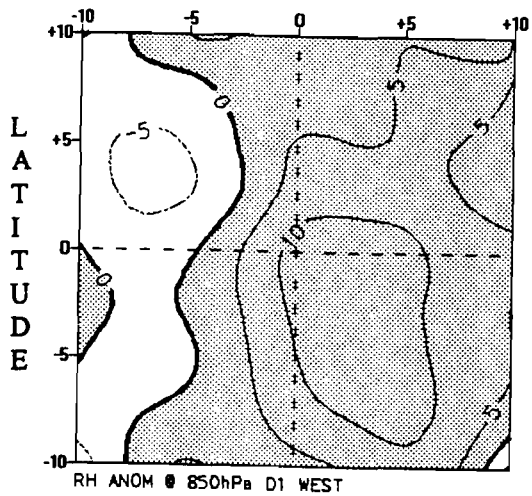

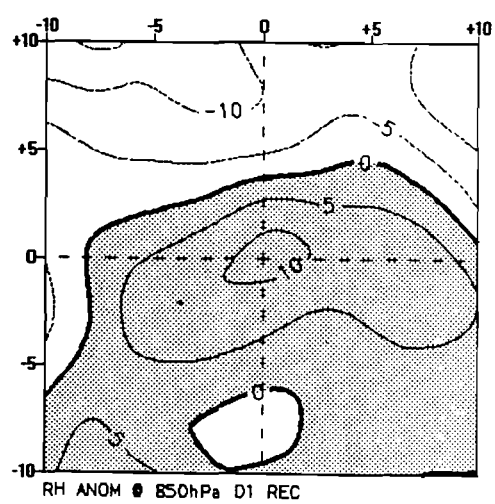

D+1

Figure 5-29a,b and c : WM relative humidity anomaly @ 850 hPa. Contour interval is 5 %.

Figure 5-30a,b and c : REC relative humidity anomaly @ 850 hPa. Contour interval is 5 %.

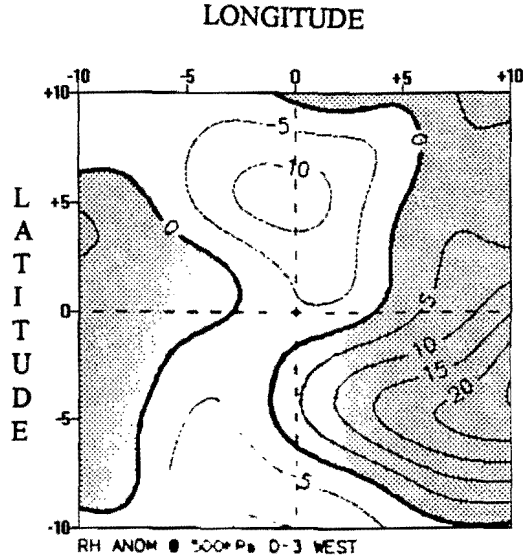

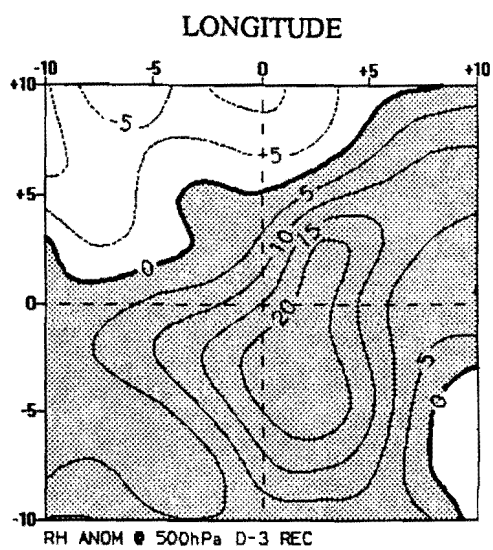

D-3

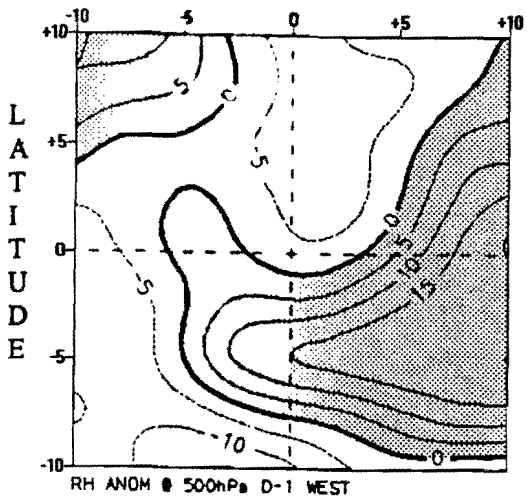

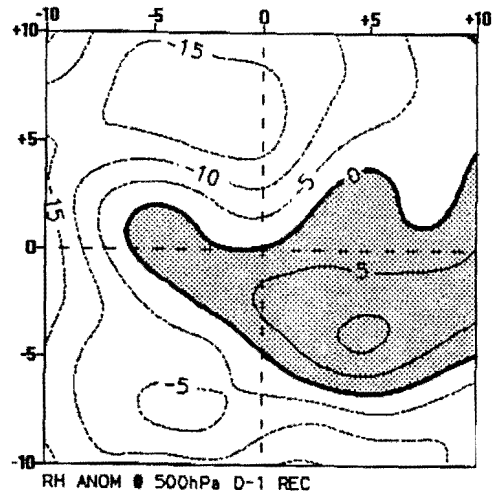

D-1

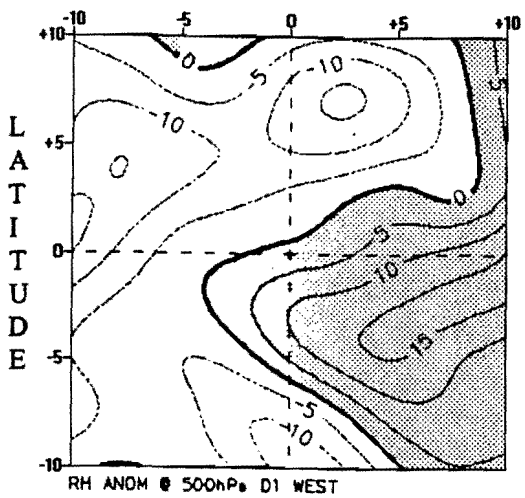

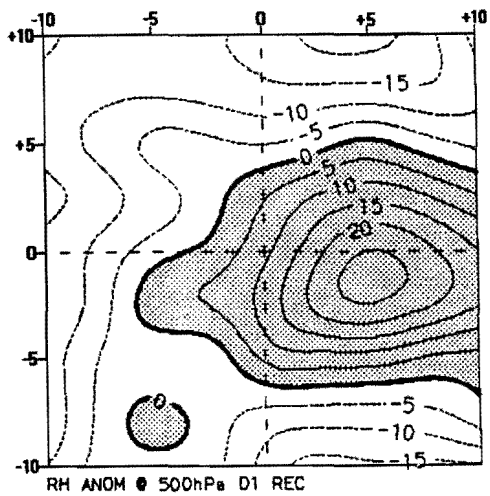

D+1

Figure 5-31a,b and c : WM relative humidity anomaly @ 500 hPa. Contour interval is 5 %.

Figure 5-32a,b and c : REC relative humidity anomaly @ 500 hPa. Contour interval is 5 %.

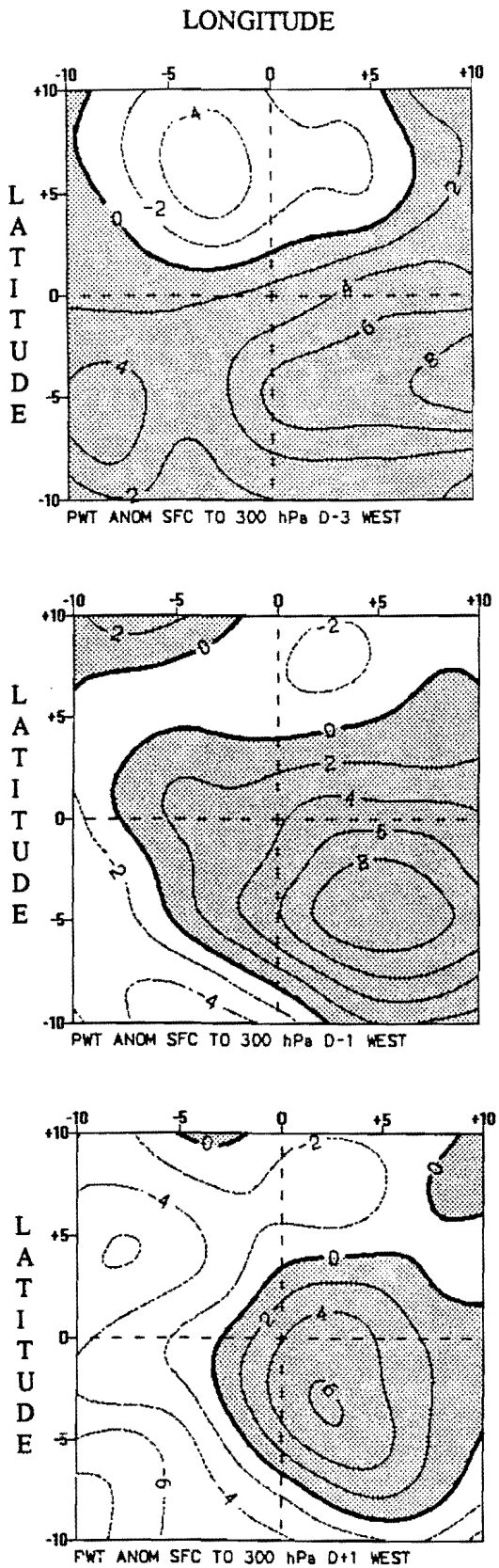

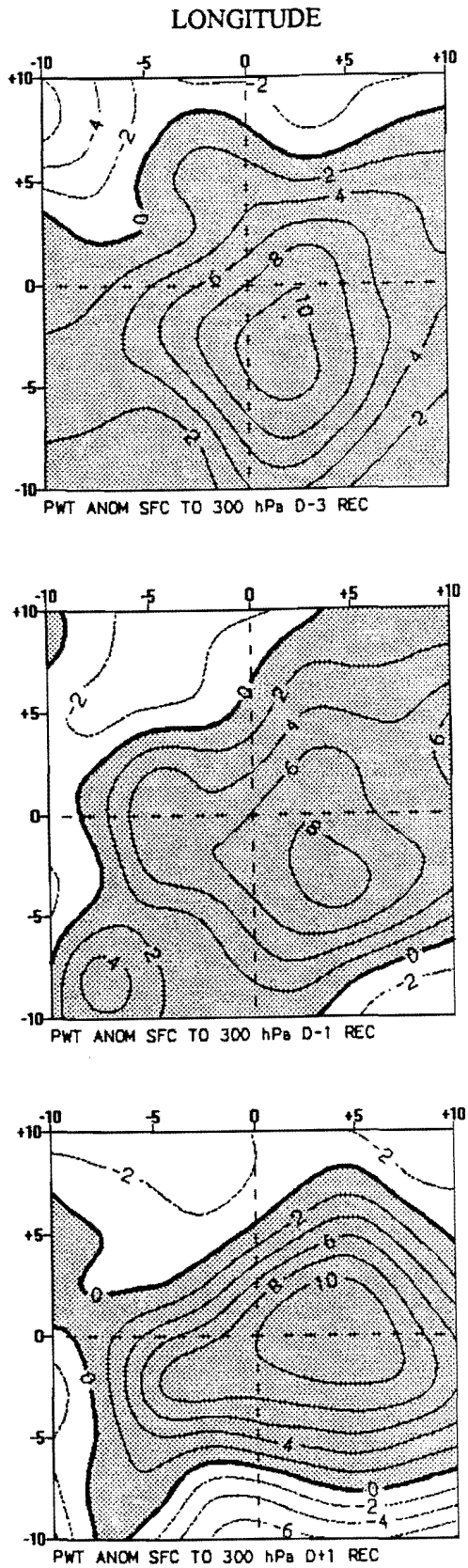

Figure 5-33a,b and c : WM precipitable water anomaly between the surface and 300 hPa. Contour interval is 2 mm.

Figure 5-34a,b and c : REC precipitable water anomaly between the surface and 300 hPa. Contour interval is 2 mm.

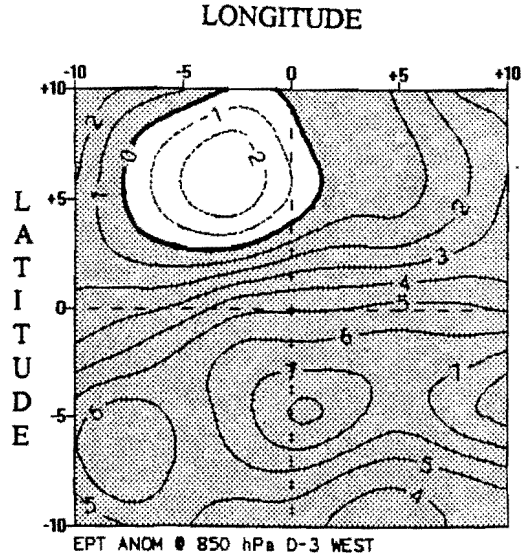

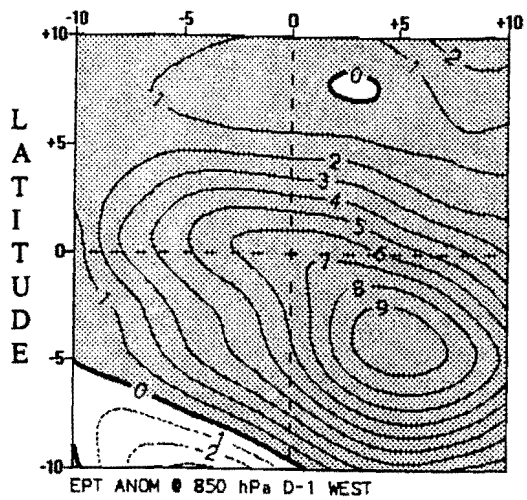

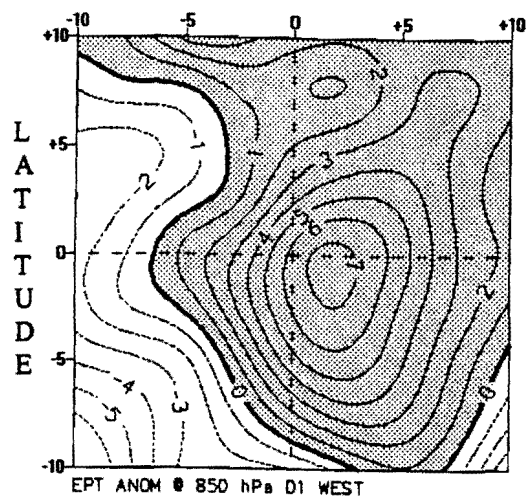

D-3

D-1

D+1

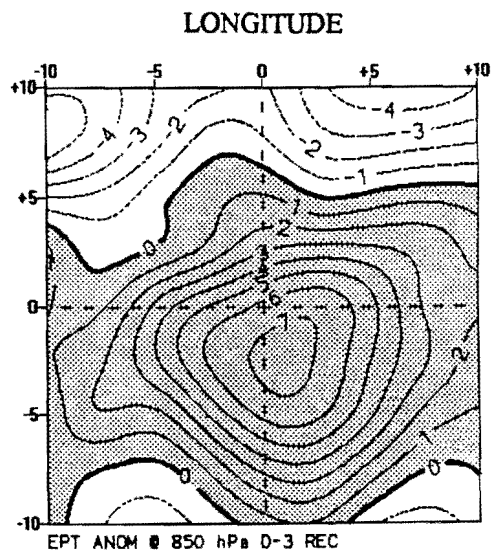

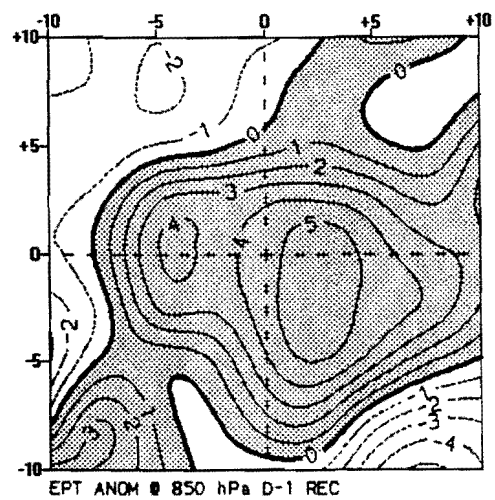

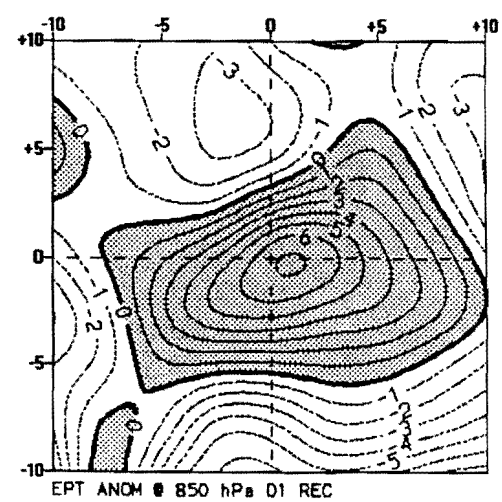

Figure 5-35a,b and c : WM equivalent potential temperature anomaly @ 850 hPa.
Contour interval is 1 °K.

Figure 5-36a,b and c : REC equivalent potential temperature anomaly @ 850 hPa.
Contour interval is 1 °K.

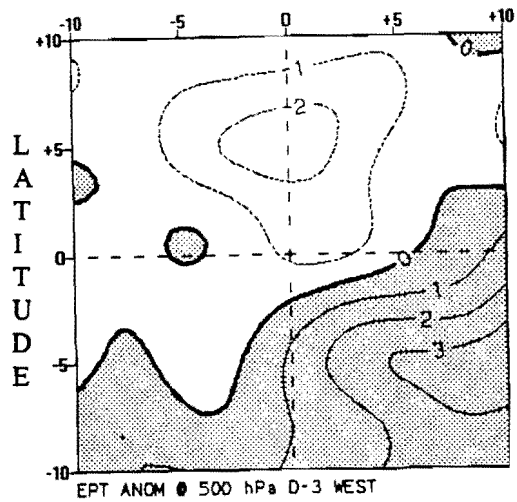

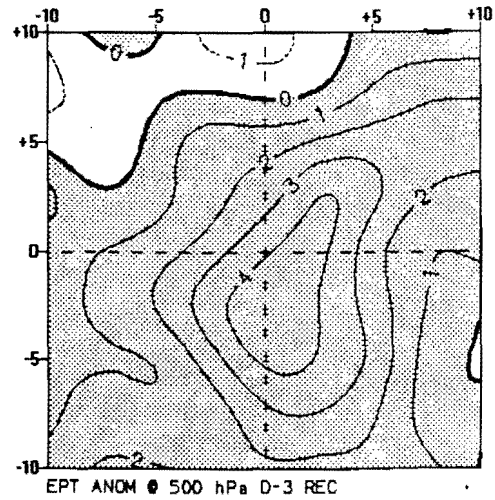

D-3

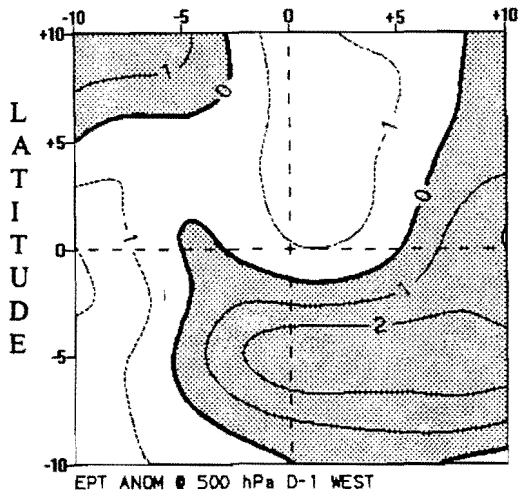

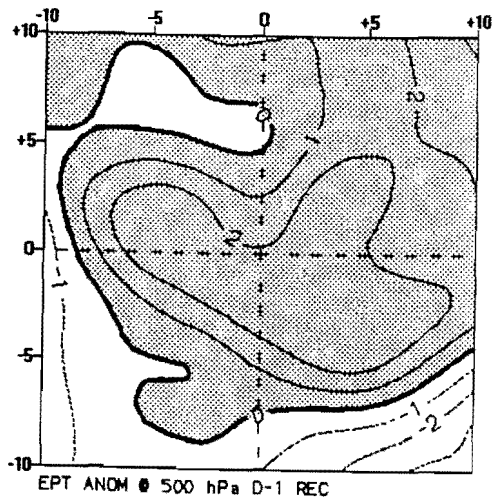

D-1

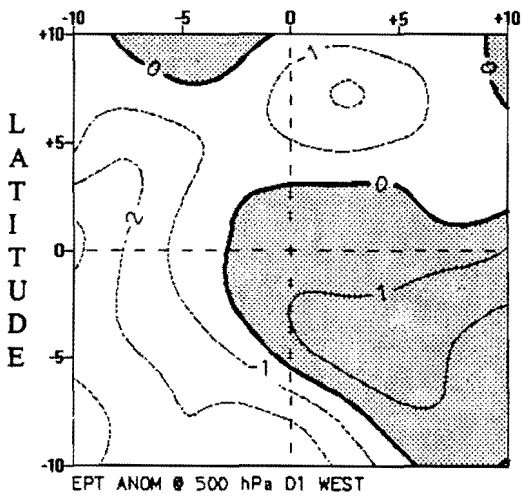

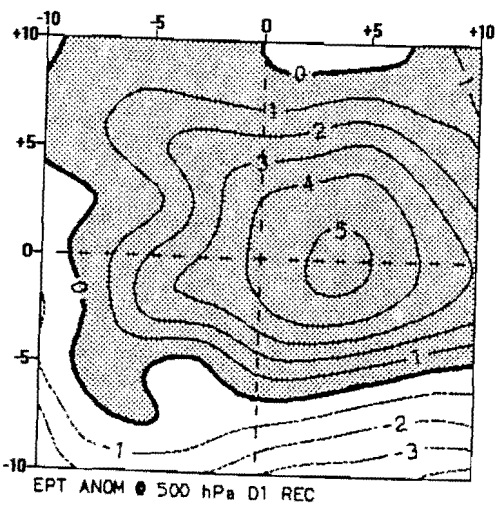

D+1

Figure 5-37a,b and c : WM equivalent potential temperature anomaly @ 500 hPa.
Contour interval is 1 °K.

Figure 5-38a,b and c : REC equivalent potential temperature anomaly @ 500 hPa.
Contour interval is 1 °K.

Chapter 6

DISCUSSION

In this chapter the results presented in previous chapters are reviewed with a view towards answering the questions posed in **Chapter 1**, i.e. the structure of westward and recurving TC's and interaction with the surrounding environment, the evolution of meteorological fields before and after the day of maximum intensity and how these develop our understanding of tropical cyclone maturation in the SW Indian Ocean. Concluding remarks will focus on advances in short-term forecasting capabilities derived from this thesis.

6.1 Discussion

6.1.1 Mauritius rainfall variability

Rainfall at Mauritius during the period 1960 to 1990 exhibits a dominant spectral peak at the annual cycle highlighting the unimodal nature of the rainfall. Three additional oscillations are found at the intra-seasonal scale. The longest of these cycles is of a 44 day length and likely related to Madden-Julian Oscillations observed in the tropics. A stronger cycle with a period of 23.5 days is also present and has been observed in southern African rainfall by Levey (1993), and in poleward propagating OLR departures in the SW Indian Ocean (Anyamba, 1992).

6.1.2 Mean Summer Climatology

The mean summer climatology as calculated from 1987-1992 ECMWF data was found to agree well with previous studies of the region's climatology attained from different data sets (Hastenrath and Lamb, 1979; Hastenrath, 1985; Preston-Whyte and Tyson, 1988; Padya, 1989; Jury, 1993). The kinematic parameters of horizontal wind, vertical movement, upper level divergence and vorticity display characteristic interactions in the region east of Madagascar, from 10° - 20°S, required for TC formation and growth. The ITCZ, on the southern edge of which TC's form, has a strong signature along 10°S. The structure of thermodynamic and moisture parameters: relative humidity, precipitable water, water vapour flux and equivalent potential temperature possess characteristics conducive to the formation of TC's. Strong northern hemisphere winter monsoonal outflow and subtropical easterly inflow converging northeast of Madagascar provides for increased moisture inputs at the ITCZ. The lapse rate of equivalent potential temperature is consistent with convective instability, and is at a maximum along 10°S north of Mauritius.

Madagascar is observed to be a focal point for convective instability with deviations from the zonal 'average' at lower and middle levels for the horizontal wind, vertical movement, vorticity, temperature, relative humidity, water vapour flux and equivalent potential temperature parameters. Topographic interaction with the mean flow is indicated. Heavy rainfall events (> 70 mm) across NW Madagascar were observed to be a result of monsoon surges and TC's (Nassor, 1994). The study revealed that TC's traversing the eastern Mozambique Channel brought proportionally higher rainfall over shorter periods.

6.1.3 Composite TC Structure

The westward moving TC maintains a recognisable and coherent structure throughout the composite sequence. The geopotential height, horizontal wind, horizontal kinetic energy, vertical movement, divergence and vorticity are observed to decrease slightly in strength from the day before to the day after maximum intensity. This reduction in intensity is expected and accompanies TC decay. Due to the compositing effect it was found that the westward moving TC exhibited geopotential gradients, tangential winds, vertical movement, upper level divergence and low and middle level vorticity 20-50% less than TC Firinga, to which comparisons were made.

For the recurving TC a much more 'explosive' type of growth is observed. The value and gradient of most parameters was found to increase dramatically from D-1 to D+1, with peak intensity often observed on the last day of the sequence. The presence of strong westerly winds in the upper troposphere, recognised as a conditions for TC recurvature (Hodanish and Gray, 1993) is seen to be a dominant feature of the recurving TC on D-1 and D+1.

Recognising that individual TC's possess characteristics similar to the composite TC, the possibility of using these results for track prediction is possible. **Table 6-1** outlines the differences and similarities encountered between the westward moving and recurving composites. Assessment of SW Indian Ocean TC's relative to this table will improve short-term forecast capabilities by recognising the structural features which precede and accompany recurvature.

Table 6-1

Guidelines to distinguish westward moving from recurving TC's

PARAMETER	WM TC	REC TC
Geopotential	$P850_{min}$: 1465 gpm on D-3 $P200_{min}$: 12450 gpm on D+1	$P850_{min}$: 1450 gpm on D+1 $P200_{min}$: 12455 gpm on D-3
	WM weakens, REC strengthens	
Horizontal Wind	$P850_{max}$: > 10 m s^{-1} on D-3 $P200_{max}$: > 15 m s^{-1} on D+1	$P850_{max}$: 10 m s^{-1} on D+1 $P200_{max}$: > 23 m s^{-1} on D-1
	cyclonic structure for WM, strong winds shift NE to SE cyclonic structure for REC, only on D+1 upper westerlies in front of WM	
Kinetic Energy	$P850_{max}$: 70 J kg^{-1} on D-1 $P200_{max}$: 280 J kg^{-1} on D+1	$P850_{max}$: 100 J kg^{-1} on D+1 $P200_{max}$: >300 J kg^{-1} on D+1
	Strength doubles for REC, D-3 to D+1	
Vertical Movement	$P500_{max}$: -1.2 Pa s^{-1} on D-3	$P500_{max}$: -3 Pa s^{-1} on D+1
	Decreases for WM, REC intensity increases 3-fold	
Upper Divergence	$P200_{max}$: +8 x 10^{-5} s^{-1} on D-3	$P200_{max}$: +10 x 10^{-5} s^{-1} on D+1
	WM decreases, REC increases	
Vorticity	$P850_{max}$: -30 x 10^{-5} s^{-1} on D-1 $P200_{max}$: +30 x 10^{-5} s^{-1} on D-1	$P850_{max}$: -40 x 10^{-5} s^{-1} on D+1 $P200_{max}$: +20 x 10^{-5} s^{-1} on D-1
	increased low-level cyclonic vorticity for REC, constant for WM upper anticyclonic vorticity increased depth for REC, equatorward tilt for WM	
Precipitable Water	Max : 57 mm on D-1	Max : 62 mm on D+1
	REC areal extent larger input from east	
Equivalent Potential Temperature	$P850_{max}$: 346 °K on D-1 $P500_{max}$: 337 °K on D-1	$P850_{max}$: 346 °K on D+1 $P500_{max}$: 341 °K on D+1
	constant for WM and REC upper level REC higher than WM	
SYNTHESIS	**Upper level trough acts as an 'attractor' WM steady, REC intensifying**	

It is notable that both composite TC centres shift poleward by > 10° latitude. Poleward movement of the WM composite exceeds the REC composite by 2.5°, resulting in a greater increase in coriolis for the WM TC (1.5-times). Because

background zonal easterly flow is weak, sub tropical troughs act as 'attractors' of SW Indian Ocean TC's, more so than has been seen in other TC regions.

6.1.4 TC Anomaly

Previous research on TC recurvature has shown that the study of environmental wind fields poleward of cyclones are important for determining if TC's remain on a westward track or recurve. Work by George and Gray (1976) revealed that changes in zonal flow produce noticeable changes in track. Penetration of upper environmental westerly flow 8° - 20° poleward and west of the cyclone centre increased as the TC approached the point of recurvature in the NW Pacific. Horizontal wind and kinetic energy anomalies at the 200 hPa surface were found to be more intense for the recurving than the westward moving TC in this study. The results demonstrate that recurvature is accompanied by intensification of the system, exhibited in low level time tendencies of various meteorological fields.

In conclusion rather than consider mid-level wind fields for steering of TC's, it is suggested that forecasters study the manner in which sub tropical troughs and attendant westerly winds in the upper troposphere relate to subsequent changes in TC motion. This is especially relevant when it is considered that the recurving composite grows from a weak system on D-3 to an intense system within five days. Initiation of strong westerlies at the upper levels appears to trigger the growth of the recurving TC by the creation of an effective anticyclonic 'evacuation' mechanism for the mass overturning. On the other hand, upper westerlies are associated with TC decay for the westward moving composite.

Although a limited number of cases were used in the production of the TC composites, the potential for exploiting the results for improved short-term forecasting exists. Studies of individual destructive TC events using direct high resolution data, i.e. satellite microwave rainfall rate and scatterometer winds, longer ECMWF time sections (to D-7) and additional derived meteorological parameters need to be undertaken to investigate the mechanisms initiating TC intensification and track changes in the SW Indian Ocean.

REFERENCES

Anthes, R. A., 1982: Tropical cyclones, their evolution, structure and effects, *Met. Mon. 19*, 41, American Meteorological Society, Boston, 208 pp.

Anyamba, E. K., 1992: Some properties of a 20-30 day oscillation in tropical convection. *J. Afr. Met. Soc.*, 1, 1-19.

Anyamba, E. K., Kianga, P. M. R., and Patniak, J. K., 1982: The mean horizontal motions over the African atmosphere during the southern summer. *Proc. Tech. Conf. Climate Africa*, WMO 596, Tanzania, 158 - 170.

Appadu, S. N. S., and Goolaup, P., 1991: Cyclone season of the SW Indian Ocean 1990 - 1991, *Tech. Rep. CS 14*, Mauritius Met. Services, Vacoas, Mauritius.

Appadu, S. N. S., and Ragoonadeen, S., 1989a: Cyclone season of the SW Indian Ocean 1987 -1988, *Tech. Rep. CS 11*, Mauritius Met. Services, Vacoas, Mauritius.

Appadu, S. N. S., and Ragoonadeen, S., 1989b: Cyclone season of the SW Indian Ocean 1988 -1989, *Tech. Rep. CS 12*, Mauritius Met. Services, Vacoas, Mauritius.

Appadu, S. N. S., and Ragoonadeen, S., 1990: Cyclone season of the SW Indian Ocean 1989 -1990, *Tech. Rep. CS 13*, Mauritius Met. Services, Vacoas, Mauritius.

Arkin, P. A., Konsky, V. E., Janowiak, J. E., and O'Lenic, E. A., 1986; Climate Analysis Center NOAA Atlas 7, Nat. Met. Ctr., Washington DC, 8 pp. + 85 Figs.

Asnani, G. C., 1993: *Tropical Meteorology : Volume 2*, Indian Institute of Tropical Meteorology, Pune, 1202 pp.

Bannister, A. J., and Smith, K. J., 1993: The South Pacific and southeast Indian Ocean tropical cyclone season 1990 - 1991, *Aust, Met. Mag.*, 42, 175 - 182.

Bengston, L. and Shukla, J., 1988: Integration of Space and In Situ Observations to study Global Climate Change, *Bull. Am. Met. Soc.*, 69, 10, 1130 - 1143.

Bolton, D., 1980: The computation of Equivalent Potential Temperature, *Mon, Wea. Rev.*, 108, 1046 - 1053.

Challa, M., and Pfeffer, P. L., 1990: Effects of eddy fluxes of angular momentum on model hurricane development, *J. Atmos. Sci.*, 37, 1603 - 1618.

Charney, J., and Eliassen, A., 1964: On the growth of the hurricane depression, *J. Atmos. Sci.*, 21, 68 - 75.

Dennet, M. D., 1978: Variations of rainfall and seasonal forecasting in Mauritius, *Arch. Met. Geophy. Biokl.*, B, 25, 359 - 370.

Ecomier, J., 1992: *Cyclones Tropicaux du Sud-ouest de l'Ocean Indien.* Reunion Meteorological Service. Meteo France. 480 pp.

Elsberry, R. L., 1987: Tropical cyclone motion, *A Global View of Tropical Cyclones*, R. L. Elsberry, W. M. Frank, G. J. Holland, J. D. Jarrell, and R. L. Southern, Eds., ONR Marine Meteorology Program, 185 pp.

Elsberry, R. L., and Abbey, R. F., 1991: Recent advances in understanding tropical cyclone motion. Naval Post Graduate School Interim Report for the Office of Naval Research, Code 1122MM, 92 pp.

Evans, J. L., 1991: Tropical cyclone sensitivity to sea-surface temperature, *19th Conf. On Hurricanes and Tropical Meteorology*, Miami, Am. Meteorol. Soc., 471 - 477.

Gentry, C., 1983: Forecasting tropical cyclone recurvature with upper tropospheric winds, NASA Tech. Memor. 85114.

George, J. E., and Gray, W. M., 1976: Recurvature and non-recurvature as related to surrounding wind/height fields, *J. Appl. Met.*, 16, 34 - 42.

Gore, R., 1993: Andrew Aftermath, *National Geographic Magazine*, 183, 4, 2 - 37.

Gray, W. M., 1968: Global view of the origin of tropical disturbances and storms, *Mon. Weather Rev.*, 96, 669 - 700.

Gray, W. M., 1979: Hurricanes: Their formation, structure and likely role in the tropical circulation. *Meteorology over the tropical Oceans*, D. B. Shaw, Roy. Met. Soc., 278 pp.

Gray, W. M., 1984: Atlantic seasonal hurricane frequency, I: El Niño and 30 mb quasi-biennial oscillation influences, *Mon. Weather Rev.*, 112, 1649 - 1668.

Gray, W. M., and Landsea, C. W., 1992: African rainfall as a precursor of hurricane-related destruction on the U. S. East Coast, *Bull, Am. Meteorol. Soc.*, 73, 1352 - 1364.

Gray, W. M., Landsea, C. W., Mielke, P. W., and Berry, K. J., 1992: Predicting Atlantic seasonal hurricane activity 6 - 11 months in advance, *Weath. and Forecast.*, 7, 440 - 455.

Gray, W. M., Landsea, C. W., Mielke, P. W., and Berry, K. J., 1993: Predicting Atlantic seasonal hurricane activity by 1 August, *Weath. and Forecast.*, 8, 73 - 86.

Halpert, M. S., and Ropelewski, C. F., 1992: Surface temperature patterns associated with the Southern Oscillation, *J. Climate*, 5, 577 - 593.

Hastenrath, S., 1985: *Climate and Circulation of the Tropics*, D. Reidel Publishing Company, Dordrecht, 455 pp.

Hastenrath, S., and Lamb, P. J., 1979: *Climate Atlas of the Indian Ocean. Part I: Surface Climate and Atmospheric Circulation*, Univ. Of Wisconsin Press, 19 pp.

Hodanish, S., and Gray, W. M., 1993: An observational analysis of Tropical Cyclone Recurvature, *Mon. Wea. Rev.*, 121, 2665 - 2689.

Holland, G., and Merrill, R., 1984: On the dynamics of tropical cyclone structural changes, *Quart. J. Roy. Meteor. Soc.*, 110, 723 - 745.

Holton, J., 1971: A diagnostic model for equatorial wave disturbances: the role of vertical shear of the mean zonal wind, *J. Atmos. Sci.*, 28, 55 - 64.

Holton, J. R., 1972: *An Introduction to Dynamical Meteorology*, Academic Press, 319 pp.

Hoskins, B. J., Krishnamurti, T. N., and Oosterhof, D., 1989: Prediction of the life cycle of a supertyphoon with high resolution global model, *Bull. Am. Met. Soc.*, 70, 1218 - 1230.

Jury, M. R., 1992: A climate dipole governing the interannual variability of convection over the SW Indian Ocean and SE Africa region, *Trends in Geophys. Res. J.*, 165 - 172.

Jury, M. R., 1993: A Preliminary study of Climatological Associations and Characteristics of Tropical Cyclones in the SW Indian Ocean, *Meteorol. Atmos. Phys.*, 51, 101 - 115.

Jury, M. R., Parker, B. and Waliser, D.,1994: Evolution and Variability of the ITCZ in the SW Indian Ocean: 1988 - 90, *Theo. Appl. Climatol.*, 48, 187 -194.

Jury, M. R. and Pathack, B., 1991: A Study of Climate and Weather Variability over the Tropical Southwest Indian Ocean, *Meteorol. Atmos. Phys.*, 47, 37 - 48.

Jury, M. R., Pathack, B., Campbell, G., Wang, B., and Landman, W., 1991: Transient convective waves in the tropical SW Indian Ocean, *Meteorol. Atmos. Phys.*, 47, 27 - 36.

Lee, C. S., 1989a: Observational Analysis of Tropical Cyclogenesis in the Western North Pacific. Part I: Structural evolutions of cloud clusters, *J. Atmos. Sci.*, 46, 2580 - 2598.

Lee, C. S., 1989b: Observational Analysis of Tropical Cyclogenesis in the Western North Pacific. Part II: Budget Analysis, *J. Atmos. Sci.*, 46, 2599 - 2616.

Levey, K.M., 1993: *Intra-seasonal oscillations of convection over Southern Africa*, Msc. Thesis, University of Cape Town, 266 pp.

Lindesay, J. A., 1984: Spatial and temporal rainfall variability over South Africa, 1963 to 1981, *South African Geograph. J.*, 66, 168 - 175.

Lindesay, J. A., 1988: *The Southern Oscillation and atmospheric circulation changes over southern Africa*, Unpublished PhD. Thesis, University of the Witwatersrand, 283 pp.

Love, G., 1985a: Cross-equatorial influence of winter hemisphere sub-tropical cold surges, *Mon. Wea. Rev.*, 113, 1487-1498.

Love, G., 1985b: Cross-Equatorial Interactions during Tropical Cyclogenesis, *Mon. Wea. Rev.*, 113, 1499 - 1509.

Malkus, J. S., and Riehl, H., 1960: On the dynamics and energy transformations in steady-state hurricanes, *Tellus*, 12, 1 - 20.

Martin, D. W., Hinton, B. B., and Auvine, B. A., 1993: Three Years of Rainfall over the Indian Ocean, *Bulletin of the American Meteorological Society*, 74, 4, 581-590.

Matarira, C. H., and Jury, M. R., 1992: Contrasting meteorological structure of intra-seasonal wet and dry spells in Zimbabwe, *Intl. J. of Climate*, 12, 165 - 176.

McBride, J. L., 1979: Observational analysis of tropical cyclone formation, Atmos. Sci. Pap. No. 308, Colorado State University, 230 pp.

McBride, J. L., 1981: Observational analysis of tropical cyclone formation. Part III: Budget analysis, *J. Atmos. Sci.*, 38, 1152 - 1166.

Merrill, R. T., 1988: Characteristics of upper tropospheric environmental flow around hurricanes, *J. Atmos. Sci.*, 45, 11, 1665 - 1677.

Middlebrooke, M. G., 1988: Investigation of tropical cyclone genesis and development using low-level aircraft flight data, *Atmospheric Science Paper 429*, Department of Atmospheric Science, Colorado State University, Colorado.

Molinari, J., and Vallaro, D., 1989: External influences on hurricane intensity. Part I: Outflow layer eddy angular momentum fluxes, *J. Atmos. Sci.*, 46, 1093 - 1105.

Molinari, J., and Vallaro, D., 1990: External influences on hurricane intensity. Part II: Vertical structure and response of the hurricane vortex, *J. Atmos. Sci.*, 47, 1902 - 1918.

Montgomery, M. T., and Farrell, B. F., 1993: Tropical Cyclone Formation, *J. Atmos. Sci.*, 50, 285 - 310.

Nassor, A, 1994: Monsoon surges, tropical cyclones and extreme rainfall events in NW Madagascar, Msc Thesis (submitted), Oceanography Dept, Univ. Of Cape Town.

Ooyama, K., 1964: A dynamical model for the study of tropical cyclone development, *Tech. Conf. On Hurricanes and Tropical Meteorology*, Mexico, Amer. Meteor. Soc., 187 - 198.

Ooyama, K., 1982: Conceptual evaluation of the theory and modelling of the tropical cyclone, *J. Meteor. Soc. of Japan*, 60, 369 - 380.

Padya, B. M., 1989: *Weather and Climate of Mauritius*, Mahatma Gandhi Institute, Mauritius, 283 pp.

Palmén, E., 1948: On the formation and structure of tropical hurricanes, *Geophysica*, 3, 26 - 38.

Pathack, B. M. R., 1993: *Modulation of South African Summer Rainfall By Global Climate Processes*, PhD. Thesis, University of Cape Town, pp 180.

Pfeffer, P., and Challa, M., 1981: A numerical study of the role of eddy fluxes of momentum in development of Atlantic hurricanes, *J. Atmos. Sci.*, 38, 2393 - 2398.

Preston-Whyte, R. A. and Tyson, P. D., 1988: *The Atmosphere and Weather of Southern Africa*, Oxford University Press, Cape Town, 374 pp.

Riehl, H., 1979: *Climate and Weather of the Tropics*, Academic Press, London, 611 pp.

Sadler, J. C., 1978: Mid-season typhoon development and intensity changes and the tropical upper tropospheric trough, *Mon. Weath. Rev.*, 106, 1137 -1152.

Shapiro, L., and Willoughby, H., 1982: The response of balanced hurricanes to local sources of heat and momentum, *J. of Atmos. Sci.*, 39, 378 - 394.

Simpson, R. H. and Riehl, H., 1981: *The Hurricane and Its Impact*, Basil Blackwell Pub., Oxford, 398 pp.

Singh, S. V., Kripalani, R. H., and Sikka, D. R., 1992: Interannual variability of the Madden-Julian oscillations in Indian summer monsoon rainfall, *J. of Clim.*, 5, 973 - 978.

Taljaard, 1967: Development, distribution, and movement of cyclones and anticyclones in the Southern Hemisphere during IGY, *J. Appl. Met.*, 6, 973 - 987.

Tuleya, R. E., 1994: Tropical storm development and decay: Sensitivity to boundary conditions, *Mon. Weath. Rev.*, 122, 291 - 304.

Uppala, S., 1987: ECMWF final level IIIb analysis: Analysis system performance and impact on forecasting. Data Assimilation Workshop, Washington DC.

Vermeulen, J. H. and Jury, M. R., 1992: Tropical Cyclones in the south-west Indian Ocean - track prediction and verification 1989 91, *Meteorol. Mag.*, 121, 186 - 192.

Walker, N. D., 1989: *Sea surface temperature-rainfall relationships and associated ocean-atmosphere coupling mechanisms in the southern African region*, PhD. Thesis, Oceanography Dept., Univ. of Cape Town, 173 pp.

Wang, B., and Rui, H., 1990: Synoptic Climatology of Transient Intraseasonal Convection Anomalies: 1975 - 1985, *Meteorol. Atmos. Phys.*, 44, 43 - 61.

Weatherford, C., and Gray, W. M., 1988a: Typhoon structure as revealed by aircraft reconnaissance: Part I: Data analysis and climatology. *Mon. Weath. Rev.*, June issue.

Weatherford, C., and Gray, W. M., 1988b: Typhoon structure as revealed by aircraft reconnaissance: Part II: Structural variability. *Mon. Weath. Rev.*, June issue.

Williams, J. B., 1990: *Some temporal and regional variations of Climate in Madagascar*, Tech. Rep. Overseas Devep., Nat. Res. Inst., Chatham Marine, Kent, 144 pp.

Xu, K., and Emanuel, K. A., 1989: Is the tropical atmosphere conditionally unstable?, *Mon. Weath. Rev.*, 117, 1471 - 1479.

ACKNOWLEDGEMENTS

I thank my supervisor Dr. Mark R. Jury, of the Oceanography Department, University of Cape Town, for his continous support at all stages of my research. Kevin Levey, gave assistance in validating the programs used to process the data, Abdallah Nassor (Madagascar Meteorological Service) and Amos Makarau (Zimbabwe Meteorological Service) offered useful advice and input. Thanks are extended to Professor Geoff Brundrit, Head of the Oceanography Department, and to Shaun Courtney for computer support. I am indebted to my family, and especially my wife Waheeda for her patience, understanding and encouragement throughout this research.

The Foundation for Research Development Special Programme on Climatic Variability (SACCAIM), Dynamics of Marine Weather Systems Project supported this research.

APPENDIX A

CALCULATION OF :

A} VAPOUR PRESSURE (e)

1) Calculate condensation level temperature (T_L)

$$T_L = [\ 1 / \{\ 1 / (\ T_K - 55\ ) - (\ \ln (\ RH / 100\ ) / 2840\ )\ \}\ ] + 55 \qquad \textbf{Eq. A-1}$$

where : T_K = temperature (°K)

RH = relative humidity (%)

$$e = \exp [\ 3.5 \times \ln T_K - \{\ 2840 / (T_L - 55\ )\} - 4.805\ ] \qquad \textbf{Eq. A-2}$$

B} MIXING RATIO (x)

The mixing ratio is the ratio of the mass of water vapour to the mass of dry air. It is dependent on vapour pressure and total atmospheric pressure and can be derived using temperature and relative humidity (Bolton,1980).

Using e from **Eq. A-2**

$$x = (\ 0.622 \times e\ ) / (\ P - e\ ) \qquad \textbf{Eq. A-3}$$

where : P = set-level pressure (hPa)

From this precipitable water and water vapour flux can be calculated.

APPENDIX B

TC FIRINGA

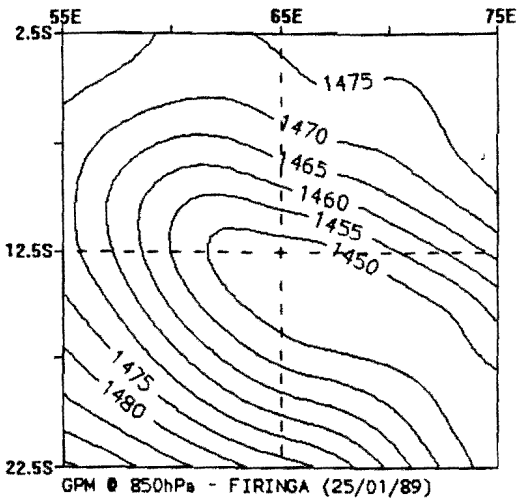

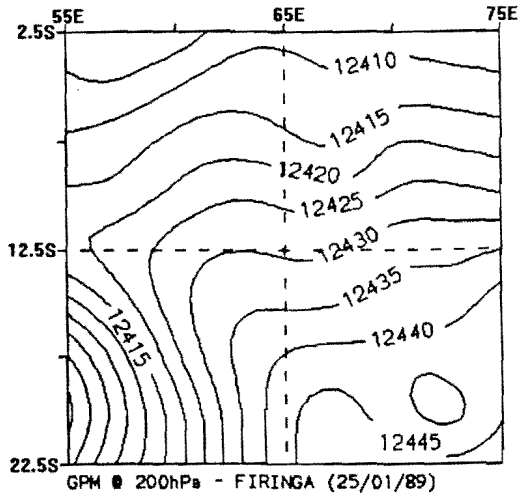

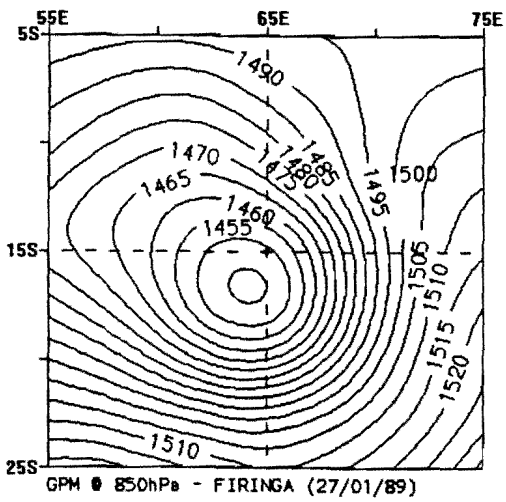

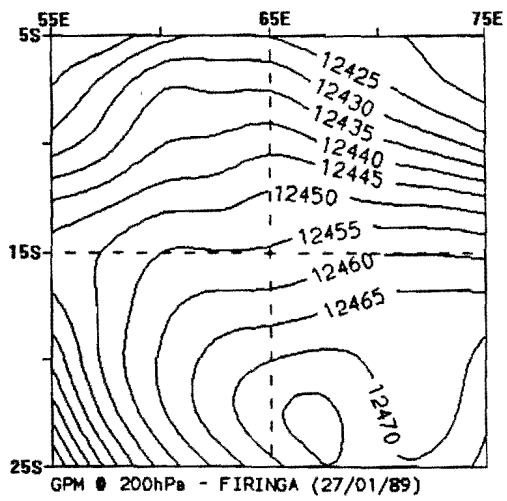

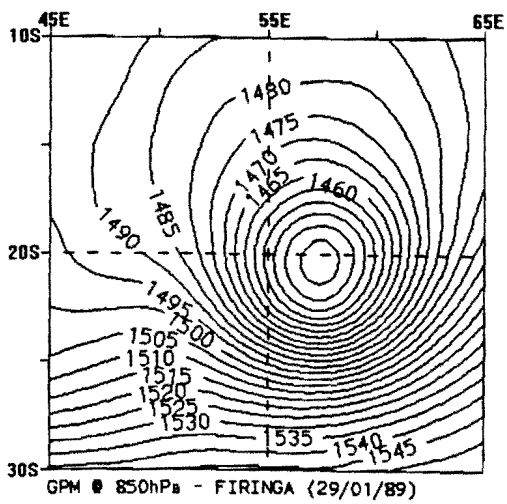

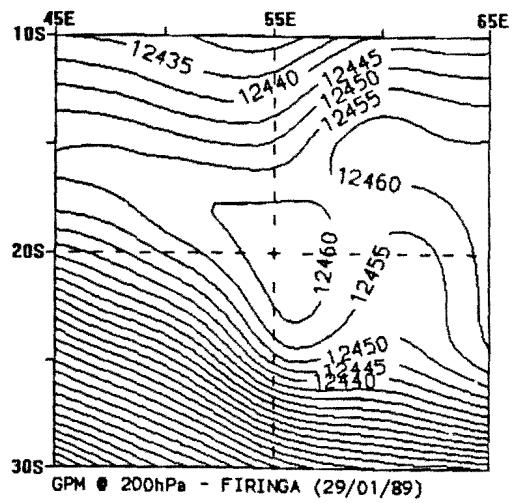

Figure B-1a,b and c : Geopotential @ 850 hPa.
Contour interval 5 gpm.

Figure B-2a,b and c : Geopotential @ 200 hPa.
Contour interval 5 gpm.

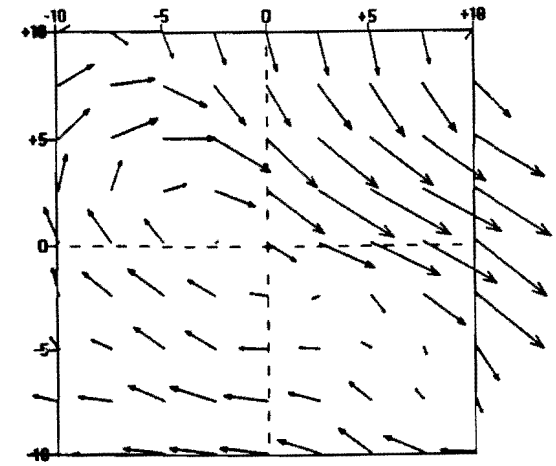

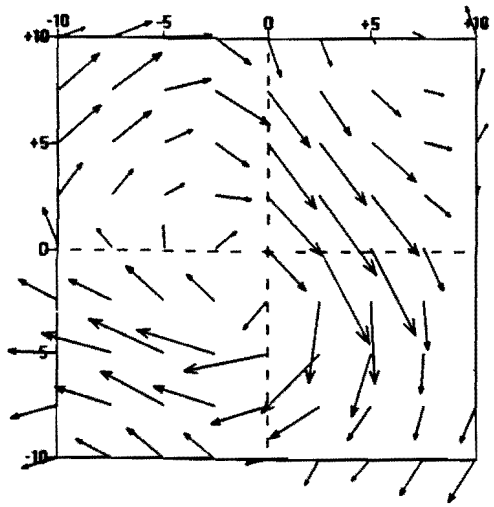

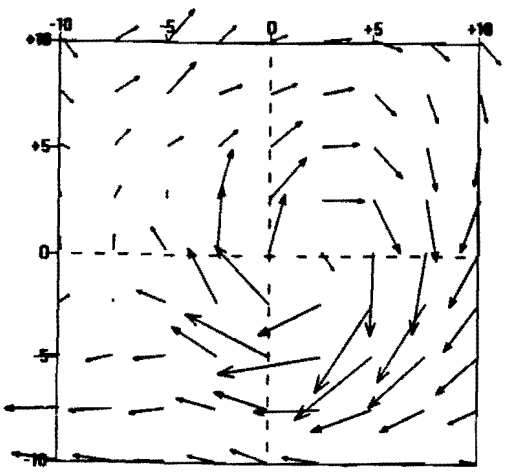

Figure B-3a,b and c : Horizontal wind @ 850 hPa.
Vector scale : ⟶ = 10 ms^{-1}.

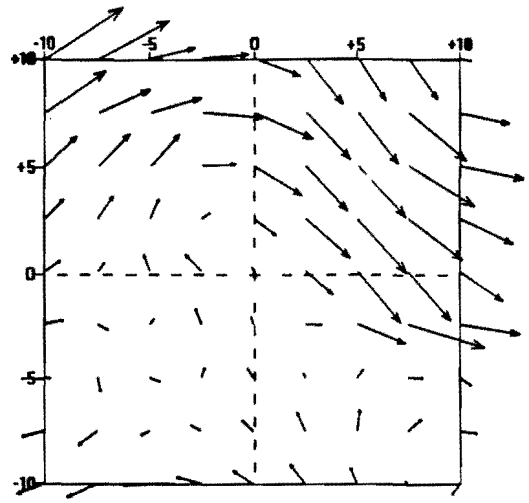

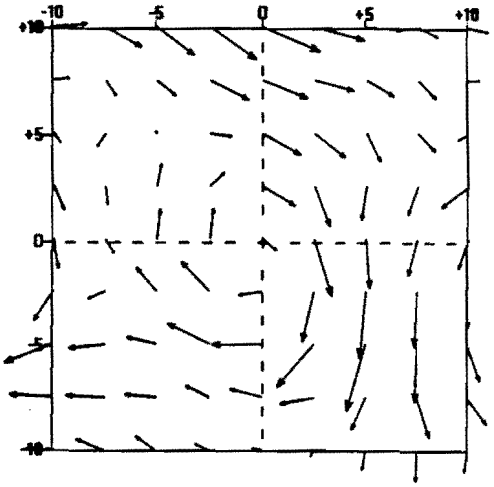

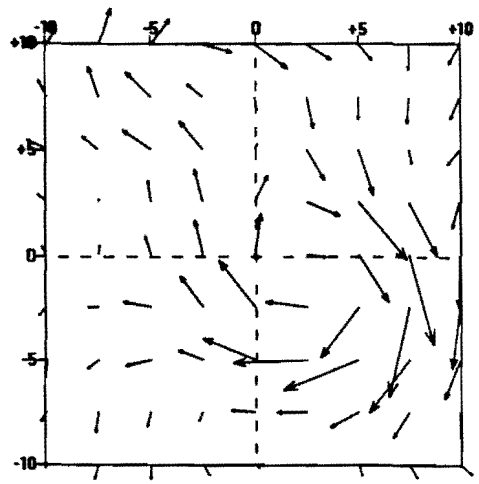

Figure B-4a,b and c : Horizontal wind @ 500 hPa.
Vector scale : ⟶ = 10 ms^{-1}.

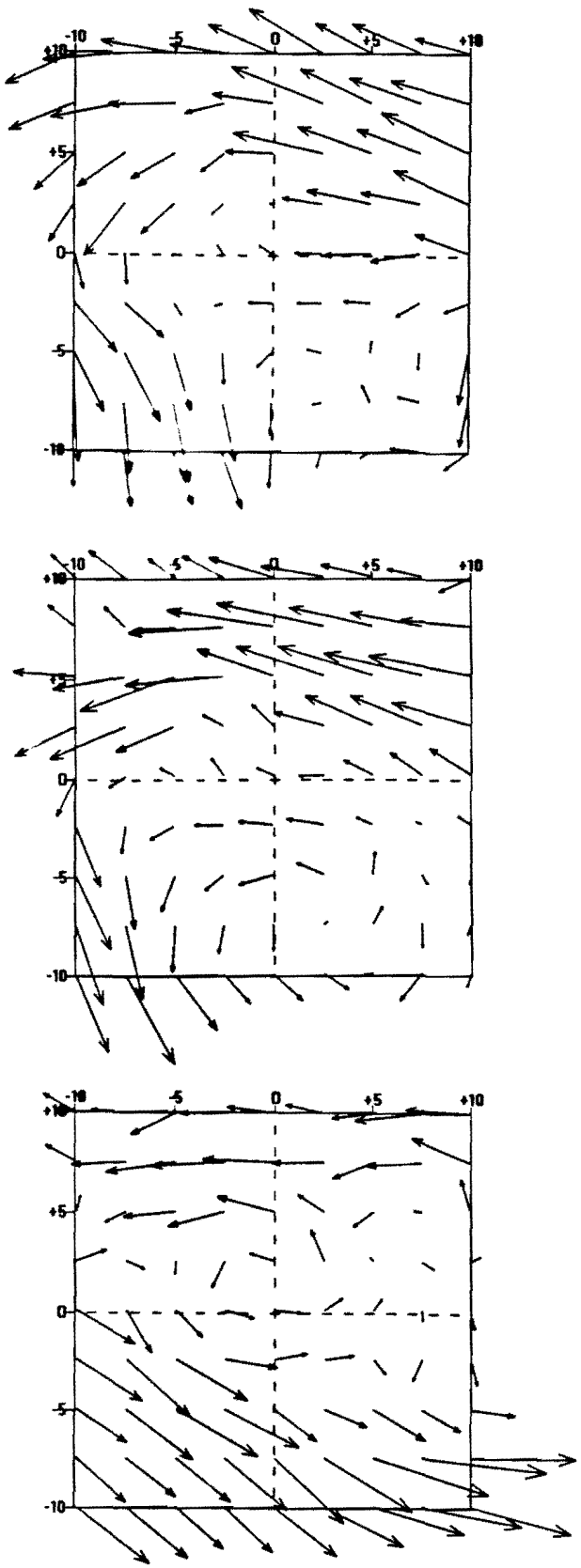

Figure B-5a,b and c : Horizontal wind @ 200 hPa.
Vector scale : ⟶ = 10 ms^{-1}.

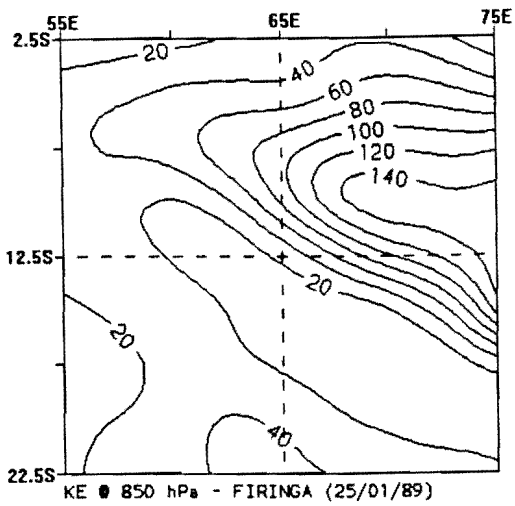

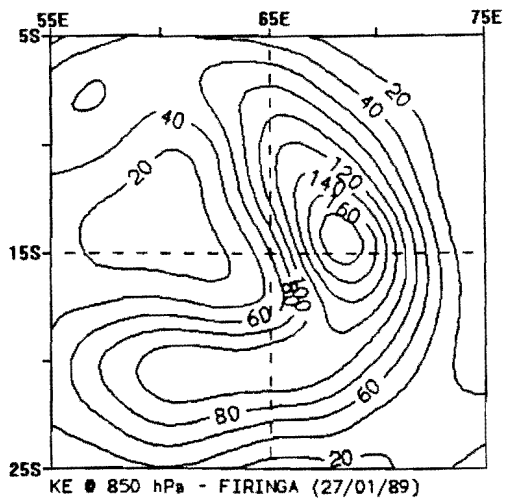

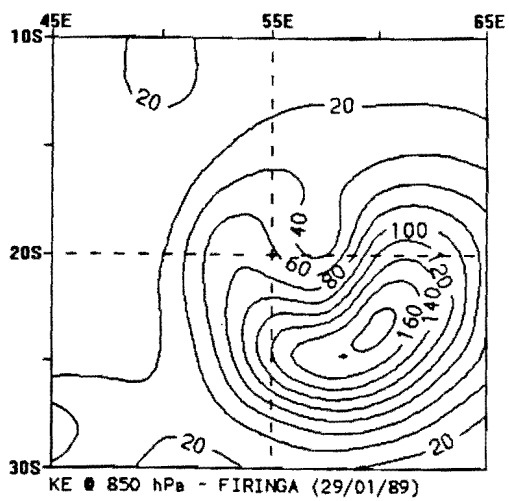

Figure B-6a,b and c : Kinetic energy @ 850 hPa.
Contour interval is 20 J kg^{-1}.

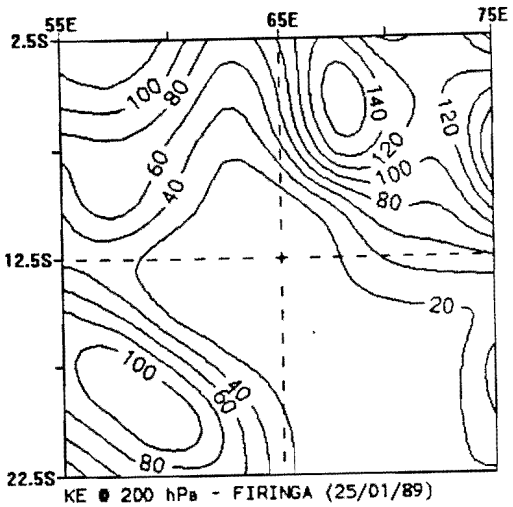

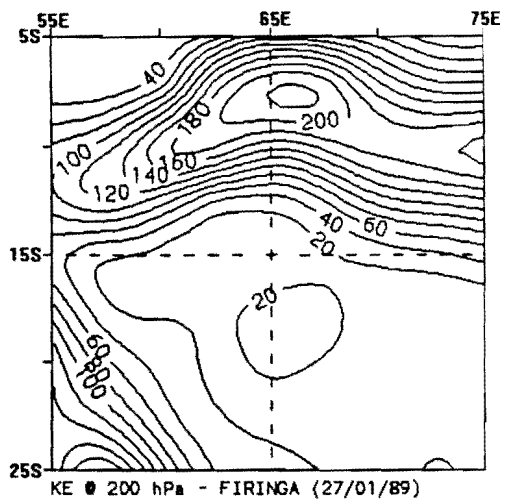

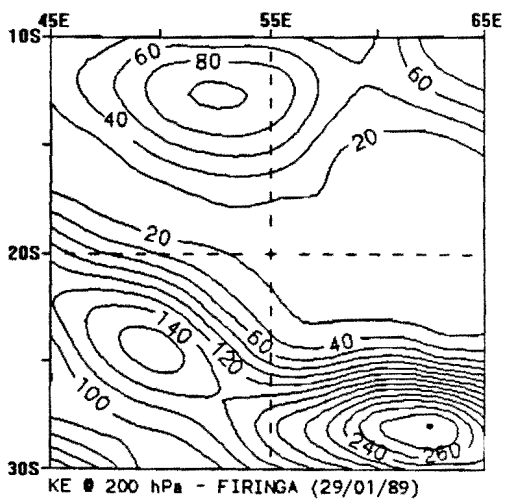

Figure B-7a,b and c : Kinetic energy @ 200 hPa.
Contour interval is 20 J kg^{-1}.

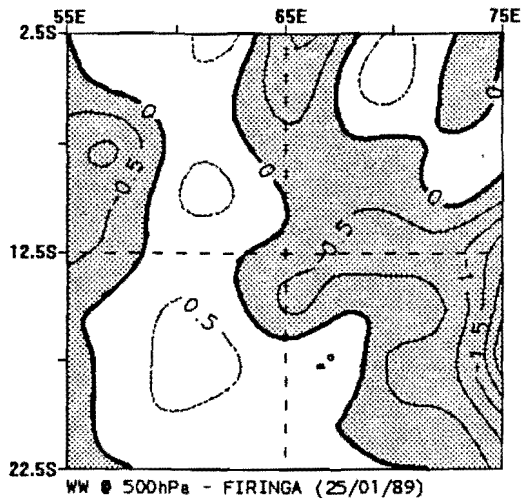

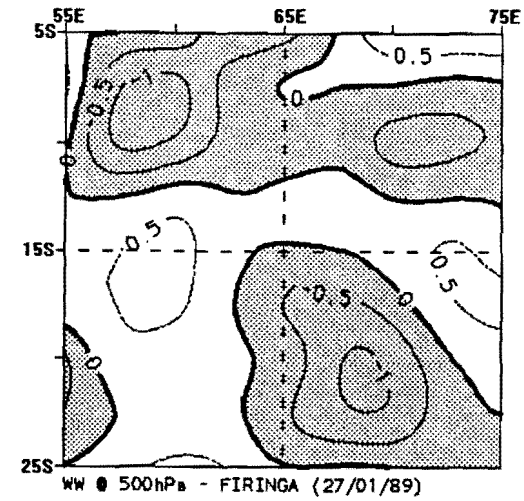

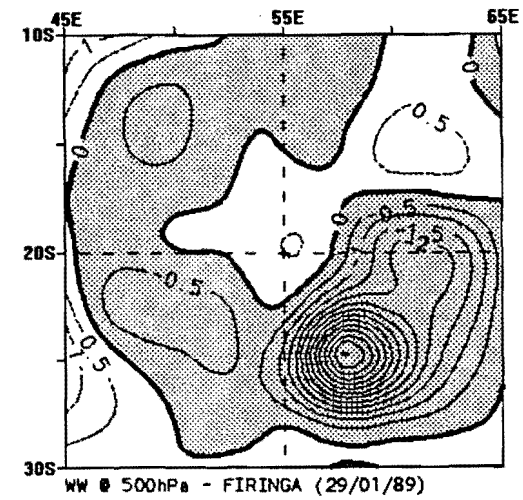

Figure B-8a,b and c : Vertical motion @ 500 hPa.
Contour interval is 0.5 Pa s^{-1}.

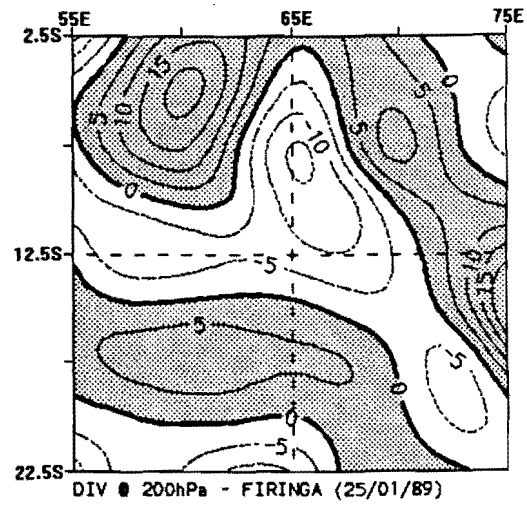

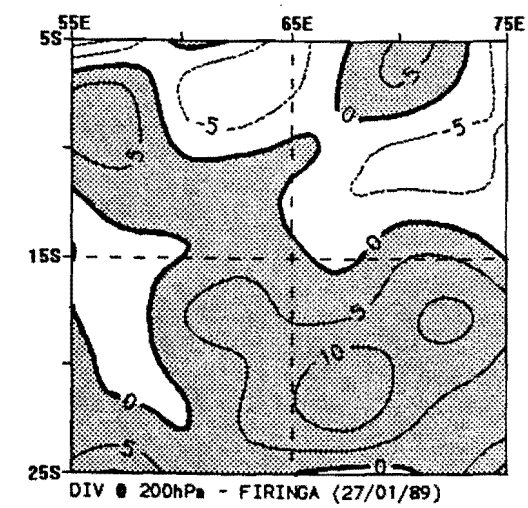

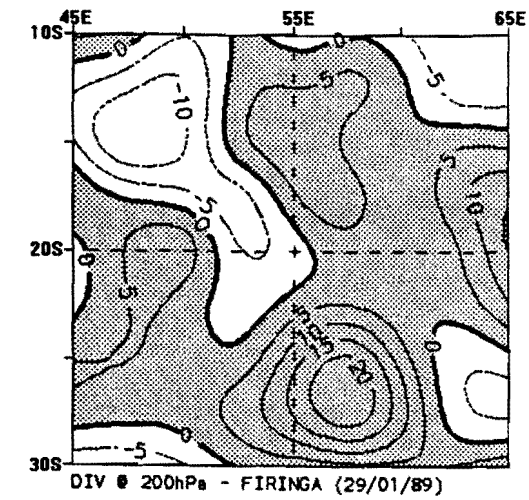

Figure B-9a,b and c : Divergence @ 200 hPa.
Contour interval is 5 x 10^{-5} s^{-1}.

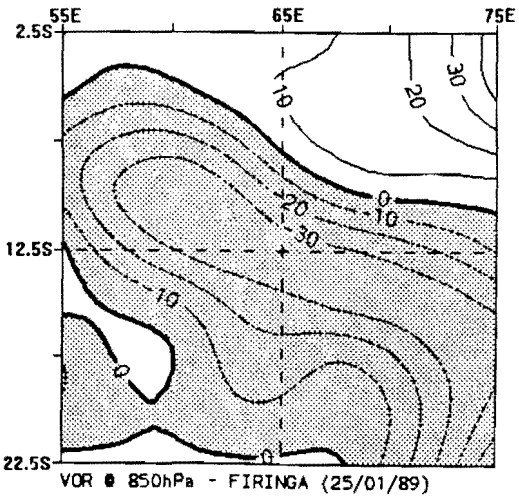

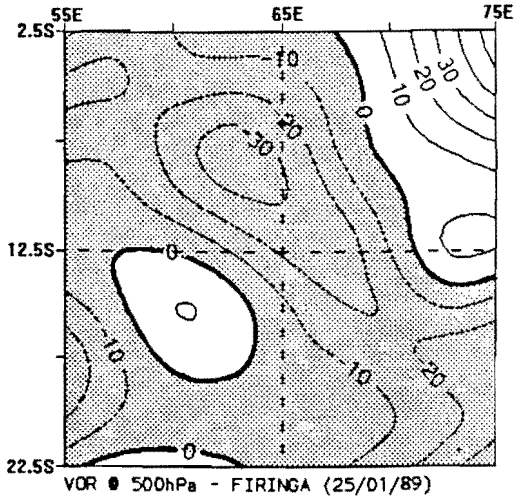

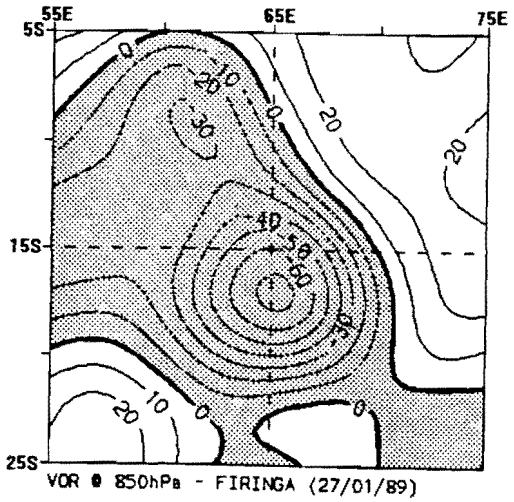

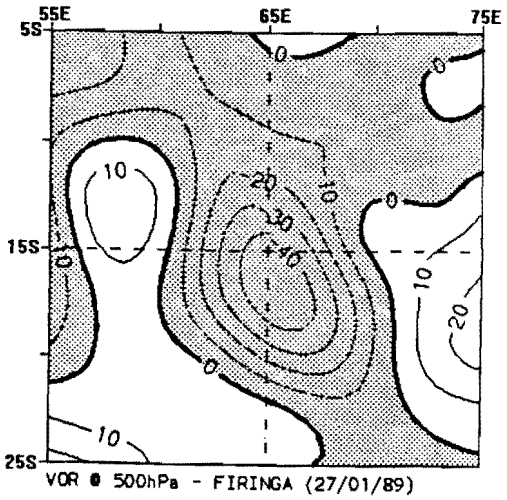

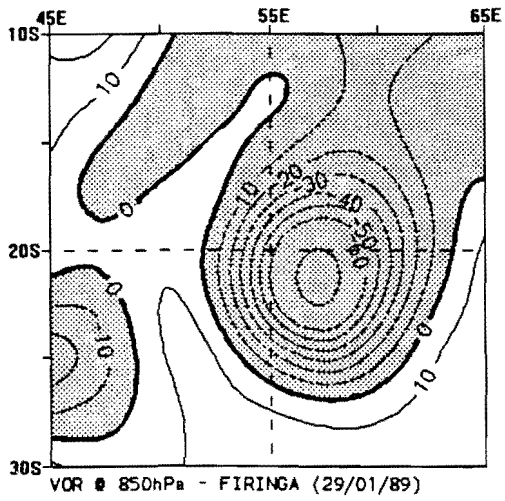

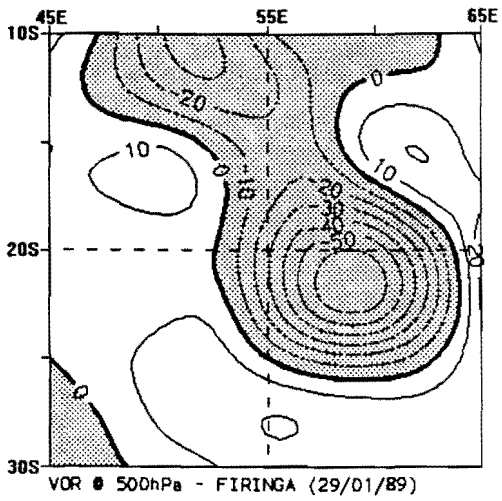

Figure B-10a,b and **c** : Vorticity @ 850 hPa.
Contour interval is 10 x 10^{-5} s^{-1}.

Figure B-11a,b and **c** : Vorticity @ 500 hPa.
Contour interval is 10 x 10^{-5} s^{-1}.

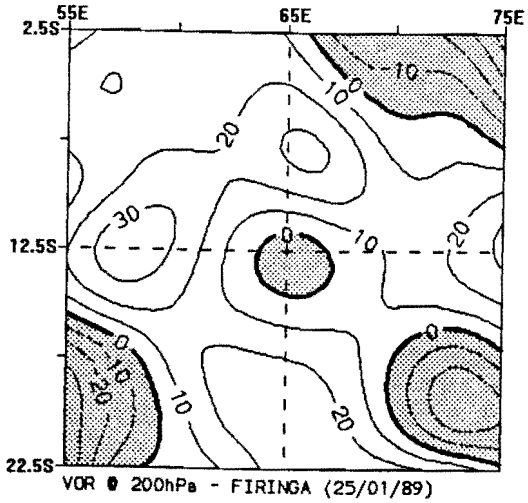

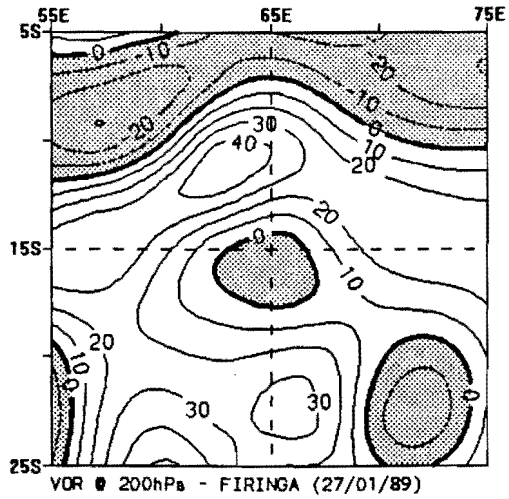

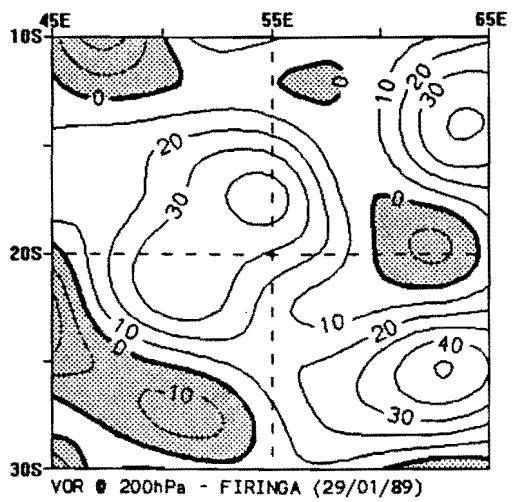

Figure B-12a,b and **c** : Vorticity @ 200 hPa.
Contour interval is 10 x 10^{-5} s^{-1}.

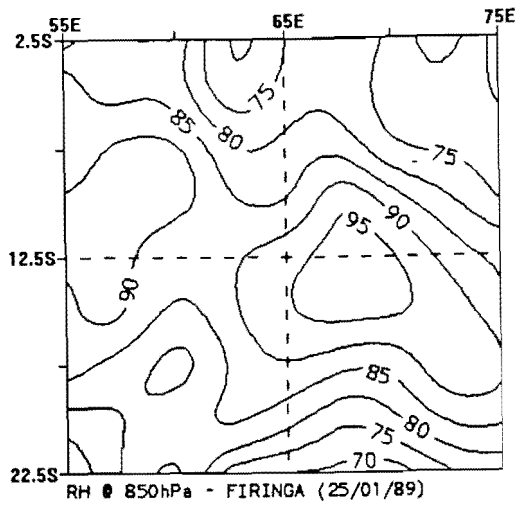

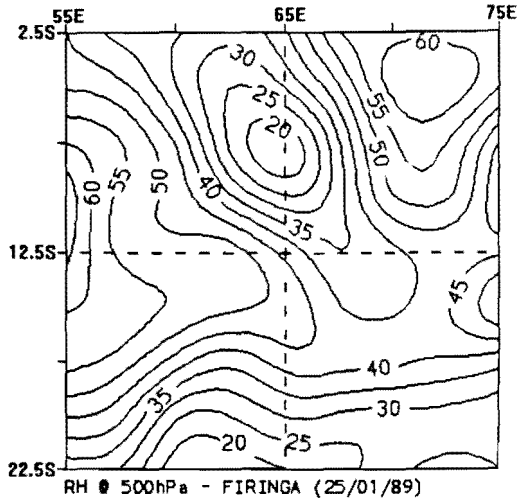

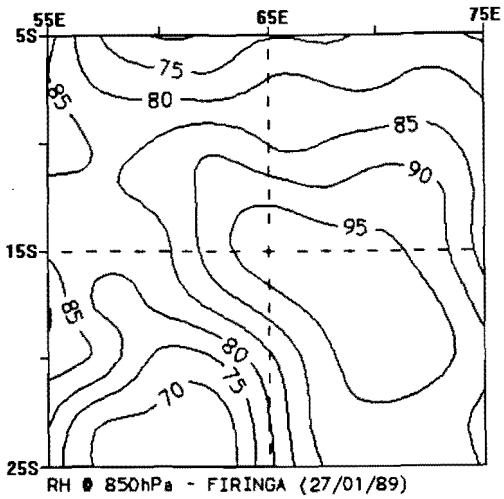

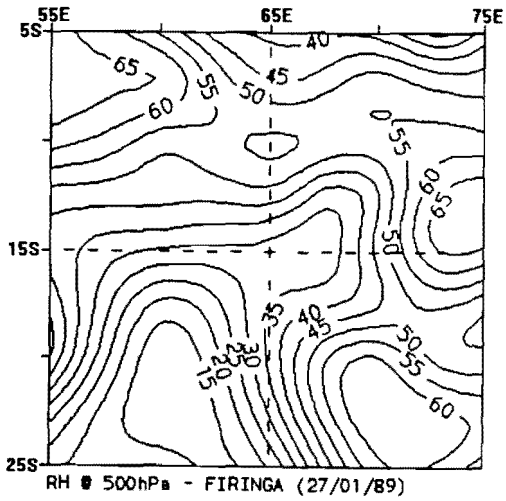

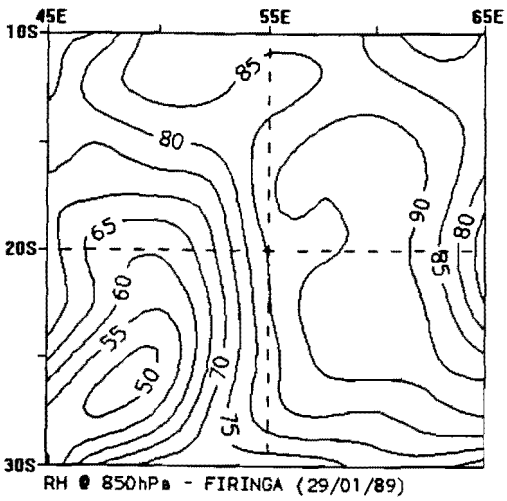

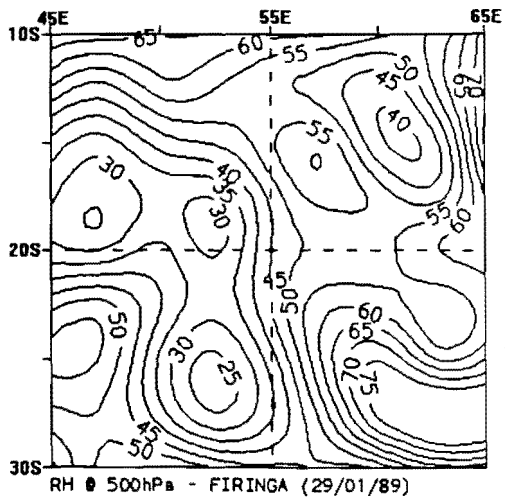

Figure B-15a,b and **c** : Relative humidity @ 850 hPa. Contour interval is 5 %.

Figure B-16a,b and **c** : Relative humidity @ 500 hPa. Contour interval is 5 %.

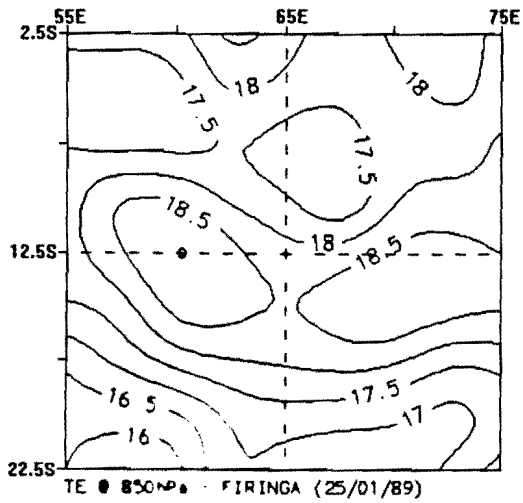

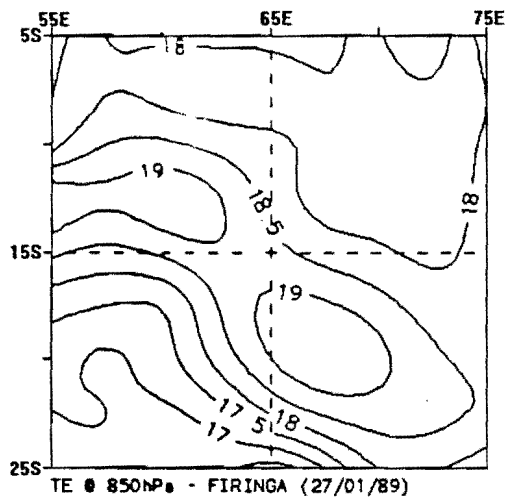

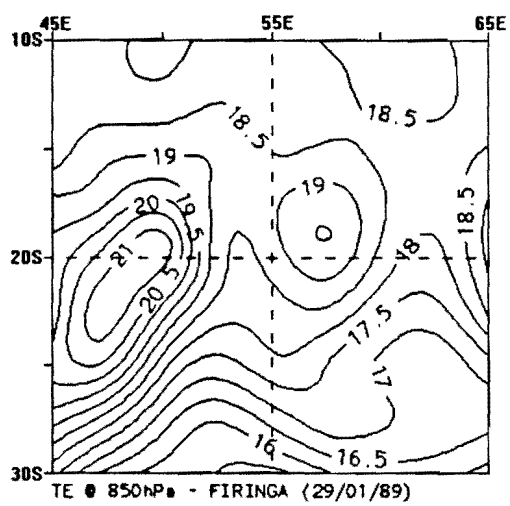

Figure B-13a,b and c : Temperature @ 850 hPa.
Contour interval is 0.5 °C.

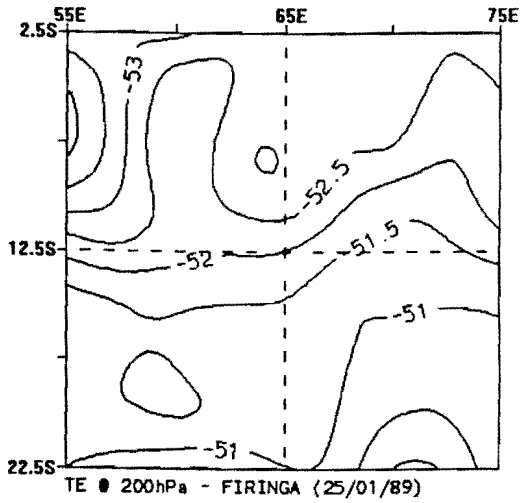

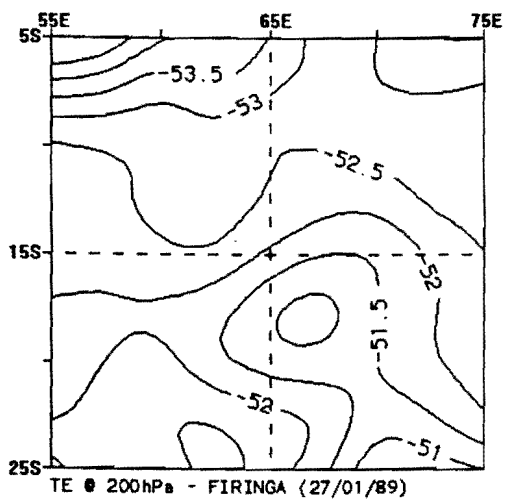

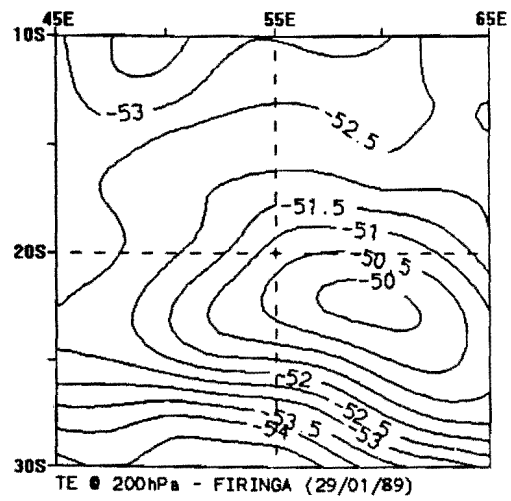

Figure B-14a,b and c : Temperature @ 200 hPa.
Contour interval is 0.5 °C.

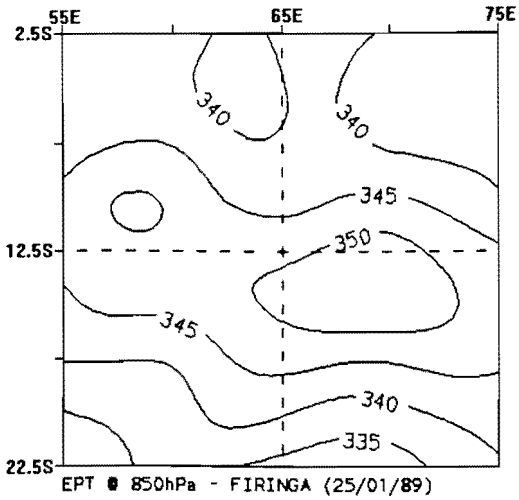

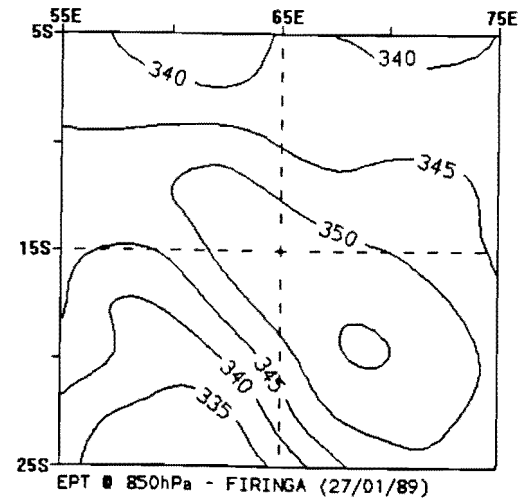

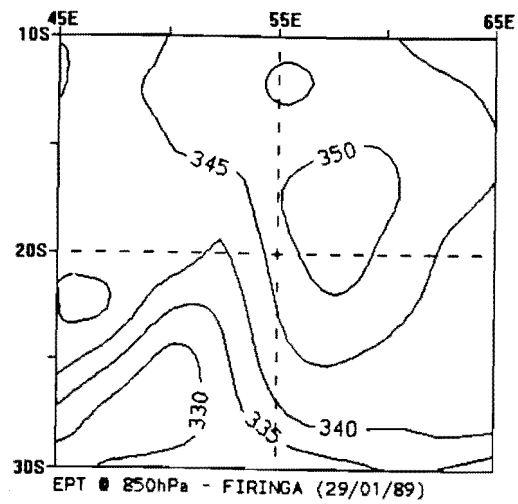

Figure B-18a,b and c : Equivalent potential temperature @ 850 hPa.
Contour interval is 5 °K.

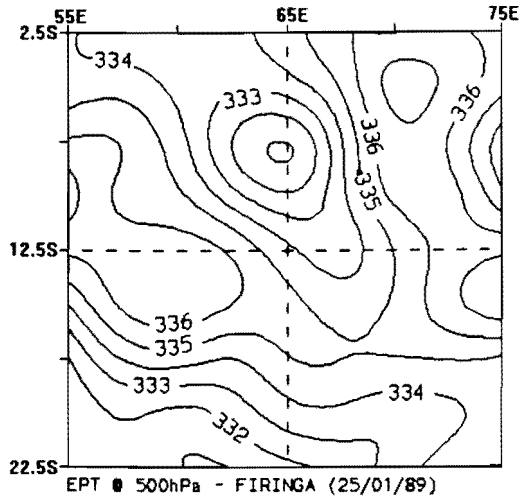

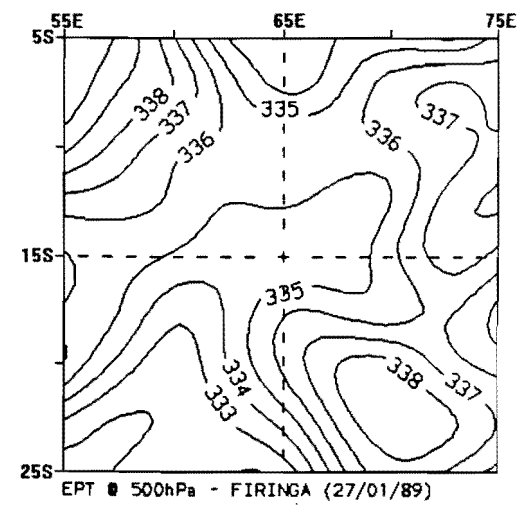

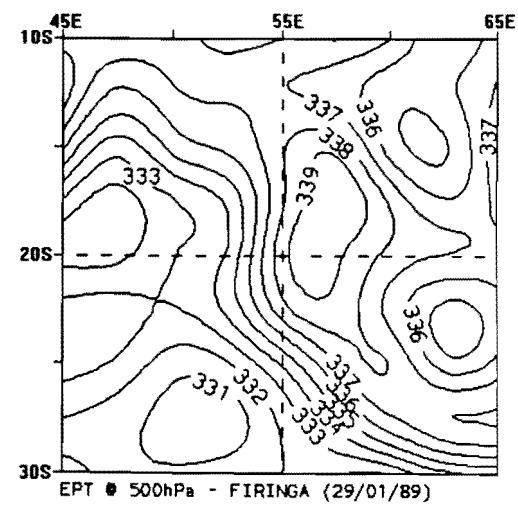

Figure B-19a,b and c : Equivalent potential temperature @ 500 hPa.
Contour interval is 1 °K.

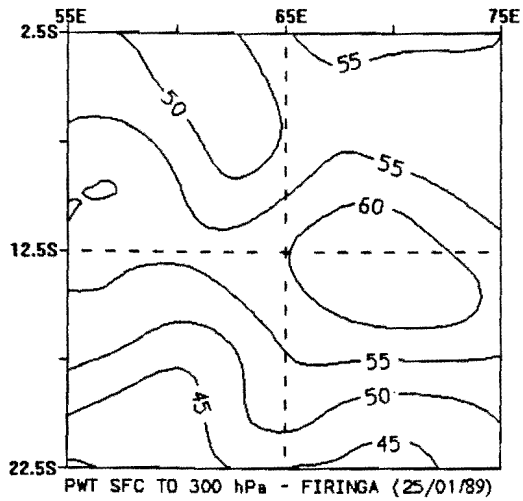

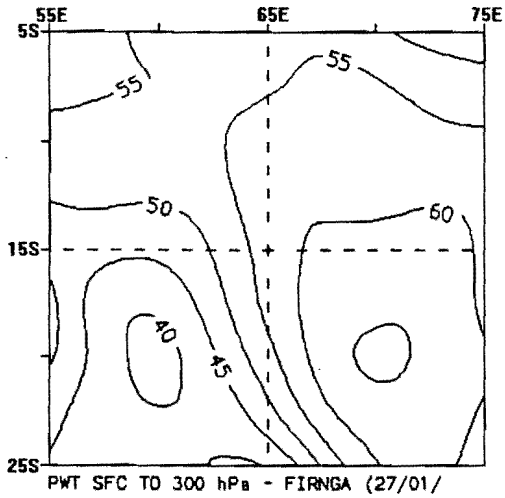

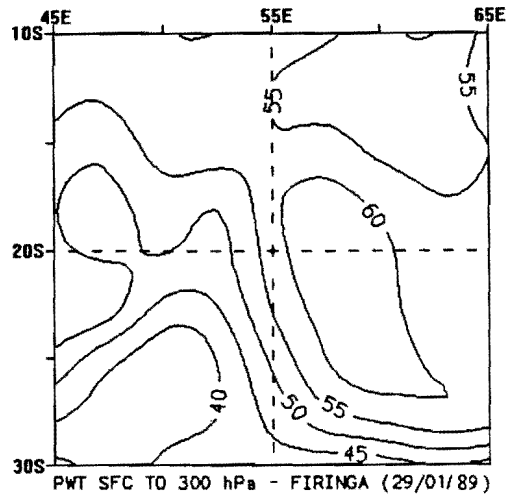

Figure B-17a,b and c : Precipitable water between the surface and 300 hPa.
Contour interval is 5 mm.

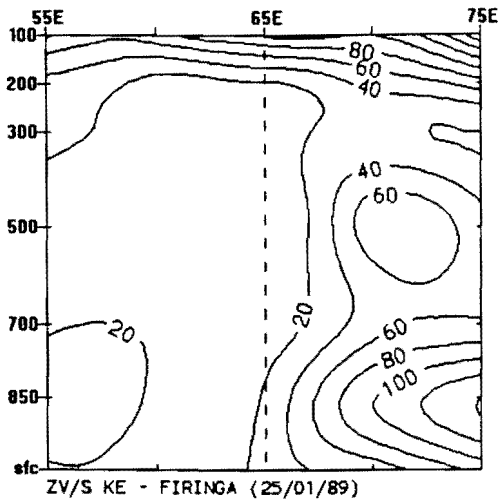

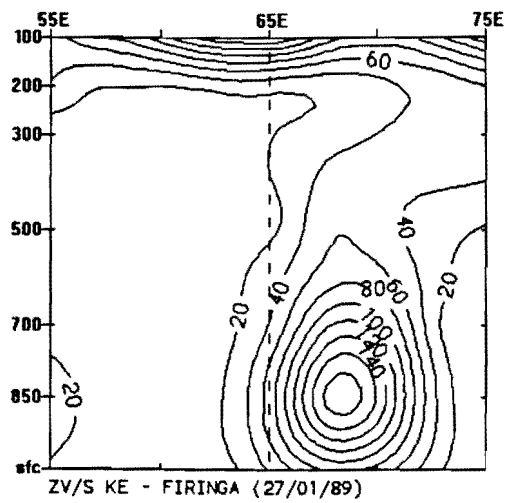

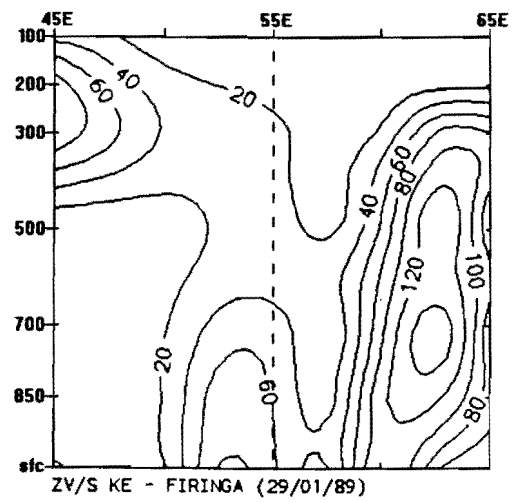

Figure B-20a,b and c : Zonal kinetic energy.
Contour interval is 20 J kg^{-1}.

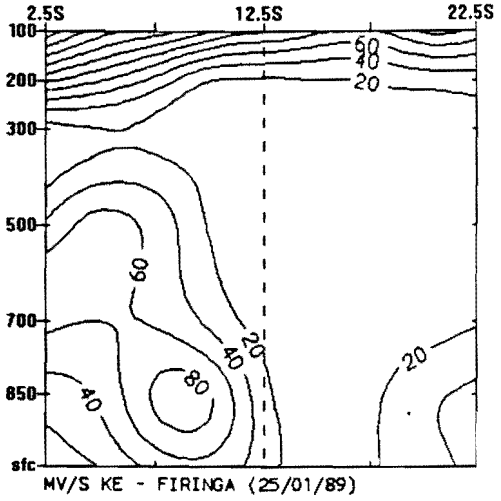

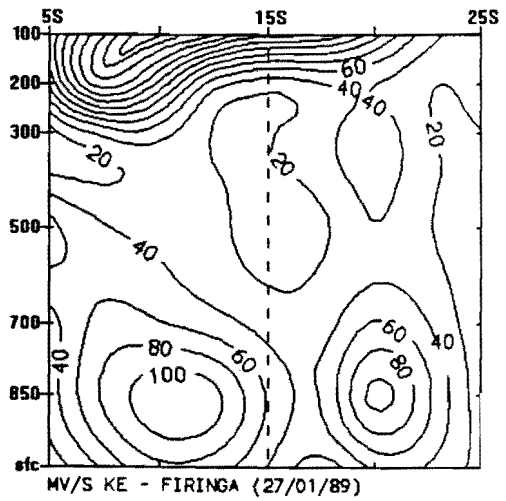

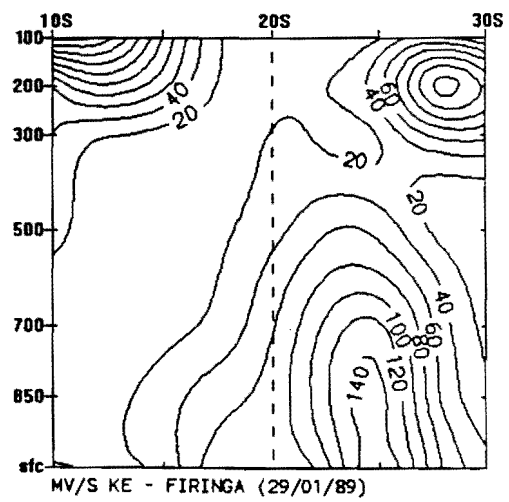

Figure B-21a,b and c : Meridional kinetic energy.
Contour interval is 20 J kg^{-1}.

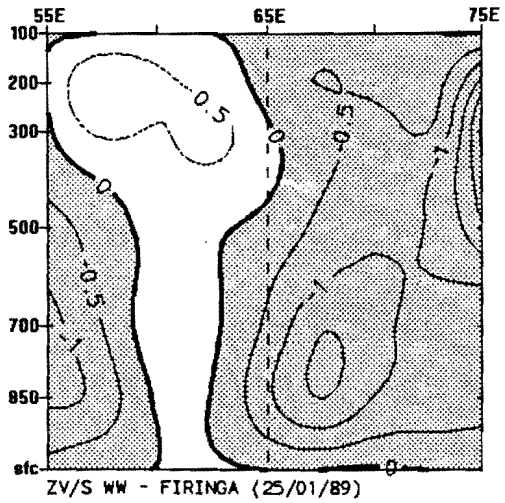

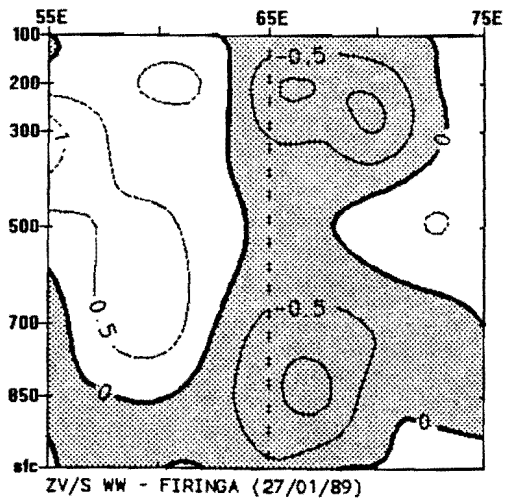

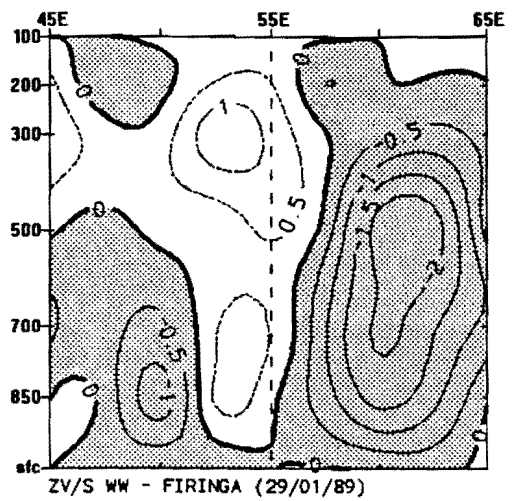

Figure B-22a,b and c : Zonal vertical motion.
Contour interval is 0.5 Pa s^{-1}.

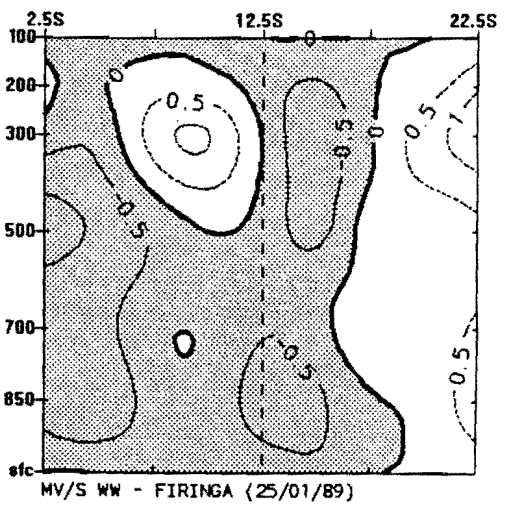

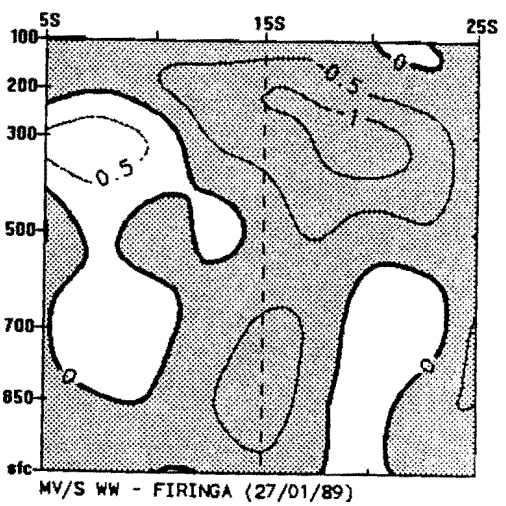

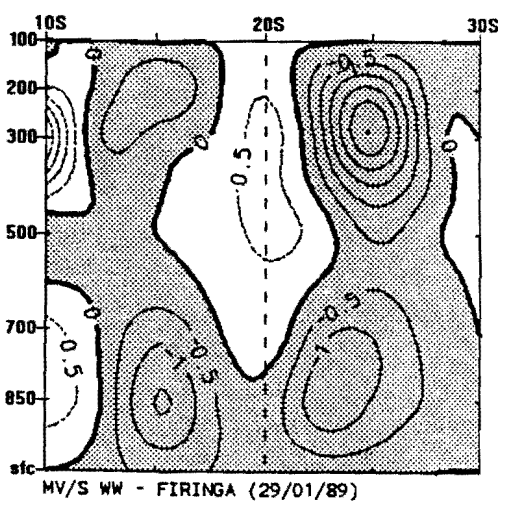

Figure B-23a,b and c : Meridional vertical motion.
Contour interval is 0.5 Pa s^{-1}.

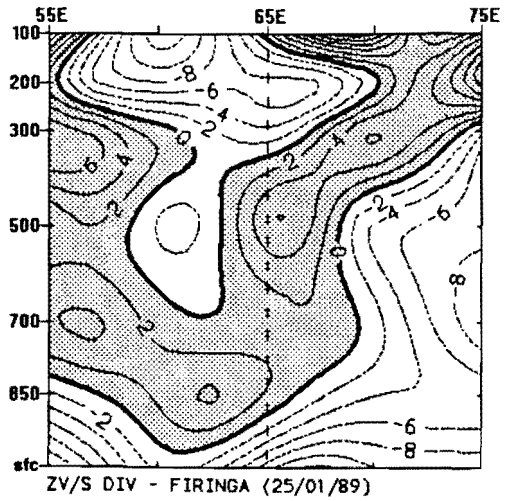

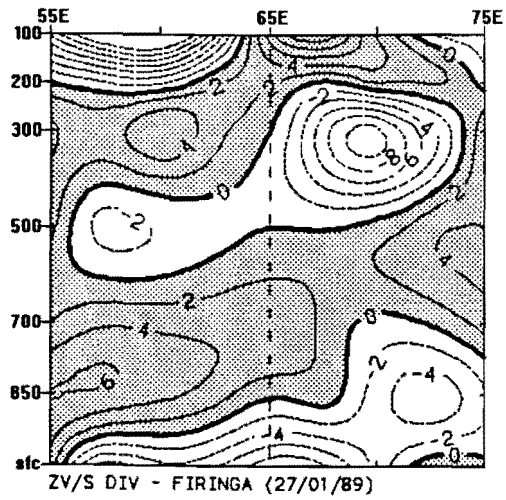

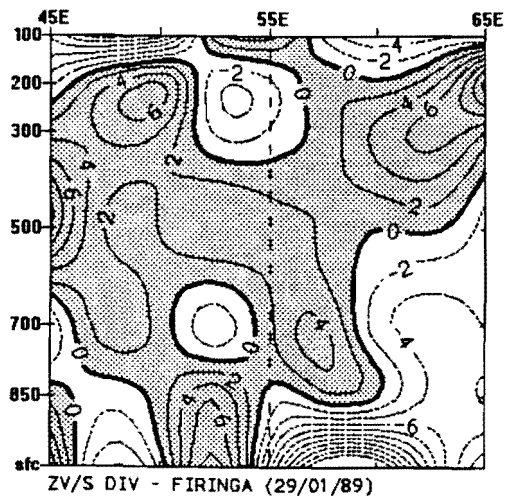

Figure B-24a,b and c : Zonal divergence.
Contour interval is 2 x 10^{-5} s^{-1}.

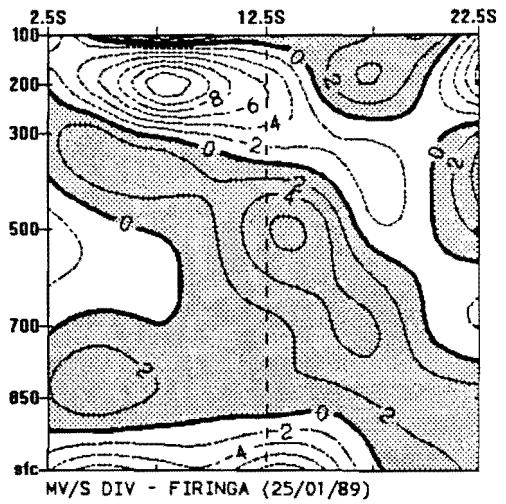

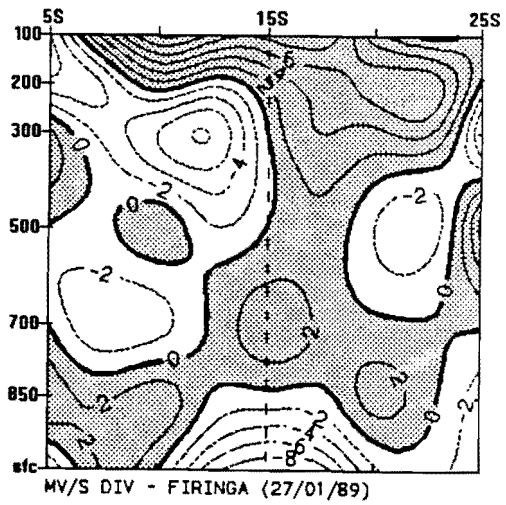

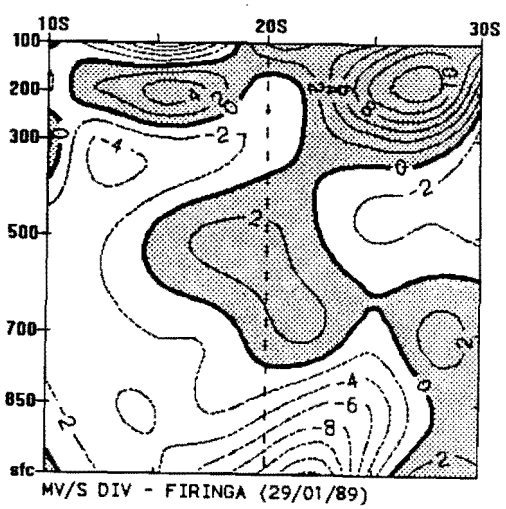

Figure B-25a,b and c : Meridional divergence.
Contour interval is 2 x 10^{-5} s^{-1}.

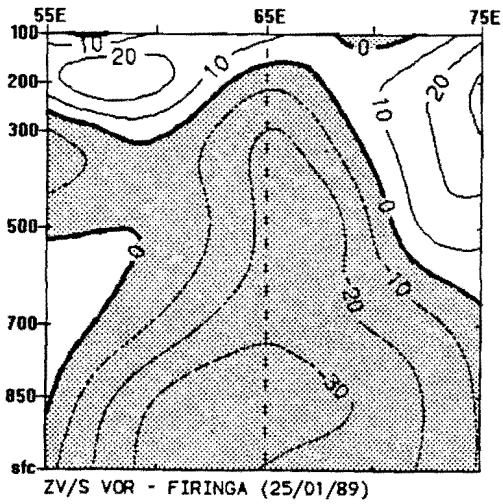

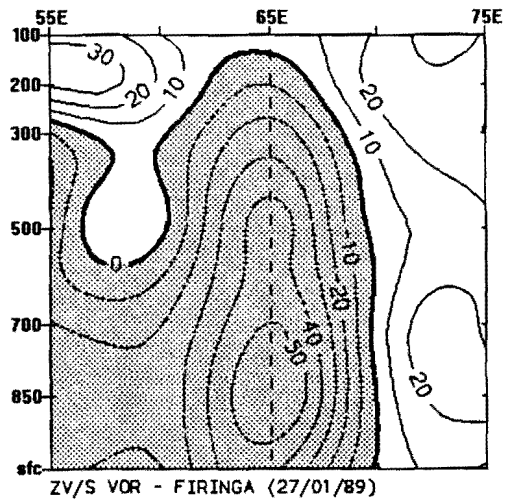

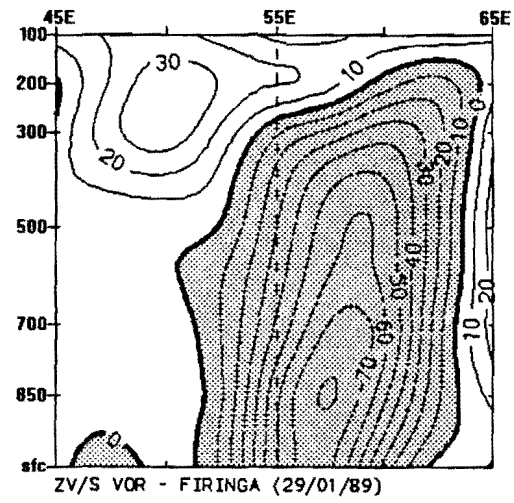

Figure B-26a,b and c : Zonal vorticity.
Contour interval is 10 x 10^{-5} s^{-1}.

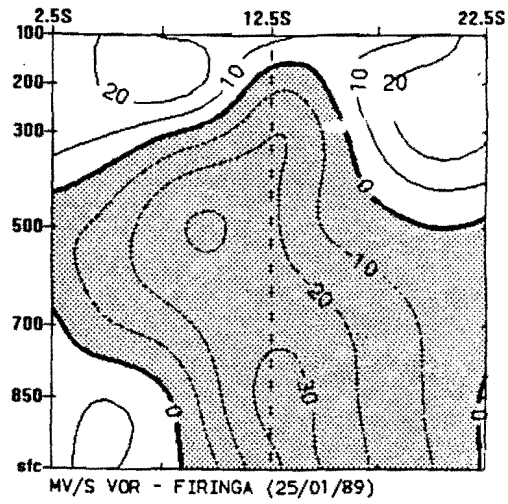

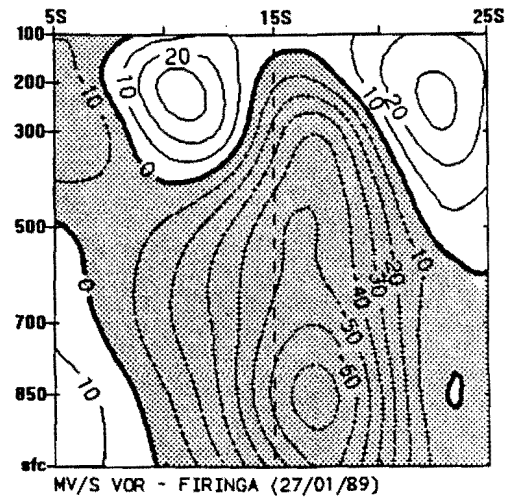

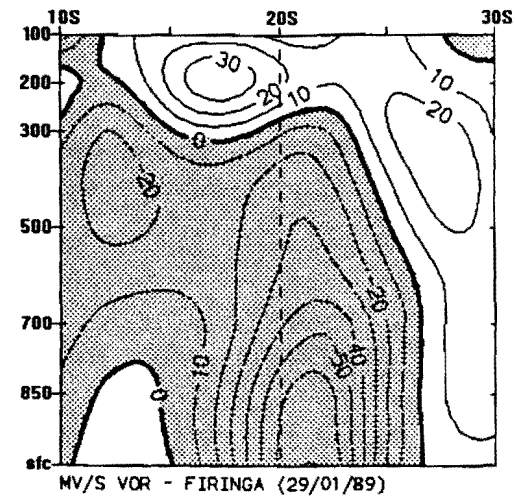

Figure B-27a,b and c : Meridional vorticity.
Contour interval is 10 x 10^{-5} s^{-1}.

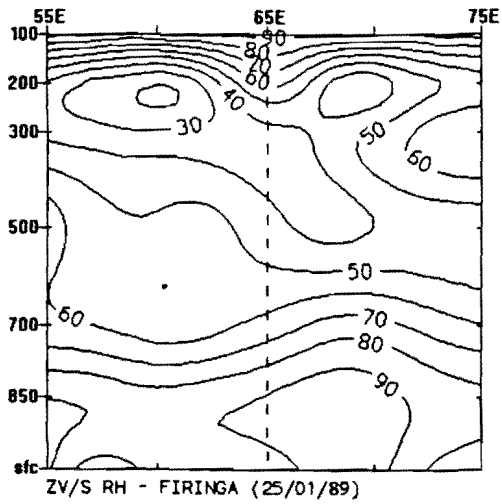

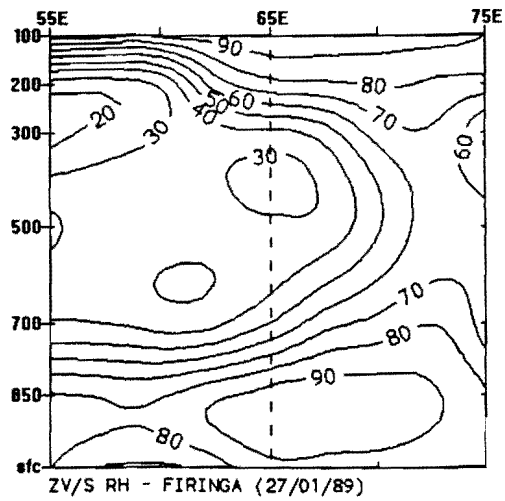

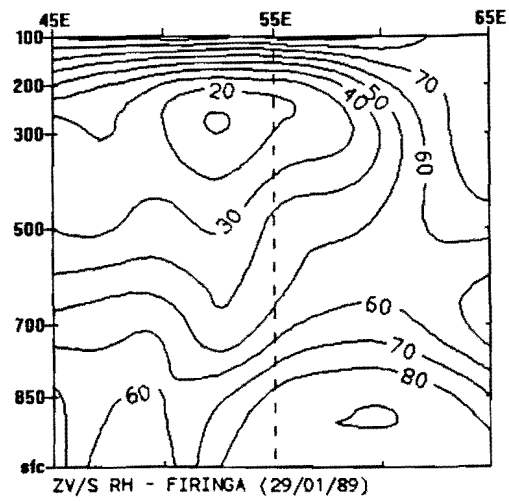

Figure B-28a,b and c : Zonal relative humidity. Contour interval is 10 %.

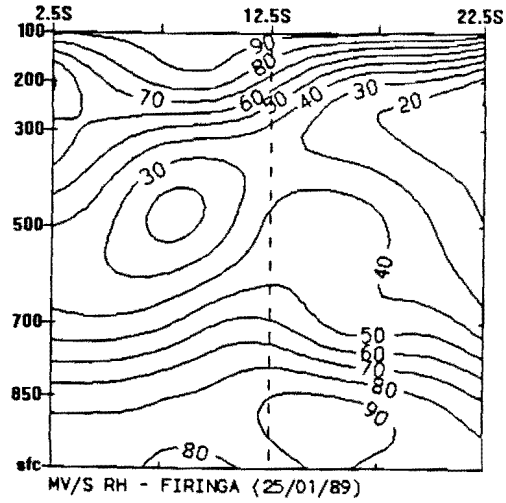

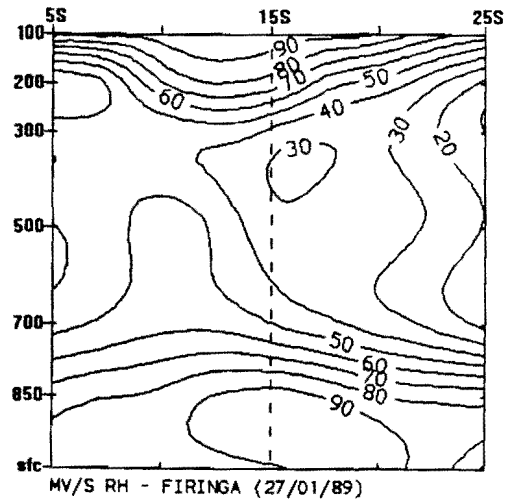

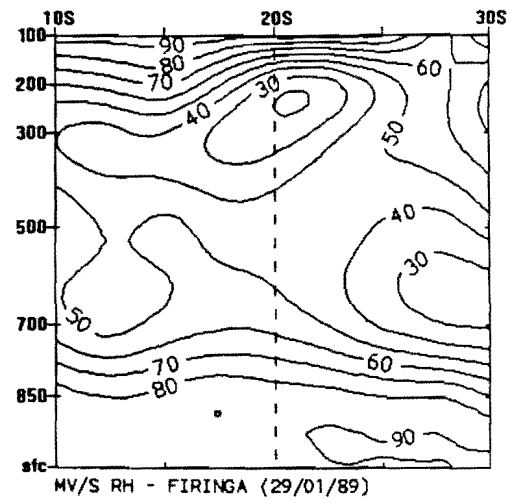

Figure B-29a,b and c : Meridional relative humidity. Contour interval is 10 %.

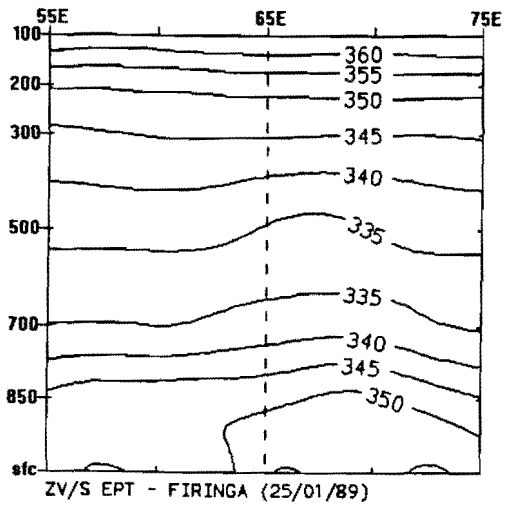

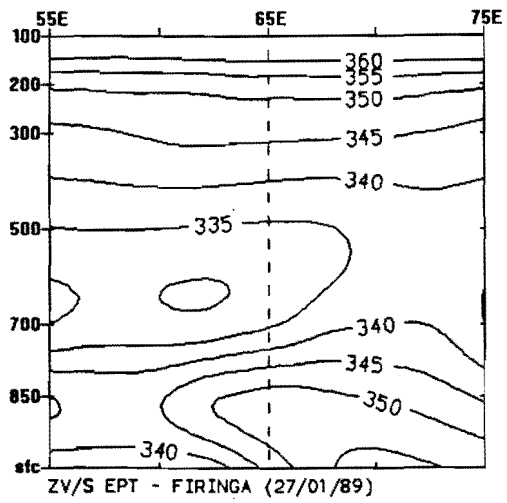

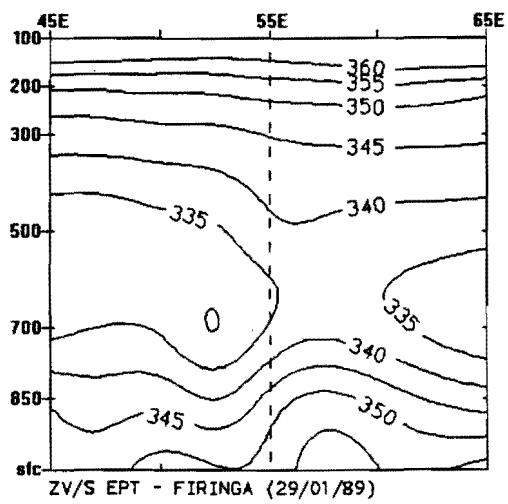

Figure B-30a,b and c : Zonal equivalent potential temperature.
Contour interval is 5 °K.

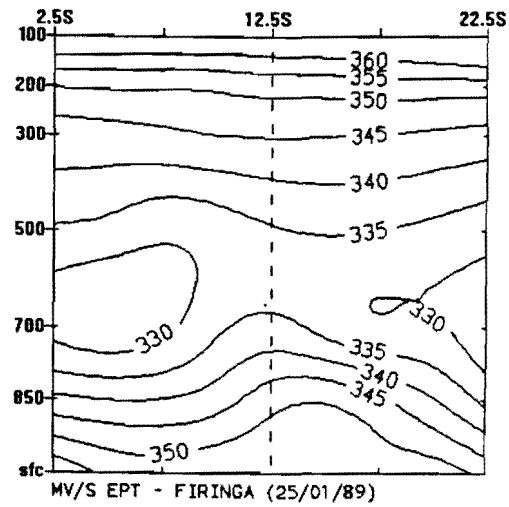

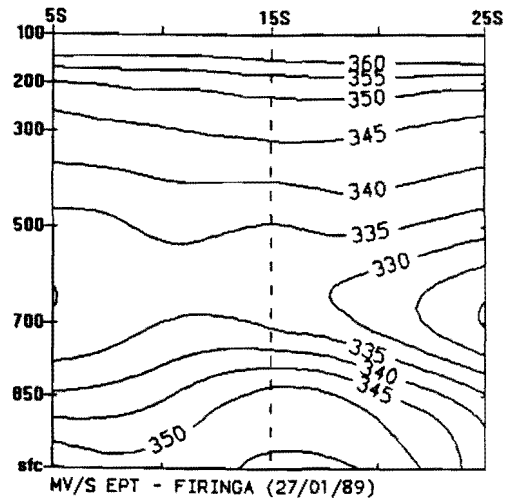

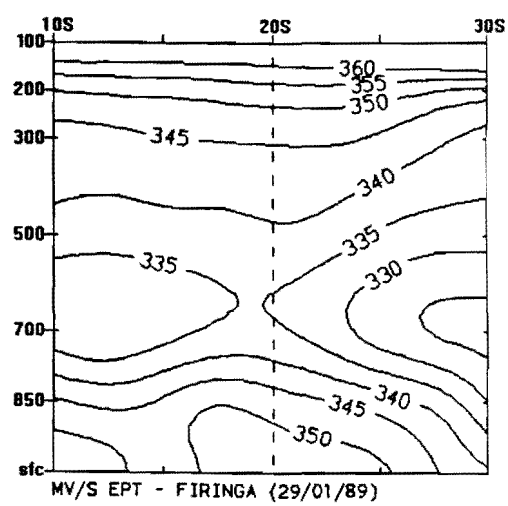

Figure B-31a,b and c : Meridional equivalent potential temperature.
Contour interval is 5 °K.